NOTICE

AVIS

The quality of this microform is heavily dependent upon the quality of the original thesis submitted for microfilming. Every effort has been made to ensure the highest quality of reproduction possible.

La qualité de cette microforme dépend grandement de la qualité de la thèse soumise au microfilmage. Nous avons tout   pour assurer une qualité   périeure de reproduction.

If pages are missing, contact the university which granted the degree.

S'il manque des pages, veuillez communiquer avec l'université qui a conféré le grade.

Some pages may have indistinct print especially if the original pages were typed with a poor typewriter ribbon or if the university sent us an inferior photocopy.

La qualité d'impression de certaines pages peut laisser à désirer, surtout si les pages originales ont été dactylographiées à l'aide d'un ruban usé ou si l'université nous a fait parvenir une photocopie de qualité inférieure.

Reproduction in full or in part of this microform is governed by the Canadian Copyright Act, R.S.C. 1970, c. C-30, and subsequent amendments.

La reproduction, même partielle, de cette microforme est soumise à la Loi canadienne sur le droit d'auteur, SRC 1970, c. C-30, et ses amendements subséquents.

UNIVERSITY OF ALBERTA

BEHAVIOR OF GIRTH-WELDED LINE PIPE

BY

© NADER YOOSEF-GHODSI

A THESIS SUBMITTED TO THE FACULTY OF GRADUATE
STUDIES AND RESEARCH IN PARTIAL FULFILLMENT OF THE
REQUIREMENTS FOR THE DEGREE OF
MASTER OF SCIENCE

IN

STRUCTURAL ENGINEERING

DEPARTMENT OF CIVIL ENGINEERING

EDMONTON, ALBERTA
SPRING, 1995

UNIVERSITY OF ALBERTA

Library Release Form

Name of Author: NADER YOOSEF-GHODSI

Title of Thesis: BEHAVIOR OF GIRTH-WELDED LINE PIPE

Degree: MASTER OF SCIENCE

Year This Degree Granted: 1995

Permission is hereby granted to the University of Alberta Library to reproduce single copies of this thesis and to lend or sell such copies for private, scholarly, or scientific research purposes only.

The author reserves all other publication and other rights in association with the copyright in the thesis, and except as hereinbefore provided, neither the thesis nor any substantial portion thereof may be printed or otherwise reproduced in any material form whatever without the author's prior written permission.

Nader Yoosef-Ghodsi

75, Piroozi-Gharbi Street
Gisha Avenue
Tehran, Iran   14477
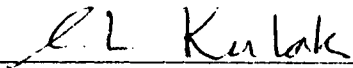
Date: *April 13, 1995*
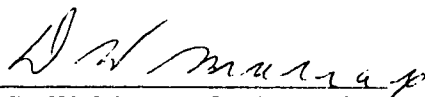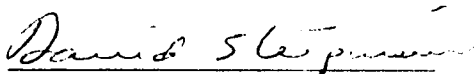
UNIVERSITY OF ALBERTA

FACULTY OF GRADUATE STUDIES AND RESEARCH

The undersigned certify that they have read, and recommend to the faculty of Graduate Studies and Research for acceptance, a thesis entitled BEHAVIOR OF GIRTH-WELDED LINE PIPE submitted by NADER YOOSEF-GHODSI in partial fulfillment of the requirements for the degree of MASTER OF SCIENCE in STRUCTURAL ENGINEERING.

_____
Dr. G. L. Kulak, Supervisor

_____
Dr. D. W. Murray, Co-Supervisor

_____
Dr. D. J. Steigmann

Date: April 13, 1995

ABSTRACT

Buried pipelines as a means of transportation of oil and gas have become increasingly important in the last few decades. As new oil and gas resources are exploited in remote regions, pipelines are being extended into more challenging environments. Two important environmental loadings, namely, temperature variation and imposed deformation are considered in this study.

One of the frequent fabrication features in steel pipelines is the presence of girth welds connecting the successive lengths of pipe. In order to study the effect of the girth weld connections on the behavior of pipelines, a series of seven tests was carried out on two sizes of girth-welded pipeline. Four specimens had a diameter of 20 in. (508 mm) and a D/t ratio of 63. The other three had a diameter of 12.75 in. (324 mm) and a D/t ratio of 50. All specimens were 1.69 m long and contained girth welds at their mid-length. The specimens were subjected to constant internal pressure, constant axial load, and monotonically increasing curvature.

The test results consist of the load vs. rotation responses and the strain, curvature, and displacement profiles along the length of each specimen. Global and local moment vs. curvature responses are also developed for the test specimens. The local buckling and wrinkling phenomena in the test specimens are studied. The wrinkling compressive strains are determined and critical strain values are recommended. Empirical equations for critical strain values are presented for both plain pipe and girth-welded pipe. It is concluded that the critical strain values used in the current guidelines are overly conservative for pressurized pipes. In the moment vs. curvature curves for the wrinkled segments (i.e., the local response), the softening point always coincided with the limit point. The presence of the girth weld connection decreased the deformation capacity and critical strain values; however, it did not affect the ultimate moments at the specimen ends significantly.

A numerical model was developed to obtain the local and global moment vs. curvature response of a pipe similar to the test specimens up to local buckling. The model is b.   remental theory of plasticity using different types of strain-hardening and stress vs   n measures. Two computer programs were developed in order to produce the local and global moment vs. curvature response of the pipe. It is concluded that updated Lagrangian formulation with isotropic-hardening is the most appropriate model for the analysis of line pipe under combined loadings.

ACKNOWLEDGEMENTS

TABLE OF CONTENTS

LIST OF TABLES

LIST OF FIGURES

LIST OF SYMBOLS

a	a positive proportionality factor in the Ziegler hardening rule
a_i	coordinates in global coordinate system for undeformed configuration
$\bar{a}$	longitudinal ordinate after the application of internal pressure and axial load
A	area of the pipe cross-section
A_0	original area of the pipe cross-section
A_i	inside area of an arbitrary infinitesimal slice of pipe in deformed configuration
C	total axial force in the pipe wall, used in Chapter 2 and 3
C	work-hardening constant in the Prager hardening rule, used in Chapter 5
C^*	prescribed value of the pipe axial force
C_A	total axial force in the pipe wall prescribed in active loading mode
C_j	curvature of the jth element of pipe used in developing global response
C_R	total axial force in the pipe wall prescribed in reactive loading mode
C_y	axial load at yielding in uniaxial loading condition, $C_y = A\,\sigma_y$
C_{ijkl}	elastic constitutive tensor
C^*_{ijkl}	elastic–plastic constitutive tensor
d	depth of the top and bottom arms in the test set-up
d_0	distance between tensile and compressive gages on undeformed section
$d\lambda$	positive factor of proportionality in the flow rule
$d\mu$	a positive proportionality factor in the Ziegler hardening rule
$\{d\varepsilon\}$	vector of principal strain increments
$\{d\sigma\}$	vector of principal stress increments
D	outside diameter of pipe
D_o	outside diameter of pipe
D_i	inside diameter of pipe
e	eccentricity of the jack load with respect to the centerline of pipe, used in Chapters 2 and 3
e	engineering longitudinal strain at an arbitrary point around the cross-section, used in Chapter 5 and Appendix E
e_0	engineering longitudinal strain of cross-section at the start of bending
e_i	engineering principal strains
E	modulus of elasticity of the pipe material

E_i Green-Lagrange principal strains

E_s effective modulus of elasticity of steel pipe (in CAN/CSA-Z662-94)

E_x Green-Lagrange longitudinal strain, $E_x = E_1$

$[E]$ elastic constitutive matrix

$f(\ )$ yield function

F eccentric load applied by the jack

F_y yield strength of the cylinder material in Sherman's study

$g(\ )$ plastic potential function

G shear modulus

h length of an infinitesimal slice at an arbitrary ordinate around the cross-section in deformed configuration

H_b horizontal component of P_i at the bottom end of pipe

H_t horizontal component of P_i at the top end of pipe

H_p plastic modulus

$\overline{H}_p$ reduced plastic modulus

k hardening parameter

$\overline{k}$ reduced hardening parameter

ℓ length of an arbitrary small length of pipe

L length of pipe

M bending moment, used in Chapters 2 and 3

M parameter of mixed hardening, used in Chapter 5

M_0 moment required to initiate yielding

M_b moment at the bottom end of pipe

M_{end} average of the two end moments

M_k moment at the kth element of pipe used in developing global response

M_P plastic moment capacity of the pipe cross-section

M_P^C plastic moment capacity of the pipe cross-section modified for axial load

$M_P^{C\theta}$ plastic moment capacity of the pipe cross-section modified for axial load and internal pressure

M_t moment at the top end of pipe

$\overline{M}$ initial moment in Step 4 of the algorithm for developing local response

N_C prescribed number of curvature increments used in developing local response

N_{el} number of elements around one-half of cross-section

p internal pressure of pipe

p_0 pressure at the first occurrence of the proportional limit

p_e external pressure in pipe (in CAN/CSA-Z662-94)

p_i internal pressure in pipe (in CAN/CSA-Z662-94)

p_y internal pressure when the hoop stress equals the yield stress

P concentric load applied by the testing machine, used in Chapters 2 and 3

P^* prescribed value of the load applied by the testing machine

$P^{\bullet}$ prescribed e~·~rnal axial load

P_0 axial load r ʌ· d to reach the proportional limit

P_{cal} calculated external axial load

P_i tensile axial force in the pipe wall due to internal pressure

$\overline{P}$ initial axial load in Step 3 of the algorithm for developing local response

q distributed resultant load of the pressure forces (acting in the plane of bending)

Q a constant in terms of Lame's constants, $Q = \dfrac{\lambda_E^2}{2G + \lambda_E}$

R radius of bending neutral axis

R_i inside radius of pipe

R_m average of inside and outside radii

s_i 2nd Piola-Kirchhoff principal stresses

s_{ij} 2nd Piola-Kirchhoff stress tensor

S cross-section modulus

S_{ij} deviatoric stress tensor (generic)

$\overline{S}_{ij}$ reduced deviatoric stress tensor (generic)

$\overline{S}_i$ reduced deviatoric principal stresses (generic)

$\overline{S}_x$ reduced deviatoric longitudinal stress (generic), $\overline{S}_x = \overline{S}_1 = \overline{S}_{11}$

$\{\overline{S}\}$ vector of reduced principal deviatoric stresses (generic)

t thickness of pipe

T_l longitudinal force acting on the cross-section

T_o operating temperature of pipe

T_ℓ ambient temperature when pipe is laid down

$T_i^{(k)}$ virtual forces used to define 2nd Piola-Kirchhoff stress

u_i displacement in the ith direction of the coordinate system (x_1, x_2, x_3)

U resultant of the pressure forces (acting in the plane of bending)

v deflection of the centerline of pipe

V_b	vertical component of λ_i at the bottom end of pipe
V_t	vertical component of P_i at the top end of pipe
x	ordinate of pipe cross-section measured from the bottom end of centerline
x_i	coordinates in global coordinate system
y	ordinate of an arbitrary point around the cross-section measured from the center, used in Chapter 3
y	ordinate of an arbitrary point around the cross-section measured from the bending neutral axis, used in Appendix E
y_1	depth of the strain gages from the center of the pipe cross-section
y_2	depth of the extreme fibers from the center of the pipe cross-section
y_k	deflection of the kth element of pipe used in developing global response
α	Slenderness parameter in Sherman's study, $\alpha = (E / F_y) / (D / t)$, used in Chapter 1
α	thermal expansion coefficient for the pipe material, used in Chapter 2
α	rotation of the centerline of pipe, used in Appendix E
α_{ij}	coordinates of the yield surface center in stress space
β	prescribed tolerance in determining the position of the bending neutral axis
β_C	prescribed tolerance in determining deformed configuration of pipe
$\{\delta\sigma\}$	stress correction vector
Δ_P	stroke of the testing machine
Δ_P^*	limiting value for the stroke of the testing machine
Δ_F	stroke of the jack
ΔT	temperature differential
$\Delta\varepsilon_x$	longitudinal strain increment for a small element of cross-section
$\Delta\varepsilon_x^*$	strain increment that moves the stress state onto the yield surface
ε	longitudinal strain at an arbitrary point around the cross-section
ε^c	longitudinal strain at the compressive gage location
ε_1^c	longitudinal strain at the strain gage location on the compression side
ε_2^c	longitudinal strain at the extreme compression fiber
ε_c^{crit}	compressive strain limit (in CAN/CSA-Z662-94)
ε^t	longitudinal strain at the tensile gage location
ε_1^t	longitudinal strain at the strain gage location on the tension side
ε_2^t	longitudinal strain at the extreme tension fiber
ε_i	true (logarithmic) principal strains

ε_i	principal strains (generic)
ε_{ij}	true (logarithmic) strain tensor
ε_{ij}	strain tensor (generic)
ε_{ij}^e	elastic strain tensor (generic)
ε_{ij}^i	isotropic portion of the plastic strain tensor (generic)
ε_{ij}^k	kinematic portion of the plastic strain tensor (generic)
ε_{ij}^p	plastic strain tensor (generic)
ε_L	local strain
ε_m	longitudinal strain at mid-section
ε_O	overall strain
ε_p	effective strain
$\bar{\varepsilon}_p$	reduced effective strain
ε_s	softening strain
ε_x	longitudinal strain (generic), $\varepsilon_x = \varepsilon_1 = \varepsilon_{11}$
ϕ	curvature
ϕ_0	curvature at the first yield during bending
ϕ^*	prescribed upper limit of curvature used in developing local response
$\bar{\phi}$	initial curvature in Step 4 of the algorithm for developing local response
γ	a proportionality factor used in correction vector
λ	stretch (current length divided by the original length)
λ_E	Lame's constant, $\lambda_E = \dfrac{\mu E}{(1+\mu)(1-2\mu)}$
μ	Poisson's ratio for the pipe material
θ	relative rotation of the pipe ends, $\theta = \theta_b + \theta_t$
θ_b	absolute rotation of the bottom arm
θ_{end}	rotation at each end of pipe used in developing global response
θ_t	absolute rotation of the top arm
σ_0	longitudinal stress in a thin-walled, closed-ended pipe that is elastic and subjected to internal pressure only, $\sigma_0 = \dfrac{p R_i}{2t}$
σ_e	effective stress

$\overline{\sigma}_e$ reduced effective stress

σ_i engineering principal stresses

σ_i principal stresses (generic)

σ_{ij} engineering stress tensor

σ_{ij} stress tensor (generic)

σ_p proportional limit of the pipe material

σ_x longitudinal stress (generic), $\sigma_x = \sigma_1 = \sigma_{11}$

σ_y specified minimum yield stress of the pipe material

σ_θ hoop stress (generic), $\sigma_\theta = \sigma_2 = \sigma_{22}$

$\overline{\sigma}_i$ Reduced principal stresses (generic)

$\overline{\sigma}_{ij}$ Reduced stress tensor (generic)

τ_i true (Cauchy) principal stresses

τ_{ij} true (Cauchy) stress tensor

ψ position angle around the cross-section of pipe

ψ_0 position angle of the bending neutral axis

ζ a positive constant in terms of Lame's constants, $\zeta = \dfrac{4G\,(G + \lambda_E - Q)}{2G + \lambda_E - Q}$

1 INTRODUCTION AND LITERATURE REVIEW

1.1 INTRODUCTION

In the last few decades, buried pipelines have become more widespread as a means of transporting oil and gas. They are replacing other means of transportation in oil and gas industries as the most economical alternative. As new oil and gas resources are explored in remote regions, such as the Arctic and sub-Arctic, pipelines are being extended into new and more severe environments. This requires a better understanding of pipeline behavior and rational design procedures to address all the potential adverse conditions.

Two important environmental loadings are those due to temperature variation and imposed deformation. The effect of temperature variation on a long pipeline appears as axial force. Imposed deformation for a pipeline can be produced by factors such as slope movements, frost heave, and thaw settlements. The most important effect of imposed deformation is the bending of the pipe due to the imposed curvature. Pipelines subjected to imposed deformation often deform into elastic–plastic range. Because of the self-limiting nature of the deformations arising from imposed deformations, the load-carrying capacity is not a major concern. However, the pipeline may not remain functional under the imposed deformation, and this then becomes a design consideration.

One of the frequent fabrication features in steel pipelines is the presence of girth welds connecting the successive lengths of pipe. There have been no systematic experimental studies in the past on the effect of girth welds on the structural behavior of the pipe. However, it is obvious that the girth weld connection introduces residual stresses and imperfections into the pipeline, and the resultant behavioral effects need to be investigated. A series of tests on girth-welded pipe specimens comprise the first part of this project. The specimens are subjected to constant internal pressure, constant axial load, and monotonically increasing curvature. The latter two features idealize the thermal and differential settlement effects. A comparison of the test results with the results of the tests on plain pipes carried out at University of Alberta by Mohareb et al. (1994) will lead to a better understanding of the structural implications of girth weld connections.

In the second part of this project, a numerical model is developed to obtain the analytical moment vs. curvature response of a pipe similar to the test specimens up to local buckling. The model is based on incremental theory of plasticity for a strain-hardening material.

1.2 OBJECTIVES

This project is one of four studies on pipeline behavior that have been carried out at University of Alberta over the past six years. The tests on plain pipes have been performed by Mohareb et al. (1994) and numerical investigations have been carried out by Zhou and Murray (1993), Souza and Murray (1994), and Mohareb et al. (1994).

The present research has the following objectives:

1. To establish an experimental data base for the structural response of girth-welded pipes under conditions similar to those which they are subjected to in the field.

2. To compare these test results with the results of the tests on plain pipes in order to determine the effects of girth welds on the structural behavior of pipe.

3. To define and propose a more rational basis for determination of the critical compressive strain than is presently available in design codes for pipelines.

4. To develop a numerical model, based on incremental theory of plasticity, to predict the local and global moment vs. curvature responses of pipes up to the point of wrinkling.

1.3 LITERATURE REVIEW

1.3.1 General

Buried pipelines must be able to function in complex environments. They are laid in various types of terrain and subjected to different environmental loads. This gives rise to a variety of structural problems. A number of these involve local shell buckling, soil-structure interaction, and combinations of externally applied loads and imposed deformations.

Despite the significance of imposed deformations in the design of pipelines, the current specifications for pipeline design do not fully address the problem. This is because

imposed deformation usually produces plastic deformations in the pipe, whereas the current specifications are based on working stress design principles (elastic design). Recently, however, there has been an attempt to introduce limit states design into the Canadian code (CAN/CSA-Z662-94) through Appendix H, which is still in draft form. The design procedure in the code, the literature on limit states design, and the draft Appendix H are discussed in Sections 1.3.2, 1.3.3, and 1.3.4, respectively.

The experimental and analytical studies done in the past on the behavior of cylindrical shells under different loading are reviewed in Sections 1.3.5 and 1.3.6, respectively.

1.3.2 Design Procedure in the Canadian Standard

The current Canadian design code for pipeline design (CAN/CSA-Z662-94) is based on linear elastic stress analysis. The stress design requirements in the code are based on the design conditions for operating pressure, thermal expansion, temperature differentials, and sustained force and wind loadings. According to Clause 4.2.4.1 of the Standard, no additional loading other than the specified operating loads is specifically addressed; however, the designer is required to determine whether supplemental design criteria are necessary for such loadings and whether additional strength or protection against the damage modes, or both, should be provided. Such additional loadings, as identified in the Standard, include slope movements, fault movements, seismic-related earth movements, thaw settlement, frost heave, loss of support, and deformations resulting from construction and maintenance. These imposed deformations normally result in nonlinear response, which is not covered by the Standard.

The general design criteria for pipeline systems, as stated in Clause 4.6.1.1 of the Standard, provide design specifications for:
(a) design wall thickness;
(b) maximum allowable temperature differential in restrained sections;
(c) maximum allowable freely supported spans for axially restrained sections;
(d) minimum required flexibility in partially or fully unrestrained sections;
(e) maximum allowable support spacings for stress design of unrestrained sections; and
(f) maximum allowable cold-sprung reactions on equipment attached to flexible piping.

1.3.3 Limit States Design of Pipelines

The current Canadian design standard (CAN/CSA-Z662-94) is based on working stress design, which is relatively simple in application because it requires only linear elastic analysis. However, it does not deal with the failure conditions directly. The working stress design concept attempts to control undesirable effects indirectly by requiring that the structure have a factor of safety against the yielding of the pipe material under normal operating conditions. As a result, the design produced has variable levels of safety for different failure conditions.

The limit states design concept, on the other hand, is based on a direct evaluation of each of the limit states; thus, a more uniform level of safety can be achieved. A safe and economic design can be obtained with greater clarity and rationality for each of the limit states if every potentially unsatisfactory condition is identified as such a state. Consequently, the analytical approach for limit states design should be able to predict the response of the structure up to the attainment of all of its limit states. This means that the analytical approach consistent with limit states design must be based upon nonlinear analysis, including both large displacements and nonlinear material response.

Price (1978, 1987, and 1991) proposed supplemental limit states criteria to protect against deformation-related failure and damage modes that may be caused by various additional loadings in unstable ground. Supplemental limit states design criterion required that the following condition be satisfied (Price and Barnette, 1987):

Factored limit resistances $\geq$ Structural response to operating loads and factored additional loads

The failure and damage modes included the fracture initiation, wrinkling, denting and flattening, snap-through collapse, stability, and plastic cycling and fatigue. The limit resistance for the wrinkling failure mode was specified by a maximum allowable compressive stress. Price and Barnette (1987) also proposed monitoring and maintenance limit states criteria. In a general form, this required that:

Factored limit resistances $\geq$ Measured pipe deformations or loads computed from measurements

This was considered necessary for areas where geotechnical or other loadings are uncertain and the risk of exceeding any of the specified resistance levels is excessive. This requires a monitoring system capable of tracking deformations of the pipeline at sufficient locations and with sufficient accuracy.

Row et al. (1987) developed a limit states probabilistic design method for offshore Arctic pipelines. The potential failure and damage modes that need to be avoided were reviewed. A new probabilistic load and load combination methodology was then presented. Thereby, a limit states design approach was developed and preliminary design criteria were recommended.

Lara (1987) studied the wrinkle growth of pressurized pipe under bending moment using finite element analysis. The study was conducted in three parts. First, an analytical model was validated by comparing its results with those of tests conducted by Bouwkamp and Stephen (1973) (which will be discussed in Section 1.3.5.2). Thus, the conditions for the wrinkle onset were established. In phase two, a study of the wrinkle growth was undertaken to assess the level of conservatism of the then-current design criteria. A sensitivity study to evaluate the effect of the pipe design parameters (i.e., internal pressure, fluid temperature, pipe wall thickness, and pipe material type) was undertaken. Finally, the effect of depressurization events on the growth of the wrinkle was modeled. It was concluded that:

1. In the case of low operational pressures, where the wrinkle forms in an inward mode, the wrinkle onset is an adequate failure criterion. However, the wrinkle onset criterion is too conservative if the wrinkle occurs in an outward mode.

2. The critical strain after which rapid wrinkle development occurs is a more rational failure criterion than the strain at wrinkle onset. The maximum allowable strain on a pipe subjected to internal pressure, compression, and bending was thus obtained as follows:

   2.5 – 3.5 %   for internal pressure = 917 psi (6.32 MPa)
   0.4 %   for internal pressure =   25 psi (0.17 MPa)

3. The critical axial compressive strain was not sensitive to compressive load within the range of the loads considered.

4. Thicker pipe wall favors inward over outward wrinkles, thereby reducing the critical axial compressive strain.

5. Increasing the yield strength of the pipe reduces the critical axial compressive strain, but does not change the wrinkle shape.

Zhou and Murray (1993) defined the critical compressive strain as the compressive strain corresponding to the point at which the first significant softening on the moment vs. curvature curve is seen. The criterion for the initiation of significant softening was expressed as

Predicted maximum compressive strain $\leq$ Limiting compressive strain

According to Zhou and Murray, this criterion is not a limit states criterion; however, it is a good alternative to the criterion based on buckling strain until rational deformation limit states can be established. Improved deformation criteria were also proposed to prevent various ultimate and serviceability limit states.

1.3.4 Draft Appendix H for CAN/CSA-Z662-94

Recently, an attempt has been undertaken to introduce limit states design into the Canadian Standard (CAN/CSA-Z662-94). Appendix H of the Standard, which is still in draft form, provides guidance for the design of steel oil and gas pipelines based on the limit states method. It is intended to provide supplemental design criteria for loading conditions that are outside the scope of Clause 4.0. These loading conditions mainly consist of imposed deformations, such as slope movement, thaw settlement, frost heave, and seismic-related earth movement.

Clause H2.2 defines five safety categories. They are based on risk to life and to the environment and on the potential for economic loss. Two categories of limit states are to be considered. They are ultimate limit states and serviceability limit states, as described in the following (Clause H3.4.1).

Ultimate limit states can result in burst or collapse of the pipeline. They include (Clauses H3.4.2)
(a) loss of pressure integrity (i.e., membrane rupture);
(b) overall instability;
(c) large inelastic deformations; and
(d) fatigue or brittle fracture resulting in membrane rupture.

Serviceability limit states restrict the normal operation of pipeline or affect its durability. They include (Clauses H3.4.3)
(a) displacements or deformations that adversely affect the operation of the pipeline;

(b) local damage (e.g., local yielding, stable wrinkle growth, dents, corrosion, and non-through-thickness cracking) that adversely affects the use or durability of the pipeline; and

(c) motion, including vibration, that adversely affects the operation or durability of the pipeline.

According to Clause H5.3.1, plastic theory can be used to analyze pipe sections and pipe systems capable of developing and sustaining inelastic deformations. Such systems should satisfy requirements as to tensile and compressive strain limits, deformation limit, repeated yielding, effects of depressurization, and fatigue.

The limit on compressive strain has been set as the value of the compressive strain at the point of wrinkle initiation. This is normally taken to occur at the peak in the moment vs. curvature response. Accordingly, the compressive strain limit is given by the following formula, which was developed by Gresnigt (1986):

$$\varepsilon_c{}^{crit} = 0.5\frac{t}{D} - 0.0025 + 3000\left[\frac{(p_i - p_e)D}{2tE_s}\right]^2 \tag{1.1}$$

where t is the pipe wall thickness, D is the outside diameter, p_i is the internal pressure, p_e is the external pressure, and E_s is the effective modulus of elasticity of he steel pipe. It is admitted in the Commentary to the Appendix that the integrity of the pipeline can be preserved well past its peak bending strength. Therefore, the above limit for compressive strain can be overly conservative.

1.3.5 Experimental Studies

1.3.5.1 General

A large number of experimental studies to investigate the buckling behavior of cylindrical shells have been performed in the past. Most of them, however, focused on the buckling strength rather than on buckling strains. This is because, traditionally, the load-carrying capacity and not the deformation capacity has been the center of attention. Consequently, the design for imposed deformations receives little attention in the current design guidelines. Only a few experimental studies have considered the buckling strain and post-buckling behavior of the cylindrical shells.

The testing programs conducted by Bouwkamp and Stephen (1973 and 1974), Jirsa et al. (1972), Korol (1979), Reddy (1979), Sherman (1986), Kyriakides and Ju (1992), Mohareb et al. (1994), and Hu et al. (1993) are reviewed in the following subsections. Note that the tests by Hu et al. were carried out on large diameter tubes. Because of their fabrication process, these tubes contain a much higher level of imperfection than do line pipes.

1.3.5.2 Tests by Bouwkamp and Stephen (1973 and 1974)

Bouwkamp and Stephen (1973 and 1974) conducted a series of tests on pipe of the type that was to be used in the trans-Alaska pipeline. Seven specimens were fabricated from 48-inch diameter longitudinally seam-welded pipe. Each specimen was subjected to constant internal pressure, constant axial load, and increasing lateral load. A four-point loading system was used for the lateral load to produce pure bending in the central section of the pipe, between the two point loads. This section (called test section) was fabricated from X60 pipe with a nominal wall thickness of 0.462 in. (11.7 mm) and a yield strength of 60 ksi (413.7 MPa). In order to study the effects of full-penetration girth welds, the test sections contained girth welds at their mid-length. Three levels of internal pressure were applied: high pressures at 150 and 950 psi (1.03 and 6.55 MPa) and low pressure at 25 psi (0.17 MPa). The axial load was applied at two levels, which corresponded to the temperature differentials of 135° and 90° F. (57.2° and 32.2° C)

The results from the first test showed that the operational integrity of the pipe would not be diminished by initial development of the buckling. Therefore, the subsequent tests continued into the post-buckling region so as to measure the post-buckling strength and ductility.

The displacements at rupture were observed to be up to 20 times those under which buckling occurred. Under high internal pressure, the pipe wall exhibited an outward deformation over the total compression zone, and this extended over at least two-thirds of the pipe circumference. However, under low internal pressure the pipe wall exhibited the more common diamond-shaped inward–outward buckle. The compressive strain at buckling for these specimens ranged from 0.23 to 0.82.

1.3.5.3 Tests by Jirsa et al. (1972)

Jirsa et al. (1972) carried out a series of tests on six specimens of pipe with diameters ranging from 10.75 to 20 in. (273 to 508 mm) and with D/t ratios ranging from 30 to 80. Four of the pipes were uncoated and two were coated with concrete. The objective was to investigate the influence of ovaling on the flexural behavior of pipelines stressed beyond elastic limit. The pipes were tested as simple beams supported at the ends and loaded at two points within the span to produce a region of pure flexure. Thus, the only loading was bending. The moment vs. curvature curve was reported for each specimen. It was concluded that ovalization did not significantly reduce the moment capacity of the pipe until strains well into plastic region were developed.

1.3.5.4 Tests by Korol (1979)

Korol (1979) performed a series of 11 tests on single and double-span circular hollow tubular beams to evaluate the inelastic bending and axial compression theories of buckling. The double-span tests were carried out to ensure that the redistribution of moments would occur and thereby to identify the plastic design sections. The effects of strain-hardening and the yield strength on the limiting D/t ratios were examined for the various categories of design. It was concluded that for ductile materials, which have an essentially bilinear stress vs. strain curve and a small degree of strain-hardening, the buckling strain is inversely proportional to the yield stress raised to an exponent lying between 0.5 and 1. For elastic–plastic case, the exponent tends to 1, whereas, for a high tangent modulus and small D/t ratio, it tends toward zero. In addition, ovalization was found to have a relatively small effect on the moment capacity because local buckling occurred before large reductions in moment capacity were observed. Therefore, local buckling, rather than ovalization, was determined as the principal cause of the failure.

1.3.5.5 Tests by Reddy (1979)

Reddy (1979) carried out a series of tests on stainless steel and aluminum alloy tubes with a nominal diameter of 25 mm to investigate the plastic buckling of tubes subjected to bending moment. The D/t ratios of the ten steel tubes were in the range of 42 to 78, and those of the nine aluminum tubes were in the range of 34 to 58. Pure bending moment was applied to the specimens by four-point loading. The ratio of the unsupported length to the diameter of the test specimens was about 12; thus, the end conditions would be expected to have a negligible effect on the sections of the specimens away from the ends. Some results are summarized as follows.

1. One important observation was the appearance of wave-like ripples on the compression sides of the specimens before collapse took place. The ripples were first detected when the bending moment was about one-half the maximum value. This was attributed to the influence of the imperfections. The relatively small amounts of ovalization indicated that buckling was largely due to the growth of the ripples (bifurcation). The sine-wave nature of the ripples led to the hypothesis that the test specimens behaved as imperfect cylinders and the imperfections gave rise to a steady growth of the ripples.

2. The wavelengths of the ripples were considerably less than those predicted by the bifurcation theory based on either incremental or deformation theory of plasticity.

3. The compressive strains at the intrados were found to be slightly higher than the tensile strains at the extrados.

4. The maximum compressive strain at buckling ranged from 0.75 to 1.76 percent for the steel specimens, and from 0.70 to 1.98 percent for the aluminum alloy specimens.

1.3.5.6 Tests by Sherman

Sherman (1986) conducted a series of tests on round tubes with outside diameter of 10.75 in. (270 mm). The objective was to determine the moment redistribution capabilities of round tubes and to evaluate the application of plastic design principles to the tubes subjected to flexure. Eighteen specimens were tested. The D/t ratio ranged from 18 to 102 and there were three arrangements of support conditions. Three specimens were 10-ft. long (3.41 m) cantilevers with end loading. Six specimens were 12-ft. long (3.66 m) simply supported beams with third point loadings. The remaining nine specimens were fixed-end beams with third point loadings and lengths of 20 ft. (6.10 m) and 50 ft. (15.24 m).

The observed inelastic collapse and post-buckling behavior of the specimens in bending were grouped in three categories. This was carried out by using a slenderness limit $\alpha = (E / F_y) / (D / t)$, where E and F_y are the modulus of elasticity and yield strength of the material, respectively.

(a) For values of α greater than 22, a long plastic plateau developed in the moment vs. curvature curve. The pipe gradually ovalized and eventually the buckling waves formed, after which the load slowly decayed. In some cases, one of the waves became a single dominant local buckle.

(b) For values of α between 10 and 22, a single buckle gradually formed and the load decayed slowly with little or no plastic plateau region.

(c) For values of α less than 10, several buckles formed, with very little ovalization, and the bending moment dropped rapidly to a more stable level

As a result of the observation of the bending tests and some theoretical discussions, it was concluded that ovalization is the dominant type of instability governing the inelastic bending capacity. However, the instability is not because of a reduction in the section modulus due to flattening. Ovalization leads to the formation of an inward local buckle, which controls the subsequent load decay. If ovalization is prevented by end stiffening and a steep moment gradient (as is the case for cantilevers), the bifurcation buckling mode becomes dominant.

1.3.5.7 Tests by Kyriakides and Ju (1992)

Kyriakides and Ju (1992) conducted experiments on long aluminum 6061-T6 shells with 11 different D/t ratios ranging from 19.5 to 60.5. The diameter of the cylinders ranged from 25.34 to 38.10 mm and their length-to-diameter ratios ranged from 18.1 to 30.1. From the observations in the tests, the shells were divided into the following three categories. Note that the following D/t limits for the three categories were considered to be approximate and varying with the shell material properties.

(a) D/t > 40

In this category (relatively thin shells), the dominant mode of instability was short-wavelength rippling. The specimens ovalized uniformly up to collapse. The short-wavelength ripples were observed in small pockets randomly distributed along the length. They appeared shortly before the shell collapsed and their amplitude grew locally in a non-uniform manner. The specimens collapsed suddenly when a second instability occurred in one of the ripple pockets. The collapse formed in diamond-shape mode. It was judged that the post-buckling strength of these cylinders was too small to be of structural use.

(b) 26 < D/t < 40

In this category (moderately thick shells), short-wavelength rippling again dominated the instability. Unlike the previous category, a distinct limit moment occurred prior to failure in the moment vs. curvature response of the specimens in this category. In addition, ovalization grew non-uniformly until just before the failure. The localized deformation was 8–10 diameters long. The trough of the localized region usually contained pockets of short-wavelength ripples. After attaining the limit load, the shell collapsed suddenly by the formation of a sharp local kink (diamond shape), originated from the ripples.

(c) D/t < 26

For this category (relatively thick shells), response to bending was governed by the limit load instability caused by uniform ovalization. Long wavelength imperfections were amplified near the limit load. Following the limit load, the ovalization began to grow non-uniformly along the length and localized significantly. It was concluded that the localization was a direct result of the limit load instability and controlled the behavior of the shell after the limit load. Consequently, the limit load calculated by the assumption of uniform ovalization was very close to the actual value.

1.3.5.8 Tests by Mohareb et al. (1994)

Mohareb et al. (1994) carried out a series of tests at the University of Alberta on seven line pipe specimens. Four of the specimens had a diameter of 20 in. (508 mm) and a D/t ratio of 63. The other three had a diameter of 12.75 in. (324 mm) and a D/t ratio of 50. All specimens were 1.69 m long. The specimens came from the same lengths of pipe as used subsequently in the experimental program documented in this report. The objective of the tests by Mohareb et al. was to determine the strain at the onset of wrinkling and to study the post-buckling behavior of pipe segments subjected to combined axial load, internal pressure, and bending moment. In the following chapters of this report, the results of these tests carried out on plain pipes are cited and compared with the results of the tests on the girth-welded pipes conducted herein.

1.3.5.9 Tests by Hu et al. (1993)

Hu et al. (1993) carried out a series of tests on tubes that had a nominal inside diameter of 430 mm and had lengths of 1.5 m and 1.0 m. The wall thicknesses for the

tubes ranged from 4.5 mm to 9 mm and the D/t ratio for the tubes ranged from 50 to 100. The objective of the research was to examine the influence of imperfections on the strength of fabricated tubular beam-columns used in offshore structures. Unlike pipes, such tubes are fabricated in the shop by cold-rolling plates into cylindrical components. These are then seam and girth welded to one another to create the tubular shape. The tubes produced in this fashion have much higher levels of imperfections than do line pipes.

A finite element modeling of the test specimens followed the experimental program. For the analysis, the elastic–perfectly-plastic stress vs. strain relationship, obtained from the tension coupon tests of the virgin plate, gave unsatisfactory results. However, a bilinear kinematic-hardening material relationship, obtained from the tests on coupons cut from the tube after cold-rolling, gave analytical load vs. displacement responses that fit closely with the experimental data.

It was found that the mismatch at abutting ends was the principal factor in the initiation of local buckling. In addition, the effects of out-of-straightness and out-of-roundness on the ultimate strength of the cross-section were found to be negligible.

1.3.6 Analytical Studies

1.3.6.1 General

The local buckling of cylindrical shells in bending is characterized by two phenomena. These are ovalization and the localization of the buckling waves, and they may act alone or in combination.

Kim (1992) concluded from previous studies on cylindrical shells that the predominance of each of the two phenomena is determined by the D/t ratio, level of initial imperfections, pipe length and end conditions, and internal pressure.

The buckling phenomenon in cylindrical shells subjected to bending is further discussed in following subsections, where the work of Tvergaard and Needleman (1983), Corona (1983), and Ju and Kyriakides (1992) is reviewed.

1.3.6.2 Analysis by Tvergaard and Needleman (1983)

Tvergaard and Needleman (1983) studied the development of the localized buckling patterns from a broad point of view. They realized that presence of a periodic

buckling pattern is a common feature in a wide variety of structures subjected to compression. Examples of such structures are axially compressed elastic–plastic plate strips, cylindrical shells under compression or bending, elastic–plastic columns continuous over several equally spaced supports, and railway tracks subjected to thermally induced compressive forces.

Tvergaard and Needleman stated that for a cylindrical shell under bending, at or subsequent to the attainment of a maximum load, the initial periodic buckling pattern loses uniqueness. This initiates the mechanism of localization (involving bifurcation), which leads to the final buckled configuration, involving only one or a few buckles.

1.3.6.3 Analysis by Calladine (1983)

Calladine (1983), considering Reddy's test results (discussed in Section 1.3.5.5), rejected the bifurcation theory. Calladine stated that the ripples observed in Reddy's tests were not formed by bifurcation, but by a process of *propagation* from the end-fixings of the specimens soon after the specimen entered the plastic range. Calladine assumed that the ripples formed shortly after the intrados became plastic, and that they behaved as if a longitudinal strip of rippled material has a compressive stress vs. strain curve similar to that of a perfectly-plastic material. Based on these assumptions, Calladine performed a modified analysis of ovalization to obtain the maximum moment and critical compressive strain. The resulting analytical relation for the critical compressive strain agrees approximately with the Reddy test results.

1.3.6.4 Analysis by Ju and Kyriakides (1992)

Ju and Kyriakides (1992) carried out a theoretical investigation concerned with the prediction of the responses of the cylinders they obtained in their experimental program (discussed in Section 1.3.5.7). They formulated the problem using Sander's shell kinematics (Sanders 1963) and the principle of virtual work. The discretization of the problem was done by a Rayleigh-Ritz procedure. Three types of behavior were studied. These were bifurcation into short-wavelength ripples, localization following the attainment of a natural limit load (peak moment due to ovalization), and the interaction of the two. The analytical responses were found to be in good agreement with the corresponding test results. The analytical predictions for the behavior of the test specimens are summarized as follows.

The thinner shells (D/t > 40 for aluminum 6061-T6 shells) bifurcated at an increasing moment. The buckling mode consisted of axially periodic ripples on the compression side. The uniform growth of the amplitude of the ripples reduced the rigidity of the shell and this resulted in the development of a limit load. This occurred at a curvature that was significantly smaller than that corresponding to the natural limit load. Subsequently, the ripples localized and the moment dropped. A second bifurcation occurred in the ripple with the most severe deformation. This buckling mode consisted of circumferential waves. The second bifurcation and the softening nature of the response prior to it led to a catastrophic collapse.

In the case of the thicker shells (D/t > 28 for aluminum 6061-T6 shells), ovalization occurred along a localization length, which was a few diameters long. The deformation and the length of the localized region were governed by local equilibrium and not by the overall length of the cylinder. However, the overall moment vs. curvature response following the limit load was significantly affected by the overall length of the cylinder. As the overall length increased, the moment decreased at a much faster rate with curvature.

For the shells with intermediate values of D/t ratio (28 < D/t < 40 for aluminum 6061-T6 shells), the presence of small imperfections had only a relatively small effect on the predicted response up to the first bifurcation point. As was the case for the thinner shells, the first bifurcation produced short-wavelength ripples with growing amplitudes. The bias imposed by the imperfection was amplified and the growth of the ripples localized. The moment developed a maximum and dropped rapidly thereafter. Prior to the peak moment, a second localization occurred. It involved a few diameters of the cylinder on either side of the rippled section. As was the case for the thinner shells, a second bifurcation took place in the largest amplitude soon after the limit point. The limit load occurred at much smaller curvature than was the case for the uniformly ovalized shell. It was concluded that the short-wavelength ripples were the triggering mechanism for the sequence of the events that led to collapse.

1.4 LAYOUT OF THE THESIS

The remainder of this report consists of five Chapters and five Appendices. The major subjects and scope of each of the following chapters and appendices are summarized as follows.

Chapter 2 describes the experimental phase of the study. The test set-up and loadings for different specimens are reported, and the fabrication of the test specimens, instrumentation, and test procedure are described.

Chapter 3 presents the experimental results. They consist of the load vs. rotation responses and the strain, curvature, and displacement profiles along the length of each specimen. Global and local moment vs. curvature responses are also developed for the test specimens.

Chapter 4 discusses the experimental results. It compares the moment vs. cι ⸱ ⸱ses of the test specimens (girth-welded) with those of the plain pipes used by ⸱ ⸱. (1994). The local buckling and wrinkling in the test specimens are stud.. ⸱ inkling compressive strains are determined ⸱⸱d critical strain values are recomₙ.. ⸱. Empirical equations for critical strain values are presented for both plain pipe and girth-welded pipe.

Chapter 5 presents the second phase of the study, the numerical investigation. An incremental stress vs. strain formulation is used to develop the local moment vs. curvature response of a pressurized pipe up to local buckling. The numerical model considers different types of strain-hardening. A computer program is developed based on the numerical model.

Another computer program is developed to obtain the global moment vs. curvature response of a pipe with the boundary conditions and loading sequence similar to those for the test specimens. The local and global responses for the test specimens are predicted by the numerical model using different types of strain-hardening and stress vs. strain measures. The numerical results are then compared with the experimental results obtained in Chapter 3.

Chapter 6 summarizes the results of the experimental and numerical parts of this study.

Appendix A is a manual for the program developed to obtain the local moment vs. curvature response of the pipe (PAPS), and Appendix B contains the FORTRAN listing of the program. Appendix C is a manual for the program developed to obtain the global

moment vs. curvature response of the pipe (PDA), and Appendix D contains the FORTRAN listing of the program.

Appendix E develops formulae for converting and relating the different stress vs. strain measures used in Chapter 5. The curvature, as defined in this study, is related to the stress vs. strain measures in Section E.2.

2 EXPERIMENTAL PROGRAM

2.1 INTRODUCTION

The experimental program established to investigate the behavior of girth welded pipes had a two-fold purpose. One was to provide an experimental database that would enable direct comparisons with predictive methods. The other was to provide a comparison of the experimental results for pipes with transverse girth welds to the previous results for plain pipes (i.e., without transverse girth welds). Comparisons are made in various aspects; namely that of moment capacity, ductility, strains and buckled shape. In this way the effects of the girth weld on behavior can be isolated.

In order for the results to be directly comparable to the previous results of tests on plain pipe, carried out at the University of Alberta by Mohareb (1994), the same pipe sizes were selected for the experimental program. These were: (a) 508 OD x 7.9 mm DSAW Grade 386 (20 x 0.312 inch DSAW X56); and, (b) 324 OD x 6.35 mm ERW Grade 359 (12.75 x 0.25 inch ERW X52). The former is the smallest diameter DSAW (Doubly Submerged Arc Welded) pipe produced locally, and is of the greatest thickness that could be tested in axial compression in the 6200 kN capacity testing machine. The latter ERW (Electric Resistance Welded) pipe is the size that exists in the Norman Wells Pipeline, which is operated by one of the sponsors of the project (Mohareb et al. 1994). Although metric units are generally used in this report, the two pipe sizes (i.e., the 508 mm OD pipe and the 324 mm OD pipe) are called 20-inch pipe and 12-inch pipe herein. The experimental program consisted of four tests on 20-inch pipe and three tests on 12-inch pipe. All of the specimens were approximately 1690 mm (66.5 in.) long. The specimens were subject to three types of loadings, namely, internal pressure (in four tests only), axial load, and bending moment.

2.2 DESCRIPTION OF SPECIMEN DESIGNATIONS AND LOADINGS

The tests associated with the experimental program are itemized in Table 2.1. It is important to understand the specimen descriptor (or test name) for each test because this is the key which explains the rationale for the load conditions of each test. The system of notation, explained in detail in Table 2.2, is the same system as used in the reports on pipes without girth welds (Mohareb et al. 1994), with the only difference

being the addition of W to the end of the designations. The W denotes the presence of a transverse girth weld in the middle of the specimen. Specimens are identified by a specimen descriptor of the form XYZnnW, where nn is the size of the pipe in inches, and each of X, Y, and Z designates a particular characteristic of the loading simulation, as shown in Table 2.2. In order to clarify the intent of the loadings for each simulation a detailed description for the 12 inch pipe specimens is given below. This description is similar to that in (Mohareb et al. 1994).

The principal *active effect* or, more precisely, *action*, associated with each test is the imposition of a monotonically increasing curvature to the pipe. This simulates an imposed bending of the pipe due to geotechnical movements. While these imposed displacements are being applied it is assumed that the other loading conditions remain constant and at levels equal to those associated with the design conditions.

The internal pressure is an *action* at any location that is dependent on the position of the pipe segment relative to the pumping station. Immediately downstream of the pumping station the internal pressure should have its maximum value. This maximum value is limited, by the governing standard, to the pressure which will develop a circumferential stress equal to a specified fraction of the specified minimum yield stress (SMYS = σ_y). Although Canadian standards currently permit a value of $0.8\sigma_y$ for the circumferential stress, the Norman Wells line was installed at a time when the limit was $0.72\sigma_y$. Consequently, the maximum value of circumferential stress for any of the 12 inch test specimens was set to $0.72\sigma_y$ in order to simulate a location immediately downstream of a compressor station (designated by X=D in the specimen descriptor). The pressure in the line gradually reduces as the distance from the pumping station increases. Immediately upstream of a pumping station the internal pressure has been reduced to the point where it is only a small fraction of that at the downstream location. Indeed, for practical purposes it may be considered to be zero. Consequently, an upstream location (designated by X=U in the specimen descriptor) is considered to be without internal pressure. An intermediate location, halfway between the upstream and the downstream locations, is designated by X=H in the specimen descriptor.

Axial load is an *action* at any location that is dependent upon many factors. In the absence of soil movement in the direction tangential to the pipe, it is normally considered to arise from a combination of the restraint of the Poisson's ratio effect and the restraint of thermal effects relative to the installation temperature. Specimens with the greatest axial compressive force arising from this combination are designated by setting Y=G in the specimen descriptor, and those with the least are designated by setting Y=L. Unlike the previous set of tests on plain pipes, for all the specimens in this experimental program only Y=G was used.

The characteristics of the axial force are dependent on the longitudinal interaction between the pipe and the soil. If there is little longitudinal restraint from the soil to prevent relative differential tangential motion between the pipe and the soil, the longitudinal force can maintain an almost constant value as the pipe bends out of its original configuration. This is similar to a simple column with gravity loading, in which case the axial load maintains its full magnitude on the end of the column. Such a loading situation is considered to be the most severe with respect to local buckling that might be encountered in the field. It is designated as an *active* axial load by setting Z=A in the specimen descriptor. The least severe axial loading condition is considered to be one where the end segments of the pipe are rigidly clamped against longitudinal movement at points outside the region of flexural deformations. The axial force in the pipe is then controlled by the reaction against this rigid support. Such a loading condition is said to be *reactive*, and it is considered to be the least severe axial loading condition once the pipe begins to bend. It is designated by Z=R in the specimen descriptor. For all the specimens in this experimental program, the *active* loading condition was selected, that is, Z=A.

The compression axial load in the pipe wall, denoted by C in Table 2.1, is a combination of thermal and Poisson effects. For the case of no longitudinal extension of the pipe it may be expressed as

$$C = A(E\alpha (T_0 - T_\ell) - \mu \sigma_\theta)$$ (2.1)

in which A = the area of the pipe cross-section; E = the modulus of elasticity for the pipe material (200,000 N/mm^2); α = the thermal expansion coefficient for the pipe material (11.7 x 10^{-7} mm/mm/°C); T_0 = the pipe operating temperature; T_ℓ = the ambient temperature when the pipe is laid down; μ = Poisson's ratio for the pipe material (0.3); and σ_θ = the hoop stress in the pipe.

Note 1: A maximum operating temperature of around 0° C is maintained in all
pipelines through regions of discontinuous permafrost. Therefore, this value is
used in the design of the tests.

Note 2: Practical considerations for winter construction put a lower limit of -45° C on
T_1. This value is used in the design of the tests.

2.3 TEST SET-UP

The test set-up for the series of tests on girth welded pipes is shown in Fig. 2.1.
It is the same arrangement as used for the previous series of tests on plain pipes
(Mohareb et al. 1994). A picture of the set-up is also presented in Fig. 2.2. The test
set-up is similar to that used in structural steel research to investigate the strength and
behavior of beam-columns. The free body diagram in Fig. 2.3a shows the forces
applied on the upper half of the pipe specimen.

As can be seen in Fig. 2.1, the pipe specimen is welded to two end plates. In
turn, these end plates are bolted to two loading arms. The axial load is delivered
through the compression head of a universal testing machine and then through the knife
edges and the web of the loading arm to reach the end plates of the specimen. Moment
is applied to the specimen by extending the jack between the loading arms at the
location eccentric to the centerline of the pipe. In Fig. 2.3a the symbol F represents
the jack force. In this type of test arrangement, the jack is usually used in tension
because it gives a more stable loading configuration. However, in these tests this
would put the jack on the same side as the compression face of the pipe, blocking the
view of the wrinkle development. Because photogrammetric techniques were to be
used to map the buckling configuration, it was desirable that the compressive face be
free from obstructions. Therefore, the jack force applied to the loading arm was
compressive, that is, it caused the loading arms to open. The measured values of jack
eccentricity, e, for different specimens are tabulated in Fig. 2.3b.

The length of the specimen, like the previous series of tests on plain pipes, was
selected to be three and one-third times the diameter of the larger pipe (i.e., 20 inch
diameter). As observed for axially loaded specimens (Mohareb et al. 1994), the local
discontinuities associated with the testing arrangement in the regions of the end plates

can trigger local buckling and failure at the end locations. Two features of the test arrangement acted to reduce this possibility. First, collars were added to the specimens immediately adjacent to the end plates. These collars, shown in Fig. 2.1, were short segments of pipe taken from the same source as test piece itself. They were split, placed tightly around the specimen and then rewelded into a ring in such a way that there was no mechanical connection between the collar and the pipe. Second, although in the undeformed configuration the specimen is under uniform moment, the eccentricity of axial force from the deflected shape of the specimen centerline produces a moment variation along the specimen with the maximum at the mid-height. This will move the most critical stress condition away from the end support.

Each loading arm was a closed, built-up section having two 10 mm thick webs and two 25.4 mm thick flanges. Each of the 660 x 540 x 63.5 mm steel end plates was bolted to the flange extremity of a loading arm using five ASTM grade A490 bolts on the tension side of the pipe and two on the compression side. The other extremity of the loading arms received the jack fittings. The distance between the pipe and the application line of the eccentric force could be adjusted from test to test by changing the position of the jack fittings. Stiffeners were provided at all possible loading points.

Internal pressure was provided by filling the interior of the specimen with water and then using a manually regulated, pneumatically powered pump to pressurize it. The magnitude of the pressure was monitored by means of a transducer installed in the supply line. A hole was drilled through each end plate in order to be able to connect the interior of the pipe to the pump and to bleed hoses. Constant internal pressure was maintained by manual control.

In addition to providing the axial load in the pipe wall, the load applied by the universal testing machine, P, should compensate for two tensile forces. The first of these is the eccentric load, F, applied by the jack, which varies during the test. The second is the tensile force P_i due to the internal pressure acting on the closed ends of the specimen (Fig. 2.3a). This latter force may be evaluated as

$$P_i = \pi R_i^2 p \qquad (2.2)$$

where p is the internal pressure, and R_i is the inside radius of the pipe. Consequently, the longitudinal force that should be applied by the testing machine to the end of the test specimen in order to maintain the force C in the pipe wall can be expressed as

$$P = C + F + P_i \qquad (2.3)$$

2.4 FABRICATION AND ALIGNMENT OF SPECIMENS

Two 845 mm long segments of pipe were flame cut in order to make each specimen. One end of each segment was beveled at an angle of between 50 and 60 degrees so that it could be welded to the end plate. The other end of each segment was beveled at an angle of 30 degrees, as per industry standard procedures, so that it could be groove welded to the other segment. In order to simulate the fabrication procedure of the specimens to that of the pipeline industry, a contracting crew used by a pipeline company was employed. They were employed to align and weld the segments together and were expected to use procedures and equipment similar to those they would have used in the field. The girth weld connections then underwent X-ray inspection to evaluate the quality of the weld.

Strain gages were attached to the specimen after the confining collars had been placed around the specimen ends. A loading arm was placed on the floor, and then an end plate was bolted to its upper surface. The pipe was then aligned vertically over the end plate and welded to it using three welding passes. The resulting L-shaped frame was then inverted and moved under the top head of the compression machine such that the pipe centerline was concentric with the head of the compression machine. The bottom loading arm and its end plate had already been placed in position in the testing machine and the bottom of the pipe then was welded to the bottom end plate (a down-hand weld). Great care was taken to center, level, and align each of the components as they were moved into place.

After the test was completed, and if the specimen had been tested under internal pressure, the fluid was first evacuated through drainage holes in the end plates. Then the pipe was freed from the end plates by flame cutting. The arms were removed and the surface of the end plates were ground and cleaned, while still attached to the arms, so that the assembly could be reused for the next specimen. Of course, only the latter

procedures were needed for specimens that had been non-pressurized during their testing.

2.5 INSTRUMENTATION

2.5.1 Strains

Forty longitudinal strain gages were mounted on each specimen. Sixteen of these were placed along the length of the specimen near the maximum compression fiber, as shown in Fig. 2.4, in order to measure the values of the strains as buckling was approached. Another sixteen gages were attached to the tension face of the specimen in the same pattern as those of compression face. In addition, rings of strain gages were mounted near the top and bottom of the specimen. These were used in order that the alignment of the specimen could be checked during set-up, prior to applying the eccentric load. Each ring consisted of eight equidistantly placed strain gages. In addition to the strain gages, longitudinal strains based on Demec points spaced at about 115 mm along the maximum compression and tension fibers were also recorded. Fig. 2.4 shows the arrangement of the strain gages and the Demec points. A photogrammetric technique (described in Section 2.5.4) that was originally employed to record the buckling deformations, could conceptually be used to obtain the strains. However the resolution of the cameras used in the procedure was not sufficient to provide the accuracy required for meaningful results.

2.5.2 Loads and Axial Movements

The readings of load and the compression head movement for the universal testing machine were recorded by a data acquisition system. Displacement transducers were installed in order to measure the shortening of the specimen and the extension of the eccentric jack. A load cell attached to the jack piston measured the jack load.

2.5.3 Rotation Meters

Two rotation meters that used electric resistance strain gages were installed, one on the top arm and one on the bottom arm, at mid-height of the arms on the axis along the pipe centroid. They measured the end rotations of the specimen.

2.5.4 Deformation Response

Establishing a database for deformational response of the girth welded pipes was one of the main purposes of the experimental program. Three types of measurements were made in order to capture the deformation response adequately.

The first of type of measurement was that of radial displacements, and they were taken at prescribed distances along the length of the specimen. This was accomplished using a series of eight equidistantly placed linear variable differential transducers (LVDT's) aligned radially (i.e., perpendicular to the initial surface of the pipe). The arrangement of the LVDT's is shown in Fig. 2.5. These LVDT's were mounted on a frame containing a 650 mm-diameter hole, which was enough to encompass the pipe as it changed position throughout the test. The entire assembly could be moved vertically. The hole was concentric with the initial position of the test specimen and the frame slid along the fixed columns of the universal testing machine. For a given deformed configuration, the frame was stopped at twelve fixed stations along the length of the specimen to take the LVDT readings. Fig. 2.6 shows the frame supporting the LVDT's when it is positioned at the bottom of the specimen.

The second means of measuring the deformed shape of a specimen was by taking photographs of the compression face simultaneously with two different cameras. The cameras were mounted on a column and viewed the compression face of the pipes from a distance of about four meters. The coordinates of any point on the compression side, which contains most of the local deformations, can be determined by photogrammetric processing of the pictures. This photogrammetric method is still being developed in the Department of Civil Engineering at University of Alberta. Utilizing it for this series of tests permitted the effectiveness of the method to be explored, but it turned out that the resolution of the cameras for this particular test series was not adequate to provide quantitative results. However, the exercise assisted in the definition of the requirements for further development of the photogrammetric technique.

The third measurement of the deformed shape of the pipe, complementary to the LVDT results, was the utilization of a surface contour gage that could be placed against the pipe in locally deformed areas. As Fig. 2.7 shows, the contour gage was placed longitudinally against the pipe and the movable metal teeth were adjusted so that they

came into contact with the pipe. In this way the longitudinal profile of the pipe in the vicinity of the buckle could be captured by the outline of the contour gage. After the contour gage was removed from the pipe, tracing its outline on a sheet of paper reproduced a shape identical to the longitudinal profile of the pipe in the localized region.

2.5.5 Electronic Recording of Data

All the readings of the LVDT's, strain gages, rotation meters, loads and strokes were electronically stored in a 60-channel data acquisition system. In order to monitor the progress of the test, plots of loads, strokes, and arm rotations were displayed on a monitor program during the test.

2.6 TEST PROCEDURE

The general procedure for loading the specimens was first to apply the required internal pressure, then to apply the axial load, and, finally, to gradually impose curvature on the pipe by pushing apart the ends of the loading arms with jack stroke increments. Displacements during the first and second stages of loading (pressurizing and compressing) were very small and mostly in the elastic range. Thus, there was no need for a step-by-step increase of the loads to measure the intermediate deformations. The third stage of loading (imposing curvature), on the other hand, involved large displacements and localized deformations began early in this stage. Hence, it was necessary for the deformations to be monitored at a sufficient number of curvature increments so as to provide adequate information about the deformation history.

Since it was necessary to test well into the post-wrinkling range, it was possible that a snap-back situation would occur. If this occurred, a rapid, unstable increase in the buckle deformation might take place during the latter part of the test, entailing a snap-back from one axial load to a lower one, or from one moment to a lower one, under constant end displacements. Consequently, it was considered prudent to have feedback controls that would maintain the preset combinations of loading and displacements regardless of the response of the specimen.

The actuators for loads P and F were controlled through a computer program written using commercial software, namely, LabVIEW 2 (Ver. 4.2, 1990). The program ran on a Mac IIci microcomputer equipped with a card that provided two

analog output and eight analog input channels. Four of the seven inputs for the control program were P, F, Δ_P and Δ_F. The latter two are the stroke of the testing machine and jack, delivering forces P and F, respectively. The three other inputs were obtained from three displacement transducers that monitored the axial elongation of the pipe. Because of the geometry of the test set-up, the elongation of the pipe was not necessarily equal to Δ_P.

Conceptually, three loading modes could be imposed for control of loading during the increase of curvature delivered by the jack stroke, Δ_F. In Mode 1, the axial force carried by the pipe is maintained at a constant value. For this mode, the testing machine load, P, is controlled such that $P - F = C^* = C + P_i$, where C^* is the prescribed value of the pipe axial force and P_i is the force generated by the constant internal pressure in the longitudinal direction. This mode of loading corresponds to an active longitudinal pipe force, using the terminology of Section 2.2. In Mode 2, the vertical projection of the length of the pipe is kept constant. This mode corresponds to a reactive longitudinal pipe force, using the terminology of Section 2.2. In Mode 3, the goal is to maintain the testing machine load, P, at a constant value, say, $P = P^*$, in which P^* may be a minimum force to ensure that the specimen remains clamped in the machine and does not become geometrically unstable. In this series of tests on girth welded pipes only control Mode 1 (active force) was employed.

During each test, the value of $C^* = P - F$ was monitored continuously by the control program. A target value of C^* and a limiting value for the stroke of the testing machine Δ_P^* could both be changed from the keyboard at any time during the test. If Δ_P were less than Δ_P^*, the control program would adjust the axial load actuator so that the actual value of C^* equaled its target value; otherwise the limiting value of Δ_P equal to Δ_P^* would be maintained.

For operation during Mode 1 control, the value of Δ_P^* was set slightly greater than the current value of Δ_P. Whenever the value of Δ_P reached that of Δ_P^*, Mode 1 control was suspended. Mode 1 control could be reinstated by adjusting Δ_P^* so that it was again greater than Δ_P. This provided a safety control in the event of specimen snap-back.

Table 2.1
Experimental Test Specimens

Test Name	Pipe Loading			End Loading		
	Variable M	Constant p for σ_θ of :	C_A[1] = Active C_R = Reactive	P_i[8]	P[9] = C + P_i + F	F= M / e
1 : UGA20W-1	e F		$C_A=0.27\,C_y$[2]		$0.27C_y+$ F	M_P^C/e[10]
2 : UGA20W-2	e F		$C_A=0.27\,C_y$[2]		$0.27C_y+$ F	M_P^C/e
3 : HGA20W	e F	$0.4\,\sigma_y$	$C_A=0.15\,C_y$[3]	$0.2\,C_y$	$0.35C_y+$ F	$M_P^{C\theta}/e$[11]
4 : DGA20W	e F	$0.8\,\sigma_y$	$C_A=0.03\,C_y$[4]	$0.4\,C_y$	$0.43C_y+$ F	$M_P^{C\theta}/e$
5 : UGA12W	e F		$C_A=0.29\,C_y$[5]		$0.29C_y+$ F	M_P^C/e
6 : HGA12W	e F	$0.36\,\sigma_y$	$C_A=0.18\,C_y$[6]	$0.18C_y$	$0.36C_y+$ F	$M_P^{C\theta}/e$
7 : DGA12W	e F	$0.72\,\sigma_y$	$C_A=0.08\,C_y$[7]	$0.36C_y$	$0.44C_y+$ F	$M_P^{C\theta}/e$

Explanatory notes keyed to subscripts in Table 2.1. (See Fig. 2.3 for load designations.)

1. $C = A(E\alpha\,\Delta T \cdots \cdots = \cdots \alpha\,\Delta T - \mu\,\sigma_\theta)C_y$

For 20-inch pipes, $\sigma_y=56$ ksi $= 386$ MPa.
For 12-inch pipes, $\sigma_y=52$ ksi $= 358$ MPa.

$E = 200,000$ MPa, $\mu = 0.3$

$\alpha = 11.7 \times 10^{-6}$ mm / mm°C, $\Delta T = 45°C$

$E\alpha\,\Delta T = 200,000 \times 11.7 \times 10^{-6} \times 45 = 105.3$ MPa

2. $C = (\dfrac{105.3}{386} - 0.3 \times 0)C_y = 0.27C_y$

3. $C = (\dfrac{105.3}{386} - 0.3 \times 0.4)C_y = 0.15C_y$

4. $C = (\dfrac{105.3}{386} - 0.3 \times 0.8)C_y = 0.03C_y$

5. $C = (\dfrac{105.3}{358} - 0.3 \times 0.0)C_y = 0.29C_y$

6. $C = (\dfrac{105.3}{358} - 0.3 \times 0.36)C_y = 0.18C_y$

7. $C = (\dfrac{105.3}{358} - 0.3 \times 0.72)C_y = 0.08C_y$

8. $P_i = \dfrac{A\sigma_\theta}{2} = \dfrac{C_y\sigma_\theta}{2\sigma_y}$, with the values of σ_θ given in the third column.

9. P is the sum of C and P_i (given in the fourth and fifth columns) and F as a variable.

10. $M_P^C = M_P$ modified for C.

11. $M_P^{C\theta} = M_P$ modified for C and σ_θ.

Table 2.
Test Designations

XYZnn(W) : General format of a specimen descriptor		
X	**U**	U = Upstream (or empty). Upstream refers to a location of the pipe immediately upstream of the pumping station. The upstream pressures are low (e.g., approximately 0.34 MPa for the 20-inch pipe). Consequently, there is no essential difference between an empty and an upstream condition, and a zero pressure will be used to represent the upstream condition.
	D	D = Downstream (or fully pressurized). Downstream refers to the location of the pipe being immediately downstream of the pumping station. The downstream pressure is approximately 9.85 MPa for the 20-inch pipe, and 10.45 MPa for 12-inch pipe.
	H	H = Halfway between U and D (Upstream and downstream). Half of the pressures for downstream condition were used for the halfway condition.
Y	**G**	Greatest thermal effect (ΔT = 45°C)
	L	Least thermal effect (ΔT = 0°C)
Z	**A**	Active axial force (constant force)
	R	R = Reactive axial force (constant end locations)
nn	Nominal diameter of the pipe in inches	
W	Indicates the existence of a girth weld at the mid-height of the specimen (W = Weld)	
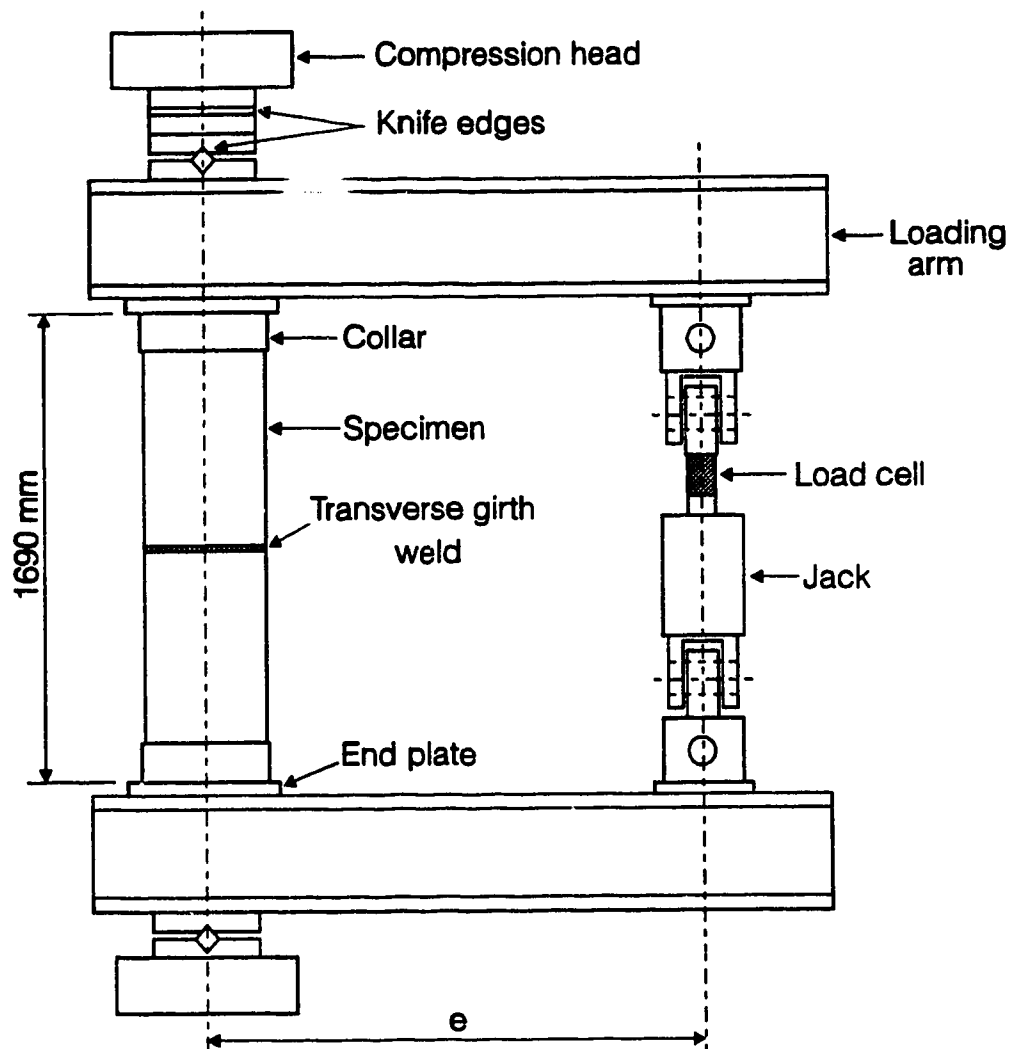
Fig. 2.1 Test set-up
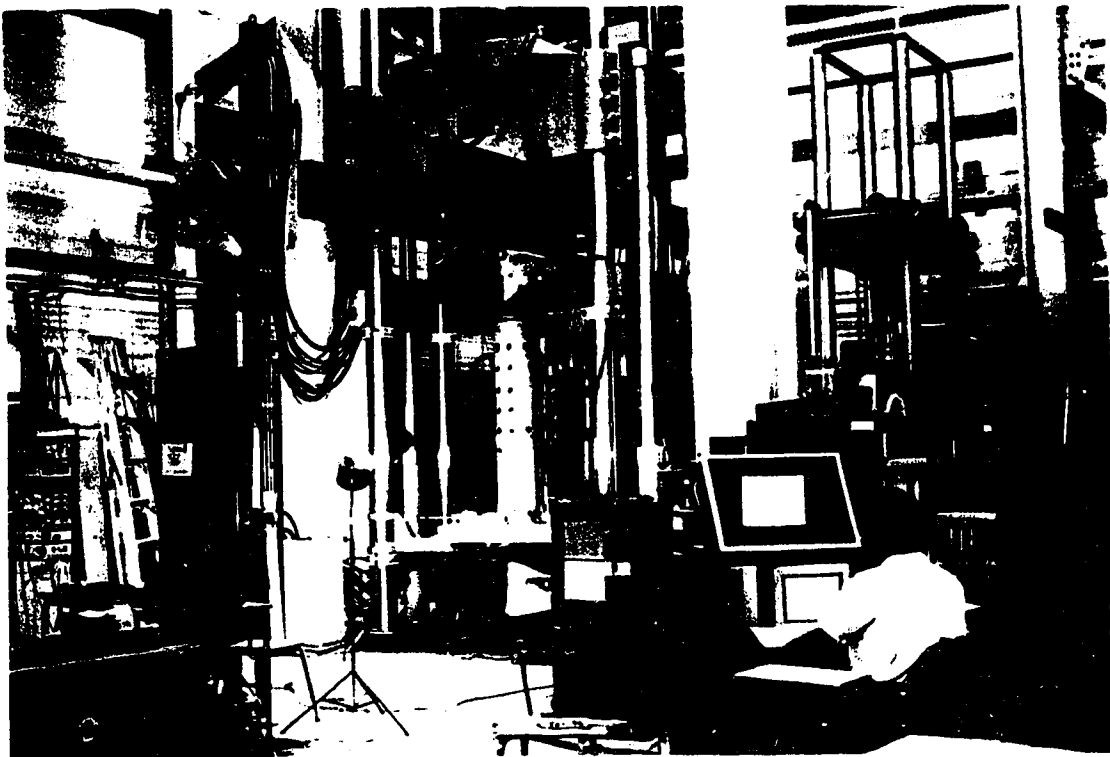
Fig. 2.2 Photograph of test set-up
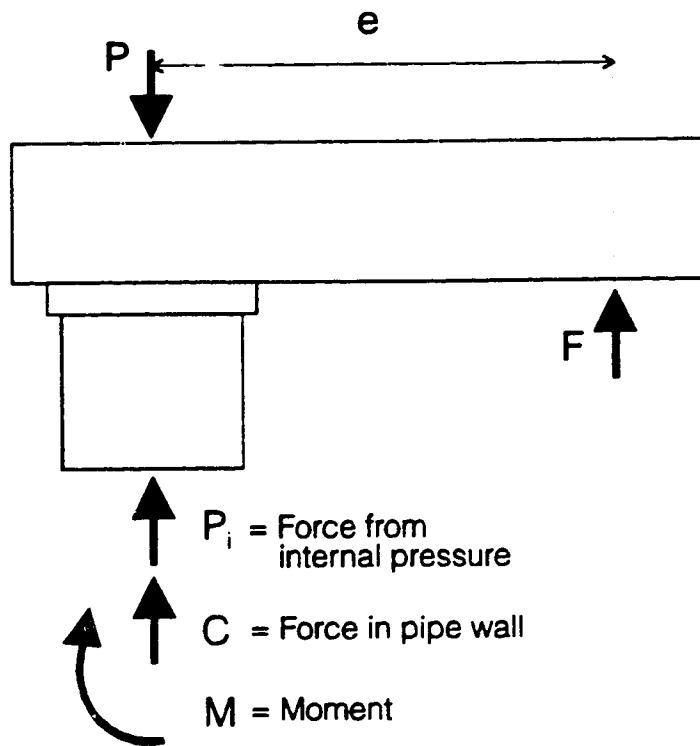
(a) Free body diagram of upper segment
of test specimens

Specimen	e (mm)
UGA20W-1	1560
UGA20W-2	1560
HGA20W	1560
DGA20W	1110
UGA12W	1005
HGA12W	1005
DGA12W	1005

(b) Eccentricities for test specimens

Fig. 2.3 Loading details for test specimens
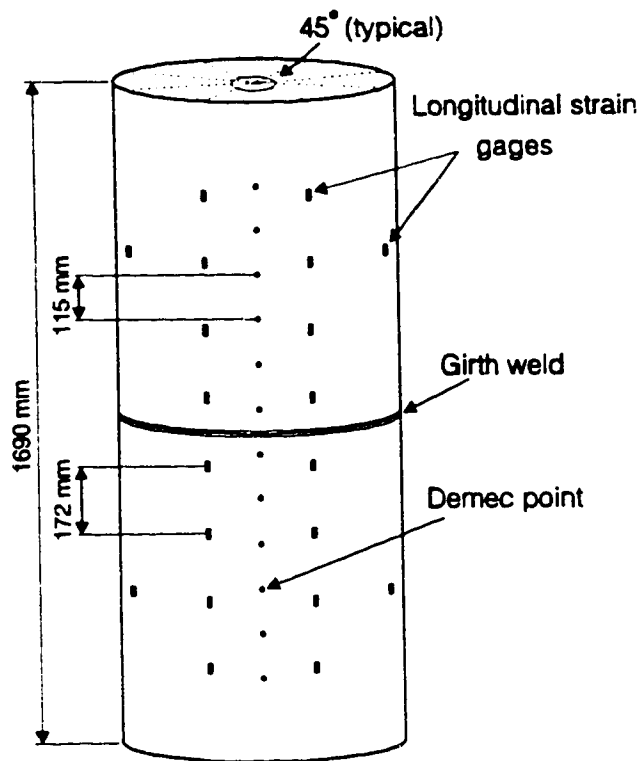
Fig. 2.4 Strain gage and Demec point arrangement
(same for compression and tension sides)
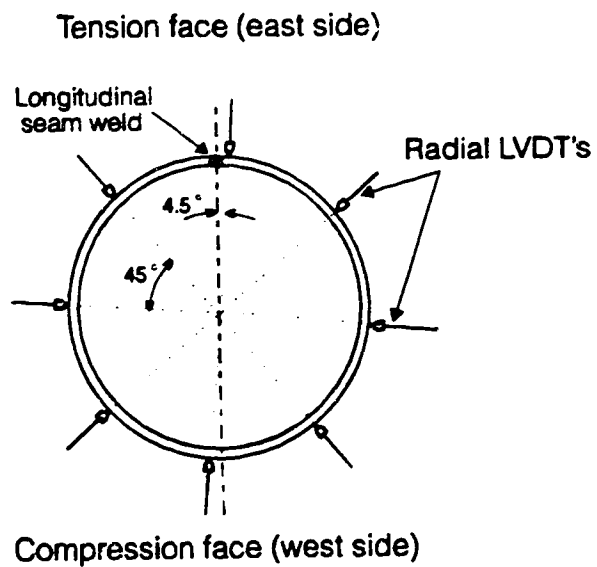
Fig. 2.5 Arrangement of radial LVDT's
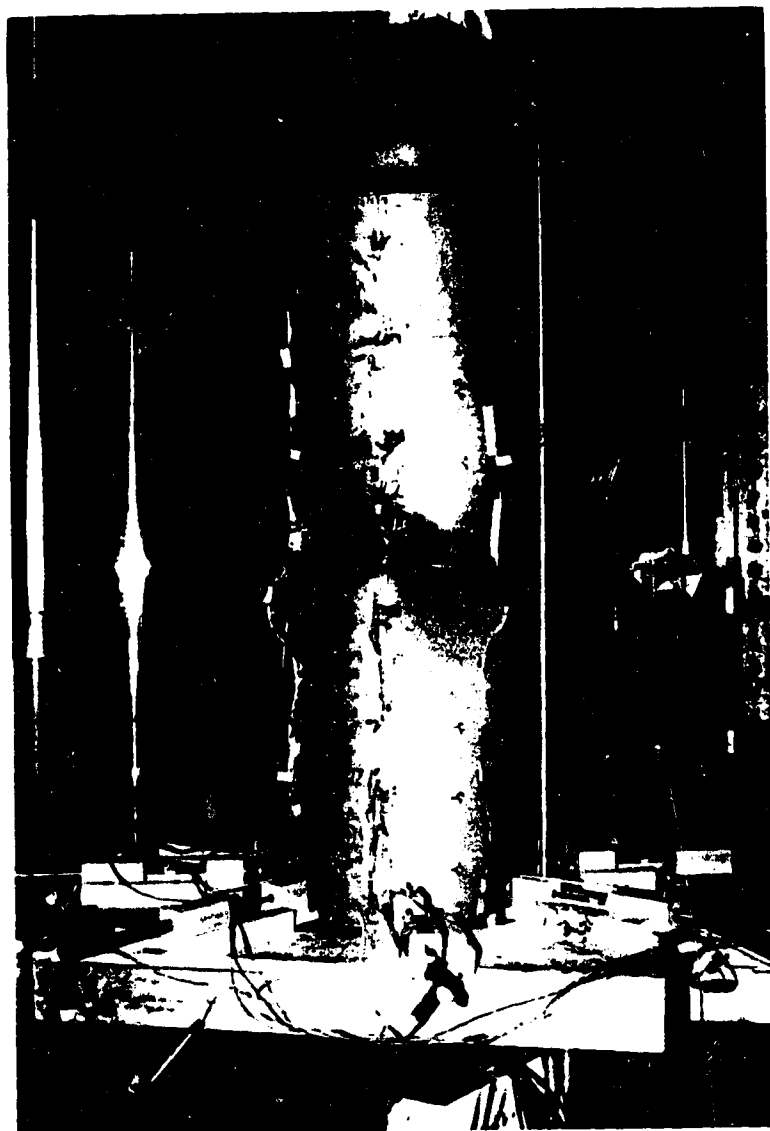
Fig. 2.6 Specimen UGA20W-2 embraced by the platform supporting radial LVDT's

Fig. 2.7 Application of contour gage to trace deformed profile

3 EXPERIMENTAL RESULTS

3.1 INTRODUCTION

The process of data reduction is described in this chapter. The results are shown graphically in six categories, selected to depict the test results in an appropriate way. In the subsequent sections, the method of obtaining the graphs from the experimental data is described. These graphs are presented for each test, along with observations of local deformations. Classification of the development of local deformation in the course of loadings concludes this chapter.

3.2 GENERAL PROCEDURE

Graphs for each of the following six categories are presented for each test:

- Applied loads vs. rotation. The rotation used in these graphs is the relative rotation θ between the two ends of the specimen. See, for example, Fig. 3.1.

- Strain distributions along extreme fibers for various rotations. See, for example, Fig. 3.2.

- Curvature along the specimen for various rotations. See, for example, Fig. 3.5.

- The local profile of wrinkled shape along the extreme fiber for various rotations. See, for example, Fig. 3.6.

- The average of the end moments and the average moment over the wrinkled segment vs. overall curvature. See, for example, Fig. 3.8. The average moment over the wrinkled segment is taken as the mean value of the moment over a gage length straddling the wrinkle (see Section 3.2.5.2). Overall curvature is taken as the rotation, θ, divided by the length of the specimen, L.

- Average moment vs. average curvature over the wrinkled segment. See, for example, Fig. 3.13. The average curvature over the wrinkled segment is taken as the mean value of the curvature over the gage length selected as wrinkled segment (see Section

3.2.5.2). This is equivalent to the relative rotation of the ends of the wrinkled segment divided by the gage length.

The procedure of obtaining each of the above graphs for a typical test will be described in the following sections. The graphs for a particular specimen are used to illustrate the descriptions associated with different categories of curves. Because a major part of the discussion for some types of graphs is concerned with the internal pressure, a typical pressurized specimen, namely, HGA12W, is selected to describe the procedures.

3.2.1 Loads vs. Rotation Response

Figure 3.1 shows four load lines plotted against the same rotation for specimen HGA12W. Two of these are the loads applied by the testing machine and by the eccentric jack, corresponding to P and F in Fig. 2.3a, respectively. Another load line is P_i, the force due to the internal pressure acting on the closed ends of the specimen, as shown in Fig. 2.3a. The value of P_i is evaluated from Eq. (2.2). For non-pressurized specimens, the value of P_i is always zero; thus, the load line associated with P_i is not shown in the plots for those specimens.

At the beginning of the test, after applying the internal pressure, the axial load in the pipe is raised to its target value, $C = C^*$, without inducing any curvature (F = 0). Then, while maintaining the axial load constant through the control program, the moment is applied to the pipe by gradually increasing the eccentric force, F. The last load line plotted is the axial load in the pipe, $C = P - F - P_i$, which is intended to have a constant value throughout the test for an active axial load.

3.2.2 Strains at Extreme Fibers for Various Rotations

As mentioned in Section 2.5, out of the three techniques used for measuring strains, i.e., the longitudinal strain gages, the Demec gages and the photogrametric pictures, only the results of the first two had adequate accuracy to be used in the study. In turn, the strain gages proved to be more accurate than the Demec gages until the wrinkle formed in the pipe wall or until unbonding of the gages took place. Therefore, it was preferable to use strain gage results wherever they appeared to be more reliable. However, upon wrinkling, the strain gage results lose their validity at the wrinkled region because the strains become highly variable locally. At the same time, because of the large overall shortening of the extreme compressive fiber at the wrinkled region, the accuracy of

the Demec gage strains improves. Consequently, for the wrinkled region, having highly variable localized strains, the Demec gages provide a more reliable measure of the average strains.

The longitudinal distributions of strains in the extreme compressive fiber of specimen HGA12W for various levels of relative rotations are shown in Fig. 3.2. Strain gage readings were used to plot these results, except when dealing with the wrinkled segment. This may be identified as the region of peak strains at high rotations, and when this occurred, the Demec gage results were employed. This is necessary because, after wrinkling, strains in the region of the wrinkle vary drastically, and pointwise strain gage readings in this region do not represent the average shortening of the wrinkled segment.

For the data shown in Fig. 3.2, the point at which Demec gage readings started to be used for the wrinkled region was a rotation of 4.52 degrees. As seen in the figure, the strains at the gage located 750 mm from the reference level started to increase significantly at some point in the interval of 3.66 degrees rotation and 4.52 degrees rotation.

When tensile strains are plotted, as for example in Fig. 3.3, they are all data from strain gage results. This is because, even in the wrinkled segment, there is no significant variation in the tensile strain along the extreme tension fiber. This is as would be expected.

For both the compression and tension sides, the results of the two adjacent lines of strain gages (shown in Fig. 2.4) were always close to each other. These two readings at each level were averaged to obtain the strain gage result. A small correction was made to the results of the strain gages, since they are located slightly off the extreme fiber, as shown in Fig. 3.4. The tensile strain at the gage location, ε_i^t, and the strain at the extreme tension fiber, ε_2^t, can be expressed as

$$\varepsilon_1^t = \varepsilon_m + \phi\, y_1 \tag{3.1a}$$

$$\varepsilon_2^t = \varepsilon_m + \phi\, y_2 \tag{3.1b}$$

where ε_m is the strain at mid-section, y_1 and y_2 are the absolute values of the y coordinates of the two points and ϕ is the local curvature at the cross-section. The amount of correction is simply

$$\varepsilon_2^t - \varepsilon_1^t = \phi \, (\, y_2 - y_1)$$ (3.2)

Similarly, ε_1^c and ε_2^c, the compressive strains at the location of strain gages and extreme compression fiber can be expressed as

$$\varepsilon_1^c = \varepsilon_m - \phi \, y_1$$ (3.3a)

$$\varepsilon_2^c = \varepsilon_m - \phi \, y_2$$ (3.3b)

Hence, the amount of the correction in compression will be

$$\varepsilon_2^c - \varepsilon_1^c = -\phi \, (\, y_2 - y_1)$$ (3.4)

In these expressions, the curvature (ϕ), as computed in Section 3.2.3, is independent of the correction because the uncorrected form of strain gage results is used to calculate curvature. The original value of ($y_2 - y_1$), i.e., that in the undeformed shape, was used in Eqs. (3.2) and (3.4) to calculate the corrections to strain gage results. This is because the strain gage results are used only for non-wrinkled regions, where the change in ($y_2 - y_1$) is small. Moreover, the fact that the corrections are a small fraction of the average strain values further justifies the approximation employed. The Demec gage results, on the other hand, do not need such a correction because the Demec points are located exactly on the extreme fibers, as is apparent in Fig. 2.4.

3.2.3 Curvature Along the Specimen

As long as plane sections remain plane, curvature is a direct reflection of the compressive and tensile strains. Here the strain gage results in their uncorrected form were used to calculate the curvature. This is because the two points on the cross-section to be used to calculate the curvature do not need to occur at the extreme fibers, as long as their locations are known.

Curvature at any section along the pipe was calculated using the following formula:

$$\phi = \frac{\varepsilon^t - \varepsilon^c}{d_0}$$ (3.5)

where ε^t is the tensile strain at the gage location (see Fig. 3.4), ε^c is the compressive strain at either the extreme compression fiber (when using Demec gage results) or the

location of strain gages (when using strain gage results), as shown in Fig. 3.2, and d_0 is the distance between the tensile and compressive gages on the undeformed section. It was assumed that the use of d_0 in the undeformed configuration will provide adequate accuracy. The strain gage results along the tensile face are plotted at different elevations than the Demec gage results used for the compressive face. Thus, linear interpolation was employed to obtain the values of tensile strain at the elevations of the Demec data points. This was not necessary where the compressive strains were obtained from the strain gage results. This is because the strain gages along the extreme tensile fiber were located at the same elevations as those along the extreme compressive fiber.

Equation (3.5) expresses the local curvature, ϕ. Distribution of ϕ for various rotations are shown in Fig. 3.5 for specimen HGA12W. For each line in Fig. 3.5, the corresponding overall average curvature over the length of the specimen can be computed as θ/L, as defined in item five of Section 3.2).

3.2.4 Profile of the Extreme Fibers

The displacement profile for the extreme compression fiber of Specimen HGA12W is presented in Fig. 3.6 for different rotation values. The displacement profile was plotted by using the readings of the closest radial LVDT to the extreme compressive fiber (see Fig. 2.5). When there was a large out-of-plane deformation between two consecutive stations of radial LVDT's in the longitudinal direction, a contour gage was employed to trace that interval along the extreme compression fiber. In Fig. 3.6, each of the profiles of the extreme compression fiber for HGA12W at the three last rotations has been augmented with two intermediate points from contour gage results. These two points on each curve are located between the heights of 693 and 768 mm, which are the two successive heights of the radial LVDT stations that straddle the major buckle.

In contrast to the compression fiber case, the profile of the extreme tension fiber always followed a smooth profile, such as would be associated with a beam deflection profile. As a sample of these curves, the profile of the extreme tension fiber for various rotations for the specimen HGA12W, as determined from the LVDT readings, is shown in Fig. 3.7.

3.2.5 Average End Moment and Average Moment over the Wrinkled Region vs. Overall Curvature

The average end moment and average moment over the wrinkled segment vs. overall curvature of the pipe for specimen HGA12W are presented in Fig. 3.8. The expression $M = F \times e$ holds true only for very small rotations. As the overall curvature increases, the simple expression given above must be modified in order to obtain the correct values of the end moments and moment at any section along the pipe. It is necessary to include these corrections in order to determine the average moment over the wrinkled segment of the pipe. In the following subsections, the procedures of calculating the end moments and the average moment over the wrinkled region are described.

3.2.5.1 End Moments

As depicted in Fig. 3.9, when the specimen is deformed, the testing machine load, P, becomes eccentric both with respect to the pipe ends and with respect to the centerline of the pipe at mid-length. From the deformed configuration shown in Fig. 3.9, the moment at the top end of the pipe can be calculated as

$$M_t = F \, e \cos\theta_t + P \, d \sin\theta_t \qquad (3.6)$$

and, similarly, at the bottom end,

$$M_b = F \, e \cos\theta_b + P \, d \sin\theta_b \qquad (3.7)$$

where d is the depth of the top and bottom arms, andθ_t and θ_b are the absolute rotations of the top and bottom arms, respectively. In the actual tests, these two rotations were always relatively close to each other. The average of the two end moments has been used in plotting the M_{end} line in Fig. 3.8.

3.2.5.2 Average Moment over the Wrinkled Region

In order to quantify the local curvature at the wrinkle, it seems rational to use the local gage length as the length of the wrinkle and to locate it on the specimen in such a way that it straddles the wrinkle. For an inward wrinkle, observed in non-pressurized specimens, the gage length was selected as D/2, where D is the outside diameter of the pipe. For an outward wrinkle, observed in pressurized specimens, the gage length was selecte⁴ ᴧᶜ Ɒ. In order to obtain the average moment over the gage length, it is necessary to b ᵃ'ᶜ ᴐ calculate the moment at an arbitrary cross-section along the specimen. By averagᵢᵢg e moments obtained at an adequate number of sections along the gage length,

the average moment over the wrinkled segment can be determined. The calculation of moment at an arbitrary cross-section is described as follows.

Figure 3.10 shows the free body diagram of a deformed test specimen. In this figure no shear reaction is considered at the ends of the pipe. This is because the compressive head of the universal testing machine is connected through a ball joint connection to the upper part of the machine; thus, it can not take any significant amount of horizontal load. It is assumed that the two ends have different rotations (θ_t and θ_b at the top and bottom end, respectively) and different moments (M_t and M_b at the top and bottom end, respectively). In reality, however, the differences are very small. The internal pressure p acting on the end plates generates tensile forces tangential to the pipe centerline at the ends. The magnitude of these forces, P_i, can be expressed as

$$P_i = \pi R_i^2 p \tag{3.8}$$

where R_i is the inside radius of the pipe.

As Fig. 3.10 shows, the vertical components of P_i at the top and bottom end of the specimen are designated by V_t and V_b, respectively. To determine the axial force in the specimen, these must be subtracted from the force P delivered by the testing machine. Because the end slopes are very small (i.e., $\theta_t, \theta_b < 5°$), the value of P_i can be used instead of both V_t and V_b. The axial force $(P - P_i)$ multiplied by the deflection of the centerline at any cross-section constitutes one of the contributions to the moment at the section. In Fig. 3.10, the deflection of the centerline at the ordinate x (measured from the bottom end of the centerline) is denoted by $v(x)$. The centerline at any horizontal cross-section is assumed to be located at the centroid of the closed curve on the middle surface of the pipe wall intercepted by the cross-section. In order to locate the centerline, readings taken by the radial LVDT's were employed. They provided the coordinates of eight points on the pipe surface at 12 cross-sections along the specimen. Using a computer program based on cubic spline method (Souza, 1991), a smooth, closed curve was fitted to the eight points of each horizontal section, passing through all of them. Then, by a simple integration and assuming a uniform thickness, the centroid of the cross-section could be located.

In addition to the end moment and the moment due to axial force, there are two other moment components to be considered. The first is the product of the horizontal

component of P_i (perpendicular to the pipe alignment) and the distance of the cross-section from the corresponding end (i.e., $H_b \cdot x$ in Fig. 3.10). The second moment component results from the internal pressure acting on a curved pipe. To describe the action, an arbitrary infinitesimal slice of the deformed pipe is considered, as indicated by Slice A in Fig. 3.10. The original length of the slice before applying any load is denoted by dx. The end cross-sections of the slice are assumed to be perpendicular to the pipe alignment in the original configuration. After introduction of curvature by applying bending moment, the length of the slice will increase from intrados to extrados. Figure 3.11 shows that this variation in length results in a non-uniformity in the intensity of the pressure line load per unit of circumferential length around the slice. In order to calculate the resultant of the pressure force acting on the slice, the deformed configuration of the slice is considered, as shown in Fig. 3.12. It is assumed for simplicity that the cross-section remains circular. As shown in Fig. 3.12b, because of symmetry about xy plane, the resultant of the pressure forces, dU, delivered on the inside of the slice is located in xy plane, and it acts in y direction. The term dU is obtained by integrating the infinitesimal components d(dU) as shown in Fig. 3.12a.

If ε is the longitudinal strain at an arbitrary ordinate y and h is the length of the slice at that ordinate, as shown in Fig. 3.12b, then

$$\varepsilon = \varepsilon_m + \phi\, y \tag{3.9}$$

$$h = dx\,(1 + \varepsilon) \tag{3.10}$$

in which ε_m is the longitudinal strain at mid-section and ϕ is the curvature at the cross-section. The curvature along the pipe is available from the curvature diagrams obtained from the experimental data. See, for example, Fig. 3.5. From Fig. 3.12a,

$$y = R_i \cos\psi \tag{3.11}$$

Substituting Eq. (3.11) in Eq. (3.9) and then putting the result into Eq. (3.10) gives

$$h = dx\,(1 + \varepsilon_m + \phi R_i \cos\psi) \tag{3.12}$$

In Fig. 3.12a, the inside area of the element confined by the angle $d\psi$, which is subjected to internal pressure, has a magnitude of

$$dA_i = h\,R_i\,d\psi \tag{3.13}$$

The y component of the force due to the internal pressure on the element can be expressed as

$$d(dU) = p \, dA_i \cos\psi \qquad (3.14)$$

Substituting Eq. (3.12) in Eq. (3.13) and then putting the result into Eq. (3.14) yields

$$d(dU) = pR_i \, dx \left(1 + \varepsilon_m + \phi R_i \cos\psi\right) \cos\psi \, d\psi \qquad (3.15)$$

To obtain dU, Eq. (3.15) is integrated to give

$$dU = 2\int_0^\pi p \, R_i \, dx \left(1 + \varepsilon_m + \phi R_i \cos\psi\right) \cos\psi \, d\psi$$

$$= \pi R_i^2 \, p \, \phi \, dx \qquad (3.16)$$

Using Eq. (3.8), the expression in Eq. (3.16) can be further simplified to

$$dU = P_i \, \phi \, dx \qquad (3.17)$$

or

$$q = \frac{dU}{dx} = P_i \, \phi(x) \qquad (3.18)$$

where q is an equivalent distributed load approximately perpendicular to the initial pipe alignment in the direction from intrados to extrados.

Now that all the moment components are known, the moment at the cross-section located at the arbitrary location x in Fig. 3.10 can be expressed as

$$M = M_b + (P - P_i) v + P_i (\sin\theta_b) x - \int_0^x P_i \, \phi(\xi) \, (x - \xi) \, d\xi \qquad (3.19)$$

In order to check the result, the moment can also be calculated by approaching from the top end:

$$M = M_t + (P - P_i) v + P_i (\sin\theta_t)(L - x) - \int_x^L P_i \, \phi(\xi) \, (x - \xi) \, d\xi \qquad (3.20)$$

The first additional term, $(P - P_i) v$, will be called 'the axial force correction," and the other two, collectively, 'the pressure force correction." These two types of corrections have been plotted separately in Fig. 3.8. Since only one correction (the axial force correction) applies to the non-pressurized pipes, there will be no correction curves shown for these specimens.

3.2.6 Average Moment vs. Average Curvature over the Wrinkled Region

At each loading step, the average curvature over the wrinkled length is simply the area under the curvature diagram over the gage length divided by that length. These curvatures for specimen HGA12W are computed by integrating the curves shown in Fig. 3.5. The calculation of the average moment over the wrinkled region for Fig. 3.8 has been described in the previous section. The curves of average moment vs. average curvature over the wrinkled segment for specimens HGA12W, UGA12W, and DGA12W are shown in Fig. 3.13. These moment vs. curvature graphs are particularly important in terms of defining the characteristic pipe properties applied directly in analysis of pipelines.

3.3 PRESENTATION OF RESULTS

In the previous sections of this chapter, the general procedures for data reduction have been discussed and illustrated through the presentation of the results for specimen HGA12W. In the following subsections, the results for the remaining tests will be discussed and the development of buckling for each specimen will be described.

3.3.1 Results for UGA12W

In the UGA12W test, the wrinkle formed in a diamond shape (inward buckle) at the midheight of the specimen and contained the transverse girth weld. (This specimen is shown on the right in Figs. 3.14 and 3.15). No other buckling wave or ripple was observed at locations other than in the wrinkled segment.

Since the specimen UGA12W was non-pressurized, the value of P_i for this specimen is always zero. Thus, only three load lines are depicted in the loads vs. rotation diagram shown in Fig. 3.16. The strain distributions along the extreme compression fiber are shown in Fig. 3.17 for various rotations. These are mostly the results of the strain gage readings: Demec gage results were used only for strains above two percent, which occurred at the wrinkled region. As Fig. 3.17 shows, at the height of 960 mm (near the top of the wrinkled segment), the strains recorded by the strain gages in fact become tensile at high levels of rotation. This is because the local bending of the pipe wall in the region of wrinkling can produce localized tensile zones on the outside surface of the pipe wall even in the region of nominal compressive stresses. Electric resistance strain gages,

mounted on the outside surface of the specimens, only measure the strain on this external surface.

The strain distributions along the extreme tension fiber, as shown in Fig. 3.18, indicate localization as well. However, the maximum tensile strain does not exceed 0.6 percent. As is apparent in Fig. 3.19, the curvature along the specimen for various rotations shows a very sharp increase at the level of the wrinkled segment for high levels of rotations. This is a basic characteristic of wrinkled segment.

The displacement profile of the extreme compression fiber for various rotations is presented in Fig. 3.20. The contour gage was used from the rotation of 2.92 degrees onwards. The results from the contour gage drawings appear as two additional complementary points around the level of girth weld in the wrinkled segment. The supplementary data frc..n the contour gage indicates the first sign of distortion at 2.92 degrees. It also provides the measures to represent the deep, inward wrinkle, that produces the sharp peaks evident in the profile curves of Fig. 3.20 for high rotations.

The average end moment and average moment over the wrinkled segment vs. overall curvature are depicted in Fig. 3.21. This figure shows that the difference between the two moments, which is the additional moment due to the eccentricity of axial load with respect to the wrinkled segment, increases with the overall curvature. The curve of average moment vs. average curvature over the wrinkled segment for specimen UGA12W, along with those for HGA12W and DGA12W, is shown in Fig. 3.13.

3.3.2 Results for HGA12W

The plots for specimen HGA12W have all been presented in the subsections of Section 3.2 as illustrations of the different categories of graphs for various specimens. Consequently, only the observation of buckling needs to be discussed here.

In specimen HGA12W, the wrinkle formed as a single outwardly bulging wrinkle (see the central specimen in Figs. 3.15 and 3.16). This was initially one of four waves that could be detected by close visual examination. Two of these waves are apparent at, and below, the rotation level of 3.66 degrees in the profile of the extreme compression fiber (Fig. 3.6). Subsequently, one of the waves, just below the girth weld, grew to become the wrinkle while the others died out. The other two waves appeared only at the early stages

of bending and had very small amplitudes. As it happened, they occurred within the spacings of the radial LVDT's. As a result, the latter two waves are not apparent in the profile of the extreme compression fiber (Fig. 3.6). The contour gage was used at the higher rotation levels only for the more noticeable local deformations.

3.3.3 Results for DGA12W

In the test of DGA12W, the wrinkle formed as a single outwardly bulging wrinkle (see the specimen on the left in Figs. 3.15 and 3.16). This was initially one of the four waves that could be detected by close visual examination. One of the waves, immediately below the girth weld, grew to become the wrinkle while the others stabilized or died out.

The loads vs. rotation response for the specimen DGA12W is depicted in Fig. 3.22. The strain distributions along the extreme compression fiber for various rotations, as shown in Fig. 3.23, are taken mostly from strain gage readings. Demec gage results were used only for the strains above two percent, and these occurred in the wrinkled region. The strain distributions along the extreme tension fiber for various rotations, shown in Fig. 3.24, also indicate localization in the wrinkled region. However, the maximum tensile strain does not exceed 1.9 percent. As is apparent in Fig. 3.25, the curvature along the specimen for various rotations shows a very sharp increase within the wrinkled segment at the higher levels of rotations. This is a basic characteristic of wrinkled segment. The displacement profile of the extreme compression fiber for various rotations is presented in Fig. 3.26. These profiles capture three of the four waves observed early in the test. The fourth wave formed between two successive radial LVDT stations and, hence, remained undetected by the instrumentation. The sharp bend in the profile immediately below the girth weld level at high rotations identifies the outwardly bulging wrinkle evident in Fig. 3.15.

The average end moment and average moment over the wrinkled segment vs. overall curvature are depicted in Fig. 3.27. This figure also shows the curves of axial force correction and the pressure force correction to the end moment diagram needed in order to get the average moment in the wrinkled segment. The sum of the two corrections for any value of overall curvature makes the difference between the two moments at that curvature. The curve of average moment vs. average curvature over the wrinkled segment for specimen DGA12W, along with those for UGA12W and HGA12W, is shown in Fig. 3.13.

3.3.4 Results for UGA20W-2

Because of inadequate safety measures in the control program (see Section 2.6), control of the jack that exerts the eccentric load was lost near the beginning of the test of the specimen UGA20W-1. As a result, the specimen was plastically deformed and permanently bent at the beginning of the test. That left residual stresses and strains in the specimen. The same thing happened to the second specimen, UGA20W-2, though to a lesser extent than in the previous one. Thus, it was decided to abandon the data from UGA20W-1, but to proceed with the results of UGA20W-2. For the rest of the tests, sufficient safety measures were provided in the control program and the tests were performed successfully in these cases.

In the UGA20W-2 test, the wrinkle formed in a diamond shape (inward buckle) at the midheight of the specimen and in the region containing the transverse girth weld. This is the specimen on the right in Fig. 3.28. No other wave or ripple was observed at locations other than in the wrinkled segment.

Since the specimen UGA20W-2 was non-pressurized, the value of P_i for this specimen is always zero. Thus, only three load lines are plotted in the loads vs. rotation diagram shown in Fig. 3.29. The strain distributions along the extreme compression fiber for various rotations, as shown in Fig. 3.30, are the results of the Demec gage readings. This is because, after the initial plastification of the specimen, the two lines of strain gages on the compression side gave such different results that they were not reliable. The initial residual strains have been removed from the strains of the extreme compression fiber presented in Fig. 3.30. As Fig. 3.30 shows, near the top and bottom of the wrinkled segment, compressive strains become tensile at high levels of rotation. This is because the local bending of the pipe wall in the region of the wrinkle produces localized tensile zones on the outside surface.

The strain distributions along the extreme tension fiber for various rotations, as shown in Fig. 3.31, indicate localization as well. However, the maximum tensile strain does not exceed 0.3 percent. In contrast to the strain gage readings on the compression side, tension side strain gages gave consistent results. Therefore, only strain gage results were used to depict the distribution of strain on the tension side. The residual strains have been removed from the strains presented.

As apparent in Fig. 3.32, the curvature along the specimen for various rotations shows a very sharp increase in the wrinkled segment for high levels of rotations. This is a basic characteristic of wrinkled segment.

The displacement profile of the extreme compression fiber for various rotations is presented in Fig. 3.33. The contour gage was used from 2.3 degrees rotation and onwards. The results of the contour gage drawings appear as two additional complementary points around the level of girth weld in the wrinkled segment. The supplementary data from the contour gage indicate the first sign of distortion at 2.3 degrees. They also provide the measures to represent the deep, inward wrinkle, apparent from the sharp peaks in the curves for high rotations.

The average end moment and average moment over the wrinkled segment vs. overall curvature are depicted in Fig. 3.34. This figure shows that the difference between the two moments (i.e., the additional moment due to the eccentricity of axial load with respect to the wrinkled segment) increases with the overall curvature. The curve of average moment vs. average curvature over the wrinkled segment for specimen UGA20W-2, along with those for HGA20W and DGA20W, is shown in Fig. 3.35.

3.3.5 Results for HGA20W

In the HGA20W test, the wrinkle formed as a single outwardly bulging wrinkle. (See the second specimen from the left in Fig. 3.28). This was initially one of the four waves that could be detected by close visual examination. The wave immediately below the girth weld grew to become the local buckle and the others died out.

The loads vs. rotation for the specimen HGA20W are depicted in Fig. 3.36. The strain distributions along the extreme compression fiber for various rotations, shown in Fig. 3.37, are mostly the results of the strain gage readings. Demec gage results were used only for strains above two percent, which occurred in the wrinkled region. The strain distributions along the extreme tension fiber for various rotations, shown in Fig. 3.38, also indicate localization in the wrinkled region. However, the maximum tensile strain does not exceed 1.5 percent. As apparent in Fig. 3.39, the curvature along the specimen for various rotations shows a very sharp increase in the wrinkled segment for high levels of rotation. This is a basic characteristic of wrinkled segment.

The displacement profile of the extreme compression fiber for various rotations is presented in Fig. 3.40. These profiles capture three of the four waves observed early in the test. The fourth wave formed between two successive radial LVDT stations and, hence, remained undetected by the instrumentation. The sharp bend in the profile below the level of girth weld at high rotations indicates the outwardly bulging wrinkle.

The average end moment and average moment over the wrinkled segment vs. overall curvature are depicted in Fig. 3.41. This figure also shows the curves of axial force correction and the pressure force correction to the end moment diagram that are required in order to get the average moment in the wrinkled segment. The sum of these two corrections for any value of overall curvature makes the difference between the two moments at that curvature. The curve of average moment vs. average curvature over the wrinkled segment for specimen HGA20W, along with those for UGA20W-2 and DGA20W, is also shown in Fig. 3.35.

3.3.6 Results for DGA20W

In the DGA20W test, the wrinkle formed as a single outwardly bulging wrinkle. This is the specimen on the left in Fig. 3.28. This was initially one of the four waves that could be detected by close visual examination. The wave near the top of the specimen grew to become the wrinkle, and the others stabilized.

The loads vs. rotation for the specimen DGA20W are depicted in Fig. 3.42. The strain distributions along the extreme compression fiber for various rotations, shown in Fig. 3.43, are mostly from strain gage readings. Demec gage results were used only for strains above two percent, which occurred in the wrinkled region and in the wave below the wrinkled region. The strain distributions along the extreme tension fiber for various rotations, shown in Fig. 3.44, indicate localization in the wrinkled region as well. However, the maximum tensile strain does not exceed 1.7 percent. As is apparent in Fig. 3.45, the curvature along the specimen for various rotations shows a very sharp increase in the wrinkled segment for high levels of rotation. This is a basic characteristic of a wrinkled segment.

The displacement profile of extreme compression fiber for various rotations is presented in Fig. 3.46. These profiles capture all the four waves observed early in the test.

The profiles from the rotation of 5.23 degrees onwards have been supplemented with two additional points from the contour gage results. The sharp bend in the profile near the top of the specimen at high rotations indicates the outwardly bulging wrinkle.

The average end moment and average moment over the wrinkled segment vs. overall curvature are depicted in Fig. 3.47. This figure also shows the curves of axial force correction and the pressure force correction. The sum of these two corrections for any value of overall curvature makes the difference between the two moments at that curvature. The curve of average moment vs. average curvature over the wrinkled segment for specimen DGA20W, along with those for UGA20W-2 and HGA20W, is shown in Fig. 3.35.

3.4 CLASSIFICATION OF LOCAL DEFORMATIONS

In the non-pressurized tests (i.e., UGA12W and UGA20W-1&2), the wrinkle formed in a diamond shape (inward wrinkle), and no other wave or distortion was observed at locations other than in the wrinkled segment. See Figs. 3.15, 3.16, and 3.28.

In the pressurized tests (HGA20W, DGA20W, HGA12W, and DGA12W), the wrinkle formed as a single outward bulge. See Figs. 3.15, 3.16, and 3.28. This wrinkle was initially one of the four waves or ripples that could be detected by close visual examination. These buckling waves became evident at rotations approaching the softening point that is defined subsequently in Section 4.2.2. As the deformation was increased, the amplitude of the dominant wave increased and the amplitudes of the others decreased. The result was that the inelastic deformation and the strains amplified in one dominant wave (wrinkle), while the other ripples disappeared or stabilized.
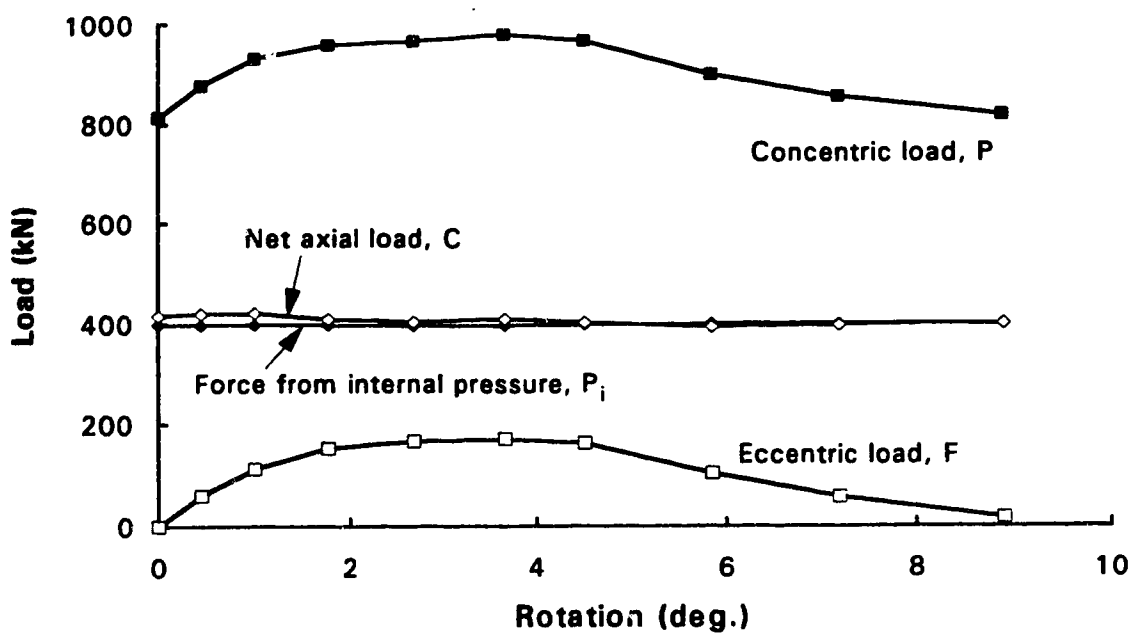
Fig. 3.1 Applied loads vs. rotation for HGA12W
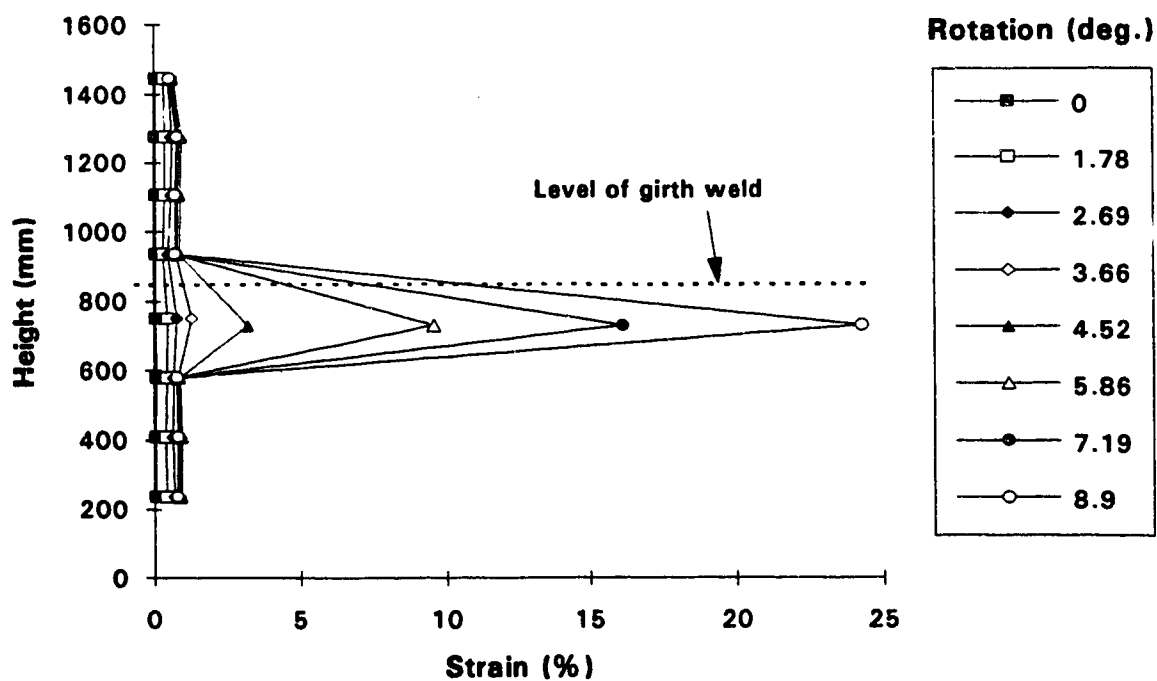
Fig. 3.2 Strain distribution along extreme compression fiber for HGA12W
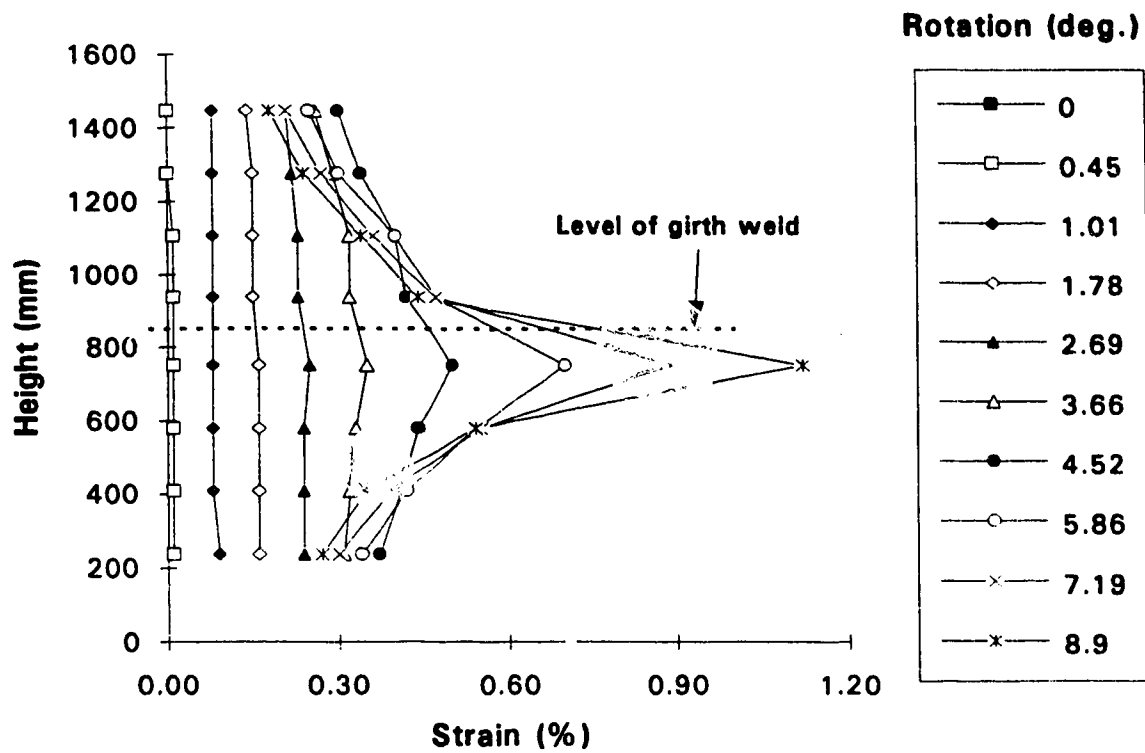
Fig. 3.3 Strain distribution along extreme tension fiber for HGA12W
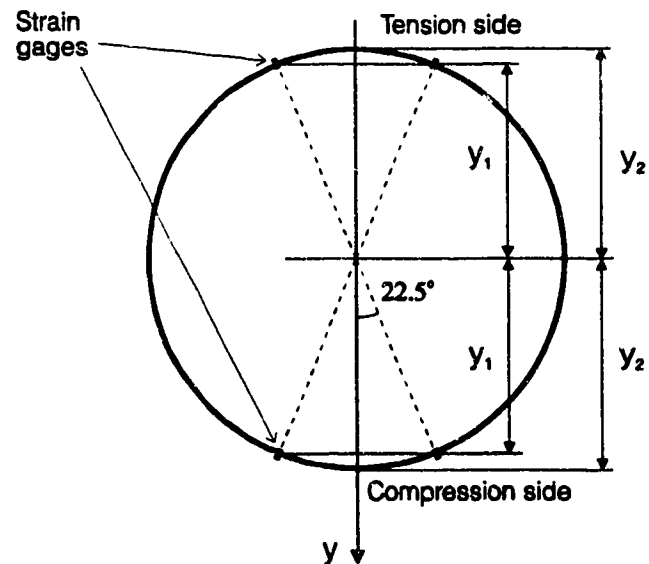
Fig. 3.4 Locations of strain gages with respect to extreme fibers
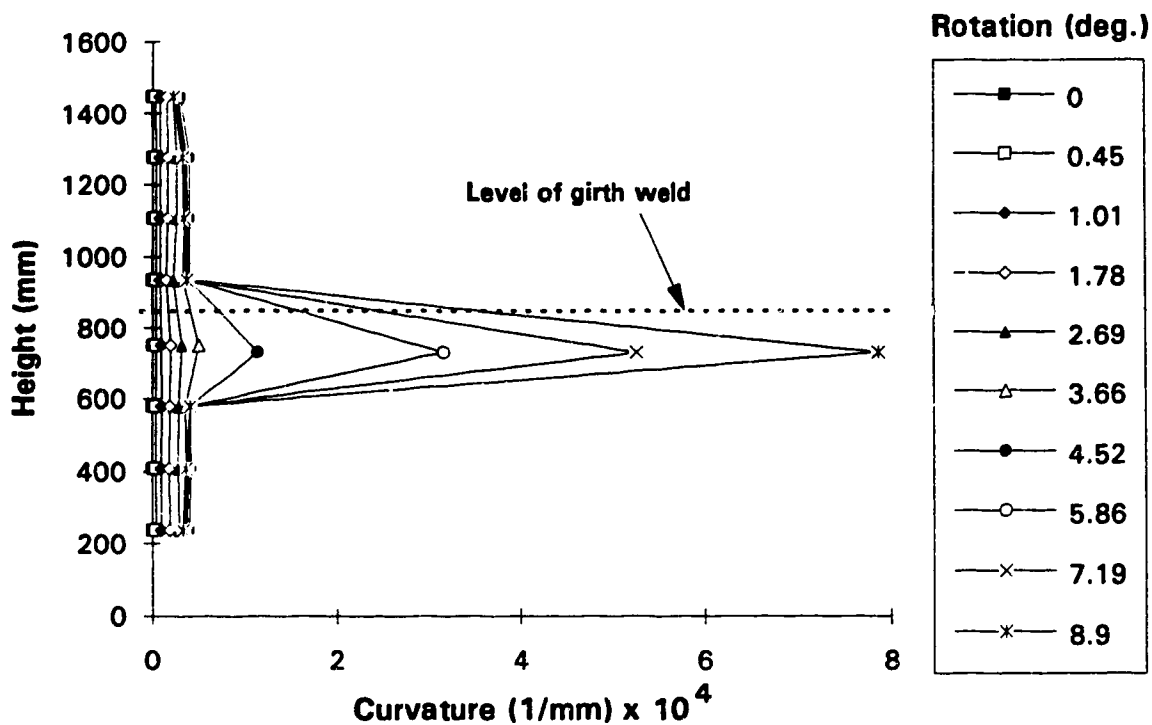
Fig. 3.5 Curvature distribution along specimen HGA12W at various rotations
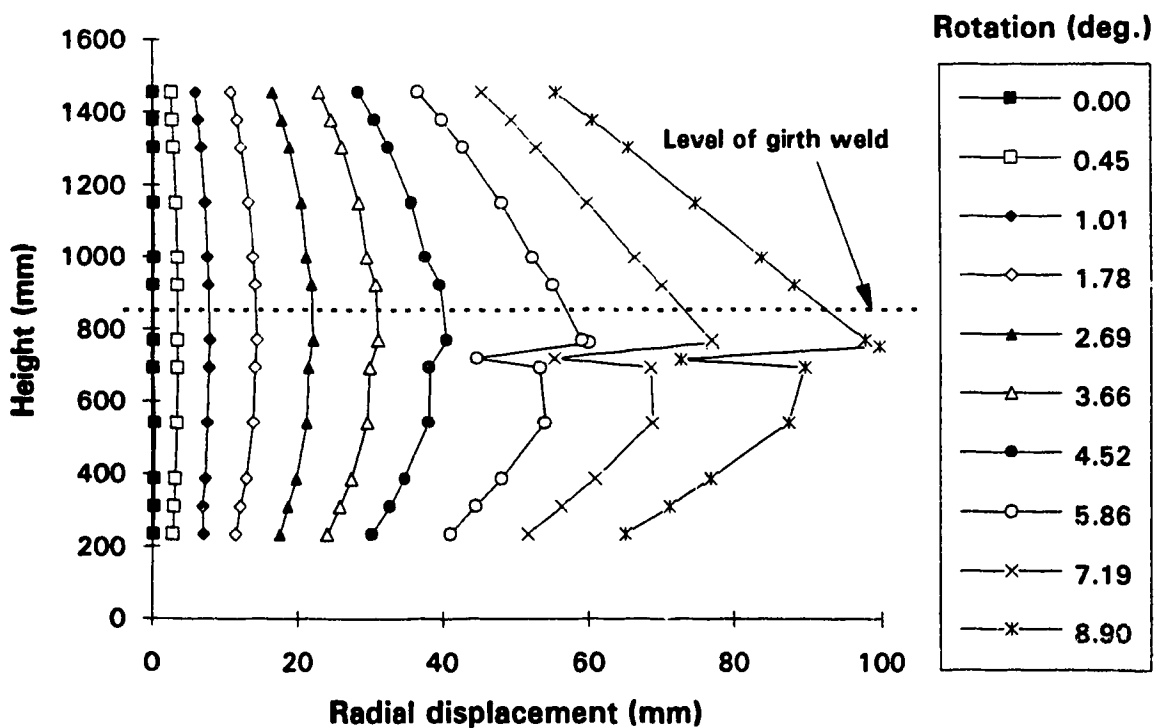
Fig. 3.6 Profile of extreme compression fiber at various rotations for HGA12W
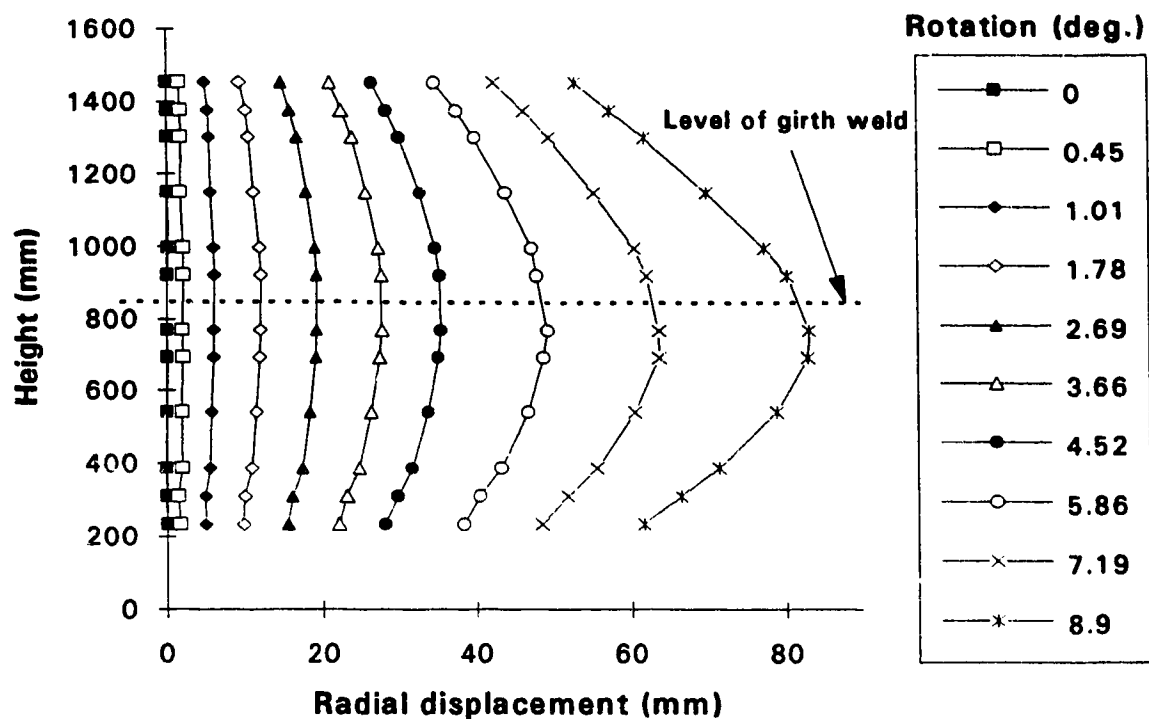
Fig. 3.7 Profile of extreme tension fiber at various rotations for HGA12W
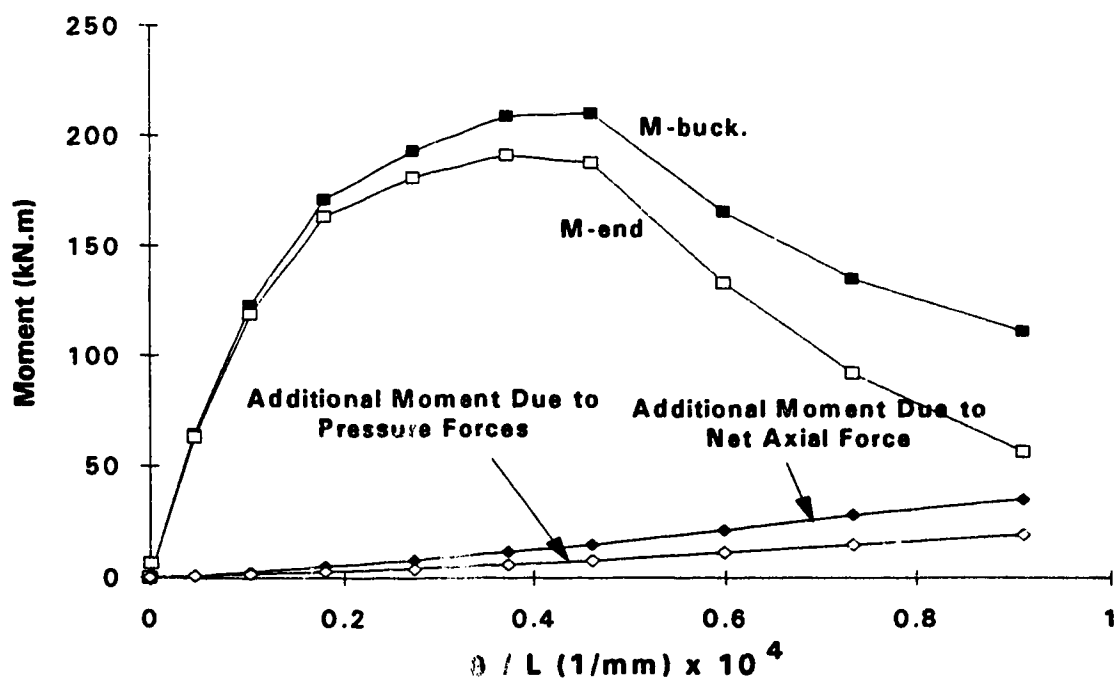
Fig. 3.8 Average of end moments and average moment over wrinkled segment vs. overall curvature for HGA12W
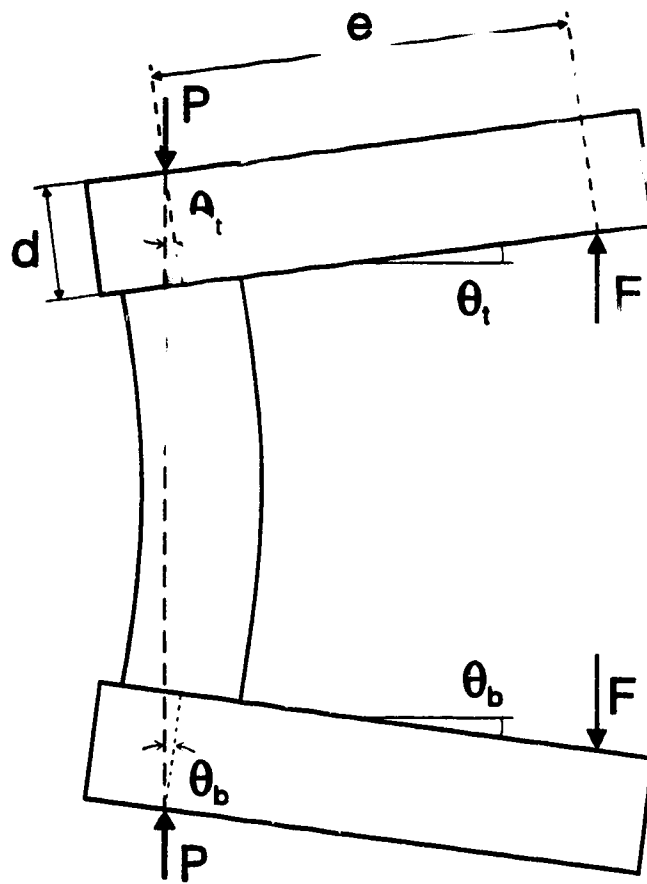
Fig. 3.9 Geometry of deformed pipe
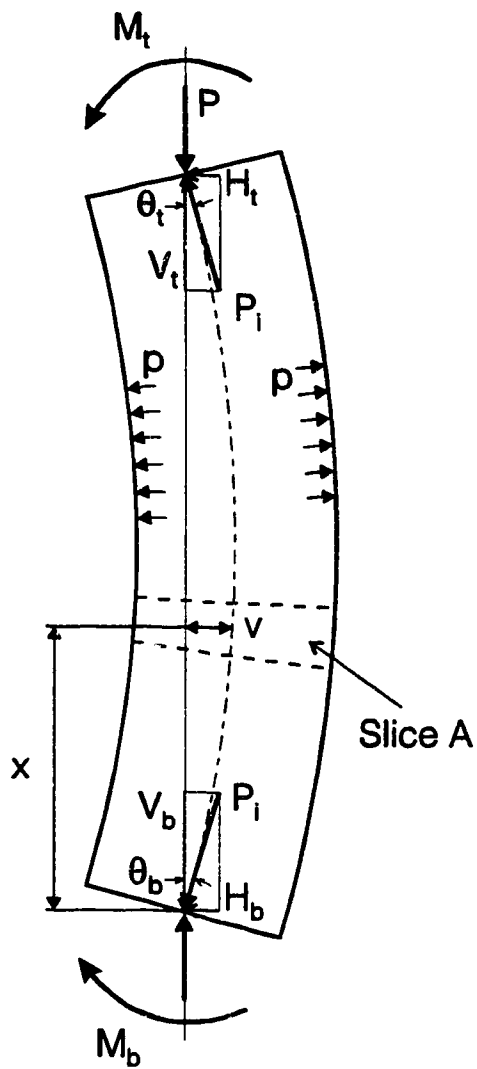
Fig. 3.10 Free body diagram of
deformed specimen
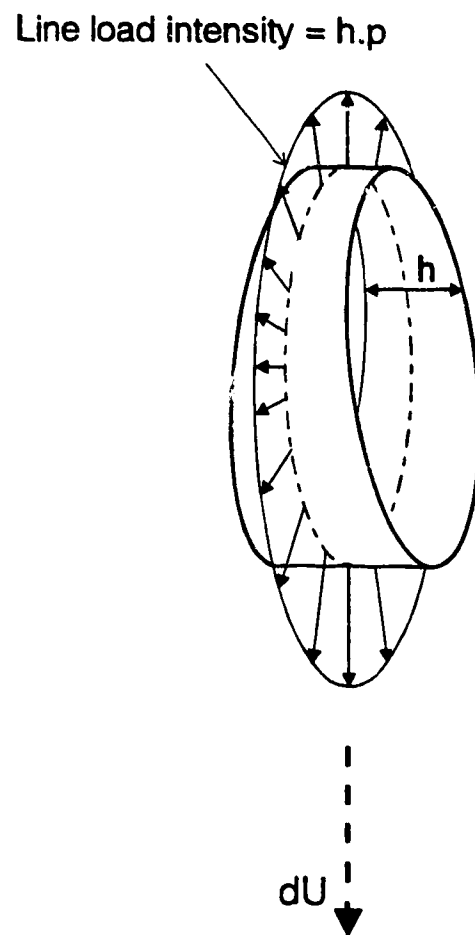
Fig. 3.11 Non-uniform pressure forces
acting on slice A
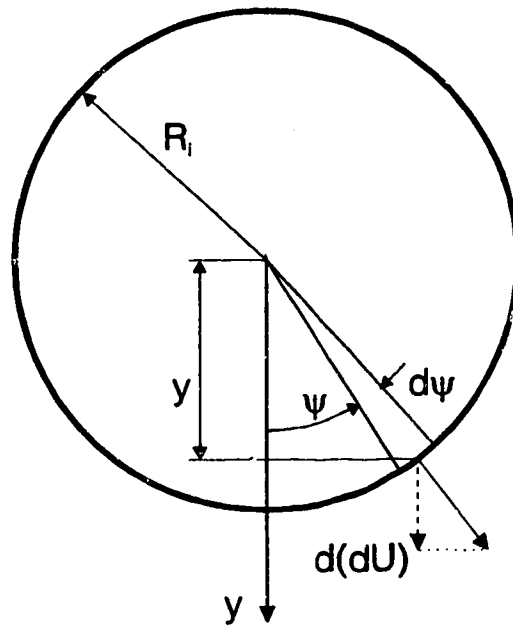
a. Plan
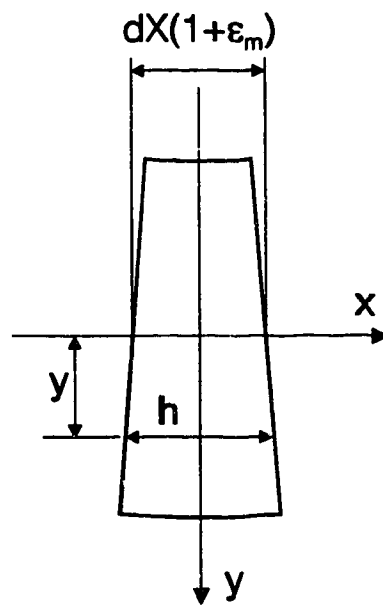
b. Profile

Fig. 3.12 Deformed configuration of slice A
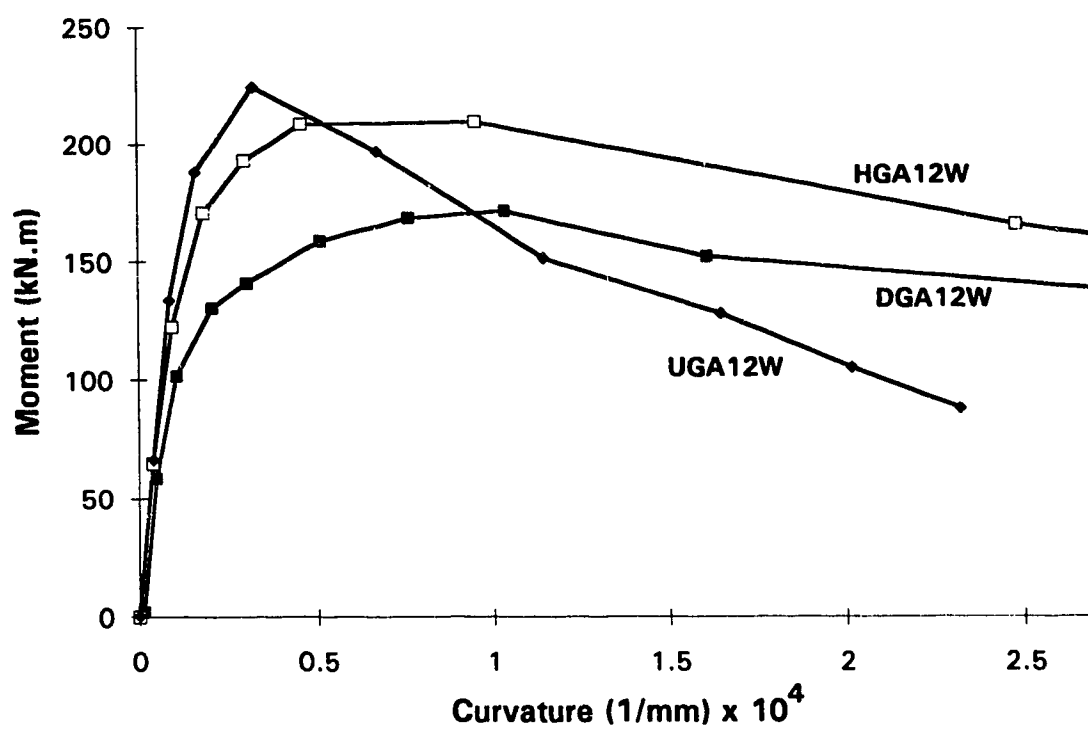
Fig. 3.13 Average moment vs. average curvature over wrinkled segment for 12-inch specimens
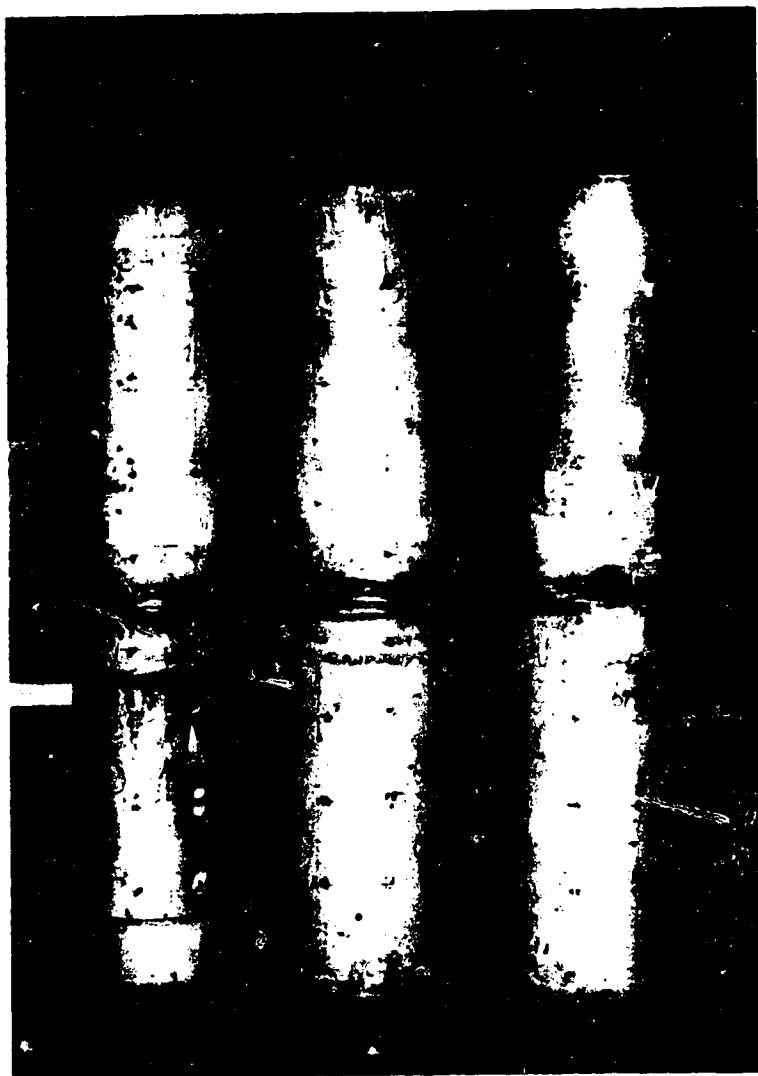
Fig. 3.14 Post-wrinkle configuration of specimens DGA12W, HGA12W, and UGA12W
(left to right)

Fig. 3.15 Close-up view of post-wrinkle configuration of specimens DGA12W,
HGA12W, and UGA12W (left to right)
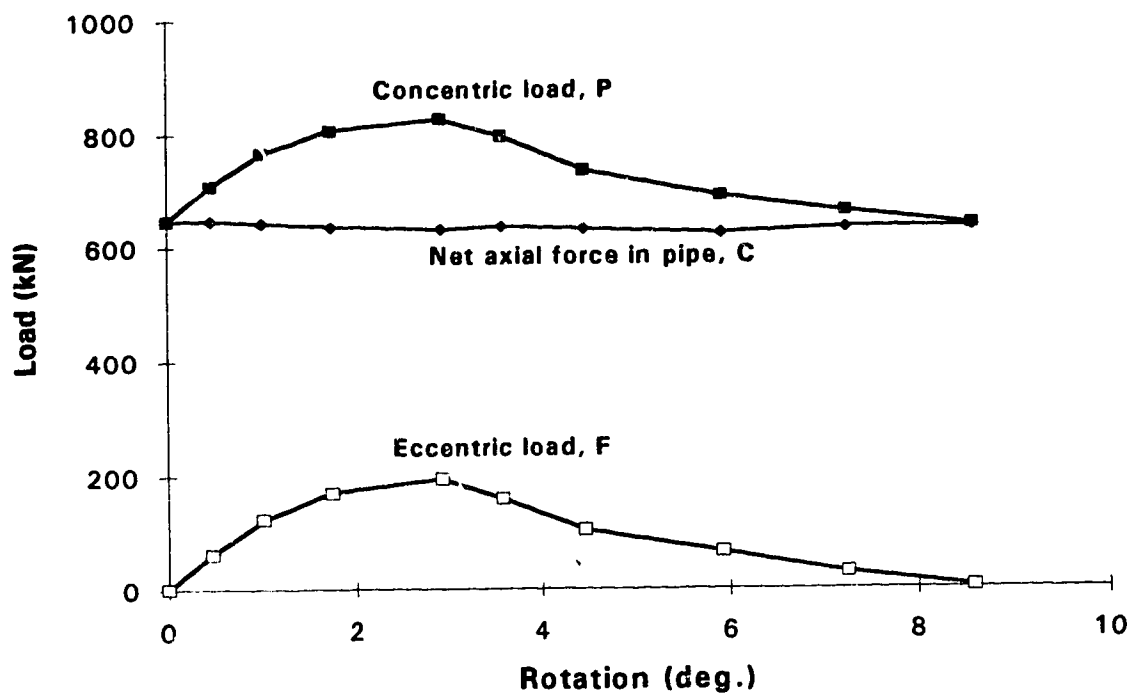
Fig. 3.16 Applied loads vs. rotation for UGA12W
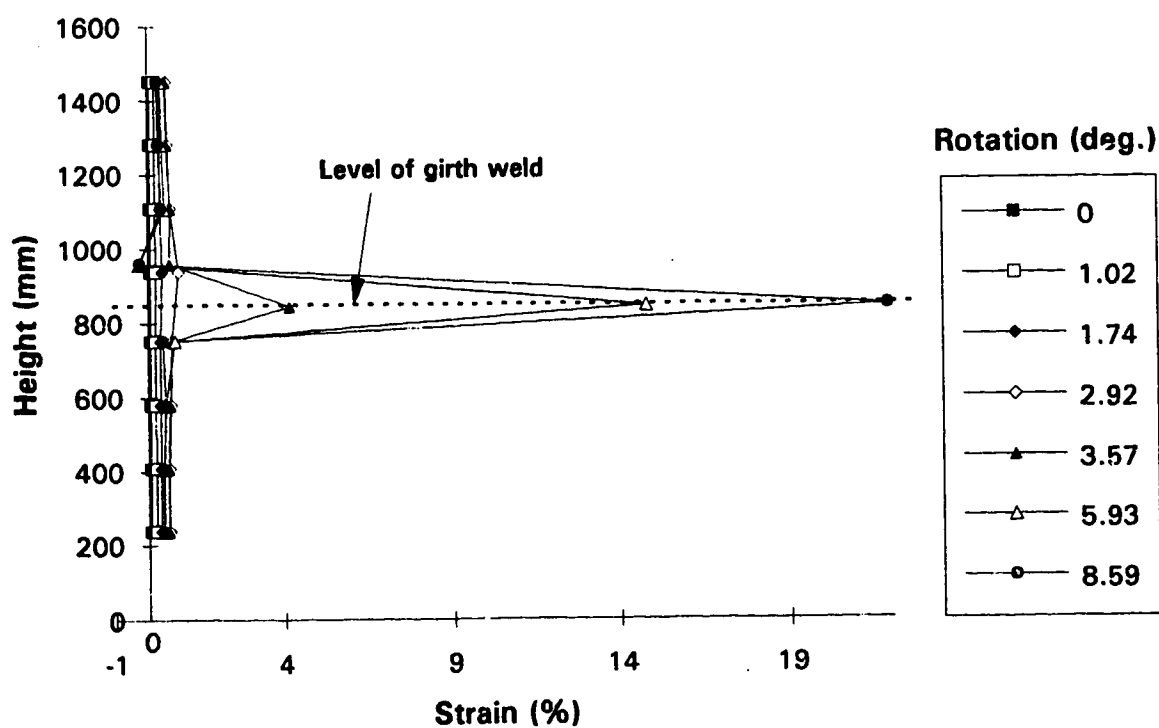
Fig. 3.17 Strain distribution along extreme compression fiber for UGA12W
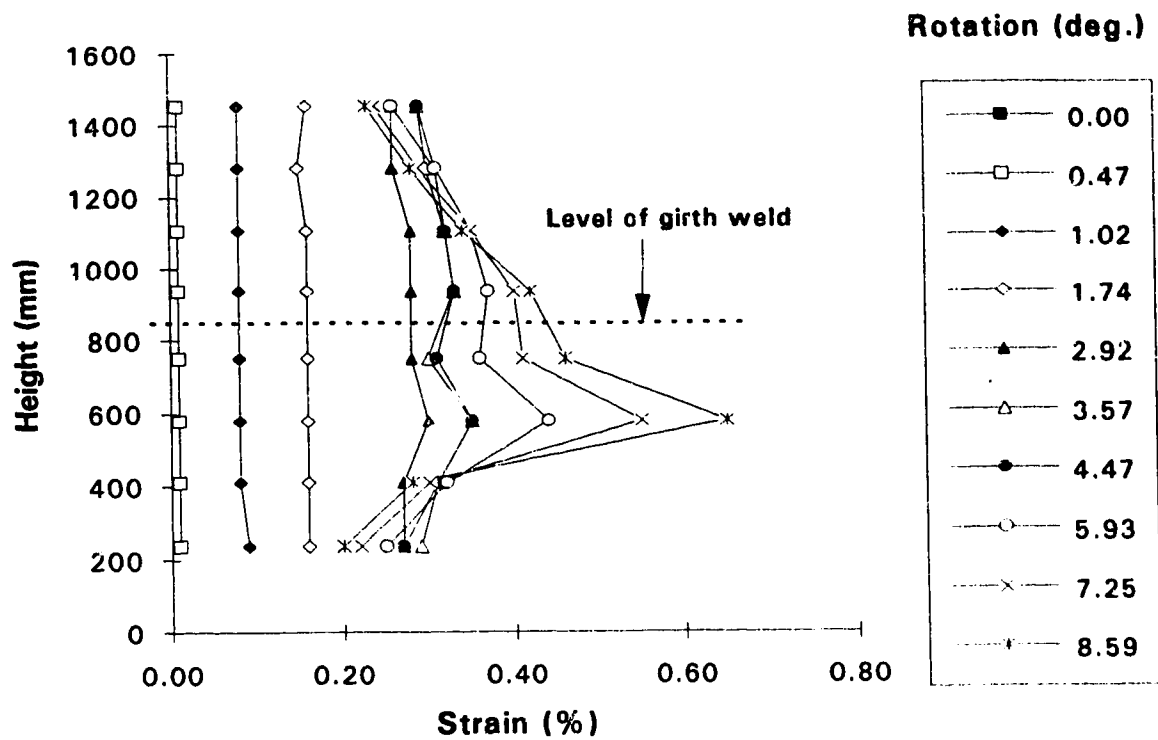
Fig. 3.18 Strain distribution along extreme tension fiber for UGA12W
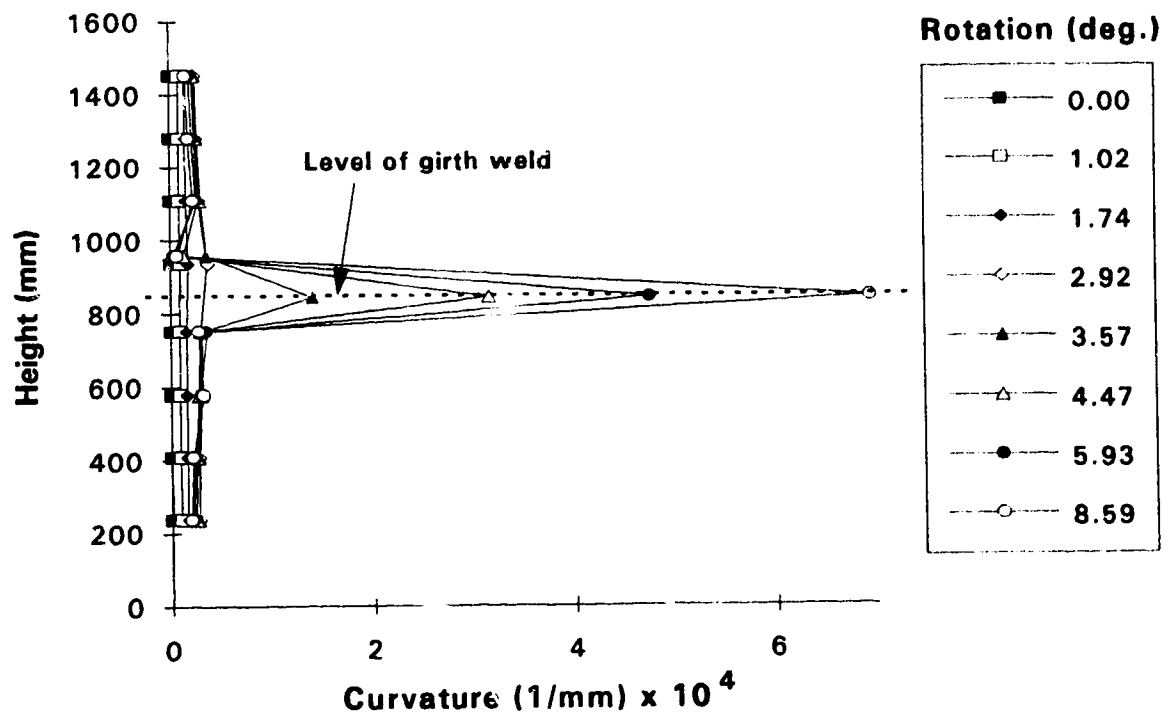
Fig. 3.19 Curvature distribution along specimen UGA12W at various rotations
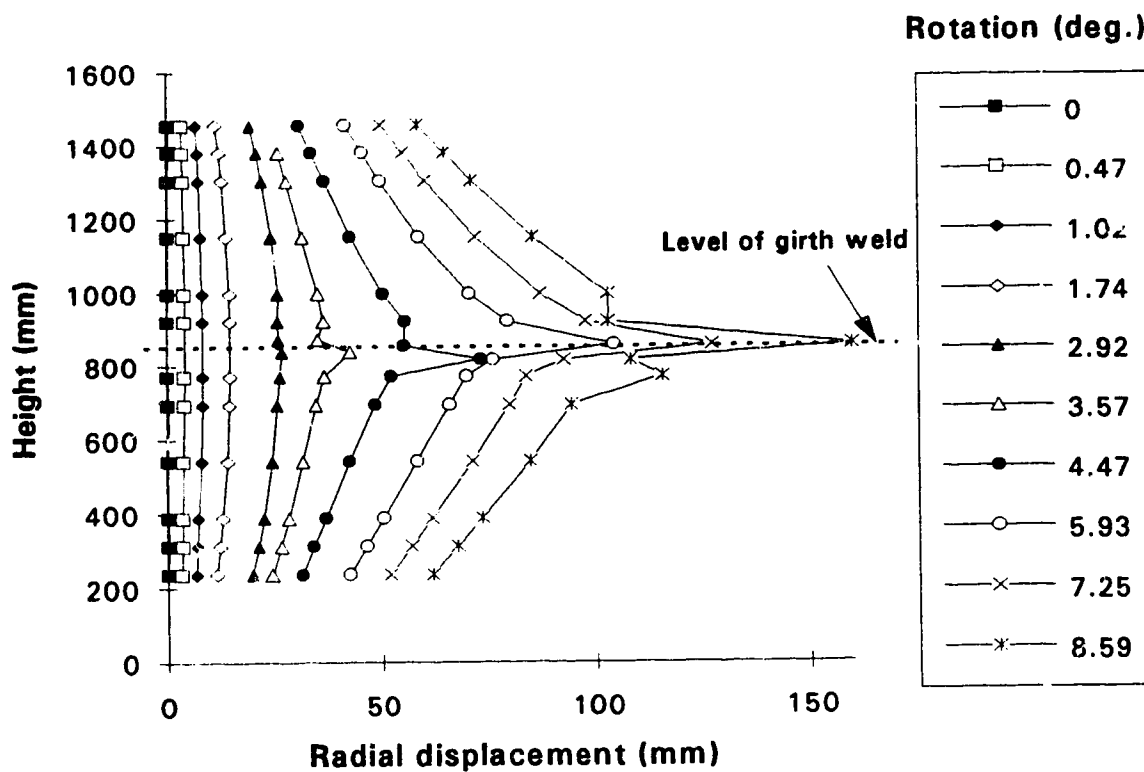
Fig. 3.20 Profile of extreme compression fiber at various rotations for UGA12W
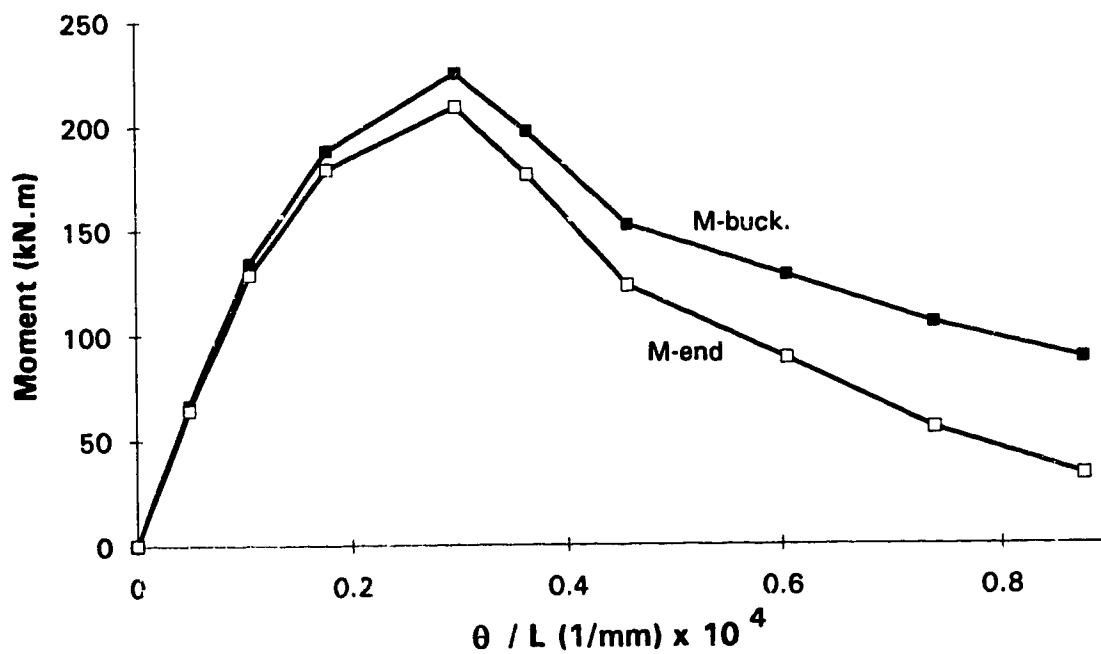
Fig. 3.21 Average of end moments and average moment over wrinkled segment vs.
overall curvature for UGA12W
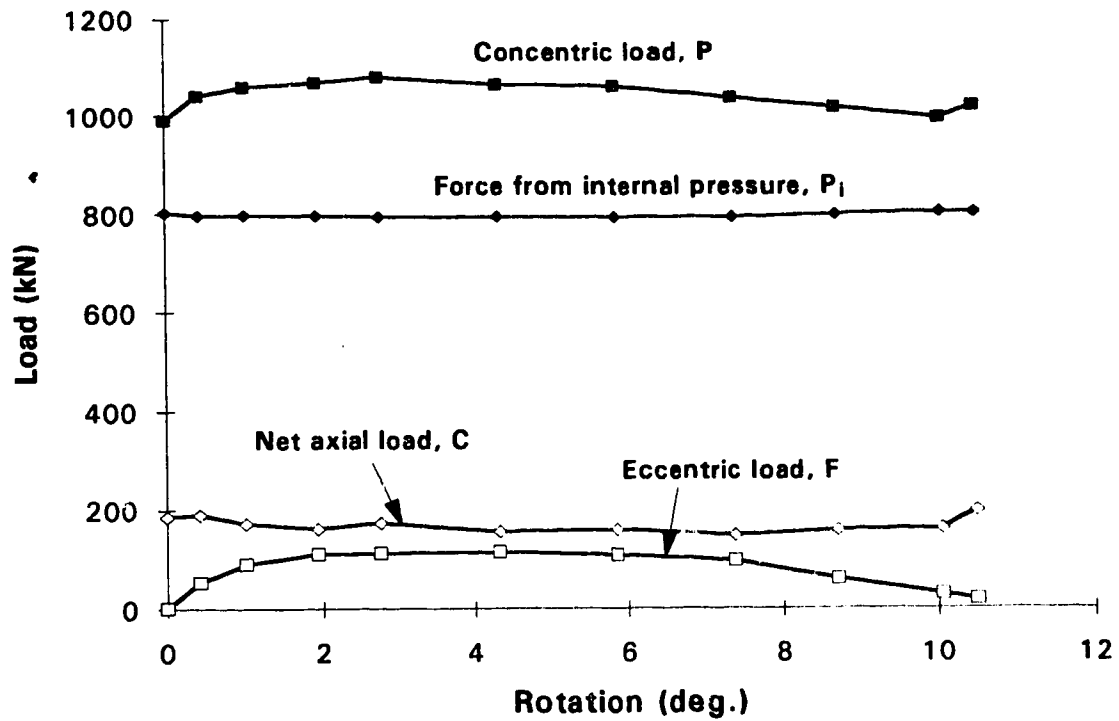
Fig. 3.22 Applied loads vs. rotation for DGA12W
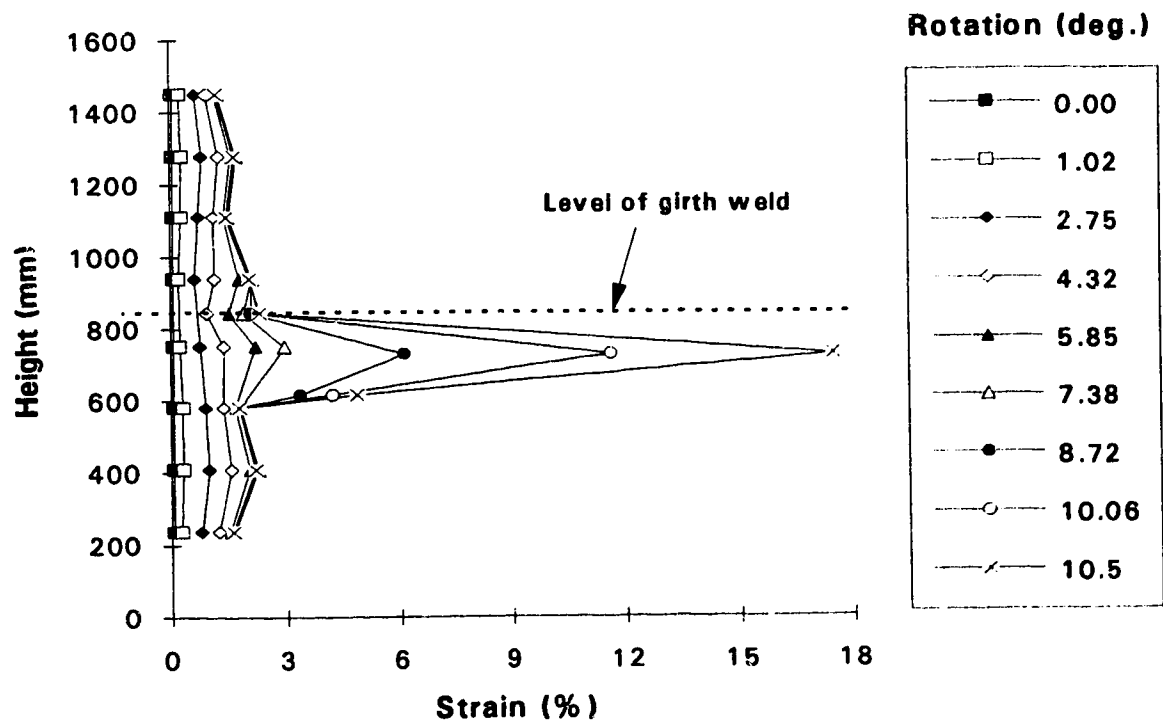
Fig. 3.23 Strain distribution along extreme compression fiber for DGA12W

Rotation (deg.)

■	0.00
□	0.43
◆	1.02
◇	1.94
▲	2.75
△	4.32
●	5.85
○	7.38
×	8.72
✳	10.50

Level of girth weld

Fig. 3.24 Strain distribution along extreme tension fiber for DGA12W

Rotation (deg.)

■	0.00
□	1.02
◆	1.94
◇	2.75
▲	4.32
△	5.85
●	7.38
○	8.72
×	10.06
✳	10.5

Level of girth weld
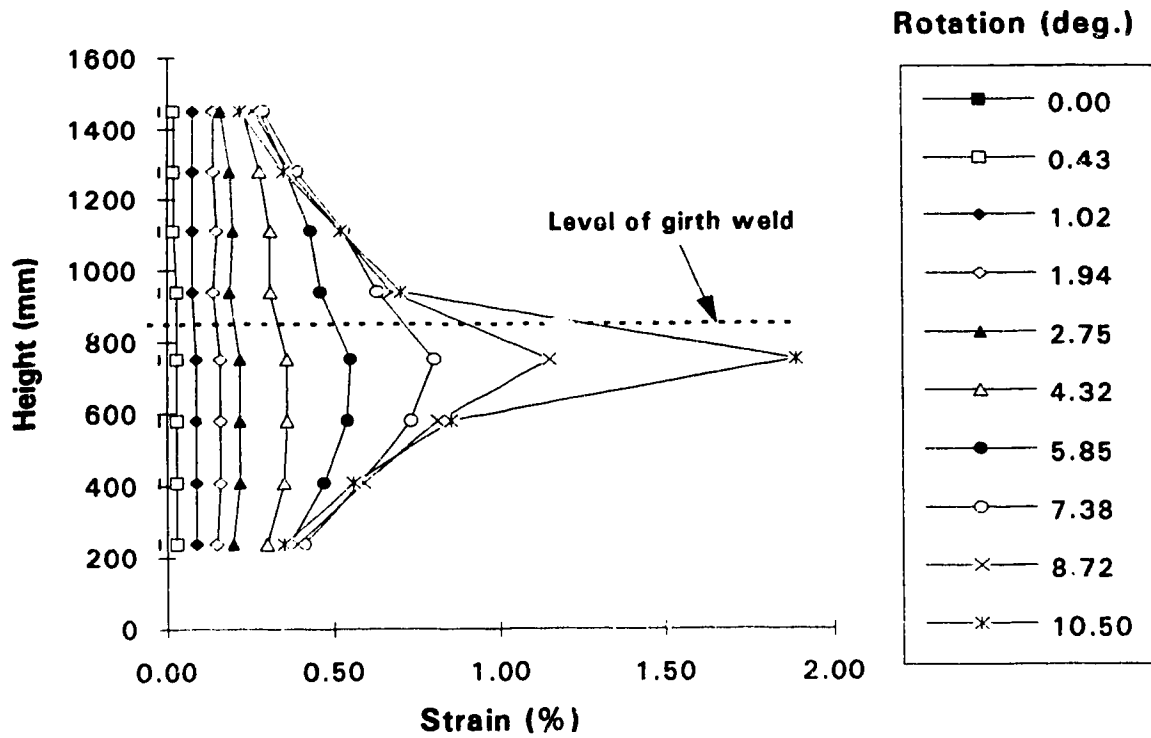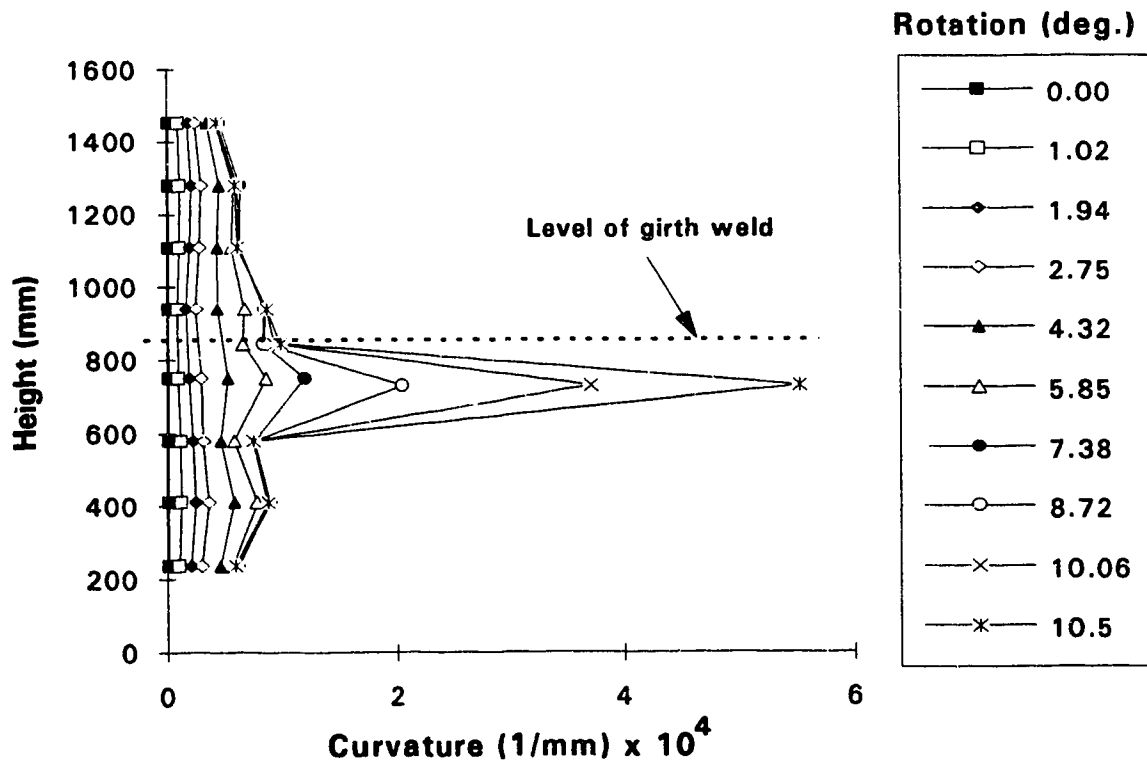
Fig. 3.25 Curvature distribution along specimen DGA12W at various rotations
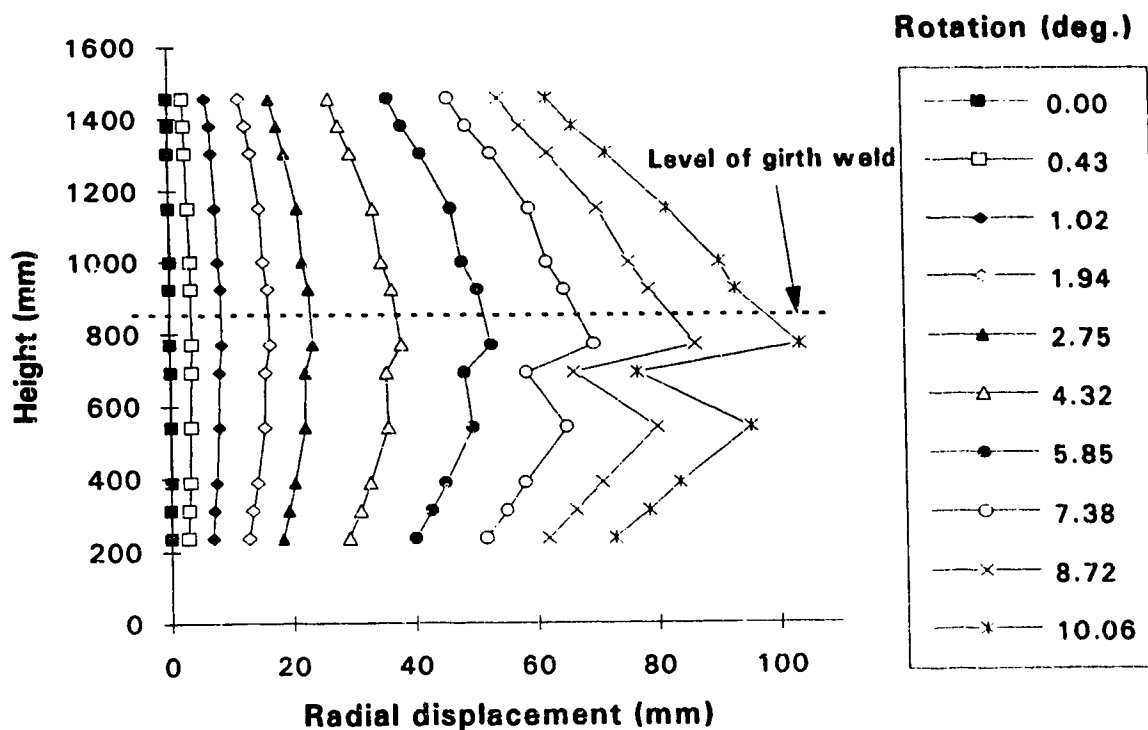
Fig. 3.26 Profile of extreme compression fiber at various rotations for DGA12W
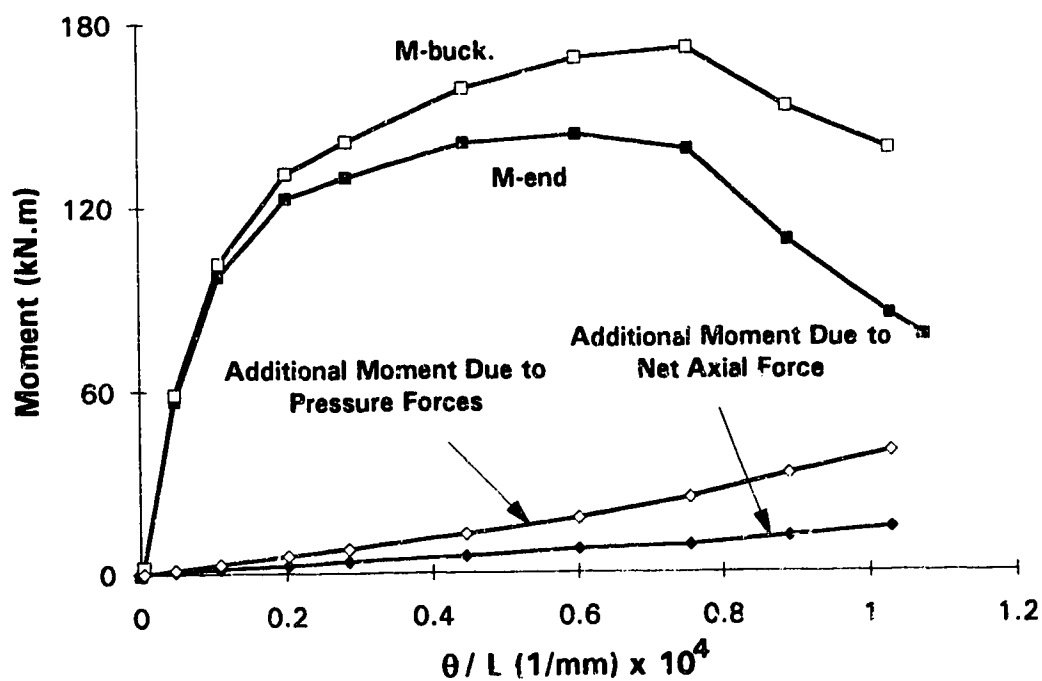
Fig. 3.27 Average of end moments and average moment over wrinkled segment vs.
overall curvature for DGA12W

Fig. 3.28 Post-wrinkle configuration of specimens DGA20W, HGA20W, UGA20W-1, and UGA20W-2 (left to right)
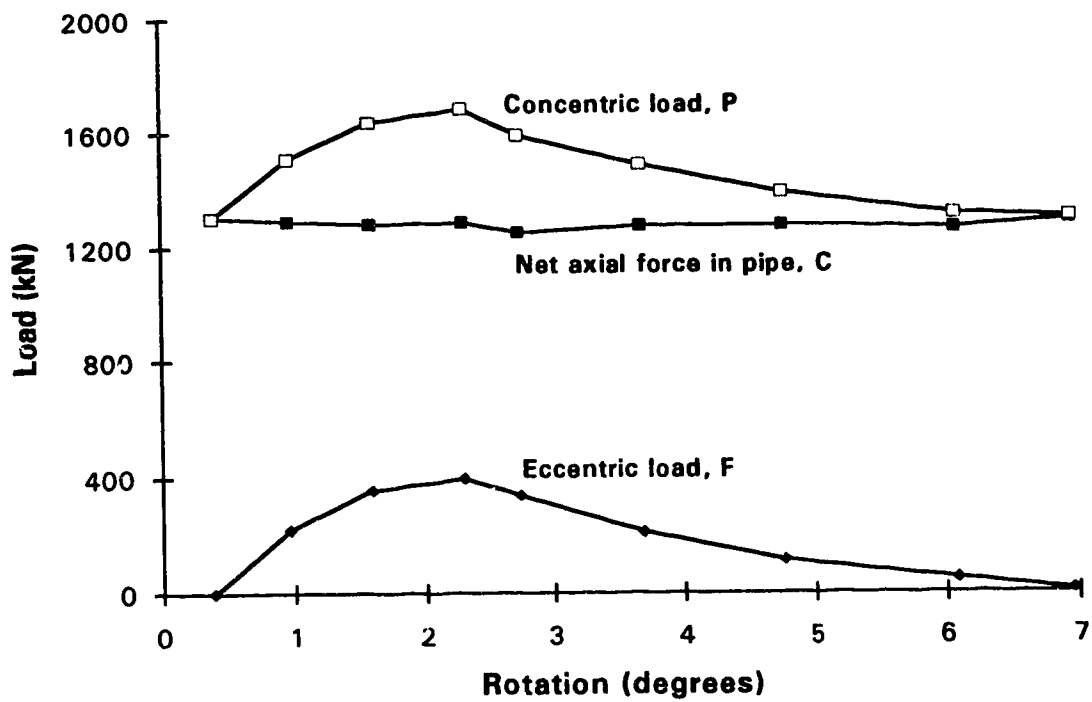
Fig. 3.29 Applied loads vs. rotation for UGA20W-2
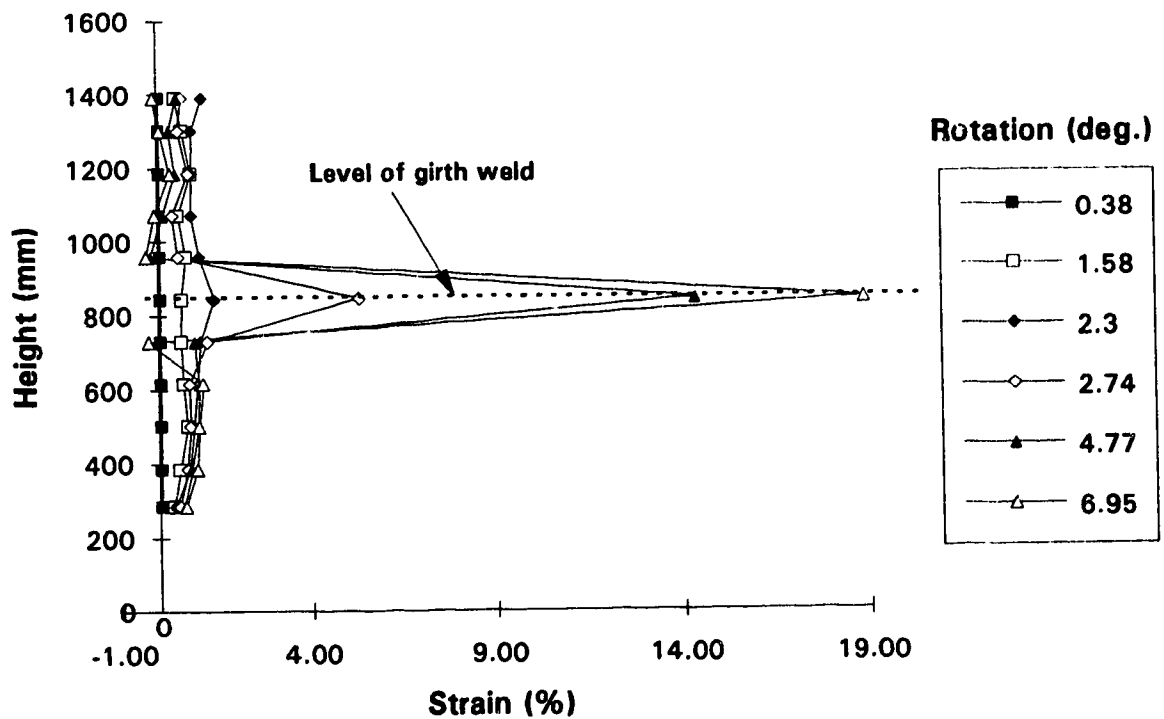
Fig. 3.30 Strain distribution along extreme compression fiber for UGA20W-2
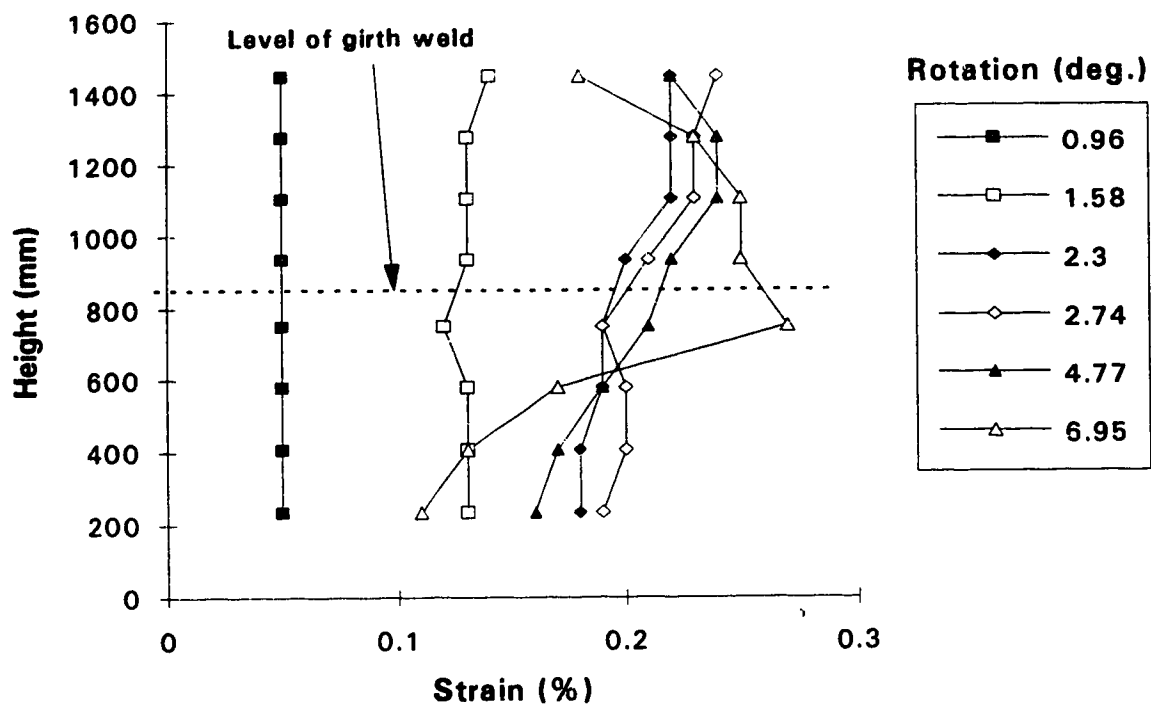
Fig. 3.31 Strain distribution along extreme tension fiber for UGA20W-2
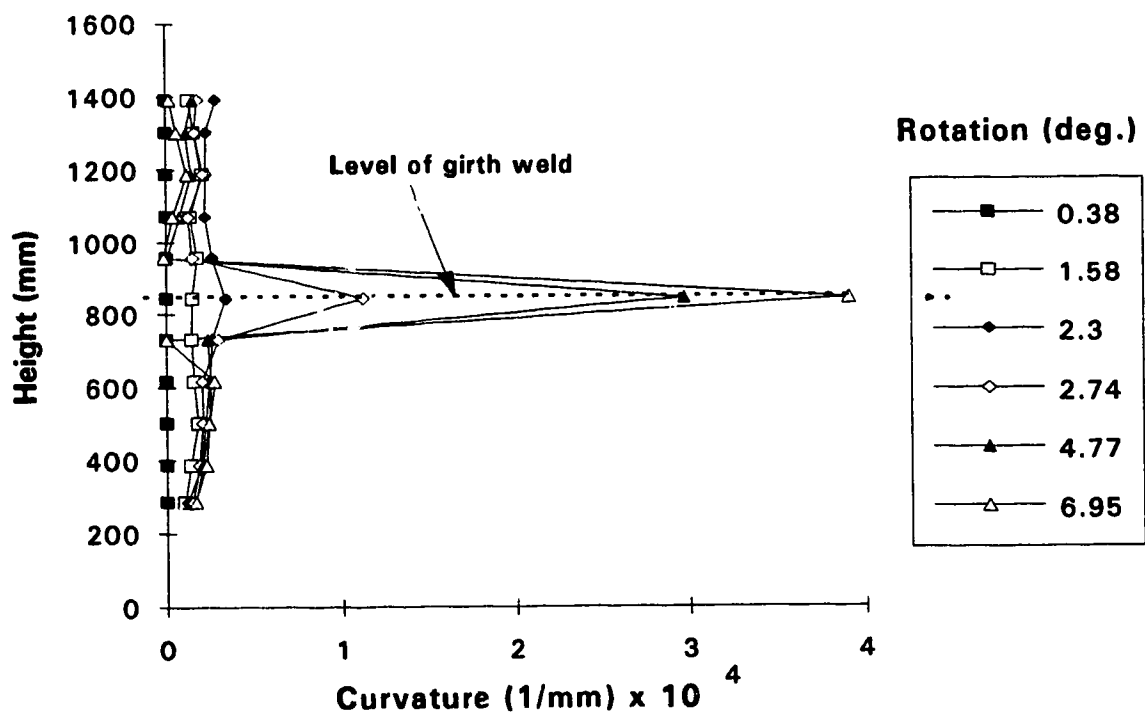
Fig. 3.32 Curvature distribution along specimen UGA20W-2 at various rotations
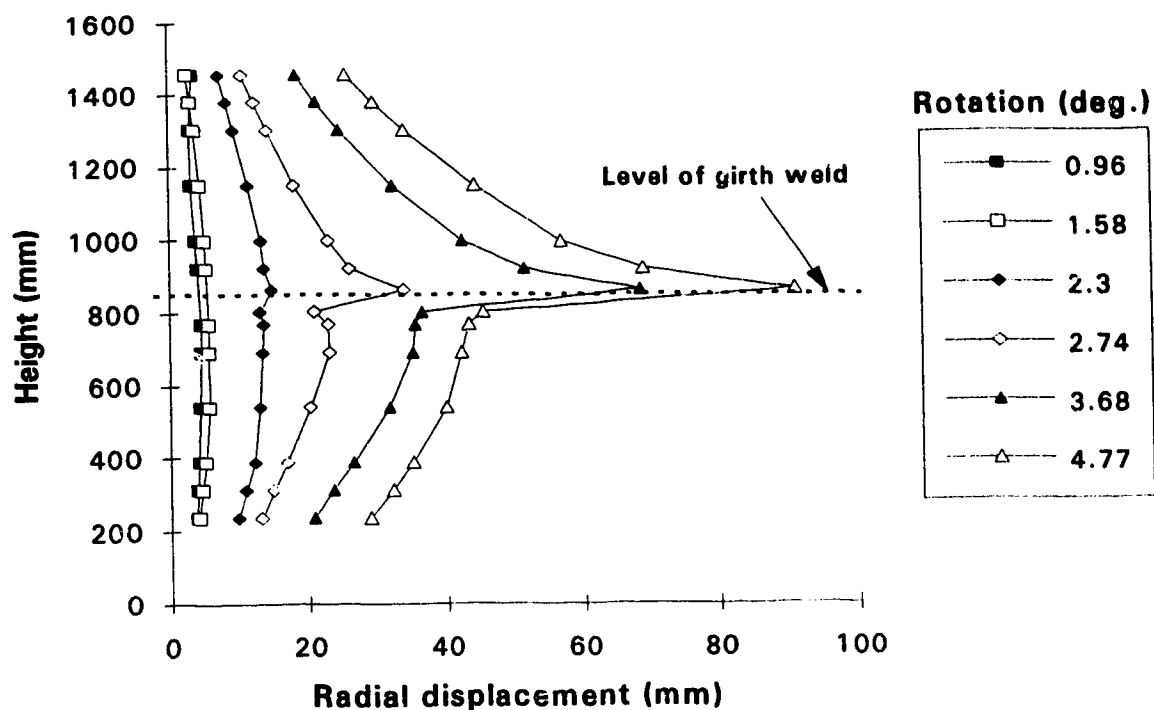
Fig. 3.33 Profile of extreme compression fiber at various rotations for UGA20W-2
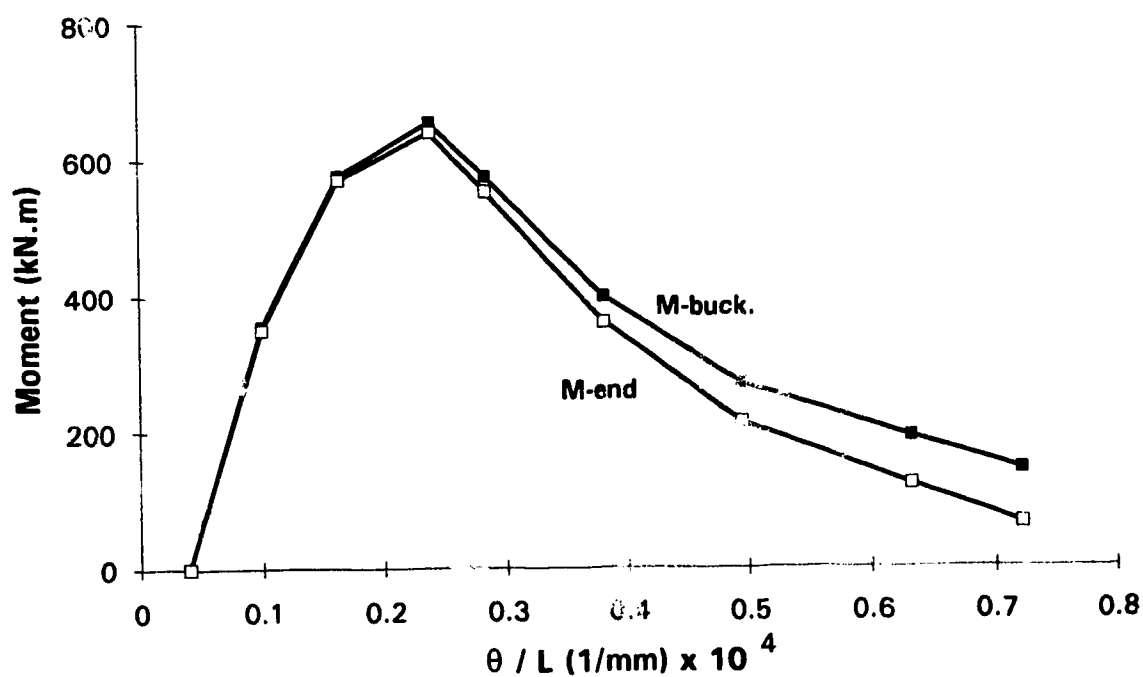
Fig. 3.34 Average of end moments and average moment over wrinkled segment vs.
overall curvature for UGA20W-2
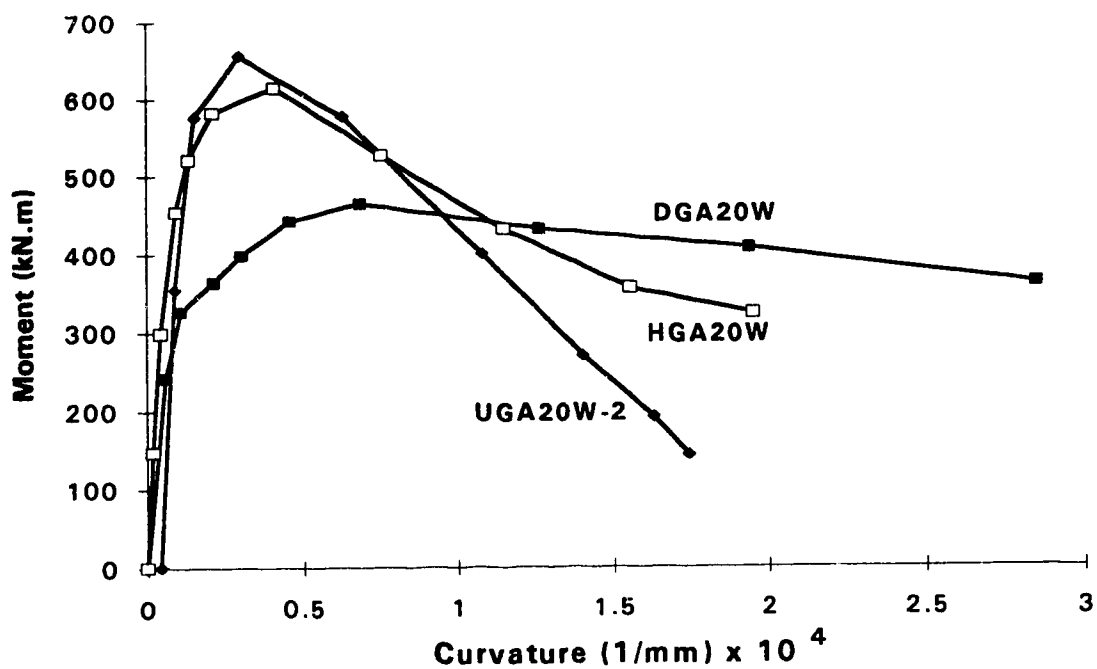
Fig. 3.35 Average moment vs. average curvature over wrinkled segment for 20-inch specimens
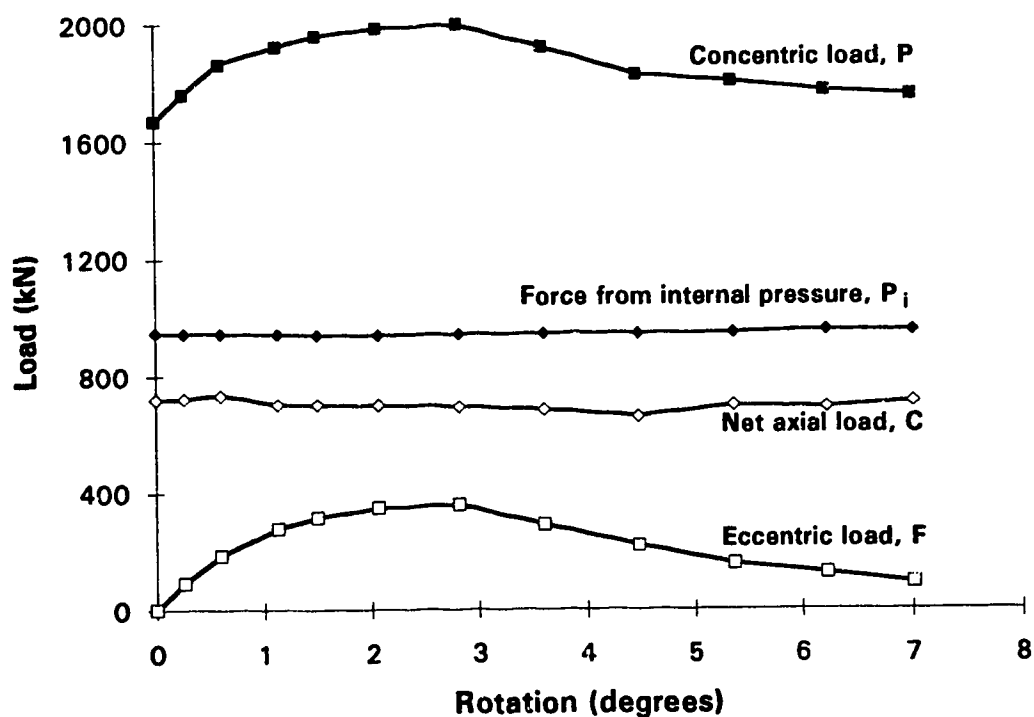
Fig. 3.36 Applied loads vs. rotation for HGA20W
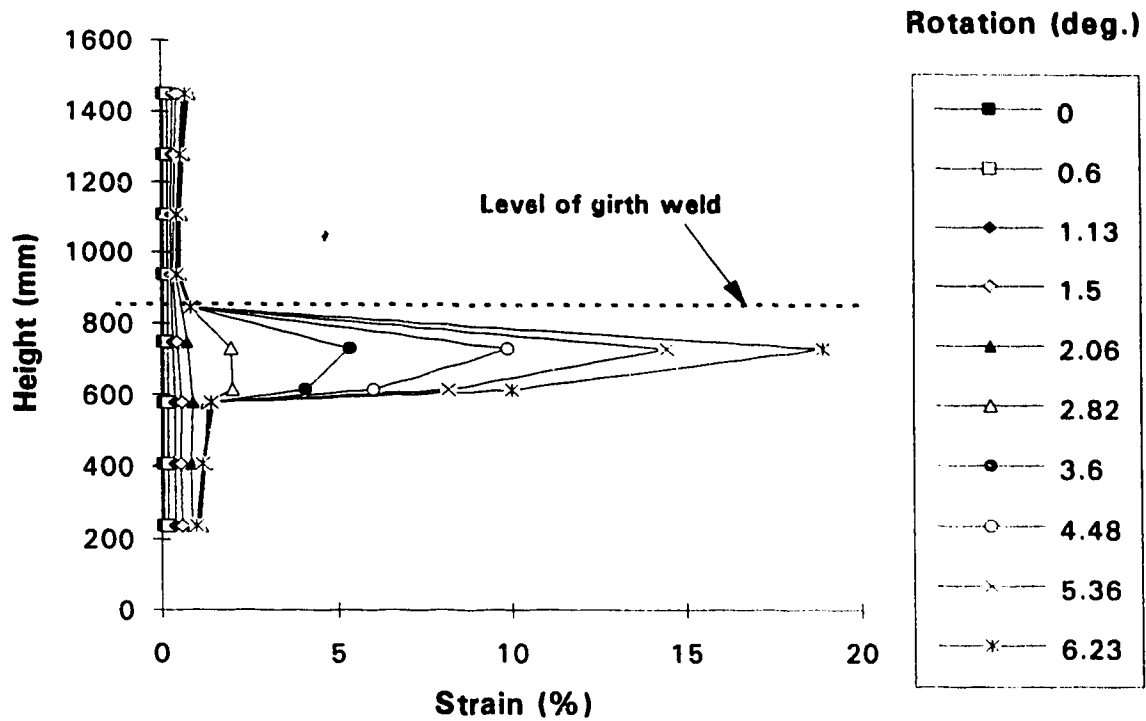
Fig. 3.37 Strain distribution along extreme compression fiber for HGA20W
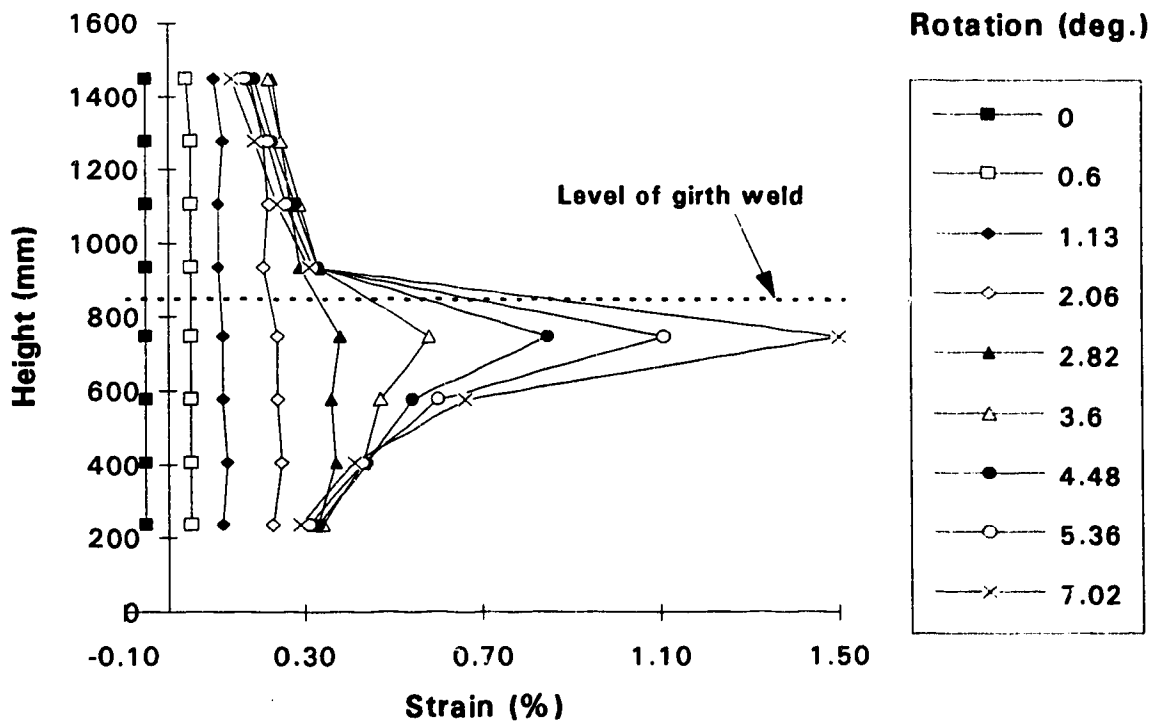
Fig. 3.38 Strain distribution along extreme tension fiber for HGA20W
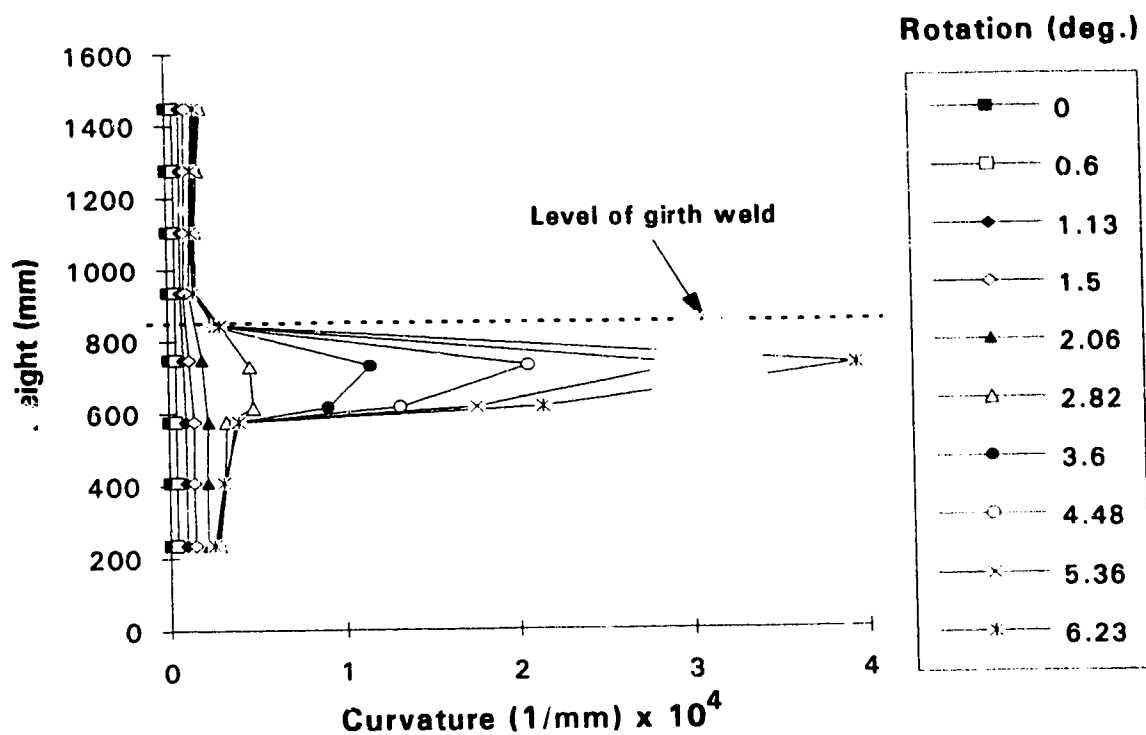
Fig. 3.39 Curvature distribution along specimen HGA20W at various rotations
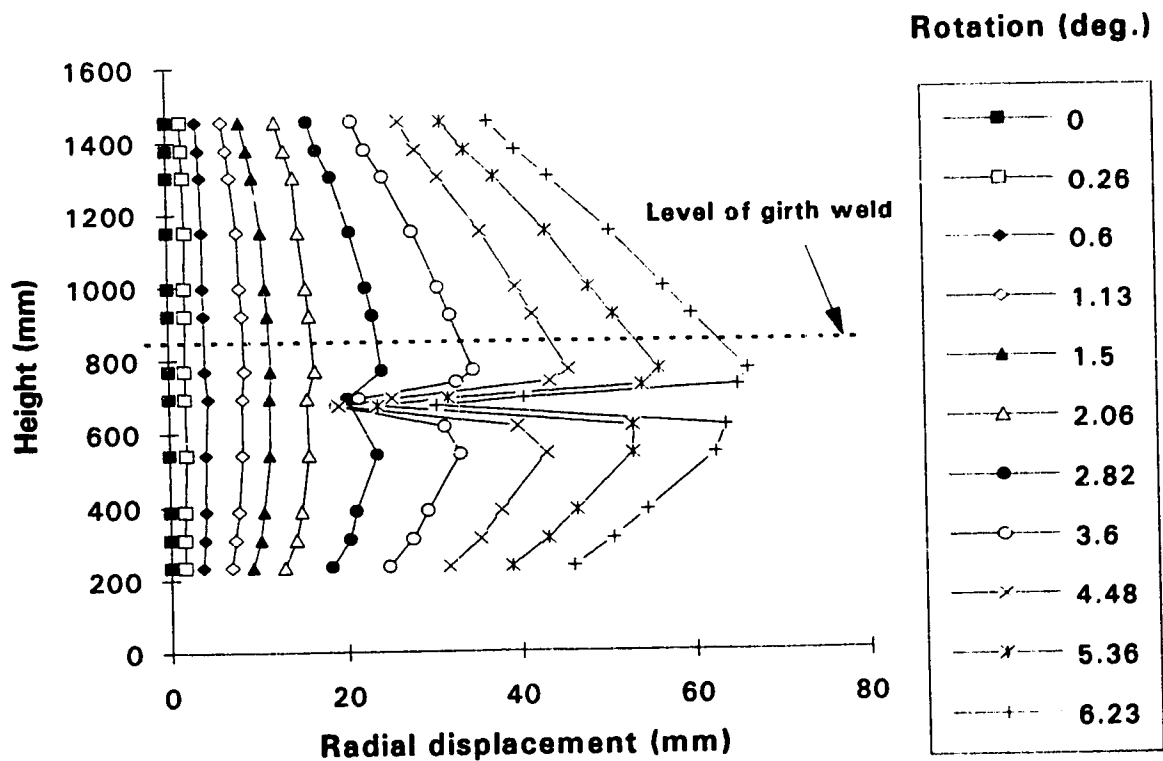
Fig. 3.40 Profile of extreme compression fiber at various rotations for HGA20W
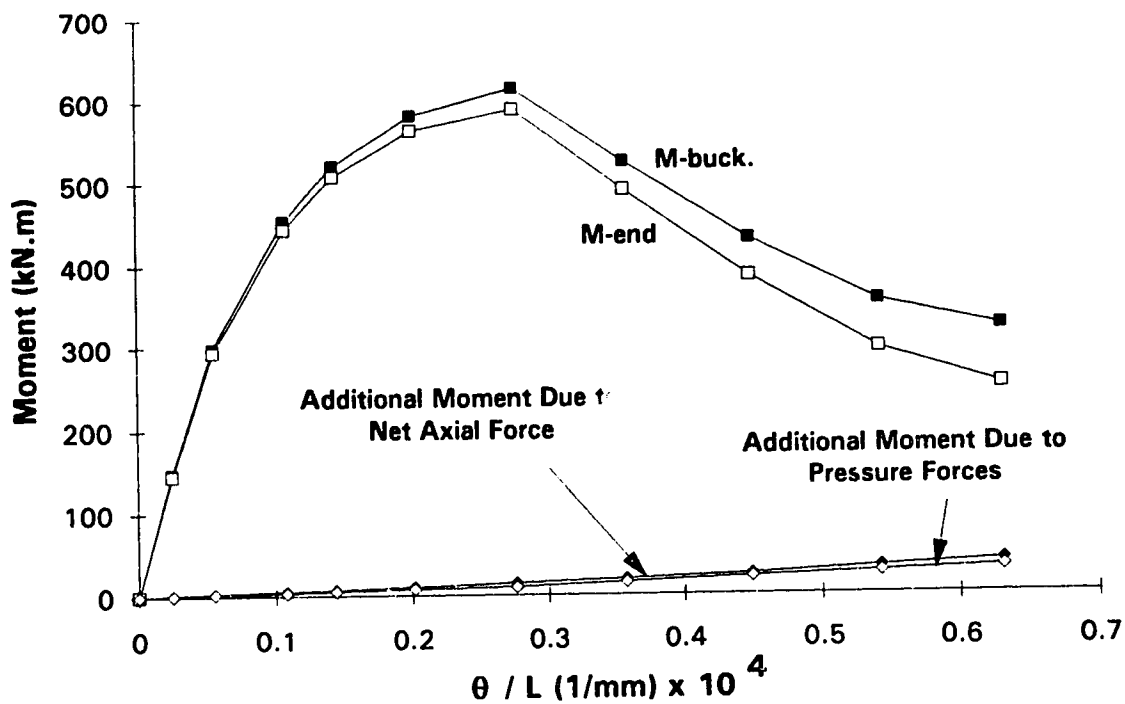
Fig. 3.41 Average of end moments and average moment over wrinkled segment vs. overall curvature for HGA20W
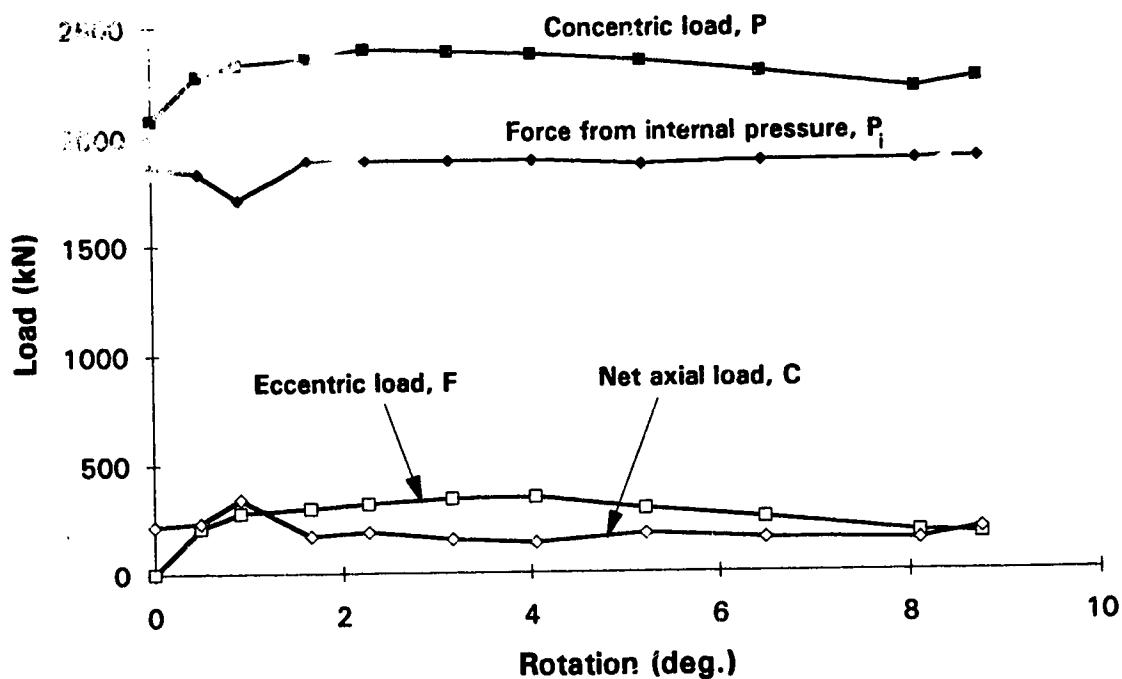
Fig. 3.42 Applied loads vs. rotation for DGA20W
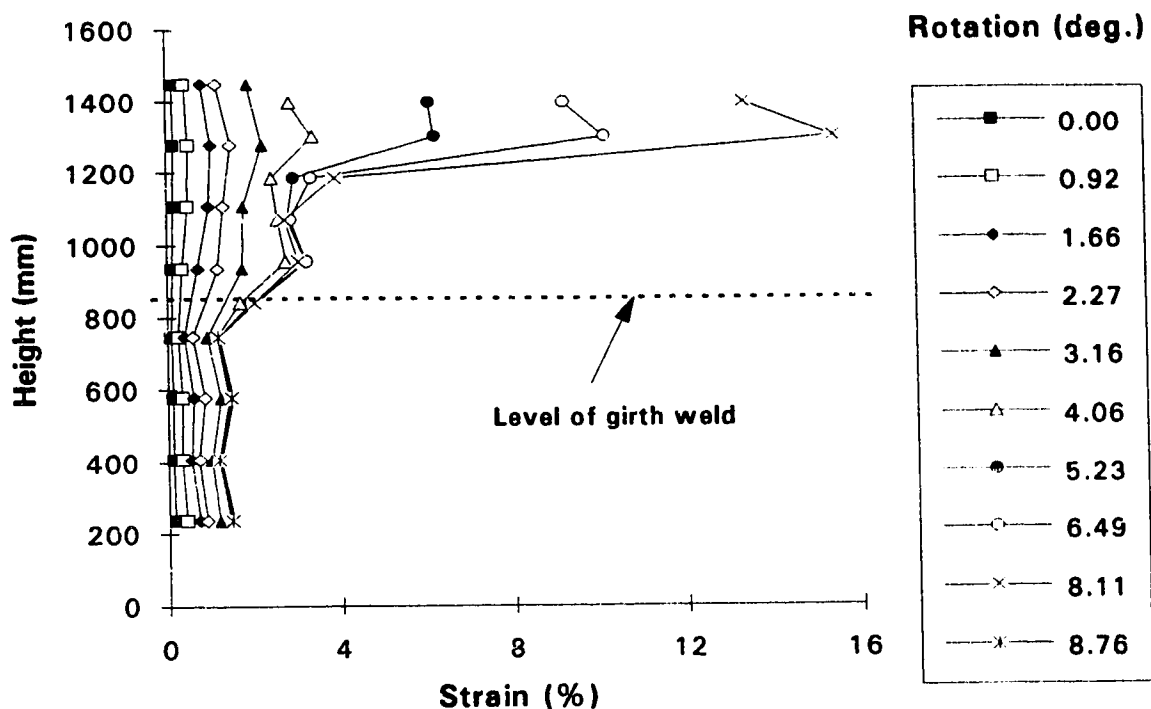
Fig. 3.43 Strain distribution along extreme compression fiber for DGA20W
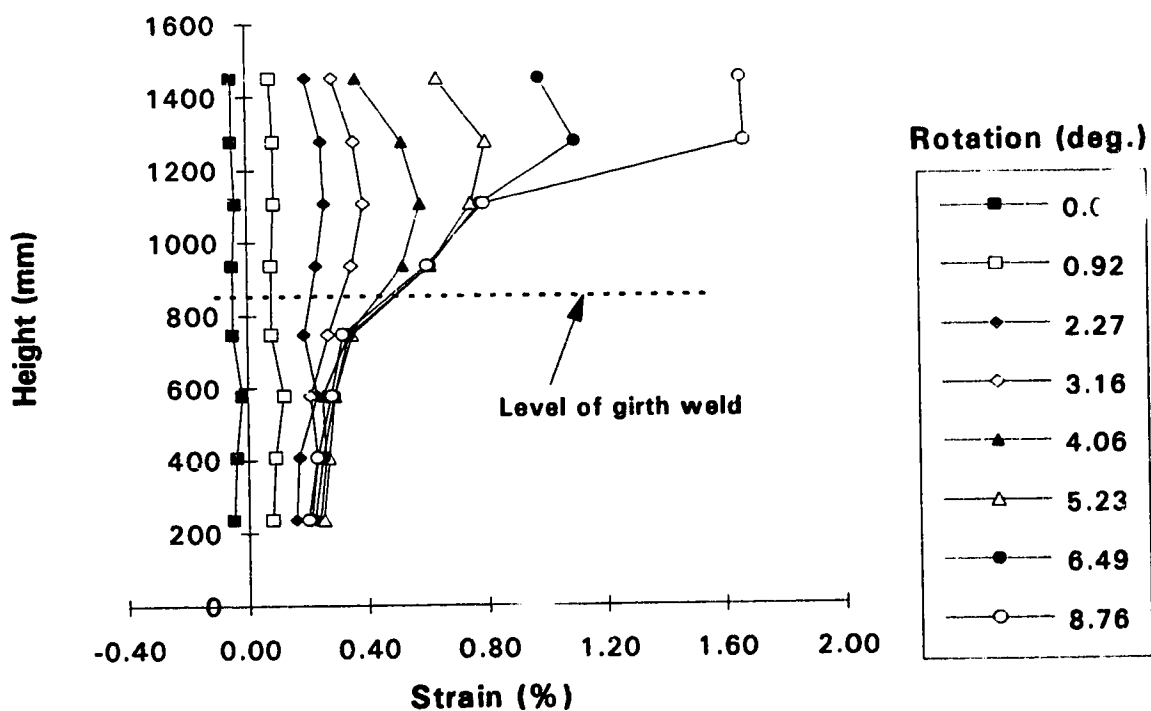
Fig. 3.44 Strain distribution along extreme tension fiber for DGA20W
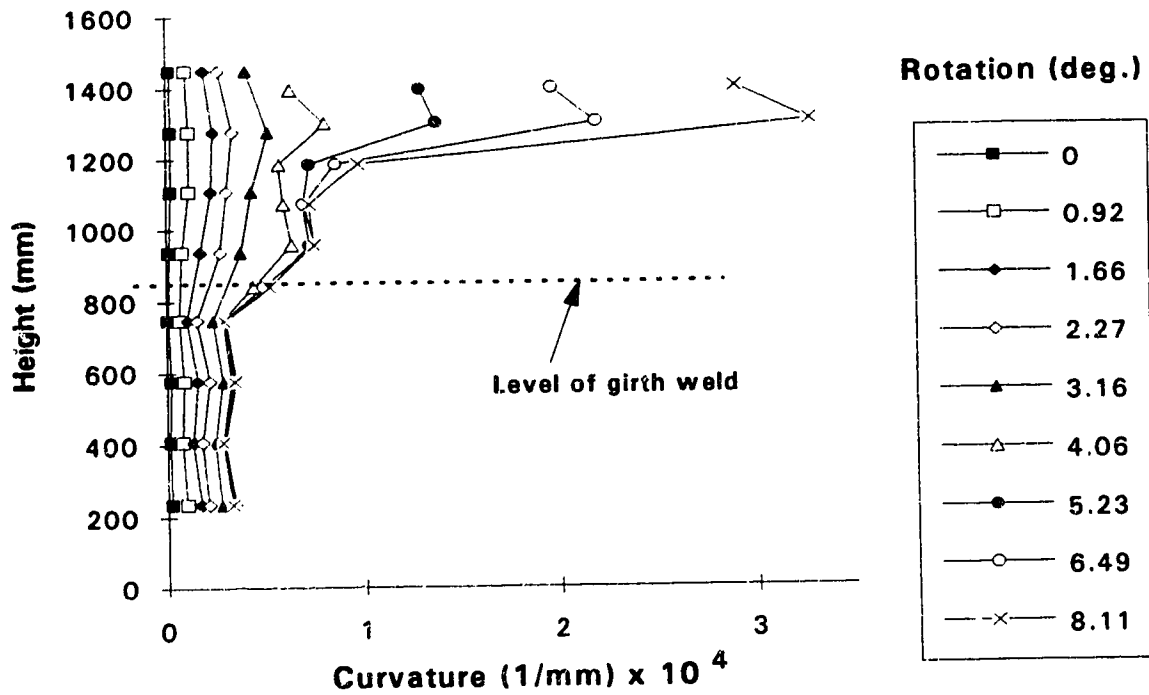
Fig. 3.45 Curvature distribution along specimen DGA20W at various rotations
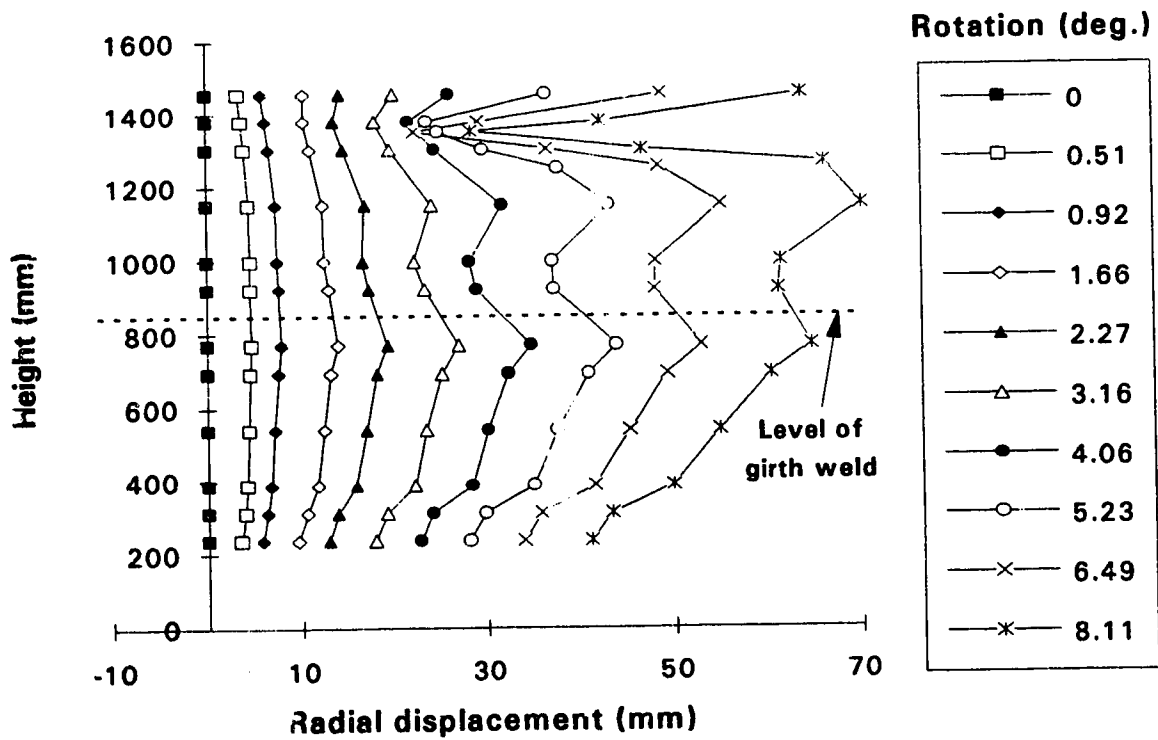
Fig. 3.46 Profile of extreme compression fiber at various rotations for DGA20W
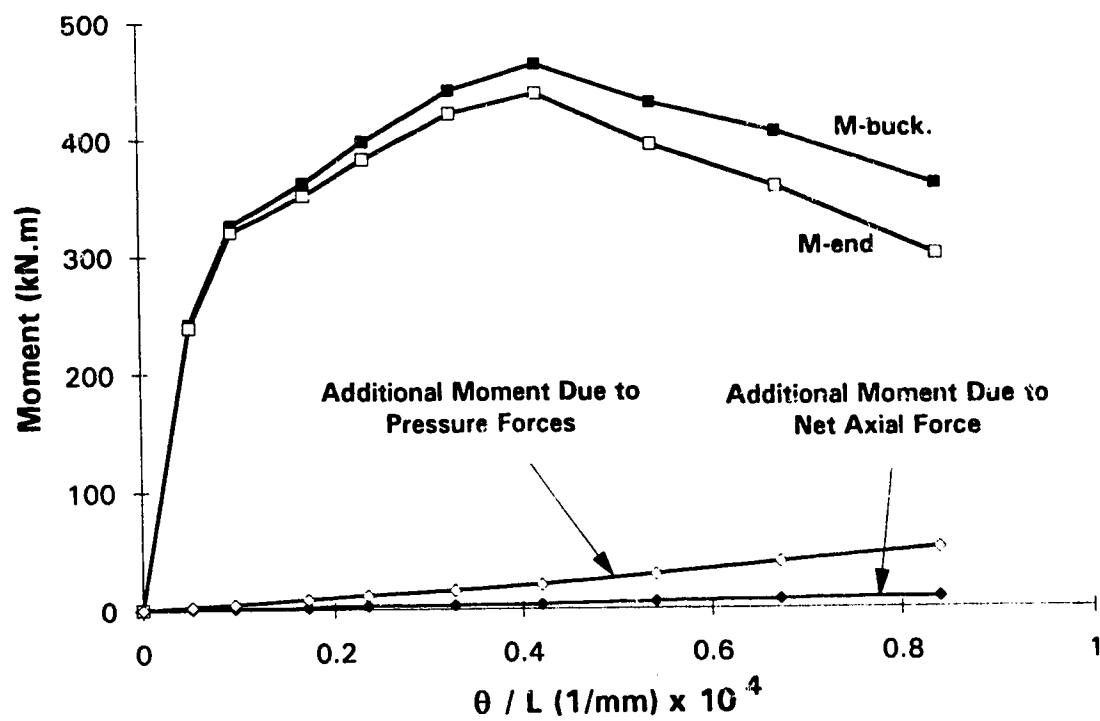
Fig. 3.47 Average of end moments and average moment over wrinkled segment vs. overall curvature for DGA20W

4 DISCUSSION OF EXPERIMENTAL RESULTS

4.1 INTRODUCTION

The experimental results and the procedures used to obtain them were presented in Chapter 3. In this chapter, the results are discussed from the viewpoint of the moment and curvature relationship and the buckling phenomenon. In addition, the experimental results for the girth-welded pipes tested in this program are compared with those for the plain pipes obtained in 1992 at University of Alberta by Mohareb et al. (1994). At the end of the chapter, the concept of the strain at the softening point is introduced It will be recommended a substitute for the limits on compressive strain currently used in design guidelines.

4.2 MOMENT VS. CURVATURE RELATIONSHIPS

In this section, the relationship between moment and curvature is studied. First, the importance of the secondary moment components for the wrinkled segment are discussed. This is followed by a description of the moment vs. curvature response. Finally, a comparison between the moment vs. curvature behavior of the girth-welded pipes and those of the plain pipes is presented.

4.2.1 Importance of Secondary Moments

In Chapter 3, the procedure for calculating those moments that are additional to the applied end moments in order to get the total moment in the wrinkled region was described. Figures 3.8, 3.21, 3.27, 3.34, 3.41, and 3.47 all indicate the significance of the additional moments. As is shown in these figures, the secondary moments are more significant in the pressurized tests than they are in the non-pressurized tests. The pressure force correction in the half-pressurized tests (HGA12W and HGA20W), defined in Section 3.2.5.2 and evident in Figs. 3.8 and 3.41, is of the same order of magnitude as the axial force correction. In the fully-pressurized tests (DGA12W and DGA20W), shown in Figs. 3.27 and 3.47, the pressure force correction constitutes the dominant portion of the secondary moment. It is concluded that neglecting the secondary moments, especially that for the pressure force correction in pressurized pipes, can cause a sizable error and one that is unacceptable.

4.2.2 Mome·   · ·rvature Relations

The averag   .d moments vs. overall curvature and the average moment vs. the average curvature o.   the wrinkled segment for the 12-inch girth-welded speci⁻ens are shown in Figs. 4.1 and 4.2, respectively. The same types of curves for the 20-inch girth-welded specimens are shown in Figs. 4.3 and 4.4, respectively. In Figs. 4.3 and 4.4, the curves for specimen UGA20W-2 start off from ʼ nonzero curvature because the specimen had been overloaded and bent permanently prior to the beginning of the test. After unloading the specimen, it was loaded again under better control. All the results for UGA20W-2 in this document refer to the second loading of the specimen.

Figures 4.2 and 4.4 show that the local moment vs. curvature curves for the non-pressurized and half-pressurized specimens start with reasonably identical slopes for the two pipe sizes. Furthermore, this slope is different from that for the fully-pressurized specimens. The same situation is observed for the end moment vs. overall curvature curves (Figs. 4.1 and 4.3) as well, though it is not as evident as it is for the local moment vs. curvature curves. This indicates that initial behavior for the non-pressurized and half-pressurized specimens is elastic, but that in the case of the fully-pressurized specimens there is little elastic response. This agrees with the results of the numerical investigation, which is described in Chapter 5. According to the analytical results, the fully-pressurized specimens start to plastify during pressurization (i.e., before bending), whereas the other specimens do not start to plastify until after bending starts.

All of the curves in Figs. 4.1 to 4.4 soften, that is, they reach a point in the moment vs. curvature relationship beyond which the moments decrease with increasing curvature. The reason for the decrease in the moment resistance is that a wrinkle forms, creating a sequence of geometric configurations in which the pipe has less capacity to resist moment than it did in its previous configuration. As the amplitude of the wrinkle continues to increase, the capacity of the pipe to resist moment continues to decrease.

It can be argued that wrinkling *effectively* begins at the point at which significant softening is initiated in the moment vs. curvature curve. In this sense, wrinkling means the amplification of local deformations that are clearly visible to the naked eye. These points, which will be called *softening points* (SP), are based upon subjective judgment, and they are identified as SP by the arrows in the figures. Obviously, for each specimen the softening points indicated in the two categories of moment vs. curvature plots correspond

to the same ading step. The total rotati'ns of the specimens ' a softening points so selected a. e tabulated in Table .1.

The softening point is more distinct for the response of the specimen as a whole (Figs. 4.1 and 4.3) than for the local moment vs. curvature curves (Figs. 4.2 and 4.4). This is to be expected because the curvature is length-dependent when the angle change deformations are localized. (Note the difference in scale between the plots of the odd and even numbered figures.) It is apparent from the figures that the effect of internal pressure is to decrease the moment capacity and to increase ductility.

It is evident that the change in the slope at the softening point in the end moment vs. overall curvature curves is greater than that in the moment vs. curvature curves for the wrinkled segment. This is because, as the curvature increases, a greater additional moment is added to the end moment to get the average moment over the wrinkled segment. See, for example, Fig. 3.8. Additionally, as the overall curvature increases and especially after the softening point, the local curvature of the wrinkled segment grows at a much faster rate than does the overall curvature. As compared to the end moment vs. overall curvature curves, the points in the moment vs. curvature for the wrinkled segment spread out as the overall curvature increases In the local moment vs. curvature response, there is a smaller moment decrease and a greater curvature increase than in the overall moment vs. curvature response. This, in turn, reduces the slope of the descending branch.

One important fact is that, in the moment vs. curvature curves for the wrinkled segment, the softening point always coincides with the limit point (i.e.. the peak point giving maximum strength). However, this is not the case for the end moment vs. overall curvature curves, where the softening point may not be the limit point. This is the situation observed for HGA12W and DGA12W in Fig. 4.1.

4.2.3 Comparison of Girth-Welded and Plain Pipe Results

One of the objectives of this project is to compare the results of the girth-welded pipes with those of the plain pipes. Thus, it was decided to carry out the same procedures as used to determine the moment vs. curvature responses for the girth-welded specimens for the plain specimens as well. The average end moments vs. overall curvature for the specimen and the average moment vs. the average curvature over the wrinkled segment

for specimens UGA12, HGA12, and DGA12, along with the results for the corresponding girth-welded specimens, are shown in Figs. 4.5 to 4.10.

It is evident from the average end moment vs. overall curvature curves shown Figs. 4.5, 4.7, and 4.9 that, for the 12-inch pipes, plain specimens demonstrate a greater ductility than do the girth-welded specimens. It is considered that this reflects the fact that the wrinkled segment includes the girth weld in all 12-inch girth-welded specimens. A girth-weld connection is generally a weak spot because of the following factors: 1) possible mismatch of the two cross-sections at the connection; 2) possible misalignment of the two pipe segments, some of which occurs during the welding process, 3) the geometric imperfection generated from the thermal contraction of the weld, 4) the residual stresses in both longitudinal and circumferential directions produced by the thermal contraction of the girth weld.

As Fig. 4.11 indicates, UGA20W-2 shows a ductility similar to that of UGA20W, even though the girth weld was located in the wrinkled segment. This is probably because a yield plateau is not present in the case of UGA20. In other words, both specimens buckled in an elastic–plastic manner prior to generalized yielding.

In DGA20W, the wrinkle formed near the top of the specimen. (See Fig. 3.28.) Consequently, the wrinkled segment does not straddle the girth weld. This eliminates the effect of the girth weld and the resulting imperfections on the behavior of the specimen. Thus, the behavior is governed by the growing wrinkle in the vicinity of the end plate for both welded and unwelded specimens. Therefore, as Fig. 4.12 shows, the responses of DGA20 and DGA20W are very close, with no significant difference in ductility and ultimate strength. (See also Table 4.2.)

Note that there is no counterpart to girth-welded specimen HGA20W in the plain pipe tests, and therefore no comparison can be made for this case.

The ultimate end moments for the 12-inch specimens with and without girth welds, tabulated in Table 4.2, are almost equal: values are within 2% of one another. (See also Figs. 4.5, 4.7, and 4.9.) The values of the average ultimate moment over the wrinkled segment for the 12-inch plain specimens, however, are slightly larger than those for the corresponding girth-welded pipes. (See Table 4.2 and Figs. 4.6, 4.8, and 4.10.) This is because the 12-inch plain pipes are more ductile and have a longer yield plateau than do

the corresponding girth-welded specimens. As Figs. 4.6, 4.8, and 4.10 indicate, the yield plateau in the moment vs. curvature response for the wrinkled segment appears as a mildly ascending branch. Consequently, a longer yield plateau in a plain pipe results in a larger ultimate moment than that in the corresponding girth-welded pipe. As mentioned in Section 4.2.2, the moment vs. curvature response for specimen UGA20W-2, shown in Fig. 4.11, is the result of well-controlled loading after being unloaded from a plastified state. Therefore, the maximum moment capacity of UGA20W-2 cannot be compared with that of UGA20.

4.3 BUCKLING AND WRINKLING BEHAVIOR

4.3.1 Behavior

In the non-pressurized tests (UGA12W and UGA20W-2), the softening points that were determined from the moment vs. curvature plots correspond approximately to the loading step at which the buckle became visible during the tests. As mentioned in Section 3.4, in the non-pressurized specimens the wrinkle formed in a diamond shape and no other wave or local distortion pattern was observed at locations other than in the wrinkled segment. In the pressurized tests (HGA12W, DGA12W, HGA20W, and DGA20W), the wrinkle formed as a single outwardly bulging shape. Initially, this was one of four ripples, or waves, that could be detected along the compressive face of the specimen by close visual examination. As emerged later, these buckling waves became evident at values of rotation immediately prior to the softening point on the moment vs. rotation curve. The physics of the situation dictates, however, that the reduction in moment resistance is governed by the wave which is of greatest amplitude a., consequently, possesses the least resistance. As the deformation is increased, the amplitude of this dominant wave increases while the amplitudes of the others decrease. The result is that the inelastic deformation and the strains concentrate in one dominant wave, i.e., the *wrinkle*, while the other ripples generally disappear. The wrinkles associated with the three 12-inch specimens are shown in Figs. 3.15 and 3.16. Figure 3.28 shows the wrinkles associated with the 20-inch specimens. All these wrinkles, except for DGA20W, are in the vicinity of the weld. Nevertheless, they correspond in their general form to the wrinkles in the 1992 test series done on plain pipe (Mohareb et al. 1994).

4.3.2 Strain Localization

The physics discussed in the previous section indicates that initiation of wrinkling is related to softening and its associated *strain localization* other words,

when wrinkling occurs through amplification of the dominant wave, the apparent longitudinal strains in the vicinity of the wrinkle increase dramatically, while the strains in the remainder of the specimen decrease somewhat. This phenomenon is evident in Figs 3.2, 3.17, 3.23, 3.30, 3.37, and 3.43, where the distribution of the longitudinal strains along the extreme compression fiber have been plotted at various load levels. It is observed that the strain localization begins slowly and before wrinkling becomes evident to the naked eye. Once wrinkling becomes visible with the formation of buckling waves, the strain localization intensifies rapidly. The strains at which wrinkling is initiated are discussed in greater detail in Section 4.4.

4.3.3 Displaced Configurations of Extreme Compression fiber

The best indicator of buckling is the shape of the lateral displacement associated with the extreme compressive fiber. The buckling waves that are observed visually should be evident in a plot of the profile of these displacements. However, the wave lengths of the ripples are of the same order of magnitude as the spacing between the LVDT reading stations. Therefore, the ripples are only evident from the fact that the displacements of points located on the wrinkle no longer follow a smooth profile, such as would be associated with a beam deflection profile. Furthermore, upon wrinkling, the distortion of the profile in the wrinkled zone grows rapidly. As mentioned in Section 3.3.2, the use of a contour gage cannot trace small local deformations, but is effective once noticeable deformations are detected visually. Nevertheless, the contour gage was of assistance in tracking down the initiation of buckling for some specimens.

In the following subsections, the initiation of buckling in comparison with the initiation of softening (i.e., wrinkling) based on the above criteria is discussed. As mentioned above, in all the pressurized tests four very small waves appeared at early stages. Some of the waves died out during the following load steps and were not captured by the instrumentation. In the following, no further comment is made on these undocumented waves.

4.3.4 Buckling and Wrinkling for Individual Specimens

4.3.4.1 Specimen UGA12W

The definition of the softening point based on the moment vs. curvature plots gives a rotation value of 2.92 degrees for UGA12W (Figs 4.1 and 4.2). Note that the points on the plots given in Figs. 4.1 to 4.12 are referred to by the values of the relative rotation

associated with them. These points correspond sequentially to the relative rotation values used for the respective specimens in Chapter 3. The relative rotation values are tabulated in the legends on the strain and profile plots of Chapter 3.

The plot of strain along the extreme compression fiber, shown in Fig. 3.17, also indicates the first sign of localization at 2.92 degrees. The profiles of the extreme compression fiber of the pipe show the first disturbance also at 2.92 degrees (Fig. 3.20).

4.3.4.2 Specimen HGA12W

From the moment vs. curvature diagrams (Figs. 4.1 and 4.2), the softening point occurs at 4.52 degrees rotation. As Fig. 3.2 shows, strain localization begins at 3.66 degrees. Figure 3.6 shows two evident distortions in the compression profile of the pipe, appearing first at the rotation of 2.69 degrees. One of these distortions dies out and the other amplifies rapidly.

4.3.4.3 Specimen DGA12W

Moment vs. curvature plots (Figs. 4.1 and 4.2) identify the rotation of 7.38 degrees as the softening point. As Fig. 3.23 shows, strains along the extreme compression fiber start to localize at 2.75 degrees. In Fig. 3.26, the first distortions in the profiles of the extreme compression fiber can be detected at 1.02 degrees in the form of two waves. One of these waves grows rapidly, while the other stabilizes. There is also an indication of a small ripple near the top of the specimen from the rotation of 4.32 degrees onward. However, it remains small throughout the loading history.

4.3.4.4 Specimen UGA20W-2

The moment vs. curvature plots for this specimen, shown in Figs. 4.3 and 4.4, suggest the rotation of 2.3 degrees for the softening point. As Fig. 3.30 shows, strain localizations in the extreme compression fiber also start at 2.3 degrees. As well, the profiles of the extreme compression fiber show the first sign of disturbance at 2.3 degrees (Fig. 3.33). Thus, as was the case with UGA12W, the initiation of buckling coincides reasonably well with the initiation of wrinkling (softening).

4.3.4.5 Specimen HGA20W

From the moment vs. curvature diagrams (Figs. 4.3 and 4.4), the softening point is at the rotation 2.82 degrees. The strains along the extreme compression fiber, shown in Fig. 3.37, start to localize at 1.5 degrees. The first distortion in the profiles of the extreme compression fiber could also be observed at 1.5 degrees (Fig. 3.40). Later, at the rotation of 2.82 degrees, two more distortions appear, near the top and bottom of the specimen. These remained stable until the end of the test.

4.3.4.6 Specimen DGA20W

For specimen DGA20W, the moment vs. curvature plots (Figs. 4.3 and 4.4) show that the softening point rotation is 4.06 degrees. The first signs of localization in the strain along the extreme compression fiber are observed at 1.66 degrees (Fig. 3.43). Although not obvious, the earliest distortions in the profile of the extreme compression fiber appear at 0.92 degrees (Fig. 3.46). These distortions become more evident in the next increment rotation (1.66 degrees), in the form of four waves. The wave near the top of the pipe amplifies rapidly to become the wrinkle. The second ripple from the top grows in several loading steps, but stabilizes in the last three loading steps. The other two, located in the lower half of the specimen, stabilize and remain small to the end of the test.

4.3.4.7 Conclusion

It could be concluded from the observations made in Sections 4.3.4.1 and 4.3.4.4 that for non-pressurized pipe the onset of buckling (i.e., formation of the buckling waves) is reasonably coincident with the onset of wrinkling (i.e., softening). However, the observations in Sections 4.3.4.2, 4.3.4.3, 4.3.4.5, and 4.3.4.6 indicate that the presence of internal pressure both delays the initiation of wrinkling and causes the onset of buckling to occur at an earlier stage. This is because, by the time wrinkling occurs, the pressurized specimens have developed plasticity over a major part of the cross-section. The highly developed plastification over a long range of global deformation facilitates the formation and growth of the small local distortions. By contrast, at the time the non-pressurized specimens wrinkle, only a relatively small part of the cross-section has become plastic. In addition, wrinkling occurs during a much shorter range of pipe rotation for non-pressurized pipe than for the pressurized specimens. Consequently, the buckling waves in the non-pressurized specimens do not have the opportunity to develop noticeably prior to the wrinkling.

4.4 DETERMINATION OF SIGNIFICANT STRAIN VALUES

Strain distributions on the three 12 inch girth-welded pipe specimens have been presented in Chapter 3 (Figs. 3.2, 3.17, 3.23, 3.30, 3.37 and 3.43). In these plots, Demec gage strains have been used for the region in the vicinity of the wrinkle and strain gage results used over the remainder of the length. In the tests on plain pipes (Mohareb et al. 1994), Demec gage results were used throughout. This was possible because a higher resolution Demec gage was available for that series than for this series of tests on the girth-welded pipes. The lower resolution Demec gage used for the tests on the girth-welded specimens made the Demec results erratic at small strains, and it is only at the larger strains in the vicinity of the wrinkle that these strain measurements become reliable.

Typical strain gage results comparing the average strain in a length of D (the pipe diameter) to the average strain over the length of the specimen, are shown in Fig. 4.13. It is seen that the local strains are erratic once wrinkling begins because the strain depends on the bending curvatures in the wrinkle at the point of application of the gage. Therefore, strain gage strains are no longer representative of the average shortening within the wrinkle. Clearly, such strains do not represent the behavior of interest. As a result, the peak strains for the last four (three, three, three, five, and four) rotations in Figs. 3.2 (3.17, 3.23, 3.30, 3.37, and 3.43, respectively) are those from the Demec readings. The majority of the other points are strain gage values. It is noted from strain results such as those shown in Fig. 3.23 that no clear rotation level is associated with strain localization because of perturbations to the curves at relatively low rotation levels. Consequently, it is necessary to search for a better technique to determine critical strain values for initiation of wrinkling. One possible technique is described below.

4.4.1 Determination of Critical Strain Values

Strain localization implies that the strain in a localized area (the area of the wrinkle) increases more rapidly than does the average strain in the specimen. For uniform strain in the specimen, the ratio of the strain in any local gage length to the overall strain is unity. Therefore, the degree of localization of strain may be detected by the degree to which the strain ratio deviates from unity. Alternatively, if the localized strain is plotted against the overall strain, the departure of the line from a 45 degree line is a measure of the strain localization. Such a plot, for example Fig. 4.13, indicates that very significant non-uniformity of strain begins at the softening point.

Because the goal is to determine the strains at the initiation of wrinkling, it is rational to select the local gage length as the length of the wrinkle and to locate it on the specimen in such a way that it straddles the wrinkle. The non-pressurized specimens (UGA12W and UGA20W-2) wrinkled in a diamond mode, whereas the others wrinkled in bulging modes. The wrinkle is somewhat shorter for the bulging mode than it is for the diamond mode. Consequently, the local gage lengths for the specimens were selected as D for the non-pressurized specimens and D/2 for the pressurized ones. Plots of these strain measures for the welded specimens UGA12W, HGA12W, DGA12W, UGA20W-2, HGA20W, and DGA20W are shown in Figs. 4.14 to 4.19. These plots indicate that there is a gradual development of non-uniformity in the strains as the specimen deforms. However, once wrinkling starts, the local strain in the wrinkling gage length increases much more rapidly than does the overall strain, and there is a relationship between overall strain and local strain that is approximately linear.

Numerical values for both the local and overall strains at the softening points, identified in Section 4.2.2, are shown on Figs. 4.14 to 4.19. In addition, the strains at the points of intersection between the lines of initial linear response and the post-softening linear response are determined. All these strains are tabulated in Table 4.1.

To make a comparison between the girth-welded pipe and the plain pipe test series of Mohareb et al. (1992), strain results for girth-welded series are plotted in Figs. 4.20 to 4.22 for specimens UGA12, HGA12, and DGA12, respectively. Somewhat surprisingly, the Demec strain results from this series deviate from uniformity almost from the initiation of loading. However, the breaks in slope at the softening points are just as distinct as they are for the girth-welded tests. The strain values, as well as the rotation values at softening points determined in Section 4.2.3, are also tabulated in Table 4.1. Because of the lack of experimental data for the 20-inch plain pipes, the corresponding plots for these specimens could not be obtained.

4.4.2 Recommended Strain Limits

The strain values in Table 4.1 indicate the great dependence of all measures of significant strain on the internal pressure. The overall strain values are generally less than the local strain values, and slightly more than the intersection point strains. They represent lower-bound strains for the softening points, determined from the moment vs. rotation curves. These strains will probably be most consistent with those that are computed for

design or assessment purposes or with those that will be measured in the field. It is, therefore, judged that these strains are the most reasonable upon which to base lower-bound estimates for design and assessment recommendations.

The minimum strains, by all measures, are associated with the empty (or upstream) pipe conditions. These values may, therefore, be considered to be the lower bound for the entire range of pressures. It is observed that the limiting overall strain for HGA12 is close to one-half that of DGA12 and, therefore, these strain limits are approximately proportional to the internal pressure. A set of recommended lower bound strains for plain pipe is that given by the upper line in Fig. 4.23. This lower bound reflects the minimum strain associated with UGA12 and the proportionality shown by the HGA₁₂ and DGA12 tests. The term p_y in Fig. 4.23 is the internal pressure when the hoop stress equals the yield stress.

It is noted that the overall strains for the girth-welded pipe for specimens UGA12W and DGA12W are very close to 60% of those for UGA12 and DGA12. Applying this factor to the limiting conditions for plain pipe to obtain limiting conditions for girth-welded pipe produces the lower line shown in Fig. 4.23. As is apparent in Fig. 4.23, this line also establishes a satisfactory lower bound for the 20-inch girth-welded specimen. Thus, in general, it can be seen that the lines shown represent good approximations to lower bounds of the experimental points. Therefore, based upon the results of the tests carried out on this project, lower bounds on the overall strains at the time of initiation of wrinkling, called the softening strain, ε_s, can be expressed by the following equations:

(a) For plain pipe $\quad\quad\quad \varepsilon_s = 4.58\dfrac{p}{p_y} \geq 1.10 \ \%$ $\quad\quad\quad\quad$ (4.1)

(b) For girth-welded pipe $\quad \varepsilon_s = 2.78\dfrac{p}{p_y} \geq 0.66 \ \%$ $\quad\quad\quad\quad$ (4.2)

As mentioned, the upper line in Fig. 4.23 (Eq. (4.1)) is based only on the results for the 12-inch plain pipes and its application must be limited to pipe of that size. However, there is good agreement between the results for the 20-inch girth-welded pipes and the lower line in Fig. 4.23 (Eq. (4.2)). This justifies the recommendation of Eq. (4.2) for both 20-inch welded pipe and 12-inch welded pipe.

It should be noted that, according to these recommendations, the limiting condition that may be applicable to the assessment of a field situation is dependent on the location between pumping stations. Also, the limit for plain pipe can be used for all locations except those in the immediate vicinity of a girth weld, say, within two diameters from the girth weld.

Table 4.1

Summary of Significant Strains and Rotations

Specimen	Softening Point			Intersection Point Strain, $\varepsilon_o = \varepsilon_L$ %
	Rotation θ °	Local Strain, ε_L %	Overall Strain, ε_o %	
UGA12W	2.92	0.86	0.68	0.64
HGA12W	4.52	2.45	1.26	1.11
DGA12W	7.38	2.51	1.93	1.90
UGA12	4.41	1.81	1.10	0.99
HGA12	6.89	2.26	1.62	1.58
DGA12	10.8	4.73	3.29	2.90
UGA20W-2	1.92	1.13	0.92	0.81
HGA20W	2.82	1.82	1.16	1.04
DGA20W	4.06	2.96	2.13	1.87

Table 4.2

Ultimate Moments for Girth-Welded and Plain Specimens (kN.m)

Girth-Welded Specimens			Plain Specimens		
Specimen	Average of End Moments	Average Moment over Wrinkled Segment	Specimen	Average of End Moments	Average Moment over Wrinkled Segment
UGA12W	209	225	UGA12	206	236
HGA12W	191	210	HGA12	187	225
DGA12W	143	172	DGA12	149	191
UGA20W-2	640	656	UGA20	680	N.A.
HGA20W	589	614	HGA20	N.A.	N.A.
DGA20W	439	463	DGA20	413	N.A.

Note: N.A. stands for Not Available because of insufficient test data.
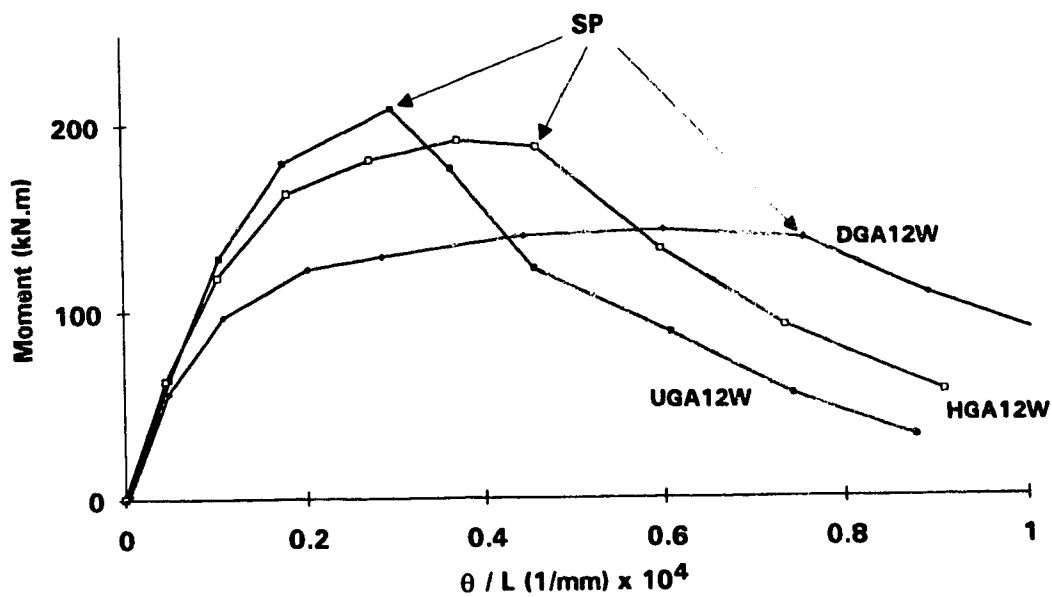
Fig. 4.1 Average end moment vs. overall curvature for 12-inch girth-welded pipes
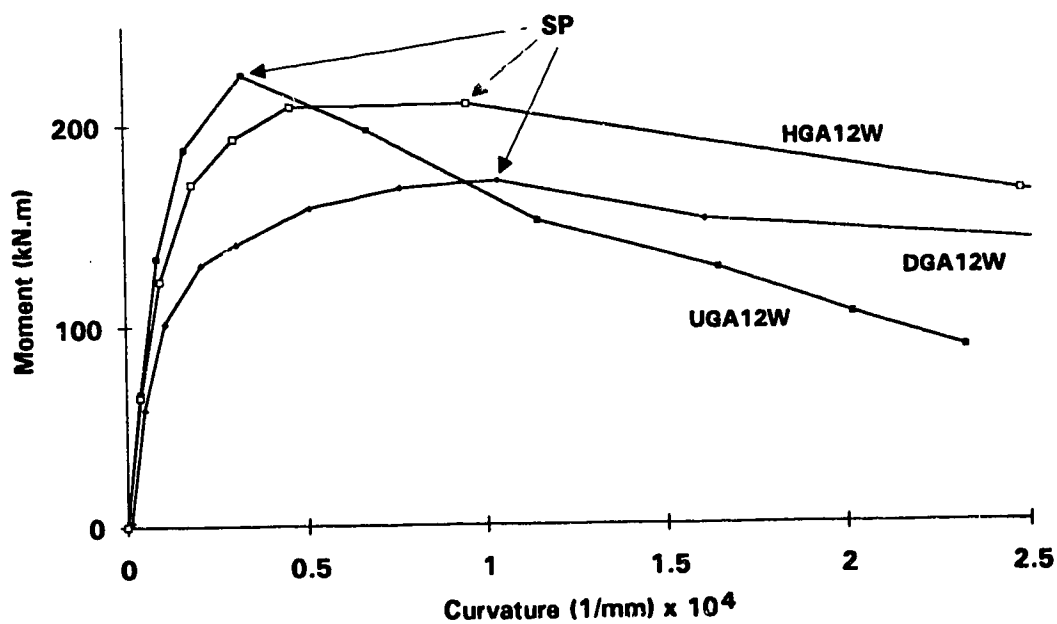
Fig. 4.2 Average moment vs. curvature over wrinkled segment for 12-inch girth-welded pipes
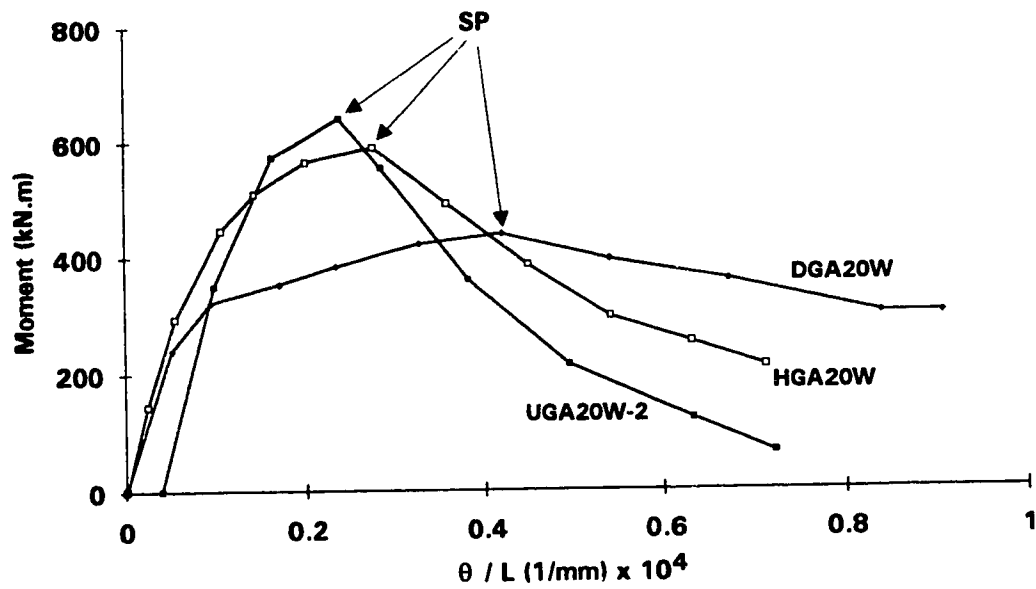
Fig. 4.3 Average end moment vs. overall curvature for 20-inch girth-welded pipes
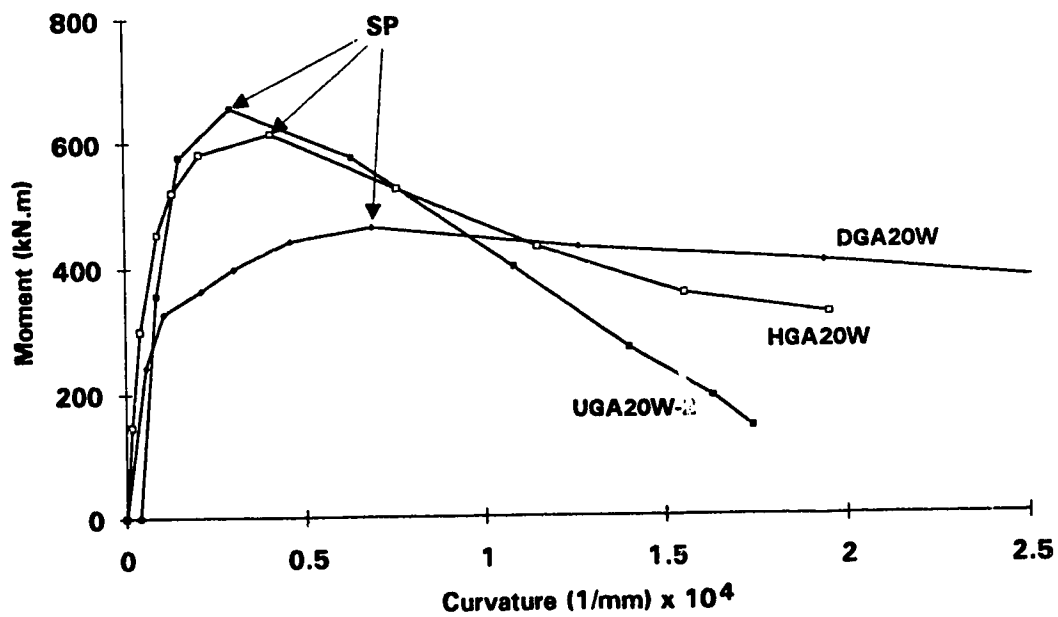
Fig. 4.4 Average moment vs. curvature over wrinkled segment for 20-inch girth-welded pipes
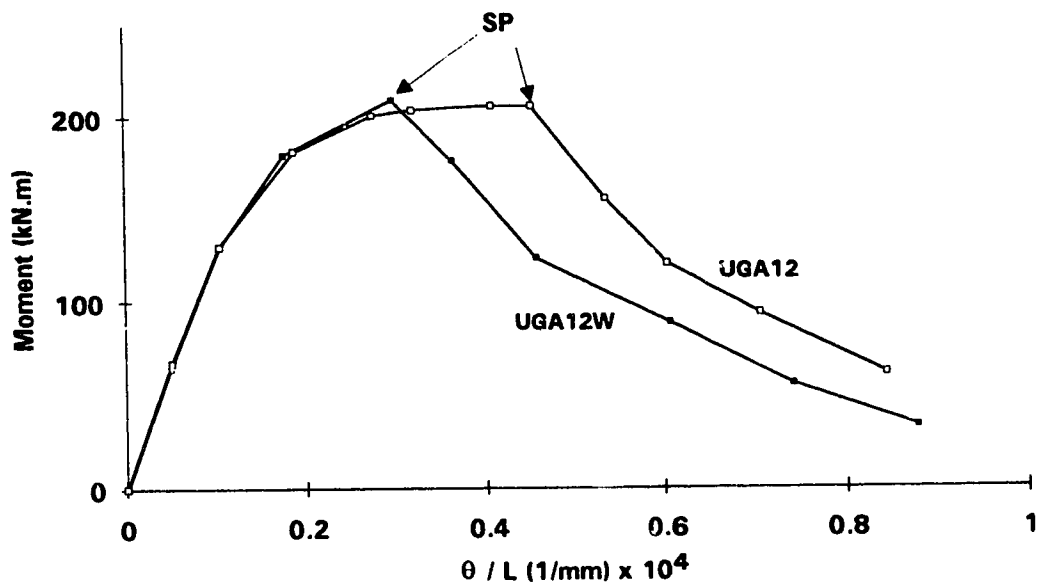
Fig. 4.5 Average end moment vs. overall curvature foi UGA12W and UGA12
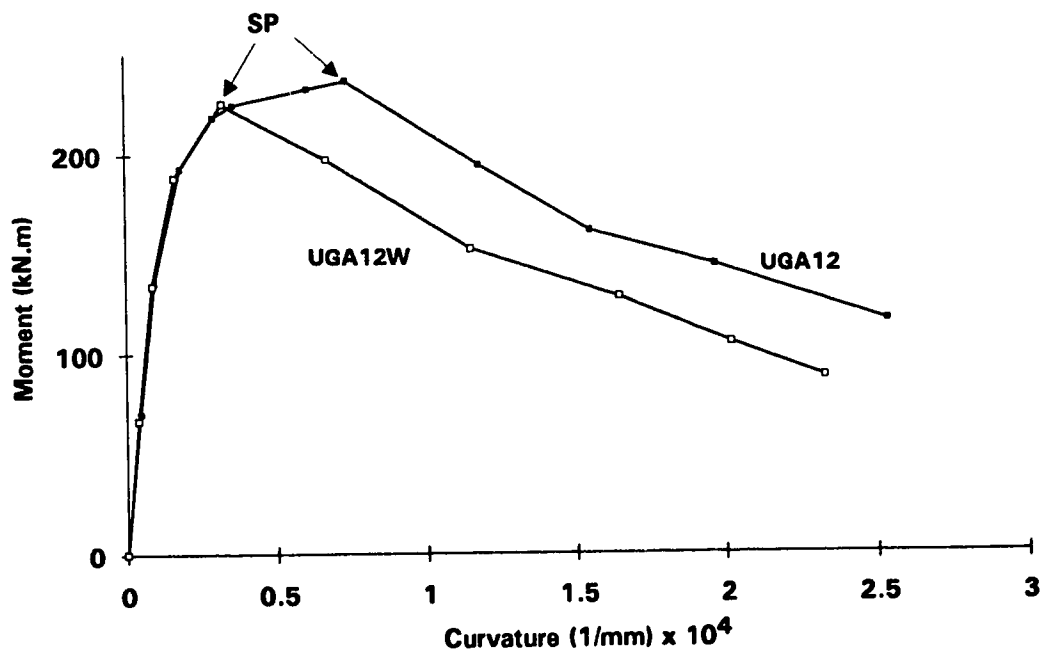
Fig. 4.6 Average moment vs. curvature over wrinkled segment for UGA12W and UGA12
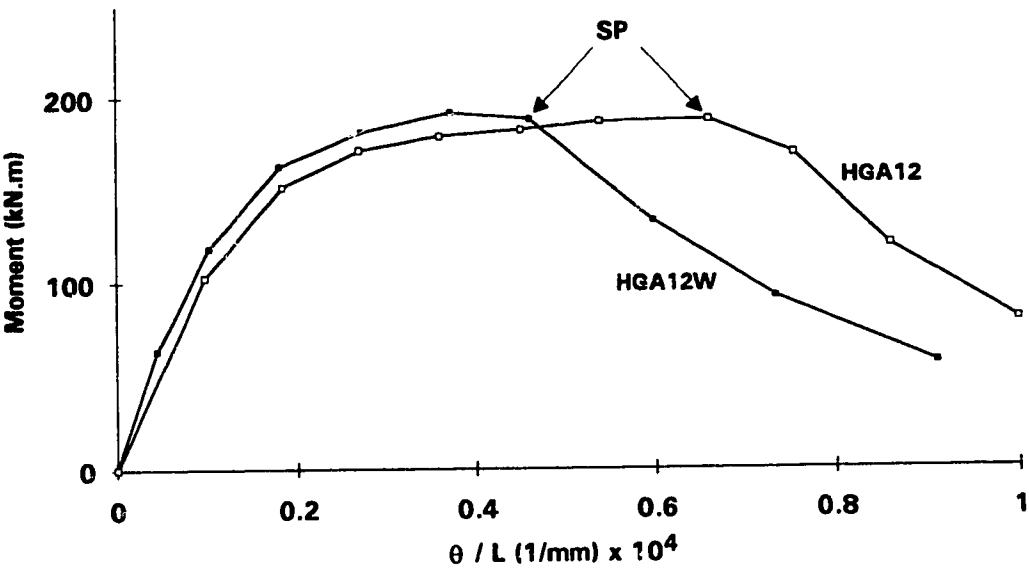
Fig. 4.7 Average end moment vs. overall curvature for HGA12W and HGA12
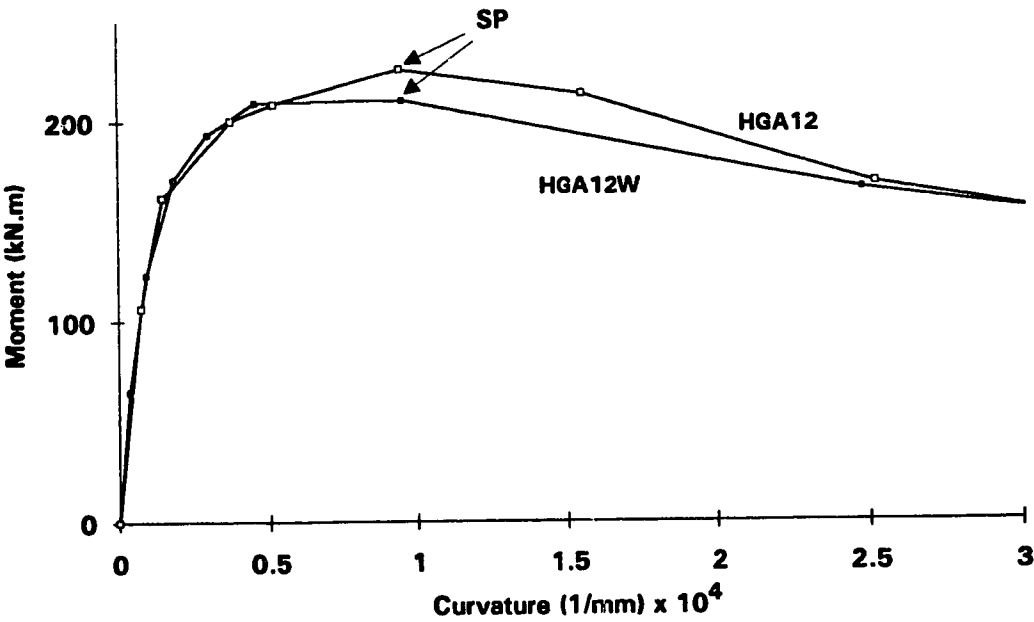
Fig. 4.8 Average moment vs. curvature over wrinkled segment for HGA12W and HGA12
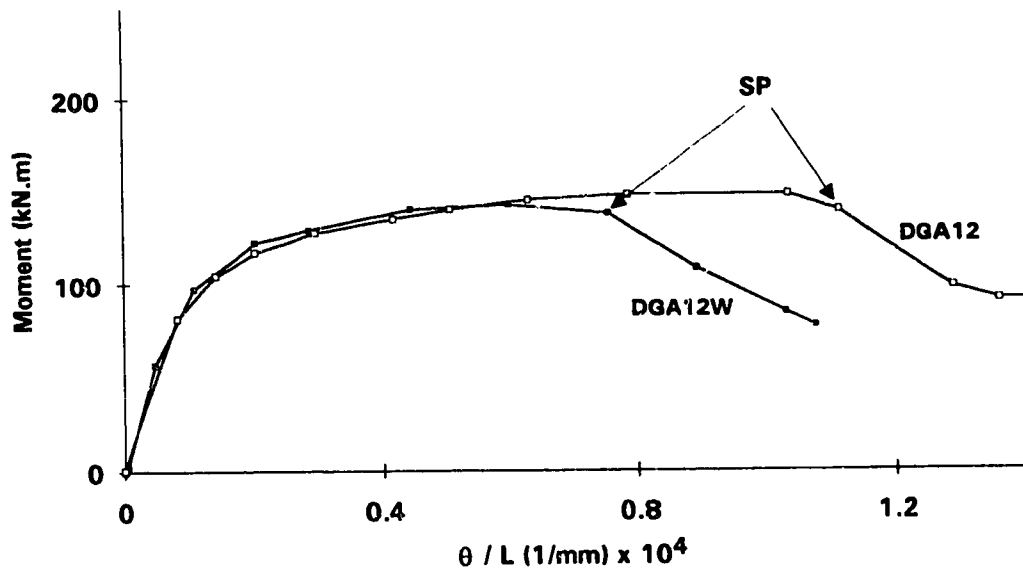
Fig. 4.9 Average end moment vs. overall curvature for DGA12W and DGA12
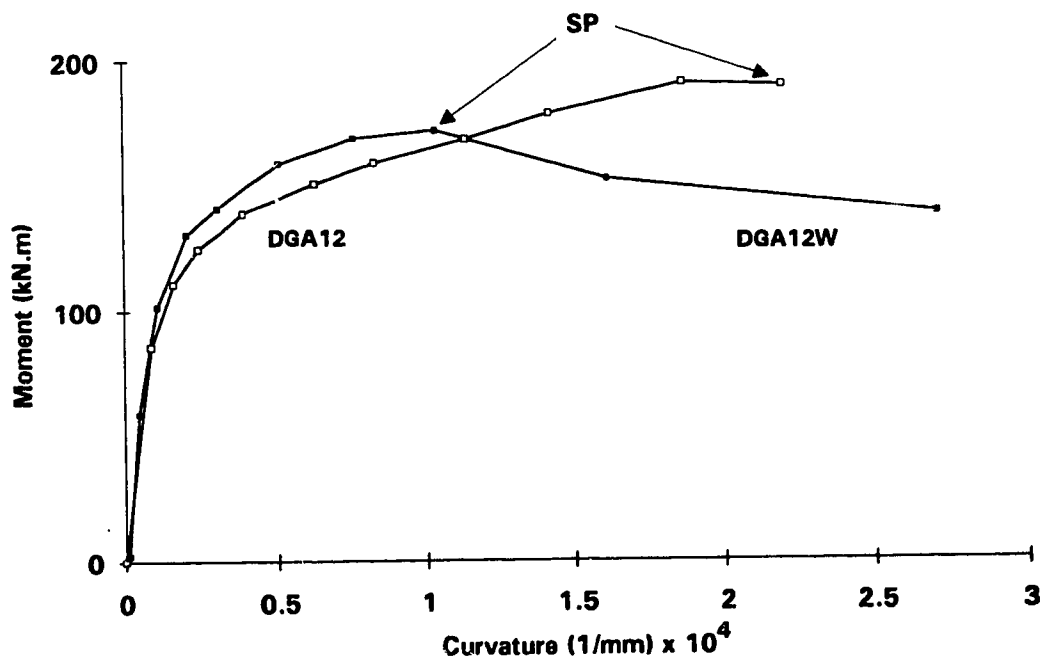
Fig. 4.10 Average moment vs. curvature over wrinkled segment for DGA12W and DGA12
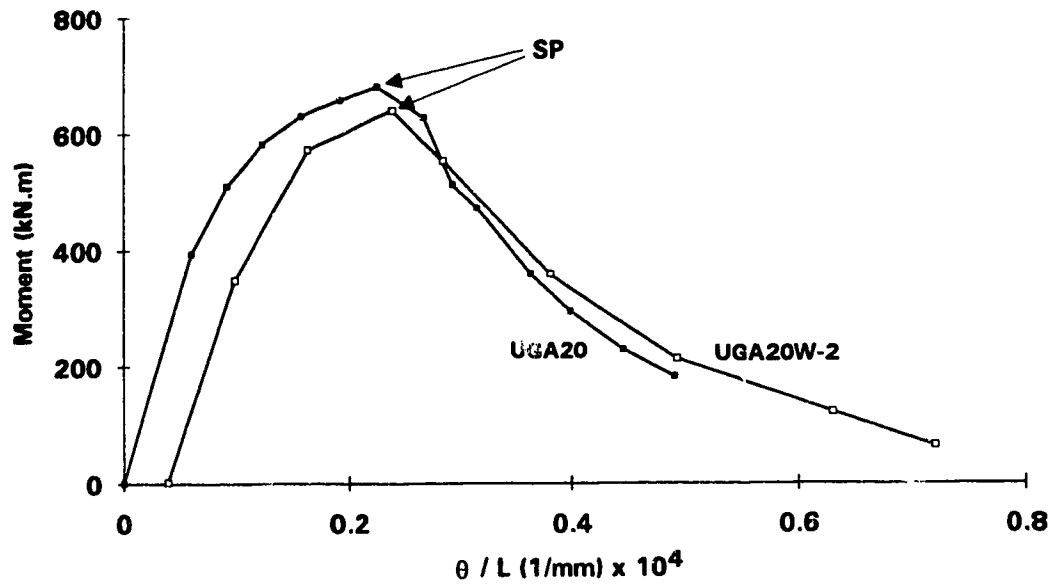
Fig. 4.11 Average end moment vs. overall curvature for UGA20W-2 and UGA20
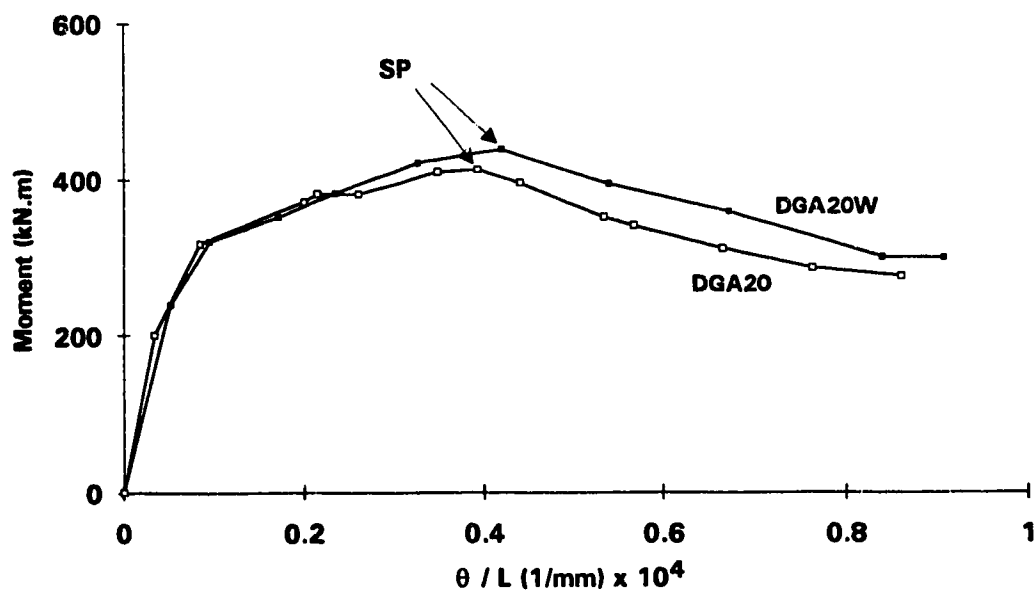
Fig. 4.12 Average end moment vs. overall curvature for DGA20W and DGA20
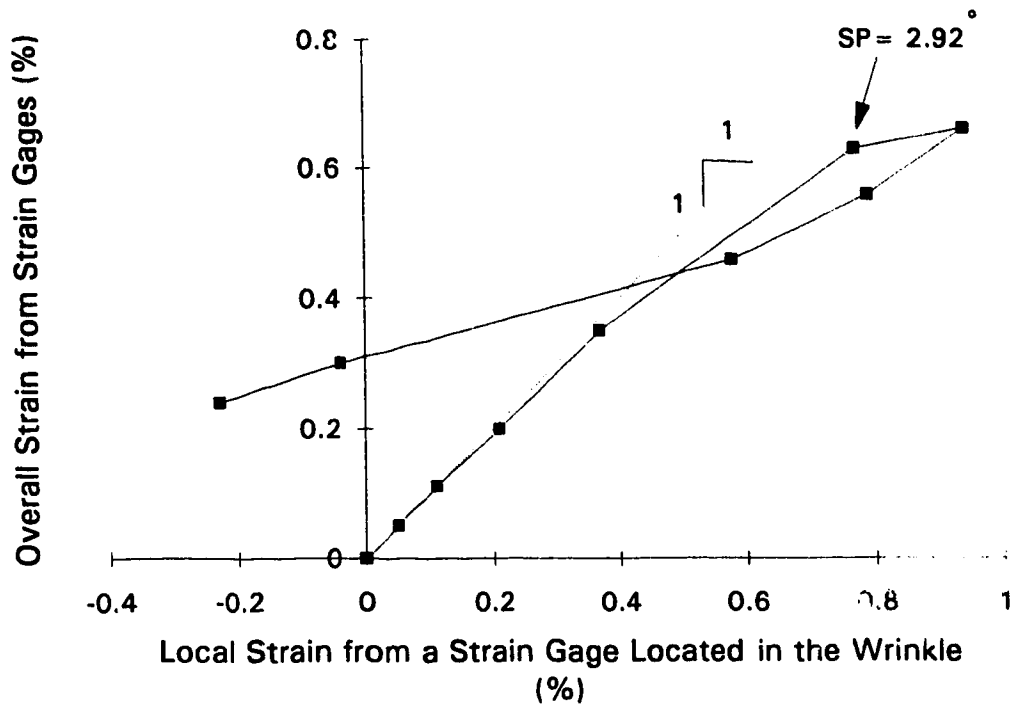
Fig. 4.13 Overall vs. local strain gage strains for UGA12W
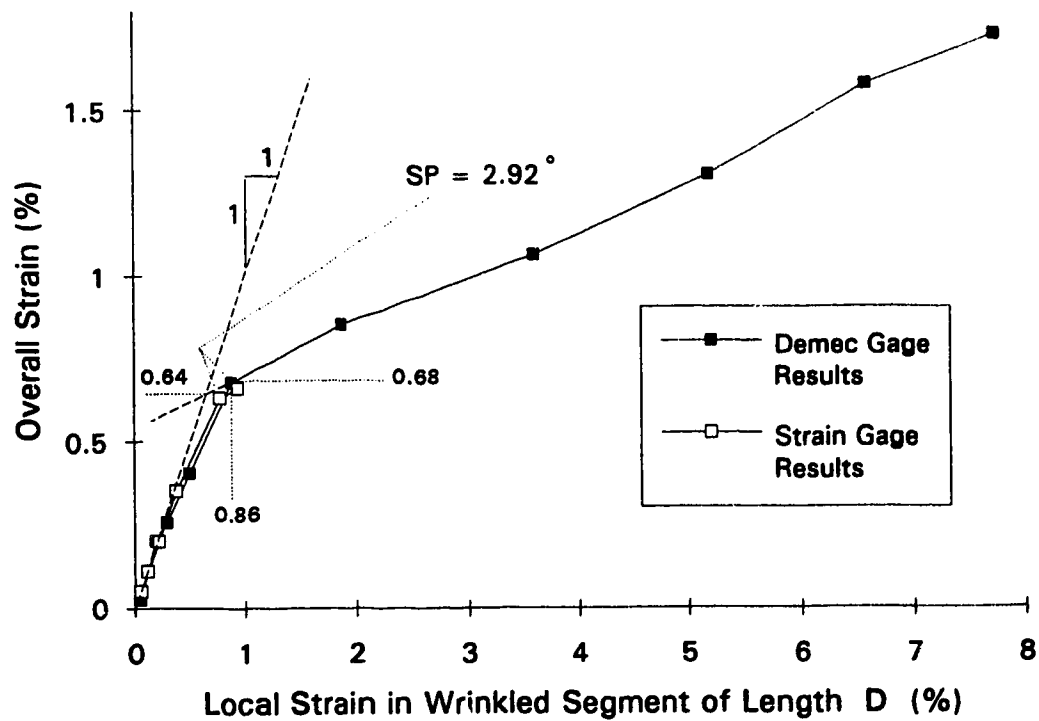
Fig. 4.14 Overall vs. local strains for UGA12W
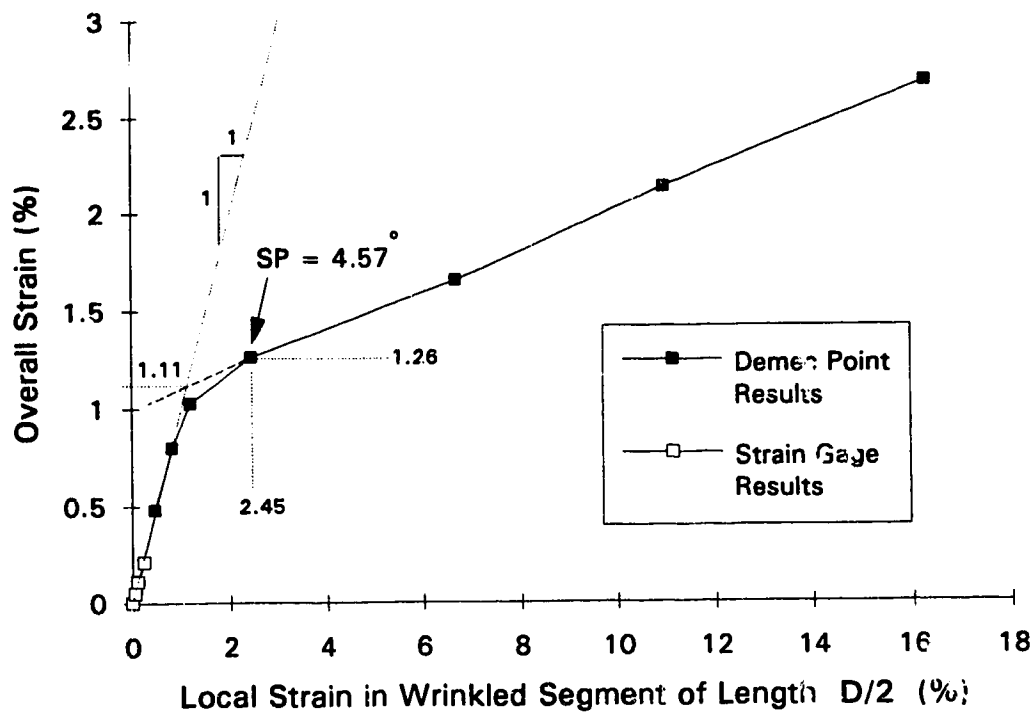
Fig. 4.15 Overall vs. local strains for HGA12W
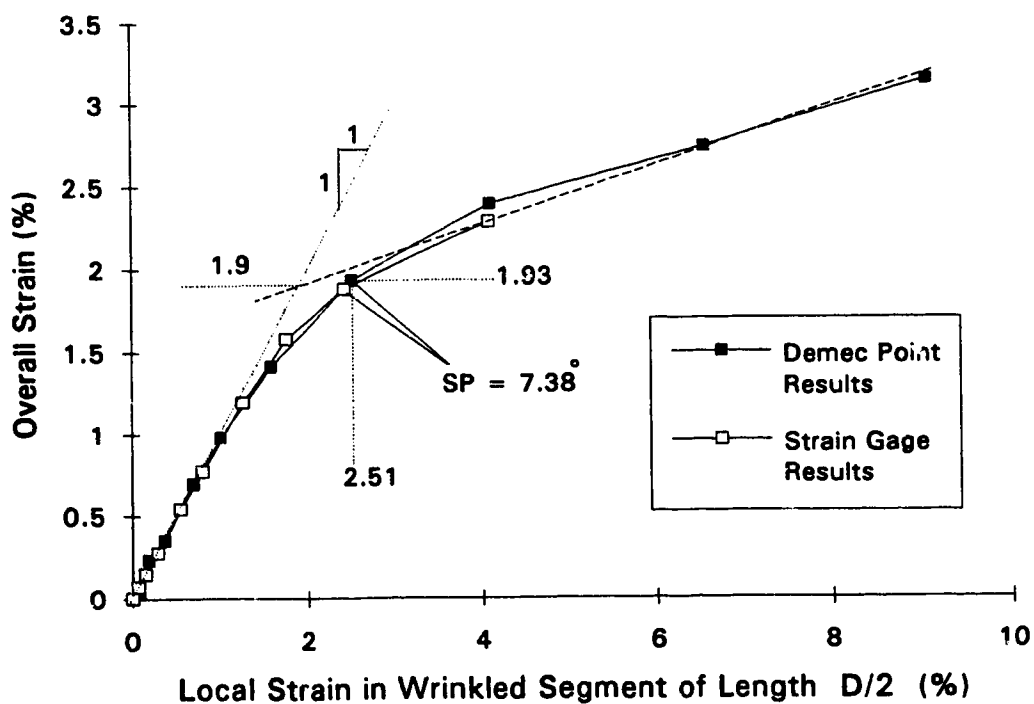
Fig. 4.16 Overall vs. local strains for DGA12W
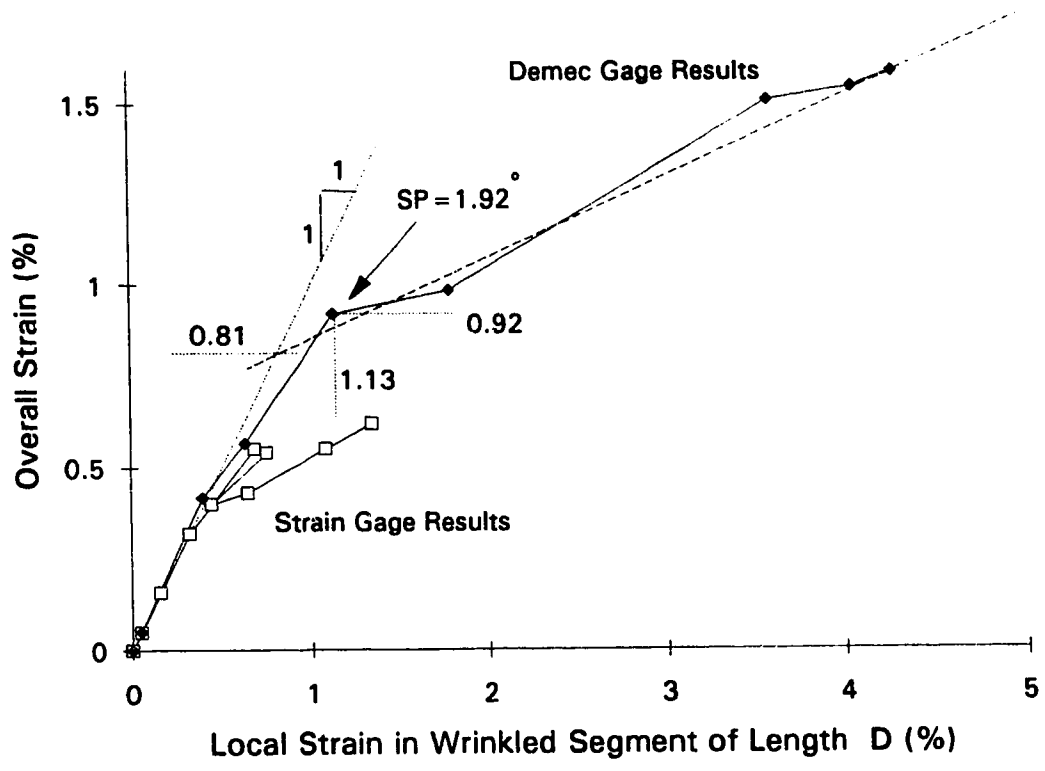
Fig. 4.17 Overall vs. local strains for UGA20W-2
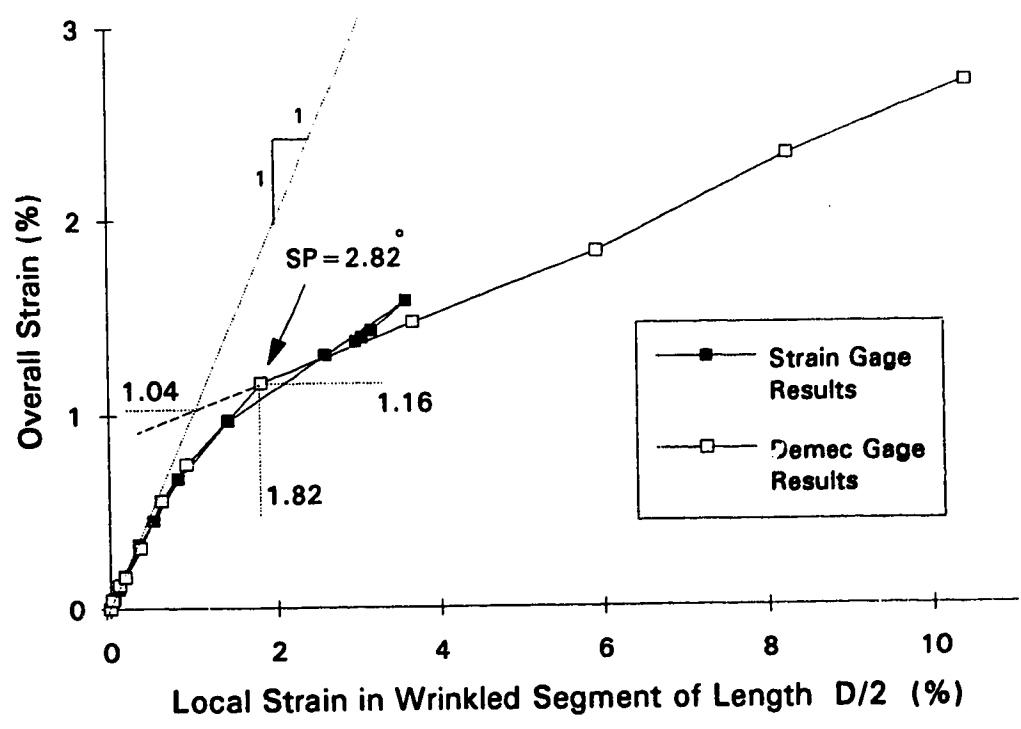
Fig. 4.18 Overall vs. local strains for HGA20W
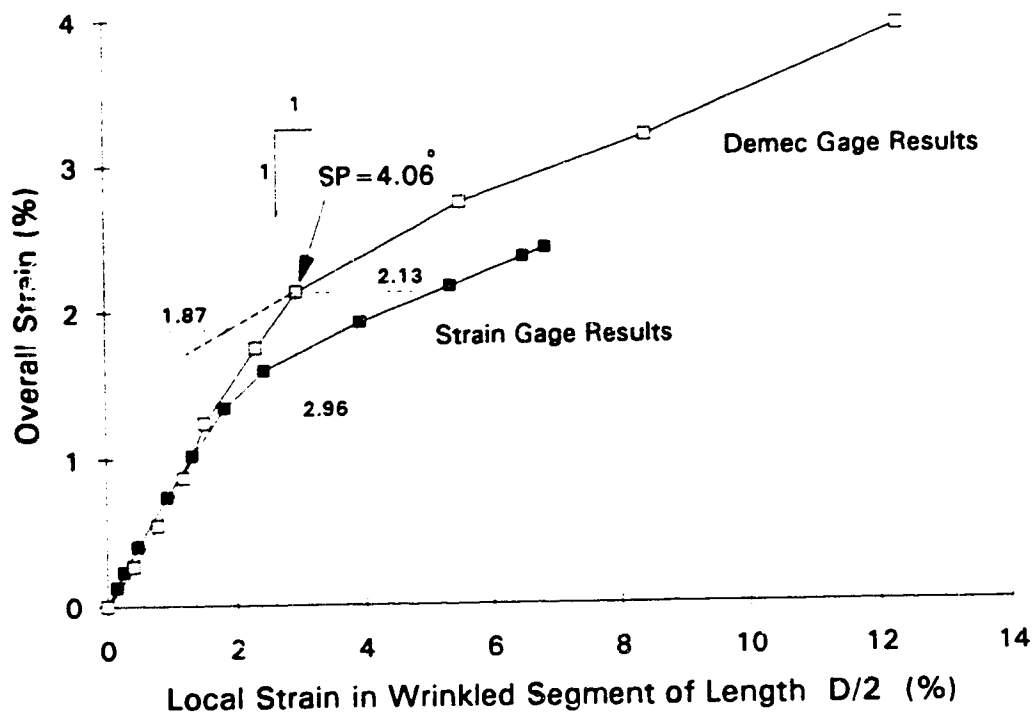
Fig. 4.19 Overall vs. local strains for DGA20W
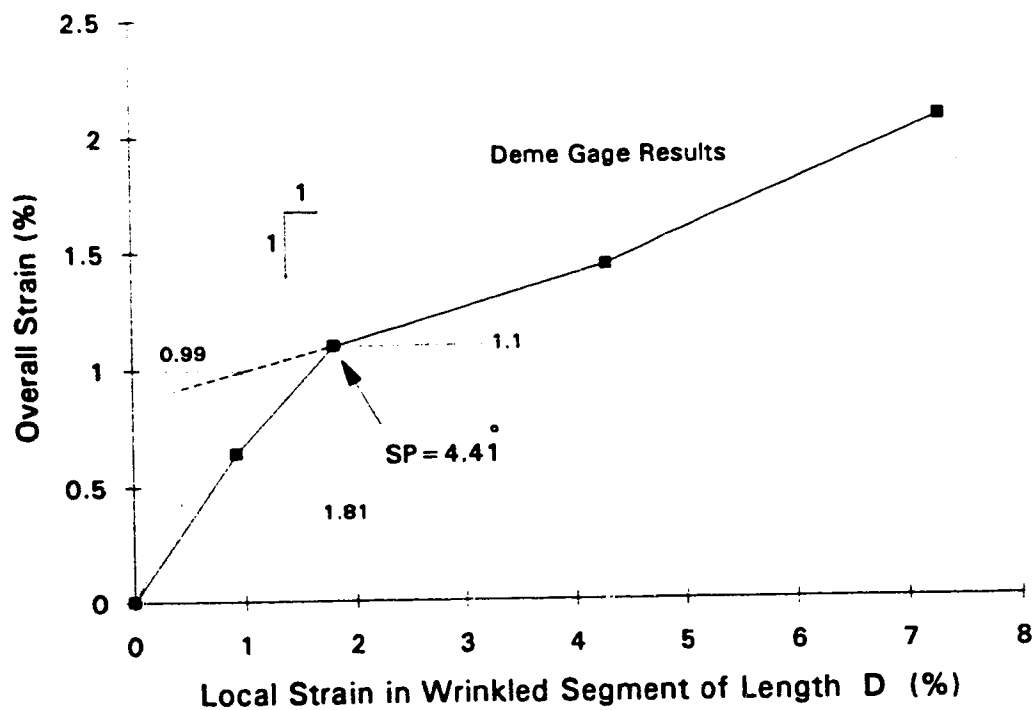
Fig. 4.20 Overall vs. local strains for UGA12
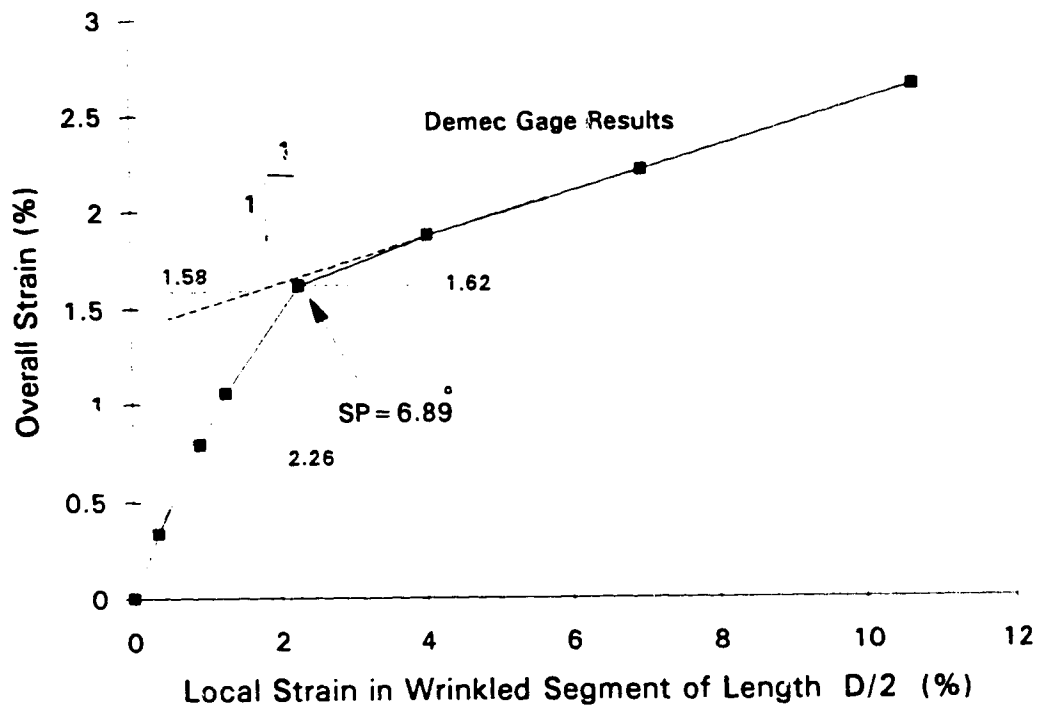
Fig. 4.21 Overall vs. local strains for HGA12
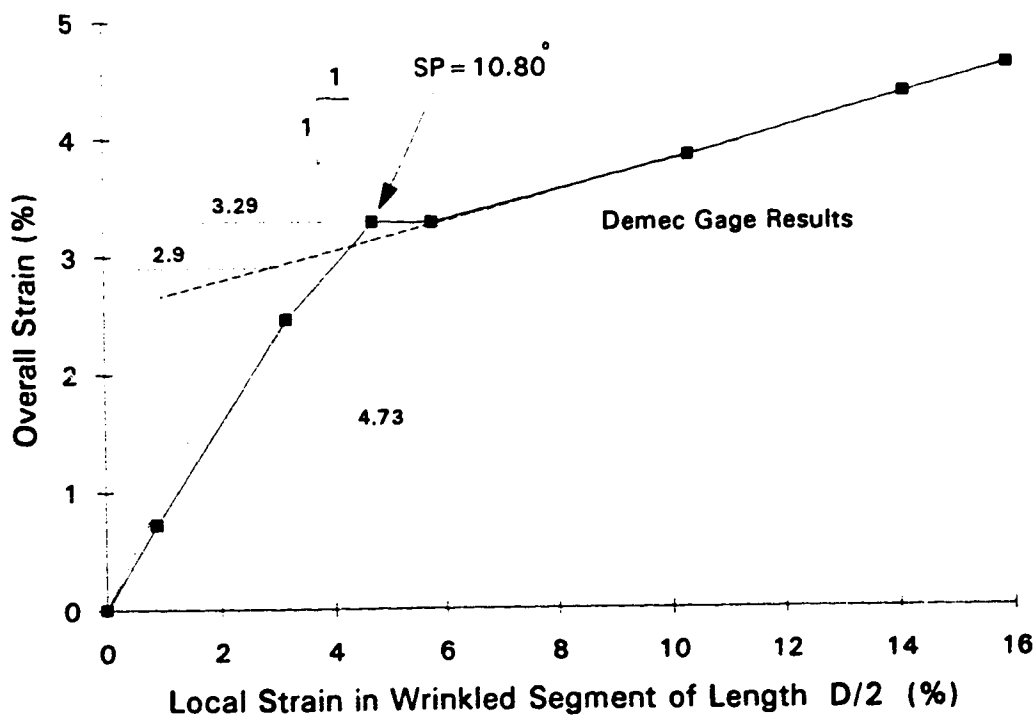
Fig. 4.22 Overall vs. local strains for DGA12
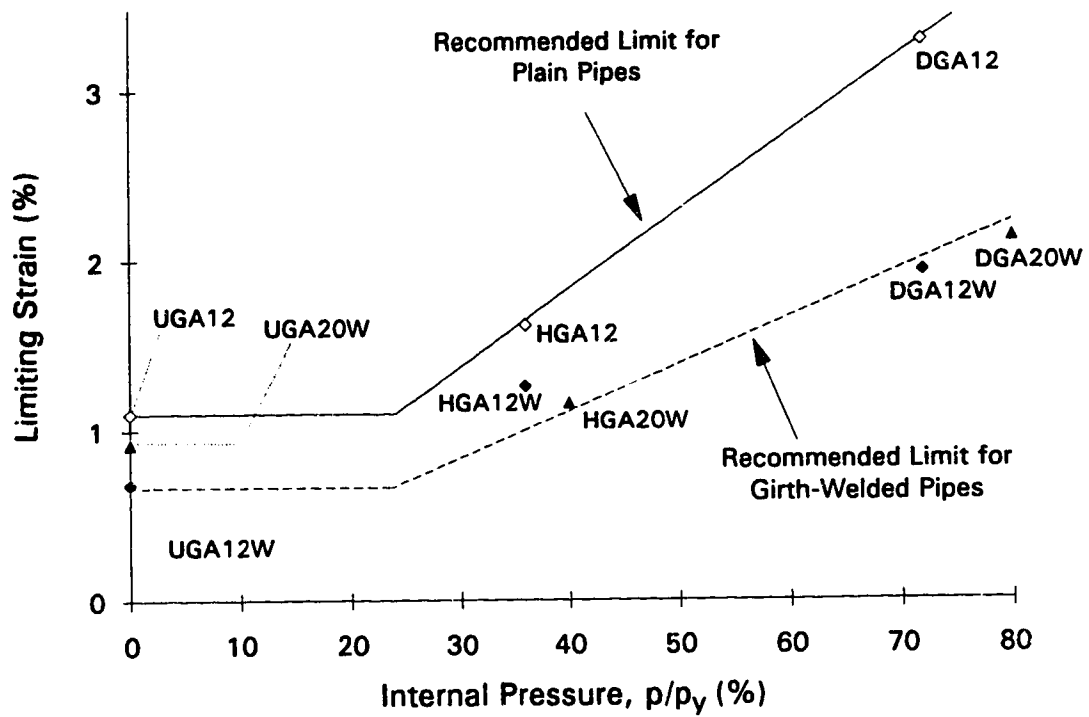
Fig. 4.23 Tentative strain limits for wrinkling for 12.75 x 0.25 inch ERW X52 and
20 x 0.312 inch DSAW X56 pipelines

5 NUMERICAL INVESTIGATION

5.1 INTRODUCTION

In the preceding chapters, the experimental program was described and the results were discussed. In this chapter, a theoretical approach describing the moment vs. curvature response of the pipes is reported. In the numerical investigation, the strain-hardening of the material is considered, using a mixed hardening formulation. However, the change in the cross-section configuration is not considered. Therefore, ovalization and local buckling are not taken into account. In addition, the residual stresses and transverse girth welds are not taken into account in this investigation. The objective is to develop a simple model capable of predicting the behavior of pipes up to the softening point.

The mathematical formulation for computing the moment vs. curvature response of a pipe cross-section has been implemented in a computer program called Plastic Analysis of Pipe Sections (PAPS). These results will be compared with the experimental moment vs. curvature results for a buckled segment up to the softening point. Another computer program called P-Delta Analysis (PDA) has been written to develop the relationship between the end moment and the overall curvature response (i.e., the global response) for a closed-ended pipe under loading conditions similar to those used for the test specimens. The program PDA uses the local moment vs. curvature curve that is output from PAPS to produce the end moment vs. overall curvature response for a closed-ended pipe specimen. This enables the experimental response to be compared with the analytically predicted response. The simplified model of this study permits the comparison to be made only up to the point of buckling.

In the following subsections, the initial elastic behavior is described. Then, various choices of stress vs. strain measures and strain-hardening rules are discussed. This is followed by the formulation of the elastic–plastic model used in this study. The analytical procedures to obtain the local and global moment vs. curvature responses of pipe are then described. Finally, the analytical results are presented and compared with the test results.

5.2 INITIAL YIELDING OF PIPES

5.2.1 General

In this section, a closed-ended pipe similar to a very short test specimen is considered. The sequence of loading is identical to that of the test specimens. Thus, it is assumed that the pipe is first pressurized to the final pressure, then it is subjected to the external axial load, and, finally, curvature is imposed. In the latter step, the very short slice of pipe is considered to be gradually subjected to the imposed curvature to some prescribed value. During this bending procedure, the moment corresponding to the increased curvature at each step is calculated by the computer program PAPS.

The behavior of the pipe is elastic from the beginning of the loading until the proportional limit is reached anywhere in the cross-section. This is the beginning of nonlinearity and plastic behavior. However, for a closed-ended pipe subjected to only internal pressure and axial load, the longitudinal stress, σ_x, and the hoop stress, σ_θ, are independent of the material properties and can be determined from statics.

In the free body diagram shown in Fig. 5.1, the equilibrium of the forces in the x direction yields

$$2 \pi R_m t \sigma_x = \pi R_i^2 p - P \qquad (5.1)$$

where t is the pipe wall thickness, R_i is the inside radius, R_m is the average of inside and outside radii, p is the internal pressure, and P is the applied axial load. The (tensile) stress σ_x can be obtained from Eq. (5.1) as

$$\sigma_x = \frac{p R_i}{2 t}(\frac{R_i}{R_m}) - \frac{P}{2\pi R_m t} \qquad (5.2)$$

The free body diagram of a half-cylindrical portion of the pipe, with an arbitrary small length ℓ, is shown in Fig. 5.2. The equilibrium of the forces in the y direction gives

$$2\ell t \sigma_\theta = 2\ell R_i p \qquad (5.3)$$

Hence,

$$\sigma_\theta = \frac{p R_i}{t} \qquad (5.4)$$

The through-thickness stress in a pressurized pipe varies from zero on the outside surface of the pipe to the internal pressure on the inside surface. However, even at its maximum (around 10 MPa for the highest pressure used in these tests), this stress is very small compared to the longitudinal and hoop stresses. Thus, for simplicity, the through-thickness stress is neglected.

The first encounter with the proportional limit could occur during any of the three stages of loading. For a given cross-section and material stress vs. strain curve, this depends on the magnitude of the final pressure and the external axial load.

Because of the biaxial state of the stress (longitudinal and hoop stress), a yield function should be adopted (here *yield* means reaching the proportional limit). There are a number of yield criteria available in the literature. In this study, the von Mises yield criterion, which is commonly used for metals, is employed. This yield criterion has been shown to be in excellent agreement with experimental results for many ductile metals, including different types of steel (Hill 1950). The form of the von Mises criterion for the biaxial state of stress, with the longitudinal and hoop stresses as the principal stresses can be expressed as

$$\sigma_x^2 + \sigma_\theta^2 - \sigma_x\sigma_\theta = \sigma_p^2 \qquad (5.5)$$

where σ_p is the yield stress (i.e., the proportional limit in a uniaxial test). The conditions for reaching the proportional limit during each of the loading stages are discussed in the following subsections.

5.2.2 Initiation of Yielding During Pressurization

Since no external axial load has been applied prior to pressurization, the value of P in Eq. (5.2) is zero. Substituting Eq. (5.2) and Eq. (5.4) into Eq. (5.5) results in

$$p_0 = \frac{\sigma_p(\frac{t}{R_i})}{\left[1 - \frac{R_i}{2R_m} + (\frac{R_i}{2R_m})^2\right]^{1/2}} \qquad (5.6)$$

where p_0 is the value of the pressure at the first occurrence of the proportional limit. Thus, if the final value of the pressure is less than p_0, the pipe remains elastic during the pressurization.

5.2.3 Initiation of Yielding During Application of Axial Load

Here the pipe has remained elastic under the prescribed final pressure, p. If it is assumed that inelasticity starts during the second stage of loading (i.e., the application of axial load), then the value of axial load, P_0, required to reach the proportional limit can be determined by substituting Eq. (5.2) and Eq. (5.4) into Eq. (5.5). This yields

$$P_0 = \pi R_m p \left[R_i (\frac{R_i}{R_m} - 1) \pm \sqrt{4(\frac{\sigma_p t}{p})^2 - 3R_i^2} \right] \qquad (5.7)$$

If the prescribed final axial load is less than P_0 determined by Eq. (5.7), then the pipe remains elastic throughout the application of axial load. It should be noted that the use of Eq. (5.7) is valid only when the pipe has remained elastic during the pressurization. This requires that the prescribed final pressure be less than p_0 obtained from Eq. (5.6).

For the usual sizes of line pipes, R_i (the inside radius) is very close to R_m (the average of the inside and outside radii). Therefore, the first term in the bracket in Eq.

(5.7) (i.e., $R_i(\frac{R_i}{R_m} - 1)$) is much smaller than the second term in a general case. Consequently, when the sign of the radical is positive, the solution for P_0 is positive, meaning compression. Since the tests carried out at the University of Alberta were always done for P_0 in compression, the only use herein for Eq. (5.7) is for the case when that equation gives a positive answer.

5.2.4 Initiation of Yielding During Imposition of Curvature

If the pipe is still elastic at the completion of application of the axial load, then plastification must begin during imposition of the curvature. Figure 5.3 illustrates the path along which the stress state proceeds during the three loading stages. As shown in Fig. 5.3, in the first loading stage (i.e., the pressurization) the stress state of the whole cross-section moves from point O to A on a straight line. This is because from Eqs. (5.2) and (5.4)

$$\frac{\sigma_\theta}{\sigma_x} = 2\frac{R_m}{R_i} = \text{constant} \tag{5.8}$$

For a very thin-walled pipe, the inside and mid-surface radii (i.e., R_i and R_m, respectively) are almost equal to each other. Hence, the above ratio is approximately 2. Therefore, the stress state proceeds along the line Om, as shown in Fig. 5.3. However, the actual path of the stress state for a closed-ended pipe segment subjected to internal pressure must be to the left of the line Om because the slope of the stress path for an actual pipe, given by Eq. (5.8), is always greater than 2.

The longitudinal movement of a pipeline in the field can be assumed to be restricted. This implies that the longitudinal strain be zero. Thus, while still elastic, the Poisson's effect gives the value of longitudinal stress as $\mu\sigma_\theta$. At the same time, the pipe segment ends are open and, consequently, Eq. (5.2) does not apply. Therefore, the stress state proceeds along the line On shown in Fig. 5.3 until it reaches the yield ellipse.

For the remaining two loading stages, the hoop stress, which depends only on the internal pressure, remains constant. Therefore, the consequent movements of the stress state for every point on the cross-section occur on the horizontal line passing through A (perpendicular to the σ_θ axis), as shown by line CD in Fig. 5.3. This line intersects the yield surface at C and D, and the longitudinal stress values can be determined from Eq. (5.5) as

$$\sigma_x(C) = \sigma_0 - \sqrt{\sigma_p^2 - 3\sigma_0^2} \tag{5.9}$$

$$\sigma_x(D) = \sigma_\cdot + \sqrt{\sigma_p^2 - 3\sigma_0^2} \tag{5.10}$$

where $\sigma_0 = \dfrac{\sigma_\theta}{2} = \dfrac{pR_i}{2t}$.

It can be seen that point A is slightly to the left of the midpoint between C and D. (The midpoint of CD in Fig. 5.3 is the point at which Om intercepts CD.) This is because the value of σ_x for the midpoint equals

$$\frac{1}{2}[\sigma_x(C) + \sigma_x(D)] = \sigma_0 = \frac{p R_i}{2 t} \tag{5.11}$$

whereas from Eq. (5.2),

$$\sigma_x(A) = \frac{p R_i}{2 t} (\frac{R_i}{R_m}) \tag{5.12}$$

Since $\frac{R_i}{R_m}$ is less than one, the longitudinal stress at point A is smaller than that of the midpoint.

Applying a compressive axial force moves the stress state from point A toward C on the horizontal path. Here it is assumed that the axial compression does not initiate the plastification. Thus, the stress state of the cross-section at the completion of application of the axial load must be between A and C, the point B in Fig. 5.3. The value of longitudinal stress for the whole cross-section at B is obtained from Eq. (5.2):

$$\sigma_x(B) = \frac{p R_i}{2 t} (\frac{R_i}{R_m}) - \frac{P}{2 \pi R_m t} \tag{5.13}$$

If the cross-section remains elastic during the application of curvature, the resulting stress distribution can be determined by superposition. From elementary beam theory, the values of stress at the extreme fibers due to the imposed curvature are $\pm \frac{M}{S}$, where M is the moment corresponding to the imposed curvature and S is the section modulus,

$$S = \frac{\pi (D_o^4 - D_i^4)}{32 D_o} \tag{5.14}$$

where D_o and D_i are the outside and inside diameters of the pipe, respectively. Therefore, for elastic conditions, the stress states of the extreme compressive and tensile fibers occur at equal distances to the left and right of point B in Fig. 5.3. Since BC is shorter than BD, the stress state of the extreme compressive fiber is the first to reach the yield ellipse (see Fig. 5.3). Thus,

$$\sigma_x(B) - \frac{M_0}{S} = \sigma_x(C) \tag{5.15}$$

where M_0 is the moment required to initiate yielding. Equations (5.9), (5.13), and (5.15) give the value of M_0 as

$$M_0 = S\left(\sqrt{\sigma_p^2 - 3\sigma_0^2} - \sigma_0 + \frac{p\,R_i}{2\,t}\left(\frac{R_i}{R_m}\right) - \frac{P}{2\,\pi\,R_m\,t}\right) \tag{5.16}$$

For the nonlinear analysis that will follow, the values of strains and stresses at the extreme fibers and the curvature corresponding to the yield moment (M_0) need to be calculated. The stress at the maximum tension fiber at the beginning of plasticity is equal to

$$\sigma_x^t = \sigma_x(C) + 2\,\frac{M_0}{S} \tag{5.17}$$

Because the through-thickness stress is small, the longitudinal strains can be obtained using the plane stress formulae. Hence,

$$\varepsilon^c = \frac{1}{E}(\sigma_x(C) - v\sigma_\theta) \tag{5.18}$$

$$\varepsilon^t = \frac{1}{E}\left(\sigma_x^t - v\sigma_\theta\right) \tag{5.19}$$

where ε^c and ε^t are the values of the longitudinal strains at the extreme compression and tension fibers, respectively. The value of curvature at the first yield, ϕ_0, is calculated by the same formula as used in Eq. (3.5),

$$\phi_0 = \frac{\varepsilon^t - \varepsilon^c}{D_0} \tag{5.20}$$

Finally, from Eq. (5.9) and (5.16) to (5.20),

$$\phi_0 = \frac{2}{E\,D_0}\left(\sqrt{\sigma_p^2 - 3\sigma_0^2} - \sigma_0 + \frac{p\,R_i}{2\,t}\left(\frac{R_i}{R_m}\right) - \frac{P}{2\,\pi\,R_m\,t}\right) \tag{5.21}$$

Using the relationship $\phi_0 = \dfrac{M_0}{EI}$ to obtain the curvature ϕ_0 gives the same result as that given by Eq. (5.21).

Note that the equations in this section are to be used only when the pipe is still elastic at the completion of the application of pressure and axial load.

5.3 INCREMENTAL STRESS VS. STRAIN FORMULATIONS

Plasticity can be accompanied by large strains and the choices of strain and stress measures become important. Some widely-used measures of stress and strain are discussed in the subsequent sections in order to determine the most appropriate ones. First, the strain-hardening of the material is examined by reviewing different theories. Then, the elastic–plastic formulation implemented in the computer program PAPS is presented.

5.3.1 Stress and Strain Measures

Among the large number of conjugate stress and strain measures in the literature, three kinematic formulations are employed effectively in elasto-plasticity (Bathe 1982):

1. Engineering Stress and Strain Formulation (ESS)

This formulation assumes infinitesimally small displacements and rotations on the basis that the strain measure is not invariant under rigid body motions (Bathe 1982). The ESS formulation is recommended only for materially-nonlinear analysis. This formulation has been chosen as one of the options in the program PAPS.

2. Total Lagrangian Formulation (TL)

This formulation employs 2nd Piola-Kirchhoff stresses and Green-Lagrange strains. This measure of strain is unaffected by rigid body motions (Bathe 1982). The kinematic assumptions for the strain measure permit large displacements and large rotations. However, this formulation is most effective only for small strains. This is because the constitutive tensor in each increment is subjected to a transformation determined by the deformation gradient with respect to the initial configuration. Nevertheless, if the strains are small, these transformations do not change the components of the constitutive tensor (provided that the material is isotropic). This formulation

without the transformation of the constitutive tensor is one of the options in the program PAPS.

3. Updated Lagrangian Formulation (UL)

This formulation employs Cauchy (true) stresses and updated Lagrangian strains. Under rigid body motion, the strain measure remains unchanged. Hence, it is applicable to general elastic–plastic analysis with large displacements and rotations and large strains. The formulation is effective in large strain analysis because the stress and strain measures used are those that describe the material response in a natural way (Bathe 1982). This strain measure is commonly used for problems in metal plasticity. One motivation for this choice is that when true stress (force per current unit area) is plotted against logarithmic strain, then tension, compression, and torsion test results coincide closely with each other (Hibbit et al. 1993a). In general, at any point of a body the updated Lagrangian longitudinal strain in the direction of an arbitrary axis attached to the body reduces to $\ln(\lambda)$, where λ is the stretch (current length divided by the original length) in that direction.

5.3.2 Elastic–Plastic Formulations

5.3.2.1 General

The elasto-plasticity formulation employed in this model, and discussed below, has been adapted from the book by Chen and Han (1988). In the subsequent derivations, σ_{ij} and ε_{ij} are general notations that could represent any of the three stress and strain measures mentioned in Section 5.3.1. The fundamentals of the elastic–plastic formulation are discussed in the following subsection.

5.3.2.1.1. Yield Function

Yield function defines the elastic limit of a material under a combined state of stress. In general, the yield stress is a function of the state of stress, σ_{ij}, and can be expressed as

$$f(\sigma_{ij}, k) = 0 \qquad (5.22)$$

where k is the hardening parameter. The yield function can be best interpreted geometrically as a surface in stress space. For a perfectly-plastic material, the yield function is assumed to remain unchanged. Thus, the parameter k in Eq. (5.22) is a

constant, and the yield surface is therefore fixed in stress space. However, for a work-hardening material the yield surface changes as elastic–plastic deformation occurs.

5.3.2.1.2. Hardening Rule

When an initial yield surface is known, the work hardening rule defines its modification during the process of plastic flow. A number of hardening rules have been proposed. The most widely used are those of isotropic hardening, kinematic hardening, and a combination of both, so-called mixed hardening.

Th.. ⸱rdening rule is based on the assumption that the initial yield surface exp⸱. . y without distortion and translation in stress space as plastic flow occurs. The ⸱⸱e yield surface is governed by the value of ⸱ parameter k, which depends upon plastic strain history.

The kinematic hardening rules assume that, during elastic–plastic deformation, the loading surface translates as a rigid body in stress space, maintaining the size, shape, and orientation of the initial surface. This rule is implemented by keeping k constant and replacing the stress tenor, σ_{ij}, in Eq. (5.22) with the reduced stress tensor, $\overline{\sigma}_{ij}$. Reduced stress components are measured from the center of the yield surface.

$$\overline{\sigma}_{ij} = \sigma_{ij} - \alpha_{ij} \tag{5.23}$$

Here α_{ij} are the coordinates of the yield surface center in stress space, and they depend on the plastic strain history.

A combination of isotropic and kinematic hardening leads to the more general mixed hardening rule. In this case, the yield surface undergoes a translation defined by α_{ij} and a uniform expansion measured by k. This constitutes a more general work hardening, which contains the isotropic and kinematic hardening rules as its two limiting conditions.

Detailed formulations of the isotropic and kinematic rules, along with their contributions in the mixed hardening model, are presented in Sections 5.3.2.2.1 and 5.3.2.3, respectively. The applicability of the isotropic and kinematic hardening rules to different loading conditions is discussed in Section 5.3.3.

5.3.2.1.3. Elastic and Plastic Strain Increment Tensors

One important assumption for elastic–plastic deformation is that the total strain increment tensor is composed of the sum of the elastic and plastic strain increment tensors:

$$d\varepsilon_{ij} = d\varepsilon_{ij}^e + d\varepsilon_{ij}^p \qquad (5.24)$$

where $d\varepsilon_{ij}^e$ and $d\varepsilon_{ij}^p$ are the elastic and plastic strain increment tensors, respectively.

Hooke's law is assumed to provide the necessary relation between the incremental changes of stress and elastic strain; hence,

$$d\sigma_{ij} = C_{ijkl}\, d\varepsilon_{kl}^e \qquad (5.25)$$

where C_{ijkl} is the tensor of elastic moduli. Substituting for $d\varepsilon_{kl}^e$ from Eq. (5.24) gives

$$d\sigma_{ij} = C_{ijkl}(\, d\varepsilon_{kl} - d\varepsilon_{kl}^p\,) \qquad (5.26)$$

This is the basic equation for developing the nonlinear constitutive relations to be discussed in Section 5.3.2.4.

5.3.2.1.4. Plastic Potential and Flow Rule

The flow rule is the kinematic assumption postulated for elastic–plastic deformation. It gives the ratio or the relative magnitudes of the components of the plastic strain increment tensor, $d\varepsilon_{ij}^p$. In other words, the flow rule defines the direction of the plastic strain increment vector, $d\varepsilon_{ij}^p$, in strain space. By defining a plastic potential function, $g(\sigma_{ij})$, which is a scalar function of the stresses, the plastic flow equations can be written in the form

$$d\varepsilon_{ij}^p = \frac{\partial g}{\partial \sigma_{ij}}\, d\lambda \qquad (5.27)$$

where $d\lambda$ is a positive scalar factor of proportionality, which is nonzero only when elastic–plastic deformations occur. Of great importance is the simplest case for which the yield function and the plastic potential functions coincide, i.e., f = g. Thus,

$$d\varepsilon_{ij}^p = \frac{\partial f}{\partial \sigma_{ij}}\, d\lambda \qquad (5.28)$$

and plastic flow develops along the normal to the yield surface. Equation (5.28) is called the associated flow rule and it has been used successfully for metals (Chen and Han 1988). This equation will be used in formulating the nonlinea^ constitutive relations developed in Section 5.3.2.4.

5.3.2.1.5. Consistency Condition

The consistency condition requires that the state of stress remain on the yield surface during plastic flow. Thus, after a small elastic–plastic deformation, the yield condition represented by Eq. (5.22) must still be satisfied. Hence,

$$f(\sigma_{ij} + d\sigma_{ij},\ k + dk) = f(\sigma_{ij},\ k) + df = 0 \qquad (5.29)$$

This, in combination with Eq. (5.22), yields

$$df = 0 \qquad (5.30)$$

The scalar $d\lambda$ can be determined from this condition, as described in Section 5.3.2.4.

5.3.2.2 von Mises Yield Function

5.3.2.2.1 Generalization of Yield Function for Mixed Hardening

The von Mises yield function for an isotropic-hardening material is expressed as

$$f(\sigma_{ij}, k) = \frac{3}{2} S_{ij} S_{ij} - k^2 = 0 \qquad (5.31)$$

where S_{ij} is the deviatoric stress, defined as

$$S_{ij} = \sigma_{ij} - \frac{1}{3}\sigma_{kk}\,\delta_{ij} \qquad (5.32)$$

In general, the hardening parameter, k, is defined as a function of either the effective plastic strain or the plastic work. Bland (1956) showed that for any yield function that is linear or quadratic (such as the von Mises yield function), using either the effective plastic strain or the plastic work as the argument for k is equivalent. Herein, the simpler choice, which is the effective plastic strain, is used as k in the von Mises yield

criterion. For a von Mises material, the effective strain, ε_p, is defined in incremental form by

$$d\varepsilon_p = \sqrt{\frac{2}{3} d\varepsilon_{ij}^p \, d\varepsilon_{ij}^p}$$

(5.33)

In the mixed hardening formulation, the plastic strain increment tensor is assumed to be the sum of the isotropic and kinematic portions, denoted by $d\varepsilon_{ij}^i$ and $d\varepsilon_{ij}^k$, respectively:

$$d\varepsilon_{ij}^p = d\varepsilon_{ij}^i + d\varepsilon_{ij}^k$$

(5.34)

The isotropic strain increment, $d\varepsilon_{ij}^i$, is associated with the expansion of the yield surface, and the kinematic plastic strain increment, $d\varepsilon_{ij}^k$, is associated with the translation of the yield surface. These two strain components can be written as

$$d\varepsilon_{ij}^i = M \, d\varepsilon_{ij}^p$$

(5.35)

$$d\varepsilon_{ij}^k = (1 - M) \, d\varepsilon_{ij}^p$$

(5.36)

in which M is the parameter of mixed hardening. It has the range $0 \le M \le 1$.

For a mixed-hardening material, the generalized form of the von Mises yield function is expressed as

$$f(\bar{\sigma}_{ij}, \bar{k}) = \frac{3}{2} \bar{S}_{ij} \bar{S}_{ij} - \bar{k}^2(\bar{\varepsilon}_p) = 0$$

(5.37)

where $\bar{S}_{ij}$ is the reduced deviatoric stress, defined as

$$\bar{S}_{ij} = \bar{\sigma}_{ij} - \frac{1}{3} \bar{\sigma}_{kk} \delta_{ij}$$

(5.38)

and $\bar{\varepsilon}_p$ is the reduced effective strain, which is defined in incremental form as

$$d\bar{\varepsilon}_p = \sqrt{\frac{2}{3} d\varepsilon_{ij}^i \, d\varepsilon_{ij}^i}$$

(5.39)

From Eqs. (5.33), (5.35), and (5.39), the relationship between the effective stress and the reduced effective stress is obtained as

$$d\bar{\varepsilon}_p = M\, d\varepsilon_p \qquad (5.40)$$

The hardening parameter for an isotropic-hardening material (i.e., k in Eq.(5.31)) is called the *effective stress* because it identifies with the yield stress in a uniaxial tension test. For a von Mises material, the effective stress, σ_e, can be expressed as

$$\sigma_e = \sqrt{\frac{3}{2} S_{ij}\, S_{ij}} \qquad (5.41)$$

For a mixed-hardening material, the *reduced effective stress*, $\bar{\sigma}_e$, is used as the hardening parameter (i.e., $\bar{k}$ in Eq.(5.37)). For a von Mises material, the reduced effective stress can be expressed as

$$\bar{\sigma}_e = \sqrt{\frac{3}{2} \bar{S}_{ij}\, \bar{S}_{ij}} \qquad (5.42)$$

Therefore, the von Mises yield condition for a mixed-hardening material becomes (upon redefining the arguments of the function f in Eq. (5.37))

$$f(\sigma_{ij}, \alpha_{ij}, \bar{\varepsilon}_p) = \frac{3}{2} \bar{S}_{ij}\, \bar{S}_{ij} - \bar{\sigma}_e^{\,2}(\bar{\varepsilon}_p) = 0 \qquad (5.43)$$

5.3.2.2.2 Plastic Moduli

The effective stress vs. effective strain relationship, characterizing the hardening process of a material, is determined by the experimental uniaxial stress vs. strain relationship, which has the general form

$$\sigma_e = \sigma_e(\varepsilon_p) \qquad (5.44)$$

In the incremental form it becomes

$$d\sigma_e = H_p\, d\varepsilon_p \qquad (5.45)$$

where $H_p(\sigma_e)$ is called the *plastic modulus*. For an isotropic-hardening material, H_p is associated with the expansion of the yield surface. For a mixed-hardening material, however, the *reduced plastic modulus* defined by

$$\overline{H}_p = \frac{d\overline{\sigma}_e}{d\overline{\epsilon}_p} \tag{5.46}$$

represents the expansion of the yield surface. However, note that the experimental relationship is always that expressed by Eq. (5.44). In a uniaxial test, $d\sigma_e$ and $d\epsilon_p$ are equal to $d\sigma_{11}$ and $d\epsilon_{11}$, respectively. (Subscript 1 represents the longitudinal direction in the uniaxial test.) However, the values of the reduced effective stress and strain depend on the choice of the mixed hardening parameter, M. Moreover, the value of $d\overline{\sigma}_e$, which is equal to $d\overline{\sigma}_{11}$, cannot be determined from the test results because the value of $d\alpha_{11}$ can be obtained only from the theory. (Note that $d\overline{\sigma}_{11} = d\sigma_{11} - d\alpha_{11}$ according to Eq. (5.23).)

5.3.2.3 Kinematic Hardening Rules

5.3.2.3.1 General Comment

The two kinematic hardening rules considered in the formulations herein are those of Prager and Ziegler. The hardening rule in each case relates the increments in the coordinates of the yield surface center, $d\alpha_{ij}$, to the strain increments and the current states of stress and strain. These relations are used to substitute for $d\alpha_{ij}$ in the derivation of the nonlinear constitutive equations to be described in Section 5.3.2.4. The two kinematic hardening rules are discussed as follows.

5.3.2.3.2 Prager Hardening Rule

It is assumed herein that $d\alpha_{ij}$ depends linearly on $d\epsilon_{ij}^p$. Thus,

$$d\alpha_{ij} = C\, d\epsilon_{ij}^p \qquad \text{or} \qquad \alpha_{ij} = C\, \epsilon_{ij}^p \tag{5.47}$$

where C is the work-hardening constant, characteristic for a given material. By adopting the "associated flow rule," the Prager hardening rule is equivalent to the assumption that the vector $d\alpha_{ij}$ moves in the direction parallel to the normal vector on the yield surface at the current stress state. For a mixed-hardening material, $d\epsilon_{ij}^k$ replaces $d\epsilon_{ij}^p$ in Eq. (5.47) and it can be shown (Chen and Han 1988) that

$$\overline{H}_p = H_p = \frac{3}{2}C \tag{5.48}$$

Thus, for a mixed-hardening material with the Prager rule,

$$d\alpha_{ij} = \frac{2}{3} H_p \, d\varepsilon_{ij}^k = \frac{2}{3} H_p \, (1-M) \, d\varepsilon_{ij}^p \qquad (5.49)$$

5.3.2.3.3 Ziegler Hardening Rule

Ziegler (1959) modified the Prager hardening rule to make it valid for subspaces. He assumed that the transition of the yield surface occurs in the direction of the reduced stress vector in the form

$$d\alpha_{ij} = d\mu \, (\sigma_{ij} - \alpha_{ij}) \qquad (5.50)$$

where $d\mu$ is a positive proportionality factor, which depends on the history of the deformation. For simplicity, this factor can be assumed to have the form

$$d\mu = a \, d\varepsilon_p \qquad (5.51)$$

in which a is a positive constant characteristic for a given material. Thus,

$$d\alpha_{ij} = a \, d\varepsilon_p \, (\sigma_{ij} - \alpha_{ij}) \qquad (5.52)$$

For a mixed-hardening material, $d\bar{\varepsilon}_p$ replaces $d\varepsilon_p$ in Eq. (5.52) and it can be shown (Chen and Han 1988) that

$$\bar{H}_p = H_p = a \, \bar{\sigma}_e \qquad (5.53)$$

Thus, for a mixed-hardening material with the Ziegler rule, from Eqs. (5.53) and (5.36),

$$d\alpha_{ij} = \frac{H_p}{\bar{\sigma}_e} (1-M)(\sigma_{ij} - \alpha_{ij}) \qquad (5.54)$$

5.3.2.4 Generalization of Kinematic Constitutive Relationships

In this section, a nonlinear constitutive relationship for a mixed-hardening material is derived. This relates the stress and strain increments during elastic–plastic deformation.

Using the consistency condition, i.e., Eq. (5.30), for the yield function expressed in Eq. (5.43) gives

$$df = \frac{\partial f}{\partial \sigma_{ij}} d\sigma_{ij} + \frac{\partial f}{\partial \alpha_{ij}} d\alpha_{ij} + \frac{\partial f}{\partial \bar{\varepsilon}_p} d\bar{\varepsilon}_p = 0 \qquad (5.55)$$

In the following, each of the six terms in Eq. (5.55) is expressed in terms of the current stress and strain states, strain increments, and the scalar $d\lambda$. After the appropriate substitutions, Eq.(5.55) is solved for the scalar $d\lambda$. The constitutive relationship is then obtained by using the expression for $d\lambda$.

i) Expression for $\dfrac{\partial f}{\partial \sigma_{ij}}$

It can be shown that (Chen and Han 1988) that

$$\frac{\partial f}{\partial \sigma_{ij}} = 3\, \bar{S}_{ij} \qquad (5.56)$$

ii) Expression for $d\bar{\varepsilon}_p$

In order to determine $d\bar{\varepsilon}_p$, the term $d\varepsilon_{ij}^p$ is first obtained from Eq. (5.28) (i.e., the flow rule) and Eq. (5.56) as

$$d\varepsilon_{ij}^p = 3\, \bar{S}_{ij}\, d\lambda \qquad (5.57)$$

Equations (5.33), (5.40), and (5.57) yield $d\bar{\varepsilon}_p$ as

$$d\bar{\varepsilon}_p = 2\, M\, \bar{\sigma}_e\, d\lambda \qquad (5.58)$$

iii) Expression for $\dfrac{\partial f}{\partial \bar{\varepsilon}_p}$

To determine $\dfrac{\partial f}{\partial \bar{\varepsilon}_p}$, Eq. (5.43) is differentiated with respect to $\bar{\varepsilon}_p$.

$$\frac{\partial f}{\partial \bar{\varepsilon}_p} = -2\, \bar{\sigma}_e\, \frac{\partial \bar{\sigma}_e}{\partial \bar{\varepsilon}_p} = -2\, \bar{\sigma}_e\, \bar{H}_p \qquad (5.59)$$

From either Eq. (5.48) for the Prager kinematic hardening rule or Eq. (5.53) for the Ziegler kinematic hardening rule, $\overline{H}_p$ equals H_p. Hence,

$$\frac{\partial f}{\partial \overline{\epsilon}_p} = -2\,\overline{\sigma}_e\,H_p \qquad (5.60)$$

iv) Expression for $\dfrac{\partial f}{\partial \alpha_{ij}}$

The chain rule can be used to derive $\dfrac{\partial f}{\partial \alpha_{ij}}$, and, with the use of Eqs. (5.23) and (5.56),

as

$$\frac{\partial f}{\partial \alpha_{ij}} = \frac{\partial f}{\partial \overline{\sigma}_{kl}}\,\frac{\partial \overline{\sigma}_{kl}}{\partial \alpha_{ij}} = 3\,\overline{S}_{kl}\,(-\overline{S}_{ik}\,\delta_{jl}) \qquad (5.61)$$

where δ_{jl} is the Kronecker delta. Hence,

$$\frac{\partial f}{\partial \alpha_{ij}} = -3\,\overline{S}_{ij} \qquad (5.62)$$

v) Expression for $d\alpha_{ij}$

The term $d\alpha_{ij}$ for the Prager rule can be obtained from Eqs. (5.49) and (5.57) as

$$d\alpha_{ij} = 2\,H_p\,(1-M)\,\overline{S}_{ij}\,d\lambda \qquad (5.63)$$

For the Ziegler rule, $d\alpha_{ij}$ can be obtained from Eqs. (5.54) and (5.58) as

$$d\alpha_{ij} = 2\,H_p\,(1-M)\,\overline{\sigma}_{ij}\,d\lambda \qquad (5.64)$$

vi) Expression for $d\sigma_{ij}$

Finally, $d\sigma_{ij}$ is obtained from Eqs. (5.26) and (5.57) as

$$d\sigma_{ij} = C_{ijkl}\,(d\epsilon_{kl} - 3\,\overline{S}_{kl}\,d\lambda) \qquad (5.65)$$

Substituting Eqs. (5.56), (5.58), (5.60), (5.62), (5.63), and (5.65) into Eq. (5.55) and solving it for $d\lambda$ results in the following equation for a mixed-hardening material with the Prager rule as the kinematic hardening part.

$$dλ = \frac{3\,\overline{S}_{ij}\,C_{ijkl}\,dε_{kl}}{9\,\overline{S}_{ij}\,C_{ijkl}\,\overline{S}_{kl} + 4\,H_p\,\overline{σ}_e{}^2} \tag{5.66}$$

In order to obtain the result for a mixed-hardening material with the Ziegler rule as the kinematic hardening part, the same substitutions are to be made except that Eq. (5.64) is used instead of Eq. (5.63). This reduces to the same expression for dλ as in Eq. (5.66).

Substituting Eq. (5.66) back into Eq. (5.65) gives

$$dσ_{ij} = (C_{ijpq} - \frac{9\,C_{ijkl}\,\overline{S}_{kl}\,\overline{S}_{mn}\,C_{mnpq}}{9\,\overline{S}_{ij}\,C_{ijkl}\,\overline{S}_{kl} + 4\,H_p\,\overline{σ}_e{}^2})\,dε_{pq} \tag{5.67}$$

This is the constitutive relationship between the stress and strain increments in an elastic–plastic deformation.

By defining C^{*}_{ijpq} as the term in the brackets in Eq. (5.67), that is,

$$C^{*}_{ijpq} = C_{ijpq} - \frac{9\,C_{ijkl}\,\overline{S}_{kl}\,\overline{S}_{mn}\,C_{mnpq}}{9\,\overline{S}_{ij}\,C_{ijkl}\,\overline{S}_{kl} + 4\,H_p\,\overline{σ}_e{}^2} \tag{5.68}$$

Eq. (5.67) becomes

$$dσ_{ij} = C^{*}_{ijpq}\,dε_{pq} \tag{5.69}$$

in which, C^{*}_{ijpq} is called the *elastic–plastic constitutive tensor*.

5.3.2.5 Matrix Representation

The objective is to simplify the constitutive relationship, expressed by Eq. (5.67), for the special conditions of the problem under study. The result, expressed in matrix notation, has been implemented in the program PAPS, as discussed in Section 5.4.1.

It is taken herein that the subscripts 1, 2, and 3 are representative of longitudinal, circumferential, and through-thickness directions, respectively. These are also the principal axes for the stress and strain tensors at any point on the cross-section. Therefore, the stress and strain tensors are each represented by their three principal values.

Thus, in matrix notation, the stress and stress tensors could be represented by 3x1 vectors and the elastic constitutive tensor could be represented by a 3x3 matrix, $[E]$. Equation (5.66) is expressed in matrix notation as

$$d\lambda = \frac{3\{\overline{S}\}^T [E]\{d\varepsilon\}}{9\{\overline{S}\}^T [E]\{\overline{S}\} + 4\,H_p\,\overline{\sigma}_e^{\ 2}}$$

(5.70)

and Eq. (5.67) as

$$\{d\sigma\} = \left([E] - \frac{9[E]\{\overline{S}\}\{\overline{S}\}^T [E]}{9\{\overline{S}\}^T [E]\{\overline{S}\} + 4\,H_p\,\overline{\sigma}_e^{\ 2}}\right)\{d\varepsilon\}$$

(5.71)

where

$$\{d\sigma\} = \begin{Bmatrix} d\sigma_1 \\ d\sigma_2 \\ d\sigma_3 \end{Bmatrix} \qquad \{\overline{S}\} = \begin{Bmatrix} \overline{S}_1 \\ \overline{S}_2 \\ \overline{S}_3 \end{Bmatrix} \qquad \{d\varepsilon\} = \begin{Bmatrix} d\varepsilon_1 \\ d\varepsilon_2 \\ d\varepsilon_3 \end{Bmatrix}$$

(5.72)

Here, the principal stresses or strains are noted by a single subscript (e.g., $\overline{S}_2 = \overline{S}_{22}$ is the reduced deviatoric stress in circumferential direction). The elastic constitutive matrix, $[E]$, can be expressed as (Chen and Han 1988)

$$[E] = \begin{bmatrix} 2G + \lambda_E & \lambda_E & \lambda_E \\ \lambda_E & 2G + \lambda_E & \lambda_E \\ \lambda_E & \lambda_E & 2G + \lambda_E \end{bmatrix}$$

(5.73)

in which

$$G = \frac{E}{2(1+\mu)} \qquad \text{and} \qquad \lambda_E = \frac{\mu\,E}{(1+\mu)(1-2\mu)}$$

(5.74)

where E is the modulus of elasticity and μ is Poisson's ratio.

5.3.2.6 Two-Dimensional Analysis

As mentioned in Section 5.2.1, the through-thickness stress is neglected in the numerical model. This means that $d\sigma_3$ always equals zero. However, to be able to carry out the above calculations in two dimensions (i.e., longitudinal and circumferential directions), the yield function needs to be reduced to a two-dimensional form. The yield function in terms of the reduced stresses, rather than the reduced deviatoric stresses, can be expressed as

$$f = \frac{1}{2}\left[(\bar{\sigma}_1 - \bar{\sigma}_2)^2 + (\bar{\sigma}_2 - \bar{\sigma}_3)^2 + (\bar{\sigma}_3 - \bar{\sigma}_1)^2\right] - \bar{\sigma}_e^2 \qquad (5.75)$$

Recall from Eq. (5.23) that $\bar{\sigma}_i = \sigma_i - \alpha_i$. Thus, in order for Eqs. (5.70) and (5.71) to be two-dimensional and since σ_3 always equals zero, the value of α_3 should remain zero during plastification. (Note that the α_i terms are zero at the beginning of plastification.)

For the Prager kinematic hardening rule, $d\alpha_3$ is obtained from Eq. (5.63) as

$$d\alpha_3 = 2 H_p (1 - M) \bar{S}_3 \, d\lambda \qquad (5.76)$$

where $\bar{S}_3$ is, in general, nonzero. For the Ziegler kinematic hardening rule, $d\alpha_3$ is obtained from Eq. (5.64) as

$$d\alpha_3 = 2 H_p (1 - M)(\sigma_3 - \alpha_3) \, d\lambda \qquad (5.77)$$

in which σ_3 is always equal to zero and α_3 is initially zero. Therefore, α_3 remains zero throughout the elastic–plastic deformation. Thus, for a mixed-hardening material using the Ziegler rule the yield function becomes two-dimensional. However, when the Prager rule is used, the yield function remains three-dimensional. Note that in the case of the isotropic-hardening material (i.e., $M = 1$), the yield function is two-dimensional because all α_i terms (including α_3) are zero.

In order to carry out the calculations in Section 5.3.2.5 in two dimensions, the constitutive matrix, $[E]$, must be that for a plane stress situation ($\sigma_3 = 0$). Thus, in this case (Chen and Han 1988),

$$[E] = \begin{bmatrix} 2G + \lambda_E - Q & \lambda_E - Q \\ \lambda_E - Q & 2G + \lambda_E - Q \end{bmatrix} \qquad (5.78)$$

where

$$Q = \frac{\lambda_E^2}{2G + \lambda_E}$$

(5.79)

5.3.2.7 Loading Criterion

The objective is to determine the loading criterion to be used during the bending process. It is assumed that the stress state of an arbitrary point on the cross-section is on the yield surface, i.e., $f = 0$. A subsequent curvature increment in the numerical procedure increases the longitudinal strain at the point by an amount $\Delta\varepsilon_x$.

One possible state of deformation due to the longitudinal strain increment is elastic unloading. In this case, the longitudinal stress increment can be large enough to produce an elastic-plastic loading subsequent to the elastic unloading (i.e., by meeting the yield surface at a new point across from the initial stress state). Therefore, the criterion to be used herein must be able to detect the immediate state of deformation. This is carried out by assuming an infinitesimal increment in the longitudinal strain, $d\varepsilon_x$, in the same direction as the original longitudinal strain increment, $\Delta\varepsilon_x$. (Note that ε_x and ε_1 are used interchangeably herein.) This is accomplished if $\Delta\varepsilon_x$ and $d\varepsilon_x$ have the same sign. In addition, it is assumed tentatively that the deformation due to $d\varepsilon_x$ is elastic (i.e., either unloading or neutral loading).

If the actual deformation is elastic, the increment in yield function, df, due to the assumed elastic deformation will be non-positive. This is because, in an elastic deformation (loading or neutral loading), the stress state either moves inside or slides on the yield surface. This implies that $df \leq 0$.

However, if the actual deformation is elastic-plastic, df, which is due to the assumed elastic deformation, must be positive. This is because the yield surface is unchanged during the assumed elastic deformation. Thus, the resultant stress state ends up outside the original yield surface. This implies that $df > 0$.

Hence, the loading criterion can be expressed as

$$df \begin{cases} > 0, & \text{loading} \\ = 0, & \text{neutral loading} \\ < 0, & \text{unloading} \end{cases}$$ (5.80)

Equation (5.55) is used to evaluate df. As mentioned, the assumed deformation is elastic; thus, the plastic parameters such as α_{ij}, ε_{ij}^p, and $\bar{\varepsilon}_p$ remain unchanged. Therefore, $d\alpha_{ij}$ and $d\bar{\varepsilon}_p$ are zero in Eq. (5.55). Hence,

$$df = \frac{\partial f}{\partial \sigma_{ij}} d\sigma_{ij}$$ (5.81)

The through-thickness stress (σ_3) is small and can be neglected in this study. In addition, during bending the hoop stress (σ_2), which depends only on internal pressure, remains constant. Consequently, $d\sigma_1$ (= $d\sigma_x$) is the only nonzero stress component in Eq. (5.81). Thus,

$$df = \frac{\partial f}{\partial \sigma_1} d\sigma_1$$ (5.82)

The term $d\sigma_1$ (= $d\sigma_x$) is the stress increment due to the assumed elastic deformation. Therefore, it can be obtained by the use of elastic stress vs. strain relationships

$$\begin{Bmatrix} d\sigma_1 \\ 0 \\ 0 \end{Bmatrix} = [E] \begin{Bmatrix} d\varepsilon_1 \\ d\varepsilon_2 \\ d\varepsilon_3 \end{Bmatrix}$$ (5.83)

where $[E]$ is given by Eq. (5.73). Solving Eq. (5.83) for $d\sigma_1$ yields

$$d\sigma_1 = \zeta\, d\varepsilon_1 \qquad \text{or} \qquad d\sigma_x = \zeta\, d\varepsilon_x$$ (5.84)

in which

$$\zeta = \frac{4G(G + \lambda_E - Q)}{2G + \lambda_E - Q} > 0$$ (5.85)

The terms $\dfrac{\partial f}{\partial \sigma_1}$ and $d\sigma_1$ are substituted into Eq. (5.82) from Eqs. (5.56) and (5.84), respectively, to give

$$df = 3\zeta \, \overline{S}_1 \, d\varepsilon_1 = ? \quad d\varepsilon_x \qquad (5.86)$$

Here only the sign of df is of interest. Since ζ is a positive constant and $d\varepsilon_x$ has the same sign as $\Delta\varepsilon_x$, the criterion expressed in Eq. (5.80) can be rewritten as

$$\overline{S}_x \, \Delta\varepsilon_x \begin{cases} > 0, & \text{loading} \\ = 0, & \text{neutral loading} \\ < 0, & \text{unloading} \end{cases} \qquad (5.87)$$

Note that the result of the expression in Eq. (5.87) never comes exactly to zero in an actual calculation by computer. Therefore, in practical terms there are only two cases, loading and unloading.

In the case of loading, the entire deformation increment is elastic–plastic. In the case of unloading, however, it must be checked whether there is an elastic–plastic deformation following the initial elastic deformation. This is done by comparing the longitudinal strain increment, $\Delta\varepsilon_x$, with the strain increment value, $\Delta\varepsilon_x^*$, that moves the stress state onto the yield surface (onto a new point on the yield surface across from the initial stress state). If $|\Delta\varepsilon_x|$ exceeds $|\Delta\varepsilon_x^*|$, then there will be an elastic–plastic deformation subsequent to the elastic deformation with a longitudinal strain increment of $\Delta\varepsilon_x - \Delta\varepsilon_x^*$.

5.3.2.8 Forcing Increments to Satisfy Consistency Condition

The consistency condition of Eq. (5.55), df = 0, must be met in an elastic–plastic loading process. However, since many approximations are made in the numerical implementation of the incremental constitutive relation, the consistency condition is often only approximately satisfied. In other words, the stress does not stay on the subsequent yield surface. A correction to the stress vector is required to meet the yield condition and to prevent error accumulation. This can be achieved by adding a correction to the stress vector in the direction normal to the yield surface. The correction vector, $\{\delta\sigma\}$, can be expressed as (Chen and Han 1988)

$$\{\delta\sigma\} = \gamma \left\{ \frac{\partial f}{\partial \sigma} \right\}$$ (5.88)

where

$$\gamma = \frac{-f(\{\sigma\}, \varepsilon_p)}{\left\{ \frac{\partial f}{\partial \sigma} \right\}^T \left\{ \frac{\partial f}{\partial \sigma} \right\}}$$ (5.89)

By substituting for $\left\{ \frac{\partial f}{\partial \sigma} \right\}$ from Eq. (5.56), the correction vector becomes

$$\{\delta\sigma\} = \frac{-f\{\overline{S}\}}{3\{\overline{S}\}^T \{\overline{S}\}}$$ (5.90)

This can be further simplified by using the yield condition Eq. (5.43) as

$$\{\delta\sigma\} = \frac{-f}{2\overline{\sigma}_e^2} \{\overline{S}\}$$ (5.91)

5.3.3 Evaluation of Strain-Hardening Rules

Isotropic hardening is generally considered to be a suitable model for problems in which the plastic straining goes well beyond the incipient yield state where the Bauschinger effect is noticeable (Rice 1975). This hardening is therefore used for such applications as large motion dynamic problems and manufacturing process involving large plastic strain, and where the plastic strain rate does not reverse direction sharply (Hibbit et al. 1993a).

In cases involved low-amplitude strain cycling, it is important to model the Bauschinger effect. Kinematic hardening is the simplest theory that does this. The basic concept is that the yield surface shifts in the stress space so that straining in one direction reduces the yield stress in the opposite direction. Various levels of sophistication in the kinematic hardening model have been reported in the literature (Hibbit et al. 1993a). Two

of these kinematic hardening models, namely, the Prager and the Ziegler models have been used in this investigation as alternatives to isotropic hardening.

Since a nonlinear stress vs. strain curve from a coupon test will be passed on to the program, the hardening is nonlinear (more precisely, multilinear). In addition, large strains form in the process of bending the pipe. The kinematic hardening theory, however, is not a good material model for nonlinear work hardening and it is not recommended for large strain problems (Hibbit et al. 1993b). This gives rise to some disadvantages in the use of kinematic hardening as the work hardening model in this study.

In many problems, when the applied loads or displacements do not increase in proportion but vary in a more complex manner (for instance, oscillating between fixed or variable limits), the simple hypotheses of work hardening models are not sufficient to describe the plastic behavior. Thus, more general work hardening models have been introduced for these cases (Mroz 1969). However, since the loading procedure for the pipe under study is rather simple and non-cyclic, only the isotropic and kinematic hardening models have been used in this investigation. These hardening models are combined in a mixed hardening model that is described subsequently.

5.4 ANALYTICAL PROCEDURES

In this section, the procedure for obtaining the local moment vs. curvature response of a pipe is discussed first. Subsequently, in Section 5.4.2, a numerical model of the test specimens is described. This latter model uses the results of the first phase of the analysis (the analytical local moment curvature curves) to produce the global moment vs. curvature response of the pipe. The computer programs developed for the analysis, namely, PAPS and PDA, will be described in Section 5.5. The results of the numerical modeling for the test specimens will be presented and compared with the experimental results in Section 5.5.4.

5.4.1 Procedure to Obtain Local Moment vs. Curvature Response

The numerical model developed herein is based on the assumptions and formulation described in the preceding sections of this chapter. This formulation has been implemented in the computer program PAPS (Section 5.1). Appendices A and B contain the user manual and the listing of the program PAPS, respectively. The output of PAPS consists of the local moment vs. curvature response and the stress and strain values around

the cross-section of tle pipe throughout the loading. The loading sequence is similar to that for the test specimens: pressure is applied first, axial load is applied next, and finally the bending moment is applied. In the first and second stages of loading, the entire cross-section has uniform states of stress and strain. Upon bending, however, the cross-section is discretized into a number of elements to represent the variation in the stress and strain values around the section, as shown in Fig 5.4. Only one-half of the cross-section needs to be considered because of the symmetry about the plane of bending.

The following steps are carried out in order to obtain the local moment vs. curvature response of the pipe.

1. *Find the stage at which plastification begins.* This is done using the criteria developed in Section 5.2. If the initiation of plasticity occurs during the pressurization, *go to Step 1a.* If plastification begins during the application of axial load, *go to Step 1b.* If the initiation of plasticity occurs during bending, *go to Step 1c.*

1a. When the initiation of plasticity occurs during the pressurization, the values of longitudinal and hoop stress upon yielding are obtained from Eqs. (5.2) and (5.4), where the pressure, p, is determined from Eq. (5.6) ($p = p_0$) and the axial load, P, equals zero. The values of strains are simply calculated by the plane stress formulae. *Go to Step 2 of the algorithm.*

1b. When plastification begins during the application of axial load, the longitudinal and hoop stresses upon yielding are obtained from Eqs. (5.2) and (5.4), in which the pressure, p, is at the prescribed (final) value and the axial load, P_0, is determined from Eq. (5.7). The strain values are calculated by the plane stress formulae. *Go to Step 3 with $\overline{P} = P_0$.* Note that $\overline{P}$ is the initial axial load used in Step 3 of the algorithm.

1c. When the initiation of plasticity occurs during bending, the values of internal pressure and axial load are at their prescribed values (final values). The longitudinal stresses at the extreme compressive and tensile fibers upon yielding are obtained from Eqs. (5.15) and (5.17), respectively. The corresponding strain values are obtained from Eqs. (5.18) and (5.19), respectively. The assumption that the cross-section remains planar after deformation results in linear variations of

stresses and strains with the depth. By interpolation of the stress and strain values at the extreme tensile and compressive fibers, the stress and strain values for each element of the cross-section are determined. The moment at first yield, M_0, and the corresponding curvature, ϕ_0, are obtained from Eqs. (5.16) and (5.21), respectively. *Go to Step 4 with* $\overline{M} = M_0$ *and* $\overline{\phi} = \phi_0$. Note that $\overline{M}$ and $\overline{\phi}$ are the initial values of moment and curvature used in Step 4 of the algorithm.

2. *Increase the pressure from* p_0 *to the final value (prescribed)*. The pressurization is carried out in a prescribed number of equal pressure increments. From Eqs. (5.2) and (5.4), the longitudinal and hoop stress increments can be expressed as

$$\Delta\sigma_x = \frac{\Delta p\,R_i}{2\,t}(\frac{R_i}{R_m}) \tag{5.92}$$

$$\Delta\sigma_\theta = \frac{\Delta p\,R_i}{t} \tag{5.93}$$

where Δp is the pressure incre nt. For each pressure increment, the increment in strain values are calculated from Eq. (5.71), and all the stress and strain values as well as the effective plastic strain and the coordinates of the yield surface center are updated. These updated values are used for the next increment; thus, the constitutive equation (Eq. (5.71)) is updated at each increment. *Go to Step 3 with* $\overline{P} = 0$ *and* $\overline{\phi} = 0$.

3. *Increase the axial load from* $\overline{P}$ *to the final value (prescribed)*. The compression of the pipe is carried out in a prescribed number of equal increments of axial load. Since the pressure has already been applied, it is constant (at its final value) from the beginning. Therefore, the hoop stress increment is zero. Thus, the only stress increment is the longitudinal one, determined from Eq. (5.2) as

$$\Delta\sigma_x = -\frac{\Delta P}{2\pi R_m t} \tag{5.94}$$

where ΔP is the axial load increment. *Go to Step 4 with* $\overline{M} = 0$ *and* $\overline{\phi} = 0$.

4. *Increase the curvature from* $\overline{\phi}$ *to the prescribed value,* ϕ^*. Bending of the pipe is carried out in a prescribed number of equal curvature increments:

$$\Delta\phi = \frac{\phi^* - \bar{\phi}}{N_c}$$
(5.95)

where $\Delta\phi$ is the curvature increment and N_c is the prescribed number of curvature increments.

Note 1: Up to Step 4, all the calculations have been for the entire cross-section. At this step, however, because of the variation in stress and strain values due to bending, the cross-section is discretized into a prescribed number of elements (see Fig. 5.4). Each element will have a separate set of stresses, strains, effective plastic strain, and coordinates of the center of the yield surface. Also, up to bending, because the strains remain small, the three stress vs. strain measures lead to almost identical results. Therefore, prior to bending engineering stress vs. strain measures are used for convenience. In the process of bending, however, large membrane strains are produced. Therefore, all the calculations in Step 4 are carried out using the stress vs. strain formulation chosen for the analysis.

Note 2: Because the axial force of the pipe remains constant throughout bending, the neutral axis of bending (i.e., the axis with zero longitudinal bending strain) stays within the cross-section (see Fig. 5.4). However, the position of the bending neutral axis varies with increasing curvature and this requires an iterative procedure to locate the bending neutral axis. As shown in Fig. 5.4, the position of the bending neutral axis is located by the angle ψ_0. This angle is set to zero at the beginning of the iterations for the first curvature increment. Thereafter, the current position of the neutral axis is taken as the initial value for the next curvature increment. Each curvature increment is carried out according to the following procedure.

Go to Step 4.a

4a. *Set the position of the bending neutral axis.* As described above, if this is the first curvature increment, set the angle ψ_0 to zero; otherwise, set ψ_0 to the last position of the bending neutral axis. *Go to Step 4b.*

4b. *Calculate the engineering longitudinal strain of each element,* e, for the increased curvature by the following formula (see Appendix E, Eq. (E.32)).

$$e = e_0 + y(\phi + \Delta\phi)(1 + e_0) \tag{5.96}$$

where e_0 is the engineering longitudinal strain of the cross-section at the start of bending and y is the depth of the center of the element from the bending neutral axis, as shown in Fig. 5.4. This engineering strain is converted to logarithmic strain or Lagrangian strain, respectively, depending upon whether the UL or TL formulation has been selected. The conversion is carried out using the conversion formulae derived in Appendix E (Eqs. (E.8) and (E.9)). Next, the increment of the longitudinal strain of the element, $\Delta\varepsilon_x$, is obtained by subtracting the initial value of the strain (known at the beginning of the iteration) from the increased one. *Go to Step 4c.*

4c. *Examine the stress state of the element with respect to the yield surface.* The stress state at the beginning of the increment is known from the previous increment. If the initial stress state is plastic (i.e., on the yield surface), *go to Step 4c.1.* If the initial stress state is elastic (i.e., inside the yield surface), *go to Step 4c.2.*

4c.1. The loading criterion for an initial state of stress that is on the yield surface has been discussed in Section 5.3.2.7. The loading criterion expressed by Eq. (5.87) determines whether there is a loading or unloading condition due to the longitudinal strain increment, $\Delta\varepsilon_x$. In the case of loading, *go to Step 4d.1.* In the case of unloading, *go to Step 4d.2.*

4c.2. When the stress state is initially elastic, the deformation may be large enough to entail an elastic-plastic loading after the elastic loading. This is checked by comparing the longitudinal strain increment with the strain increment value that moves the stress state onto the yield surface in the same direction as the strain increment. Note that there are two possible directions, opposite to each other, that can be taken to reach the yield surface. The direction in which the stress state moves is determined by the sign of the longitudinal strain increment. *Go to step 4d.3.*

4d. *Solve the constitutive equations.*

4d.1. In the case of loading, Eq. (5.71) is solved for the three unknowns which are the longitudinal stress increment (the other two stress increments are zero), the hoop strain increment, and the through-thickness strain increment. If two-dimensional analysis is selected, the two unknowns are the longitudinal stress increment and the circumferential strain increment. *Go to Step 4e.*

4d.2. In the case of unloading, a check is carried out to determine whether an elastic–plastic loading follows the initial elastic deformation (as described in Section 5.3.2.7). The elastic part of the deformation is evaluated by the plane stress formulation and the elastic–plastic part, if any, is evaluated as described in Step 4d.1. *Go to Step 4e.*

4d.3. The elastic part of the deformation is evaluated by the plane stress formulation and the elastic–plastic part, if any, is evaluated as described in Step 4d.1. *Go to Step 4e.*

4e. *Calculate the axial force for the trial position of the bending neutral axis.* When Step 4d is carried out for all the elements, the axial force of the cross-section is calculated by integrating the longitudinal stress over the area of the cross-section.

If the difference between the calculated axial force, P_{cal}, and the prescribed axial force, P^*, is small enough to satisfy the following criterion

$$\frac{P^* - P_{cal}}{P^*} < \beta \tag{5.97}$$

where β is a prescribed tolerance, *then go to step 4e.1.* Otherwise, *go to step 4e.2.*

4e.1. When P_{cal} satisfies the criterion in Eq. (5.97), the trial position of the bending neutral axis is satisfactory. Thus, all the variables associated with each element (i.e., stress and strain components, effective plastic strain, and coordinates of the yield surface center) are updated using the last results. The loading moment is also calculated by integration to obtain the moment corresponding to the current curvature. At this point, the increment is complete. *Begin the next increment from Step 4a.*

4e.2. When P_{cal} does not satisfy the criterion in Eq. (5.97), the position of the presumed bending neutral axis is moved in a way that depends on the magnitude of P_{cal} compared with P^*. If P_{cal} is less than P^*, the actual bending neutral axis is located below the position assumed. Thus, the presumed bending neutral axis is shifted downward by adding a prescribed fraction of $\delta\psi$ to ψ_0 (see Fig. 5.4) and the Steps 4b to 4e are repeated. Similarly, if P_{cal} is greater than P^*, the presumed bending neutral axis will be moved upward by the angle $\delta\psi$. This procedure continues until the actual bending neutral axis is located within the current angle increment $\delta\psi$. This happens when the inequality in Eq. (5.97) changes direction (e.g., $P_{cal} < P^*$ but after adding $\delta\psi$ to ψ_0, $P_{cal} > P^*$). When the bending neutral axis is located within the angle $\delta\psi$, the bisection method is employed to close in on the actual bending neutral axis position until the criterion in Eq. (5.97) is satisfied. Upon satisfying this criterion, the calculations for the curvature increment are final and the variables associated with each element can be updated and the bending moment corresponding to the current curvature calculated. *Go to Step 4a for the next curvature increment.*

The set of moment and curvature values obtained by following Steps 1 to 4 of the above procedure constitutes a local moment vs. curvature curve for the prescribed constant values of axial force and internal pressure. Several examples of such curves are shown in Figs. 5.8 to 5.12. They will be discussed subsequently in Section 5.5.

5.4.2 Procedure to Obtain Global Moment vs. Curvature Response.

The objective is to develop a model simulating the behavior of the test specimens up to the softening point. This model uses the moment vs. curvature response of the cross-section, obtained by the procedure described in the Section 5.4.1, and performs a $P - \Delta$ analysis to obtain the global moment vs. curvature response of the pipe.

As shown in Fig. 5.5, because of symmetry, only one-half of the specimen needs to be modeled. A fixed support is assumed to be located at the mid-length of the pipe. The half-specimen is discretized into a prescribed number (N_{el}) of elements (Fig. 5.5). Because of the variation in moment and curvature along the specimen, each element is associated with a separate set of moment and curvature values and separate values for

slope and deflection. The quantities are evaluated at the mid-length of each element, and these are considered to be the average values for the element.

The analysis is carried out by prescribing a number of increments of the end moment, M_{end}. For each end moment increment, ΔM_{end}, the corresponding overall curvature is defined as $\theta_{end}/(L/2)$ and is obtained by the following procedure.

1. Add ΔM_{end} to the moment of each element.

$$M_k^{(1)} = M_k + \Delta M_{end} \tag{5.98}$$

Here M_k is the moment at the kth element (see Fig. 5.5), and $M_k^{(1)}$ is the updated value. *Go to Step 2.*

2. Find the curvature of each element corresponding to the new moment from the local moment vs. curvature curve. *Go to Step 3.*

3. Integrate the curvature along the pipe to find the slope of each element. *Go to Step 4.*

4. Integrate the slope along the pipe to find the deflection of each element. *Go to Step 5.*

5. Calculate the modified moment of each element considering the $P - \Delta$ effects. This is carried out by the following formula (see Section 3.2.5).

$$M_k^{(2)} = M_{end} + (P - P_i)y_k + P_i(\sin\theta_{end})\left[\frac{L}{2} - \left(k - \frac{1}{2}\right)\Delta x\right] - P_i(\Delta x)^2 \sum_{j=k+1}^{N_e} C_j(j - k) \tag{5.99}$$

where $M_k^{(2)}$ is the modified moment at the kth element, y_k is the updated deflection of the kth element, θ_{end} is the updated end slope, and C_j is the updated curvature of the jth element. *Go to Step 6.*

6. Check the convergence criterion

$$\frac{C_1^{(i)} - C_1^{(i-1)}}{C_1^{(i)}} < \beta_c \tag{5.100}$$

where $C_1^{(i-1)}$ and $C_1^{(i)}$ are the curvature values of the first element at the (i-1)th and ith iteration, respectively, and β_C is a prescribed tolerance. The curvature value and its variation at each iteration are maximum at the first element (closest to the support). Thus, the above criterion checks the greatest variation in curvature along the length of the pipe at the ith iteration.

If the criterion in Eq. (5.100) is not satisfied, further iteration is required; *go to Step 2*. If the criterion in Eq. (5.100) is satisfied, the solution has converged; *go to Step 7*.

7. Calculate the overall (i.e., global) curvature for the load increment as

$$\frac{\theta}{L} = \frac{2\,\theta_{end}}{L} \qquad (5.101)$$

Go to Step 1 for the next increment.

The set of end moment vs. global curvature values obtained using the above procedure simulates the response of a test specimen such as those described in Chapter 2. Comparisons between experimental and analytical results are shown in Figs. 5.20 to 5.25. These will be discussed subsequently, in Section 5.5.4.

5.5 NUMERICAL RESULTS

5.5.1. General

In the numerical analysis, the test specimens were modeled using their average geometric measures (with no imperfection taken into account) and material response (from tension coupon test). In modeling each test specimen, the same internal pressure and axial load as applied in the real test (tabulated in Table 2.1) were used.

The analysis was carried out in three phases. First the local moment vs. curvature responses of the 12-inch test specimens were developed using the program PAPS, which considers an infinitesimal length of pipe. For each 12-inch specimen, the local response was developed for formulations with different combinations of assumptions (i.e., stress vs. strain measures) and strain-hardening types (i.e., isotropic or kinematic hardening with the Prager or the Ziegler rule). The objective is to determine the most appropriate stress vs. strain formulation. These analyses are discussed in Section 5.5.2.

In the second phase of the analysis, PAPS was used to develop the local moment vs. response for all the test specimens. The analyses were carried out using the most appropriate stress vs. strain formulation, as was determined in the first phase of the analysis. Different types of strain-hardening (i.e., isotropic and kinematic hardening) were used in the analyses. These analyses are discussed in Section 5.5.3.

In the third phase of the analysis, the global responses of the test specimens were obtained using the program PDA. The local responses of the second phase were passed into the PDA program in order to develop the global moment vs. curvature responses of the test specimens. These analyses are discussed in Section 5.5.4.

5.5.2 Local Moment vs. Curvature Response for Different Formulations

5.5.2.1 General

In the first phase of the analysis, the program PAPS was used to obtain the local moment vs. curvature response of the 12-inch test specimens. Different types of stress vs. strain formulation (i.e., ESS, UL, and TL formulations, discussed in Section 5.3.1) were used in combination with different types of strain-hardening.

The material stress vs. strain curve that is input to the program is always in terms of engineering stress and strain. However, the program converts it into true stress vs. logarithmic strain for the UL formulation and into 2nd Piola-Kirchhoff stress vs. Lagrangian strain for the TL formulation. The material stress vs. strain curves are obtained from the tension coupon tests that were carried out for both 12-inch pipe (ERW Grade 359) and 20-inch pipe (DSAW Grade 386) as part of the 1992 experimental program (Mohareb et al. 1994). The results of the tension coupon tests, for the three types of stress vs. strain measures, are shown in Figs. 5.6 and 5.7 for 12 and 20-inch pipe, respectively. The engineering stress vs. strain data were converted to the other two stress vs. strain measures using the formulae derived in Appendix E.

Although the program PAPS is equipped with a mixed hardening model, only the limiting cc to for the model, namely, isotropic and kinematic hardening were used for the presentat.. . f results. This is because the intermediate states of mixed hardening would simply give response curves lying between those for isotropic and kinematic hardening. In the case of kinematic hardening, the use of the Prager and Ziegler rules always yielded results very close to each other. Therefore, the kinematic hardening results

are all presented in one category, with no distinction on the type of hardening rule employed.

In addition, it was observed that for the non-pressurized specimens the results of the isotropic and kinematic hardening with either the Prager or Ziegler rule were essentially identical. In other words, for the non-pressurized specimens, where there is a uniaxial state of stress (only longitudinal stress), the results are independent of the value of M (the mixed hardening index in Eq. (5.35)) and the kinematic hardening rule chosen. Therefore, no distinction as to the type of strain-hardening is made in the presentation of the results for the non-pressurized specimens.

For further confirmation, a third-party finite element program, namely, ABP (Analysis of Buried Pipelines) was employed in the first phase of analysis. This program was developed by Zhou and Murray (1993) at University of Alberta. The program ABP was used in a mode that does not consider buckling so that the results could be comparable with those from PAPS. The program ABP uses the ESS formulation and is capable of handling piecewise-linear strain-hardening using a mixed hardening model with the Ziegler rule for kinematic strain-hardening.

In order to determine the most appropriate stress vs. strain formulation, the results of the three different stress vs. strain measures for 12-inch pipe specimens are discussed in the following subsections.

5.5.2.2 Results for UGA12 and UGA12W

The local moment vs. curvature results from the PAPS and ABP analyses, in addition to the test results for specimens UGA12 and UGA12W, are shown in Fig. 5.8. It is evident that all the analytical and experimental curves lie close to each other in the region prior to softening induced by local buckling. However, the PAPS result with the UL formulation (true stress vs. strain measures) has the best fit to the test results. Furthermore, Fig. 5.8 shows that the ABP result is almost identical to the PAPS result with the ESS formulation (engineering stress vs. strain).

5.5.2.3 Results for HGA12 and HGA12W

The local moment vs. curvature results from the PAPS and ABP analyses and the test results for specimens HGA12 and HGA12W are shown in Figs. 5.9 and 5.10 for the

isotropic and kinematic hardening cases, respectively. In both Figures, the curves are similar. However, the PAPS results with the UL formulation show the best fit to the test results. In Fig. 5.9, the ABP curve lies very close to the PAPS curve with the ESS formulation. In Fig. 5.10, however, the ABP curve lies closer to the PAPS curve with the TL formulation (using 2nd Piola-Kirchhoff stress and Lagrangian strain measures).

5.5.2.4 Results for DGA12 and DGA12W

The local moment vs. curvature results from the PAPS and ABP analyses and the test results for specimens DGA12 and DGA12W are shown in Figs. 5.11 and 5.12 for the isotropic and kinematic hardening cases, respectively. As these figures show, the experimental curves for the plain and girth-welded specimens are not as close together prior to softening, as had been expected. However, the analytical curves in Fig. 5.11, modeled with isotropic hardening, agree well with the experimental results. In Fig. 5.12, on the other hand, the PAPS result, modeled with kinematic hardening, does not fit the experimental results properly. Nevertheless, the PAPS curve with the UL formulation is still the closest to the test results.

5.5.2.5 Conclusions from Local Moment vs. Curvature Results for 12-Inch Specimens

As was observed in Sections 5.5.2.2 and 5.5.2.3, the PAPS analysis using the UL formulation gave the closest fit of the three formulations to the experimental results. Moreover, there is a major theoretical advantage for the UL formulation over the ESS and TL formulations. As pointed out in Section 5.3.1, when true stress is plotted against logarithmic strain, tension, compression, and torsion test results coincide closely. However, when plotted in engineering stress vs. strain or 2nd Piola-Kirchhoff stress vs. Lagrangian strain measures, these coupon test curves diverge considerably at large strains. Figure 5.13 shows an example (Crandall and Dahl 1959) for which the tension and compression tests result in divergent curves if drawn in engineering stress vs. strain measures. However, the results of the same tension and compression tests coincide if they are plotted in true stress vs. strain terms.

In the program PAPS, the results of the tension tests are used for both tensile and compressive parts of the cross-section. Therefore, only the UL formulation handles the compressive part of the cross-section properly. As a result, only the PAPS results with the UL formulation are used in the subsequent presentations.

5.5.3 Local Moment vs. Curvature Response for Test Specimens Using Updated Lagrangian Formulation

5.5.3.1 General

In this second phase of the analysis, the program PAPS was used to develop the local moment vs. curvature response for each test specimen. The UL formulation, which was determined in Section 5.5.2.5 to be the most appropriate formulation, was used in these analyses. Two different strain-hardening models, i.e., the isotropic hardening and kinematic hardening models, were used to obtain the local responses of the test specimens.

5.5.3.2 Presentation of the Results

In the following, the results of the PAPS analyses with the UL formulation and using isotropic and kinematic hardening models are presented for the local response of the test specimens. The analytical results are compared with the experimental results of both plain and girth-welded specimens. Note that the experimental data for 20-inch plain specimens was not sufficient to obtain local moment vs. curvature response curves. However, the global responses of these specimens are available, and they will be compared with the results of the third phase of the analysis in Section 5.5.4.2.

UGA12 and UGA12W

The analytical and experimental curves for the local moment vs. curvature response of specimens UGA12 and UGA12W are shown in Fig. 5.14. It can be seen that the isotropic and kinematic hardening results are identical, and they agree well with the test results up to the softening point.

HGA12 and HGA12W

The analytical and experimental curves for the local moment vs. curvature response of specimens HGA12 and HGA12W are shown in Fig. 5.15. The isotropic and kinematic hardening results are close to each other and they agree with the test results up to the softening point.

DGA12 and DGA12W

The analytical and experimental curves for the local moment vs. curvature response of specimens DGA12 and DGA12W are shown in Fig. 5.16. It can be seen that the isotropic and kinematic hardening results do not agree with each other. Figure 5.16

shows that the isotropic hardening curve is higher than the kinematic hardening curve. Also, it is evident that the isotropic hardening curve is in better agreement with the test results than is the kinematic hardening curve.

UGA20W-2

The analytical and experimental curves for the local moment vs. curvature response of specimen UGA20W-2 are shown in Fig. 5.17, where it is seen that the isotropic and kinematic hardening results are identical. The reason that the experimental curve is shifted somewhat to the right is that it is a reloading response of the pipe after it was permanently bent at the beginning of the test (see Section 3.3.4). Nevertheless, if an imaginary loading response is extrapolated from the reloading response, the analytical curve seems to fit closely.

HGA20W

The analytical and experimental curves for the local moment vs. curvature response of specimen HGA20W are shown in Fig. 5.18. As shown, the isotropic and kinematic hardening results are close to each other and they are in reasonable agreement with the test results up to the softening point.

DGA20W

The analytical and experimental curves for the local moment vs. curvature response of specimen DGA20W are shown in Fig. 5.19. It is apparent that the isotropic hardening curve is considerably higher than the kinematic hardening curve. In addition, Fig. 5.19 shows that the isotropic hardening curve is in much better agreement with the test results than is the kinematic hardening curve. This issue is addressed in Section 5.5.3.3.

5.5.3.3 Conclusions from Local Moment vs. Curvature Curves

It is concluded from the observations in Section 5.5.3.2 that the PAPS results using the isotropic hardening model fit the test results satisfactorily. The isotropic and kinematic hardening results are identical for the non-pressurized specimens (Figs. 5.14 and 5.17). However, for the half-pressurized specimens, the isotropic and kinematic hardening results, though close to each other, are not identical (Figs. 5.15 and 5.18). This is because in the pressurized pipes the state of stress is biaxial, whereas for the non-pressurized pipes a uniaxial state of stress exists.

For the fully-pressurized specimens, the kinematic hardening model gives a significantly lower response than do the experimental and isotropic hardening results (Figs. 5.16 and 5.19). This is because the fully-pressurized specimens plastify due to the internal pressure alone, and, by applying the axial load, the entire cross-section is subjected to compressive yielding. When bending is superimposed, a portion of the cross-section is unloaded elastically and undergoes tensile yielding. In these situations where reverse loading occurs, the isotropic and kinematic hardening models respond quite differently. This is because in the isotropic hardening model the yield surface expands as elastic-plastic loading progresses. In the kinematic hardening model, however, the yield surface preserves its size and only translates due to elastic-plastic loading. Under the reverse loading that occurs in the fully-pressurized specimens, the stress state moves inside the yield surface to meet the surface at a different region. Thus, the subsequent stress state at yield could be quite different in the two models.

The kinematic hardening model was created to handle the reverse loading situations. Thus, it is paradoxical that for the reverse loadings in this investigation, the kinematic hardening model does not give good results. In conclusion, while the isotropic hardening model performs satisfactorily, in this study the kinematic hardening model has proved to be unreliable.

5.5.4 Numerical Results for Global Response of Test Specimens

5.5.4.1 General

In this third phase of the analysis, the global moment vs. curvature responses of the test specimens are predicted up to the softening point. This is carried out by the PDA program using the local responses of phase two, obtained from the PAPS output. Although obtaining the analytical global response requires a second process, the situation is the reverse of that required in obtaining the experimental global response. Analytically, the local response is determined directly and the global response is derived from it. However, experimentally, the global response is determined directly and the local response is derived from it (see Section 3.2.5.2).

Because of insufficient test data for 20-inch plain specimens (Mohareb et al. 1994), the experimental local moment vs. curvature responses could not be obtained for comparison with the analytical predictions. Nevertheless, the experimental global

responses of the 20-inch plain pipes are available (presented in Chapter 3), and they are compared with their analytical counterparts in the following section.

5.5.4.2 Presentation of Results for Test Specimens

The analytical global moment vs. curvature curves presented herein are the outputs of the program PDA. They have been obtained by using the PAPS local moment vs. curvature results of Section 5.5.3 as input. The local moment vs. curvature results presented herein are those obtained by the UL formulation (the best formulation) and both the isotropic and the kinematic strain-hardening models. In the following, the analytical and experimental results for the global response of the test specimens are presented. In the plots to be presented, the moment value is the average of the two end moments and the curvature is the relative rotation of the specimen ends divided by the specimen length.

UGA12 and UGA12W

The analytical and experimental curves for the global moment vs. curvature response of specimens UGA12 and UGA12W are shown in Fig. 5.20. The isotropic and kinematic hardening results are identical and they agree with the test results up to the softening point.

HGA12 and HGA12W

The analytical and experimental curves for the global moment vs. curvature response of specimens HGA12 and HGA12W are shown in Fig. 5.21. The isotropic and kinematic hardening results are close to each other and they agree with the test results up to the softening point.

DGA12 and DGA12W

The analytical and experimental curves for the global moment vs. curvature response of specimens DGA12 and DGA12W are shown in Fig. 5.22. As can be seen, the isotropic and kinematic hardening results are not in good agreement with each other. Also, it can be seen in Fig. 5.22 that the isotropic hardening curve is in good agreement with the experimental curves but the kinematic hardening curve is noticeably lower than both the experimental curves.

UGA20 and UGA20W-2

The analytical and experimental curves for the global moment vs. curvature response of specimens UGA20 and UGA20W-2 are shown in Fig. 5.23, where it is seen that the isotropic and kinematic hardening results are identical. The good agreement between the analytical curve and the experimental curve for UGA20 is evident in Fig. 5.23. The reason that the experimental curve for UGA20W-2 has shifted somewhat to the right is that it is a reloading response of the pipe after being permanently bent at the beginning of the test.

HGA20W

The analytical and experimental curves for the global moment vs. curvature response of specimen HGA20W are shown in Fig. 5.24. The isotropic and kinematic hardening results are in close agreement, and they are in reasonable agreement with the test result up to the softening point.

DGA20 and DGA20W

The analytical and experimental curves for the global moment vs. curvature response of specimens DGA20 and DGA20W are shown in Fig. 5.25. It can be seen that the isotropic hardening curve is considerably higher than the kinematic hardening curve. As was the case in Fig. 5.19, Fig. 5.25 shows that the isotropic hardening curve is in much better agreement with the test results than is the kinematic hardening curve.

5.5.4.3 Conclusion

It can be concluded from the observations in Section 5.5.4.2 that the analytical results using the isotropic hardening model fit the test results satisfactorily. The isotropic and kinematic hardening results are identical for the n-pressurized specimens (Figs. 5.20 and 5.23). However, for the half-pressurized specimens, the isotropic and kinematic hardening results are not identical, though they are close to each other (Figs. 5.21 and 5.24). For the fully-pressurized specimens, the kinematic hardening model gives a significantly lower response than do the experimental and isotropic hardening results (Figs. 5.22 and 5.25).

These observations are similar to those for the local moment vs. curvature responses of the specimens. This is because the analytical local moment vs. curvature response (PAPS output) is used by the PDA program to obtain the global response.

Because of the poor performance of the kinematic hardening model for the global response of the fully-pressurized specimens, it is not recommended for use herein. The UL formulation with the isotropic hardening model appears to be the most appropriate for the analysis of line pipe under combined loadings.
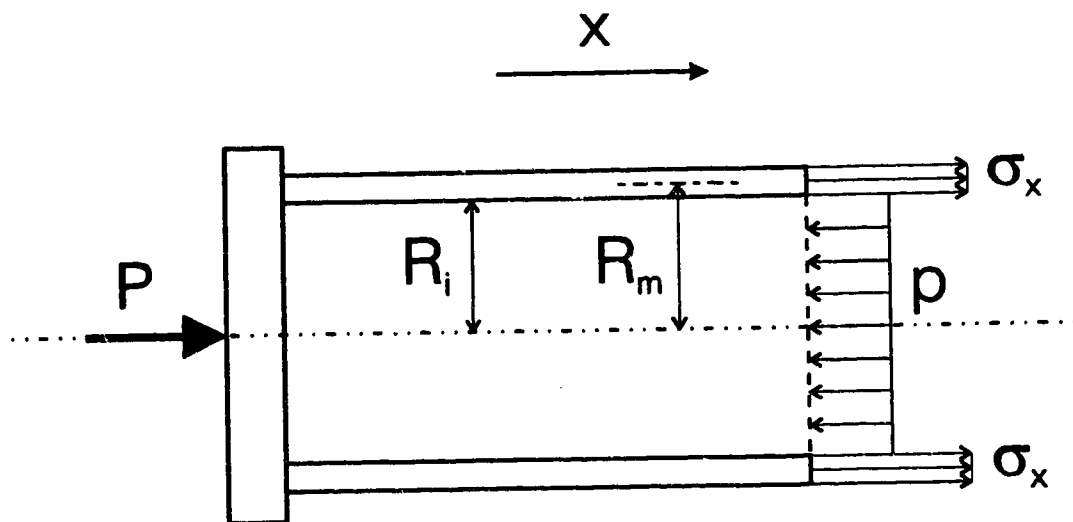
Fig. 5.1 Free body diagram of end segment
of test specimen
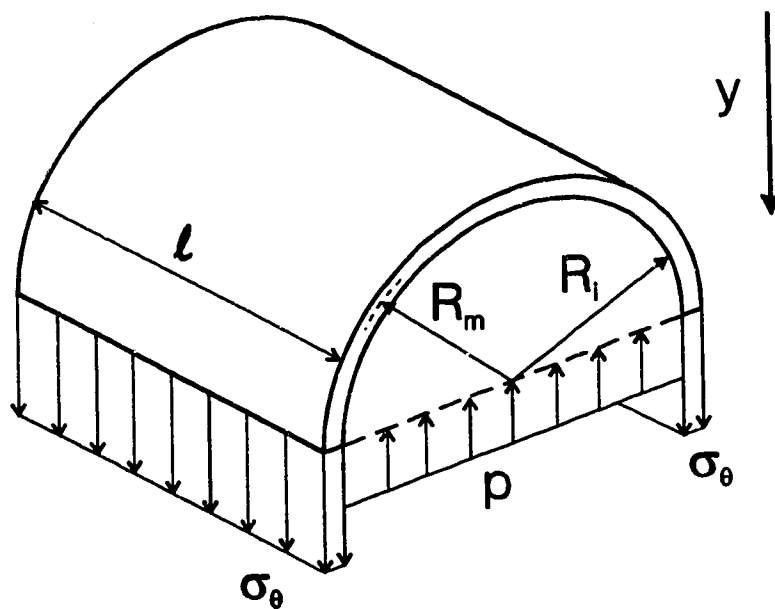
Fig. 5.2 Free body diagram of a half-cylindrical
portion of test specimen

Fig. 5.3 von Mises yield criterion in two dimensions

Fig. 5.4 Cross-section lay-out in program PAPS
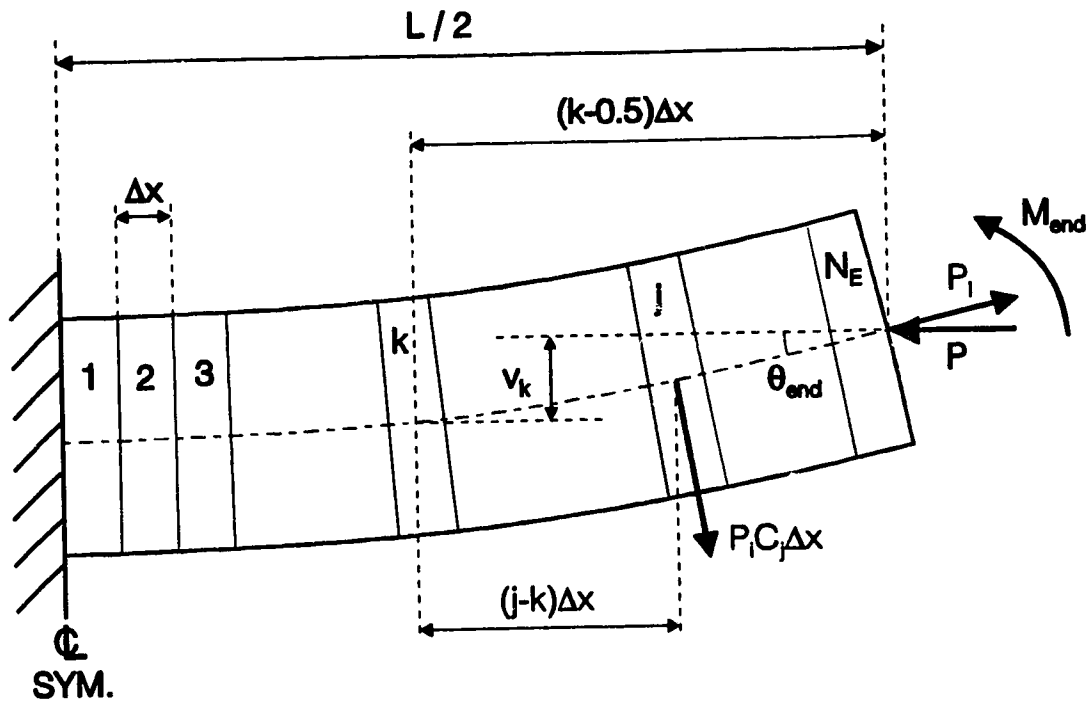
Element numbering: 1, 2, 3, ..., k, ..., j, ..., N_E

Fig. 5.5 Half-specimen lay-out in program PDA
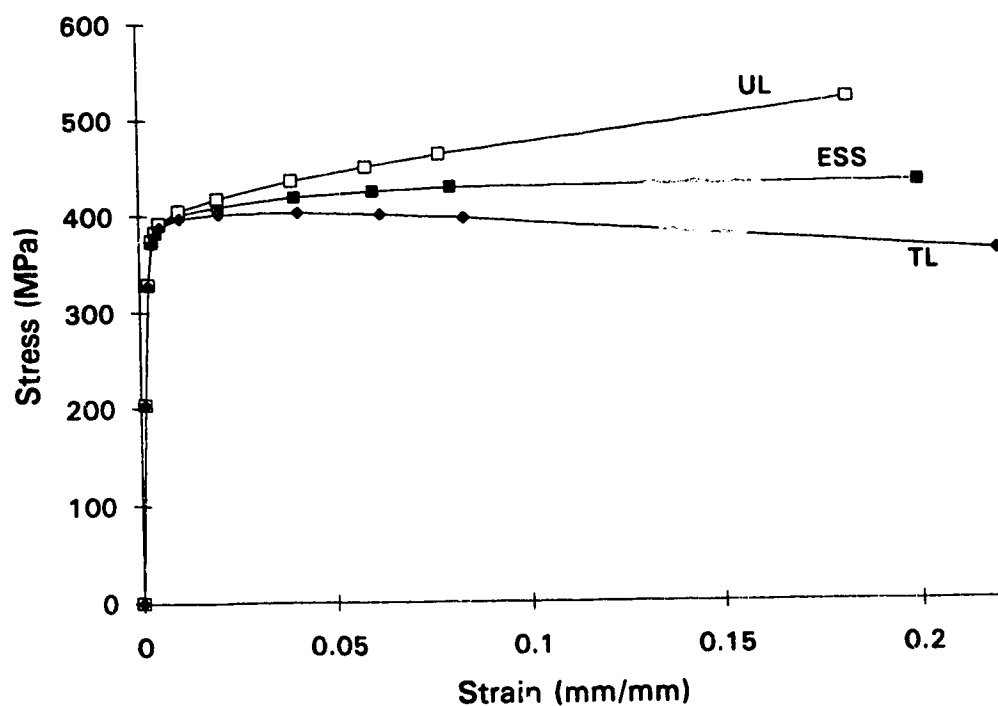
Fig. 5.6 Tension coupon test results for 12-inch pipe (ERW Grade 359)
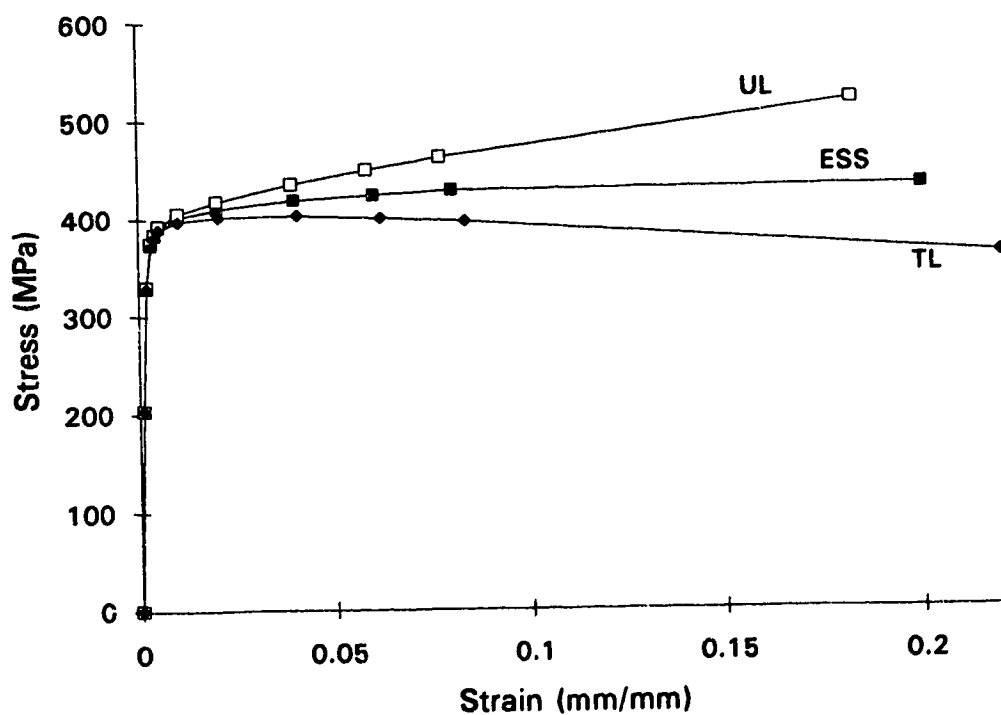
Fig. 5.7 Tension coupon test results for 20-inch pipe (DSAW Grade 386)
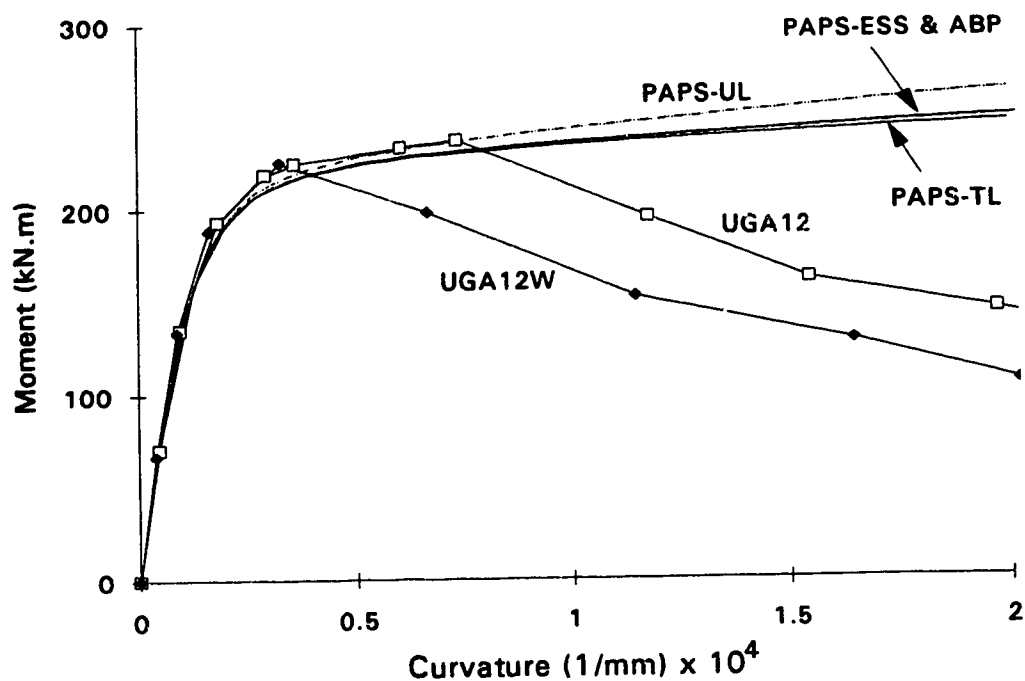
Fig. 5.8 Experimental and analytical local moment vs. curvature responses for UGA12
and UGA12W (PAPS results with different formulations)
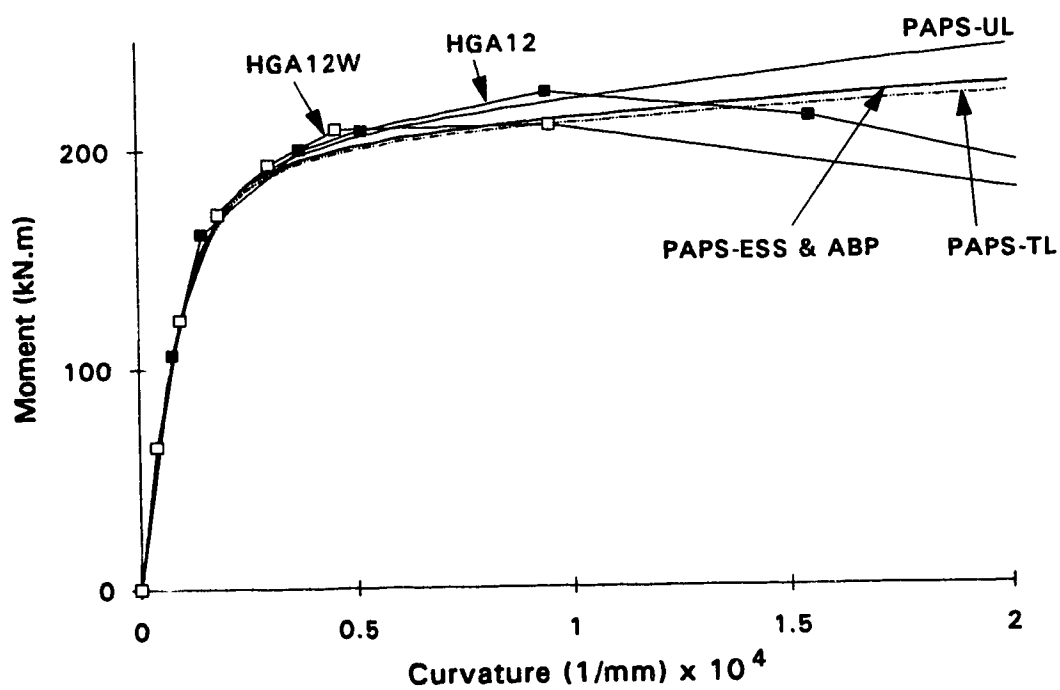
Fig. 5.9 Experimental and analytical local moment vs. curvature responses for HGA12
and HGA12W using isotropic hardening (PAPS results with different formulations)
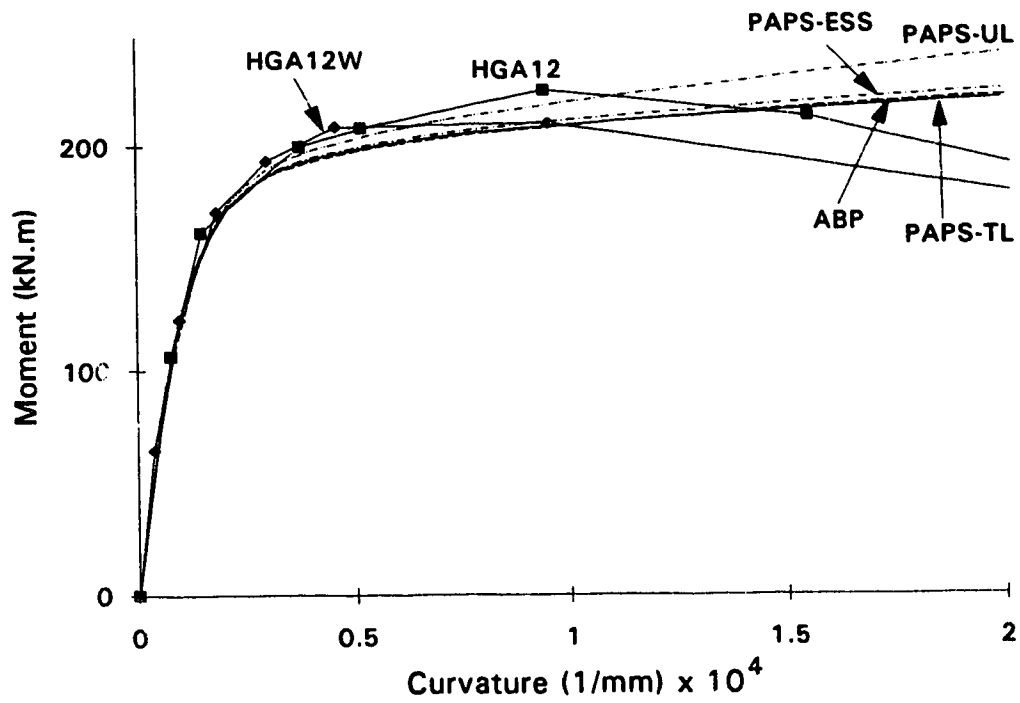
Fig. 5.10 Experimental and analytical local moment vs. curvature responses for HGA12
and HGA12W using kinematic hardening (PAPS results with different formulations)
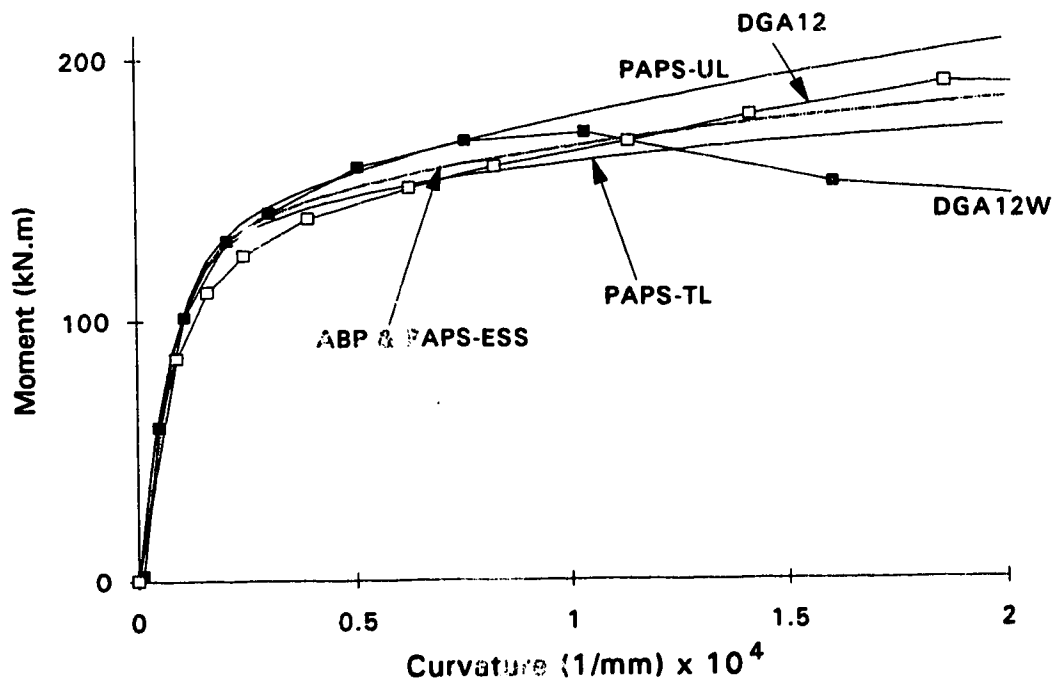
Fig. 5.11 Experimental and analytical local moment vs. curvature responses for DGA12
and DGA12W using isotropic hardening (PAPS results with different formulations)
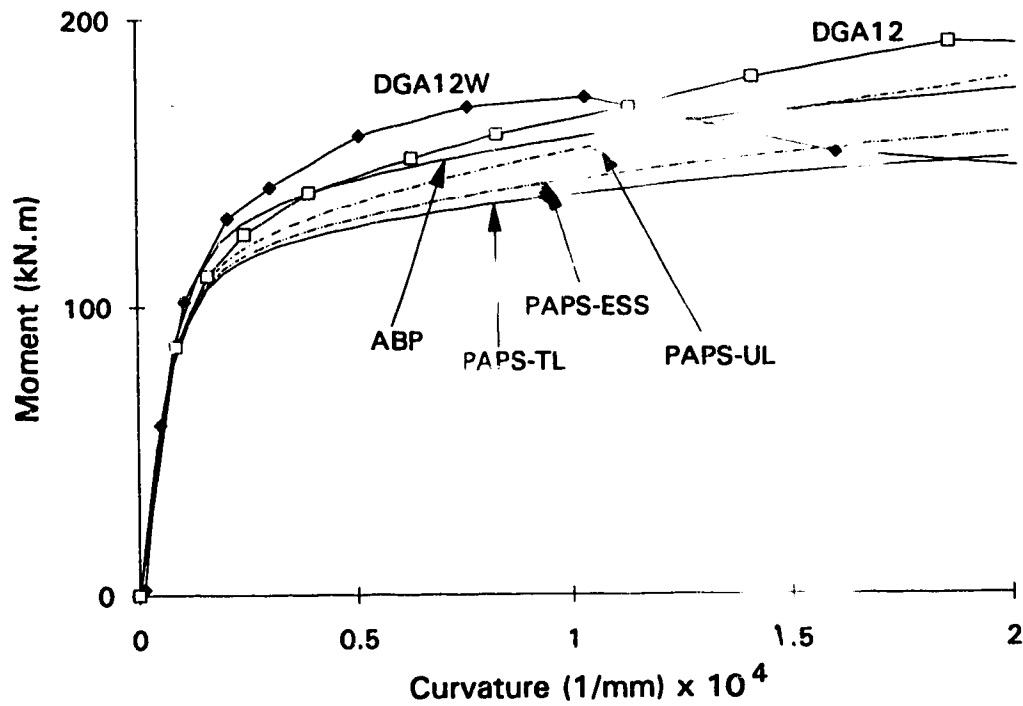
Fig. 5.12 Experimental and analytical local moment vs. curvature responses for DGA12 and DGA12W using kinematic hardening (PAPS results with different formulations)
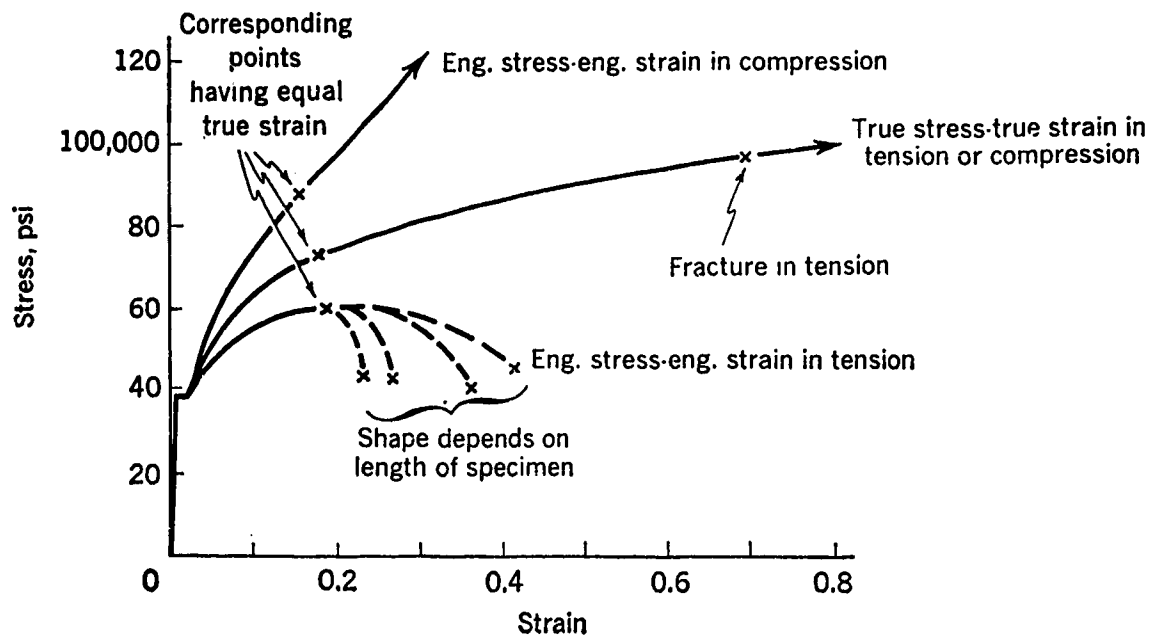
Fig. 5.13 Stress vs. strain curves for hot-rolled low-carbon steel (1020 HR) (*adapted from Crandall and Dahl, 1959*)
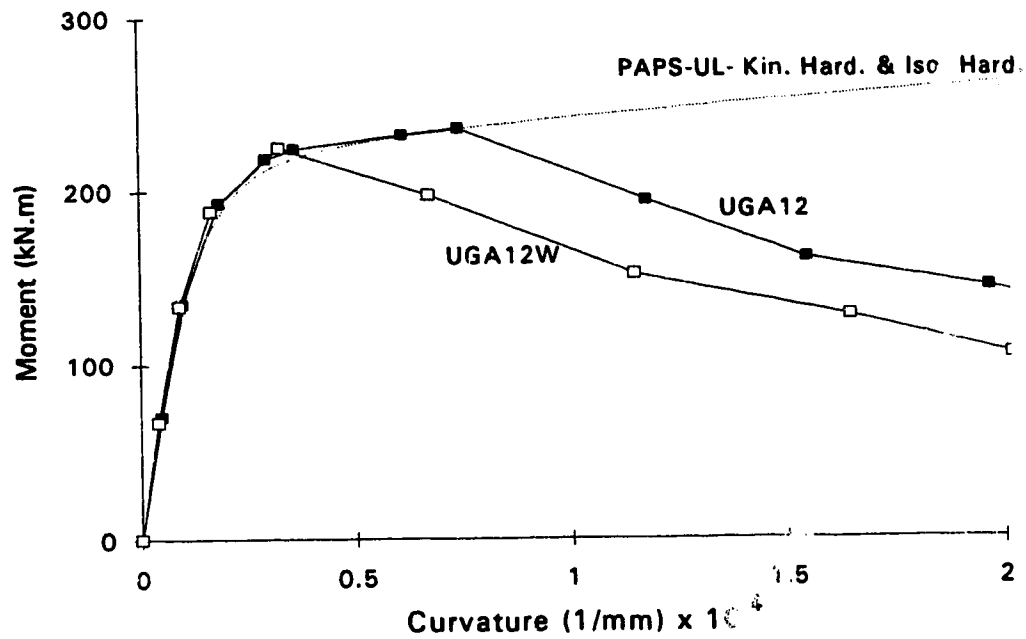
Fig. 5.14 Experimental and analytical local moment vs. curvature responses for UGA12 and UGA12W
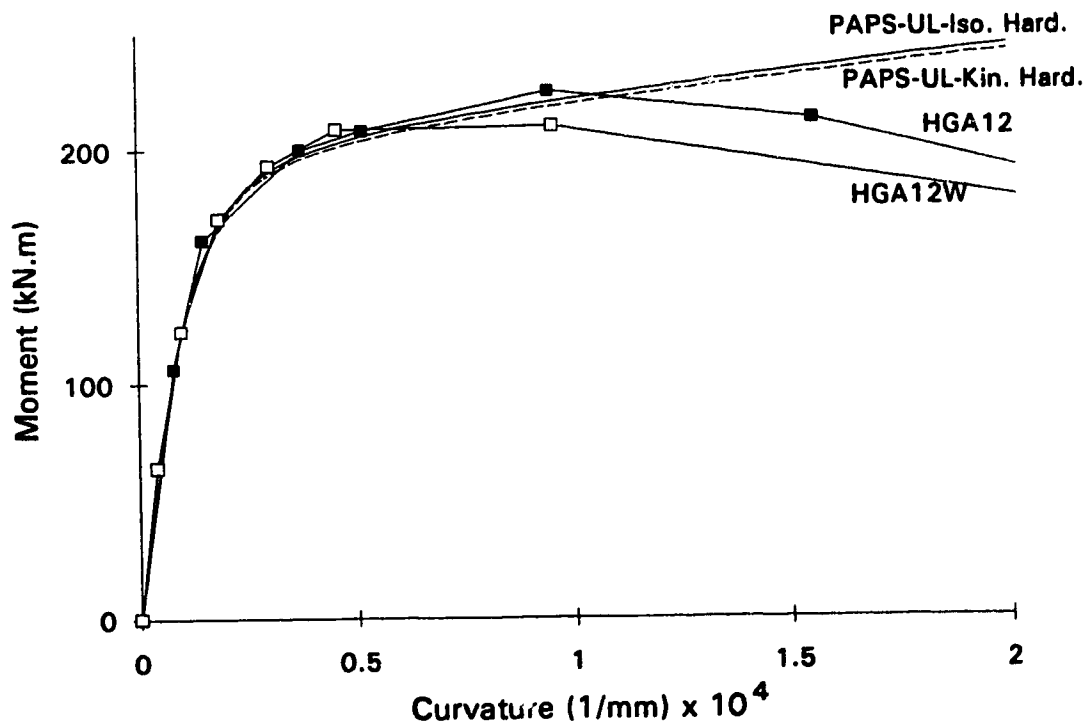
Fig. 5 5 Experimental and analytical local moment vs. curvature responses for HGA12 and HGA12W
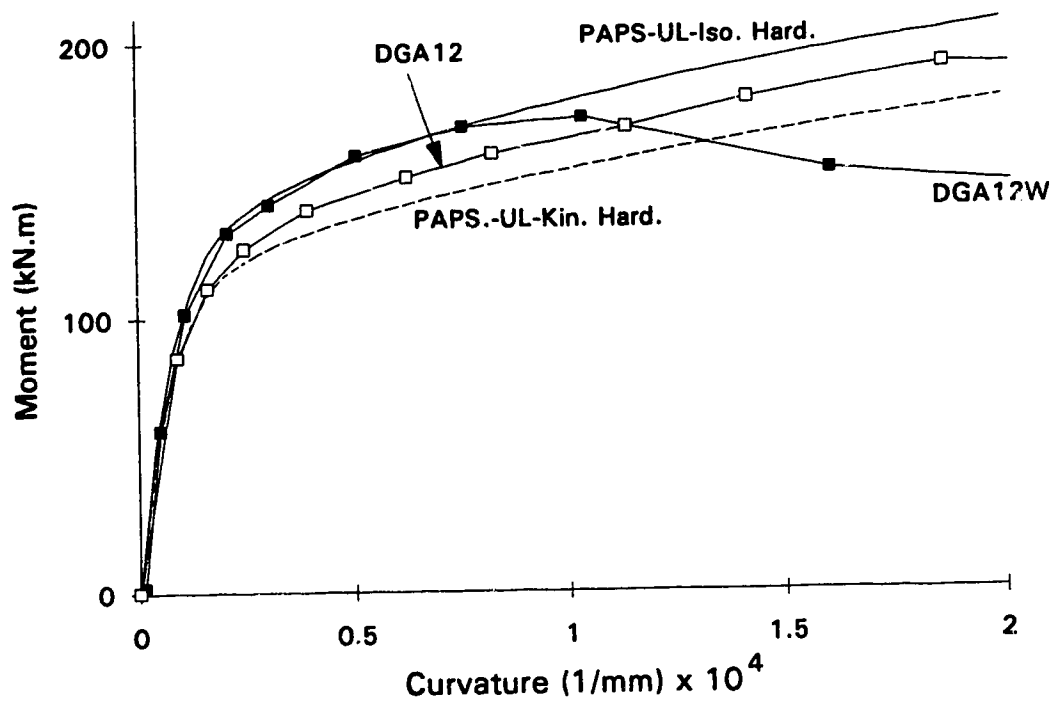
Fig. 5.16 Experimental and analytical local moment vs. curvature responses for DGA12
and DGA12W
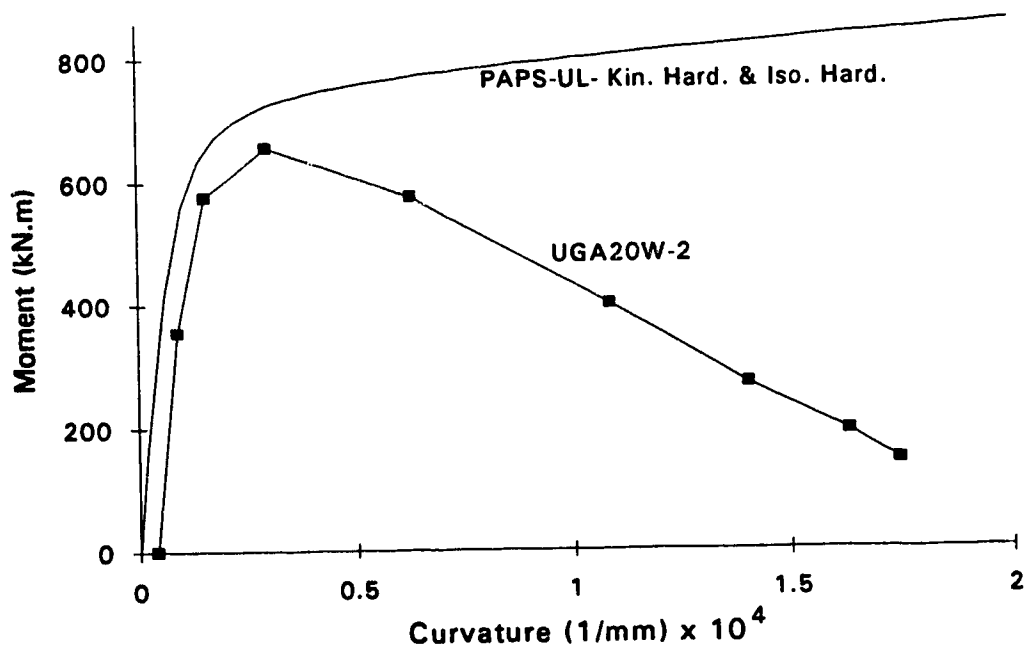
Fig. 5.17 Experimental and analytical local moment vs. curvature responses for
UCA20W-2
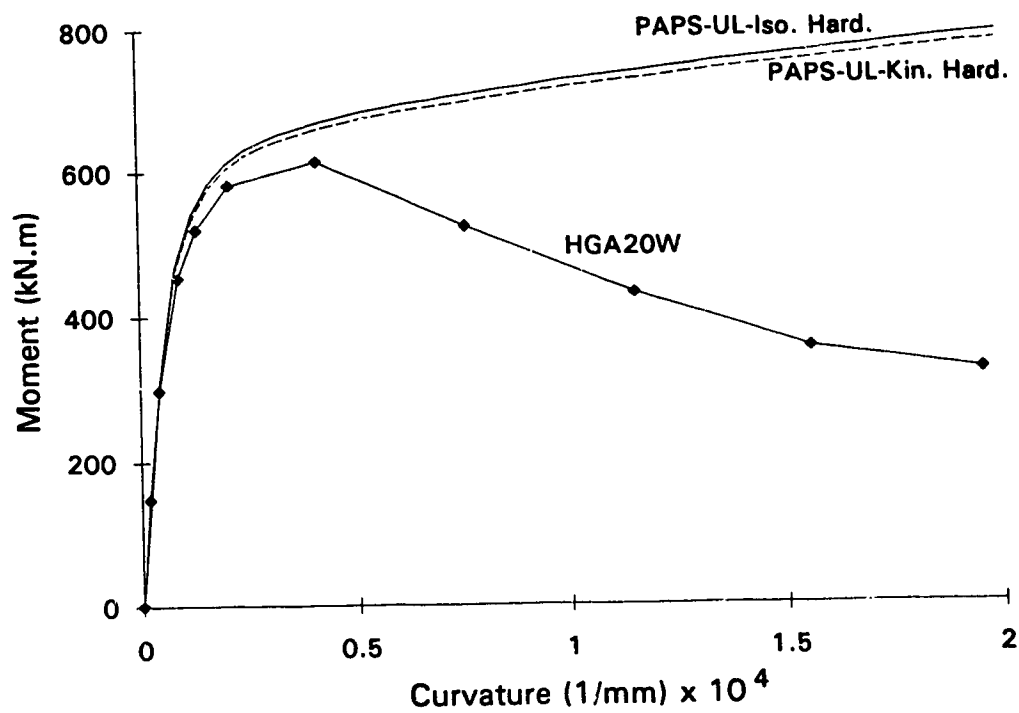
Fig. 5.18 Experimental and analytical local moment vs. curvature responses for HGA20W
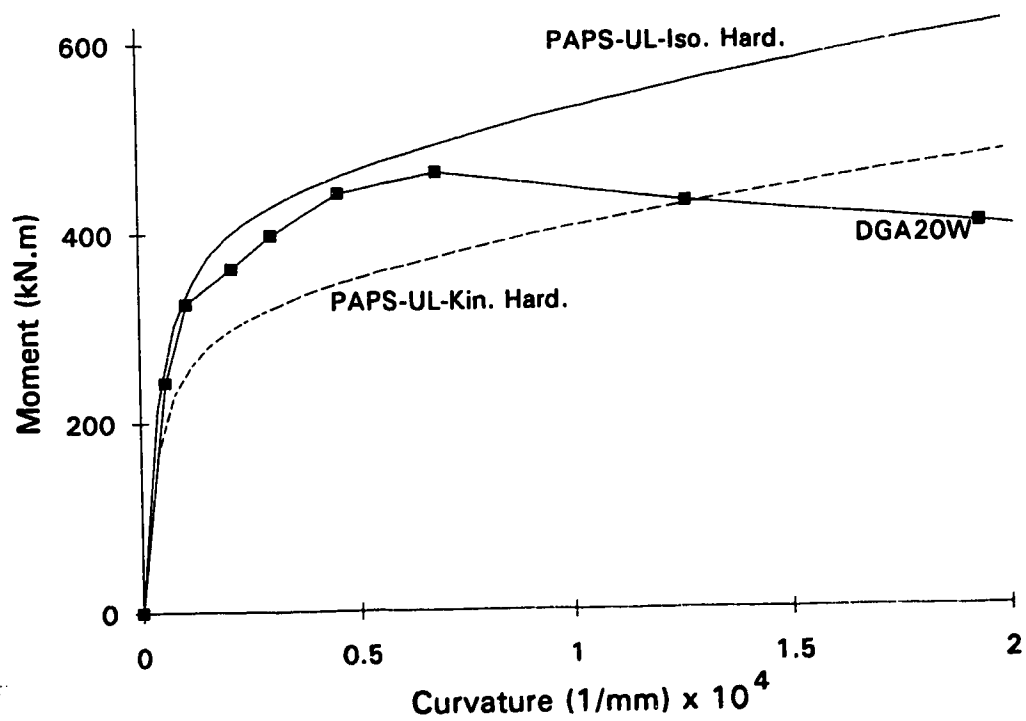
Fig. 5.19 Experimental and analytical local moment vs. curvature responses for DGA20W
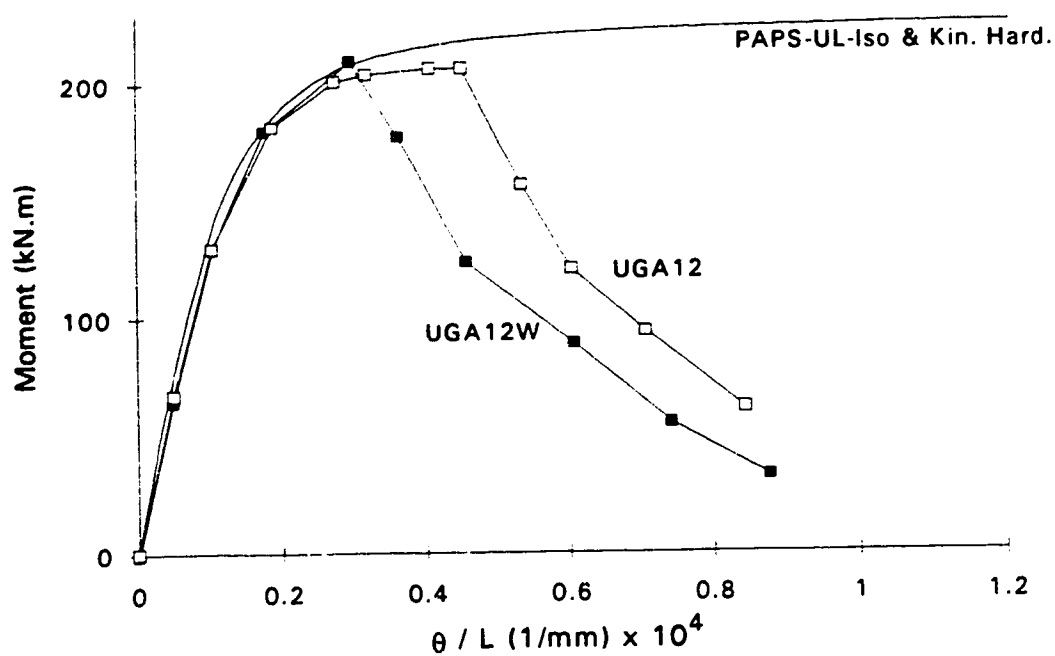
Fig. 5.20 Experimental and analytical global moment vs. curvature responses for UGA12 and UGA12W
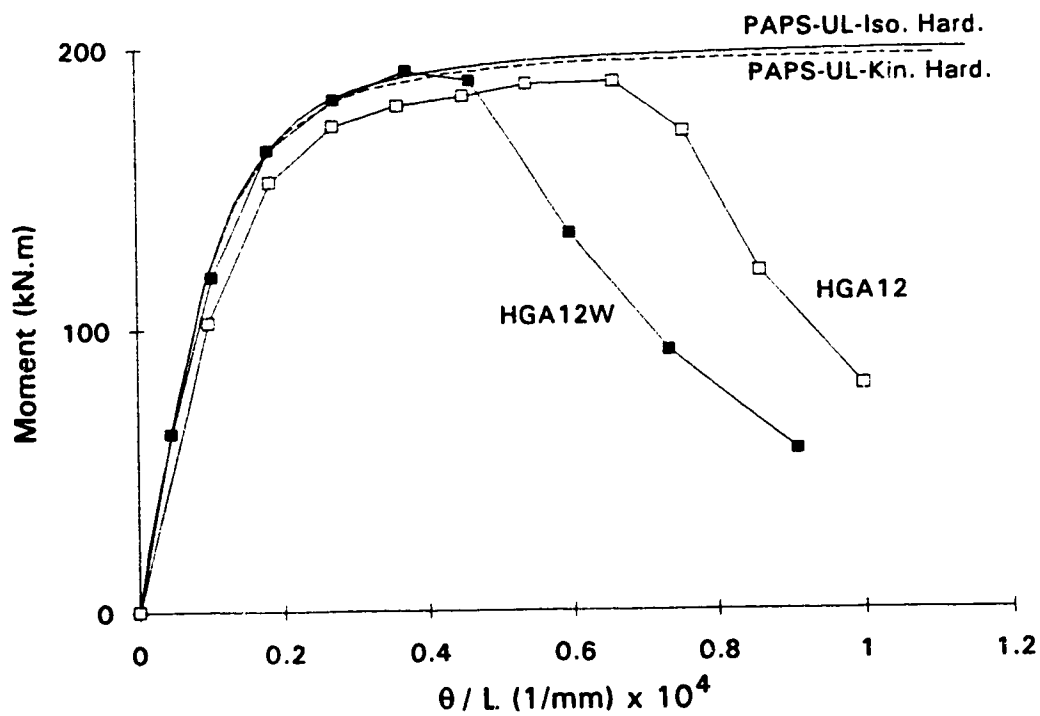
Fig. 5.21 Experimental and analytical global moment vs. curvature responses for HGA12 and HGA12W
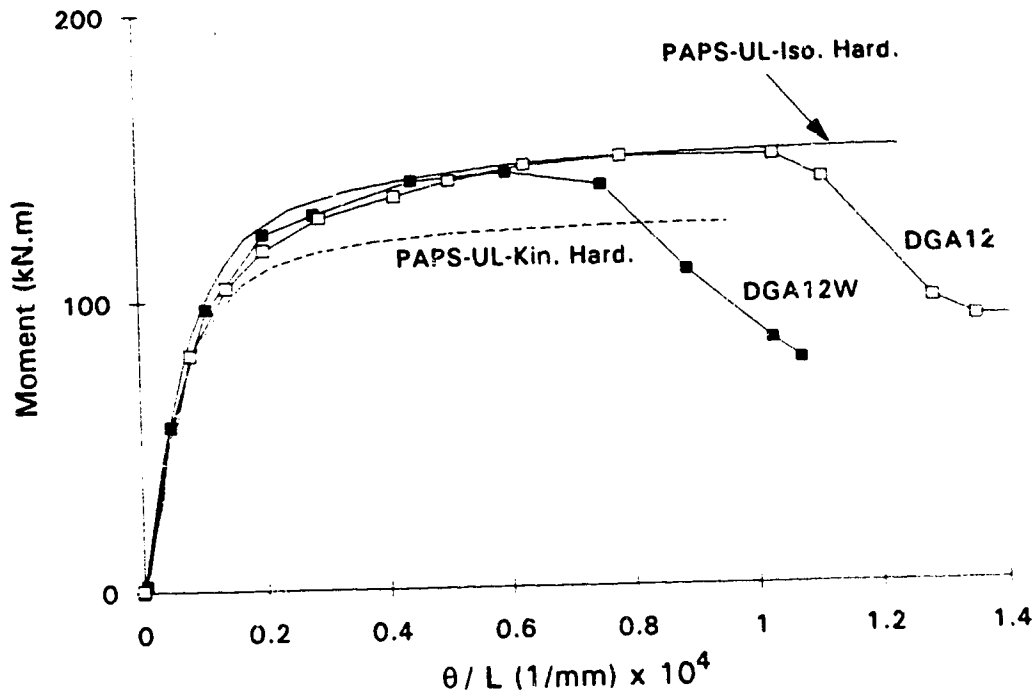
Fig. 5.22 Experimental and analytical global moment vs. curvature responses for DGA12 and DGA12W
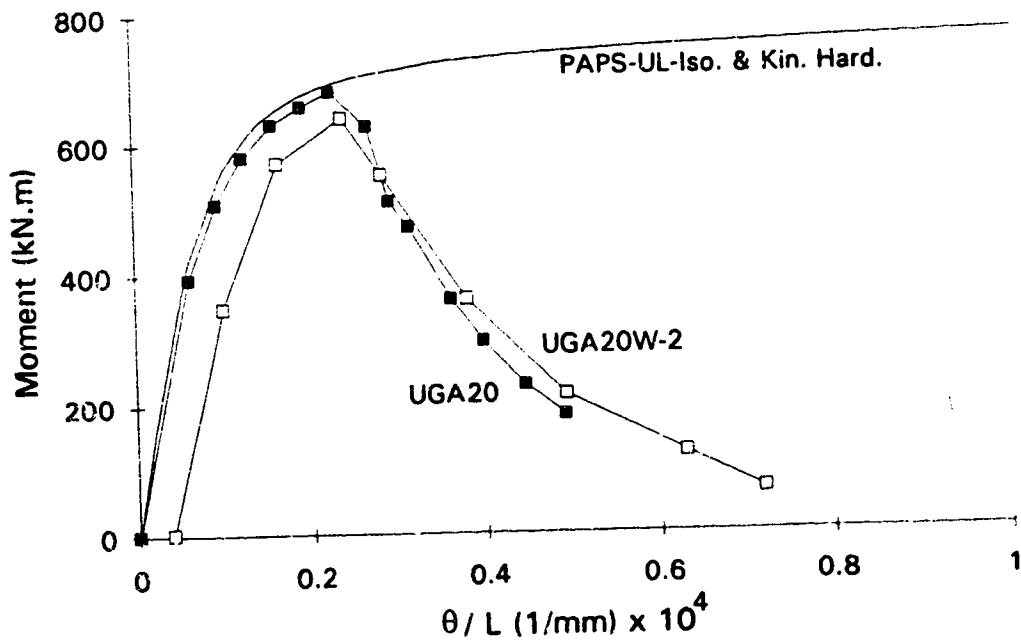
Fig. 5.23 Experimental and analytical global moment vs. curvature responses for UGA20 and UGA20W-2
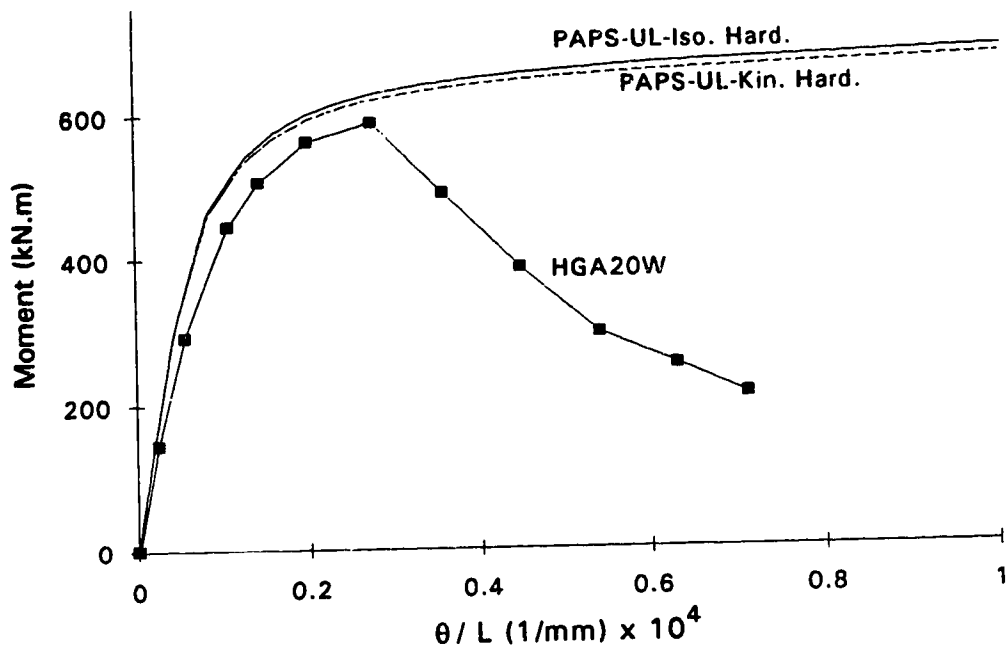
Fig. 5.24 Experimental and analytical global moment vs. curvature responses for
HGA20W
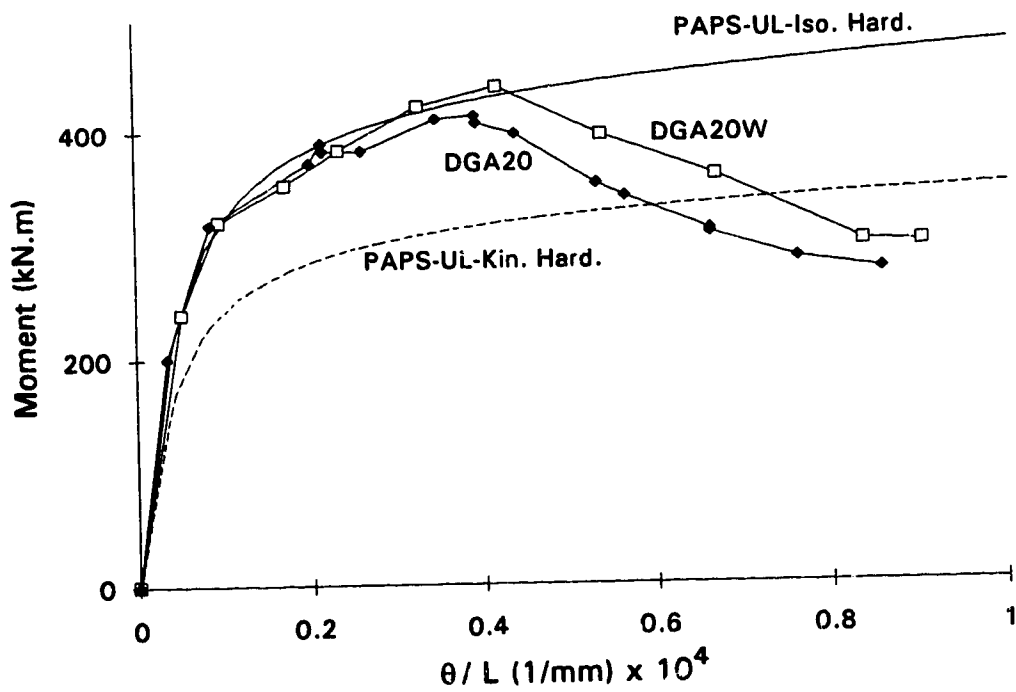
Fig. 5.25 Experimental and analytical global moment vs. curvature responses for DGA20
and DGA20W

6 SUMMARY AND RECOMMENDATIONS

6.1 SUMMARY AND CONCLUSIONS

The main objective of this work was to establish an experimental data base that describes the structural response of girth-welded pipes. To that end, a series of tests were carried out on seven girth-welded line pipe specimens. Four of the specimens had a diameter of 20 in. (508 mm) and a D/t ratio of 63. The other three had a diameter of 12.75 in. (324 mm) and a D/t ratio of 50. All specimens were 1.69 m long and contained girth welds at their mid-length. The specimens were subjected to constant internal pressure, constant axial load, and monotonically increasing curvature. The latter two loadings simulated the thermal and differential settlement effects. The experimental results consisted of the load vs. rotation response, plots of strain and displacement profiles along the extreme tensile and compressive fibers, and plots of curvature along the length of each specimen.

Ovalization was found to be of no significance in the tests. Non-pressurized specimens wrinkled suddenly in a diamond shape (inward wrinkle), and no other wave or distortion was observed at locations other than in the wrinkled segment. In the case of pressurized specimens, the wrinkle formed as a single outward bulge. This was initially one of the four waves, or ripples, that could be detected by close visual examination. All of the specimens began to soften when the wrinkles became visible.

The strain localization began slowly at the initiation of softening and intensified rapidly thereafter. For non-pressurized pipes, the initiation of buckling coincided with the initiation of wrinkling (softening). However, for pressurized pipes, the buckling waves appeared on the intrados of the pipe well before the wrinkling (softening) occurred. In addition, local deformations remained contained and relatively small prior to wrinkling. Thus, it was decided that the compressive strain at the softening point is a better measure for limiting compressive strain than is the compressive strain at the onset of buckling. These observations agree, in general, with those for the plain pipes reported by Mohareb et al. (1994). Empirical equations for critical strain values were obtained for both plain pipe and girth-welded pipe based on the onset of wrinkling. The critical strain values for girth-welded pipes were found to be approximately 60% of those for corresponding plain pipes.

Both global and local moment vs. curvature responses were obtained for each of the plain and girth-welded specimens. The secondary moments used to obtain the moment at the wrinkled segment (i.e., local moment) were found to be significant. In the moment vs. curvature curves for the wrinkled segment (i.e., the local response), the softening point always coincided with the limit point. However, this was not the case for the end moment vs. overall curvature curves (i.e., the global response), where the softening point sometimes occurred shortly after the limit point.

As was the case for the plain pipes, when the internal pressure was increased, the rotation capacity increased as well but the ultimate moment decreased. The global moment vs. curvature responses showed that the ultimate end moments for the pipes with and without girth weld were almost equal. Nevertheless, the pressurized girth-welded pipes showed less rotation capacity than did their plain counterparts.

In the second phase of this project, a numerical model was developed to simulate the local and global moment vs. curvature responses of line pipe up to local buckling. The model is based on incremental theory of plasticity and employs several types of strain-hardening models. Different stress vs. strain measures were provided in the numerical model. The computer programs PAPS and PDA were developed to generate the local and global moment vs. curvature responses based on the numerical model. Analytical results were obtained for the test specimens and were compared with the test results. It was concluded that the UL (updated Lagrangian) formulation with isotropic-hardening is the most appropriate model for the analysis of line pipe under combined loadings.

6.2 RECOMMENDATIONS FOR FUTURE RESEARCH

The number of tests that have been carried out on girth-welded line pipe is very small. More tests need to be performed on a wider range of pipe size in order to establish a reliable experimental data base.

Future experimental programs on line pipe should include pipes produced by different manufacturing processes. The influence of the effects of fabrication on pipe behavior, such as the difference in behavior between spiral pipe and DSAW pipe, is expected to be significant. However, to date the effect of the manufacturing process has not been adequately investigated. It is anticipated that each manufacturing process will

have its own characteristic strain values associated with the local buckling phenomenon. It would be desirable to establish the limiting values relevant to each manufacturing process.

Bending is not the only effect of imposed deformations. Depending on the ground slope and pipe lay-out, imposed deformations can subject the pipe to high shear and torsional loadings. Therefore, it is desirable that tests that include shear and torsion in combination with bending be carried out on line pipe.

REFERENCES

Bathe, K. J. (1982). *Finite Element Procedures in Engineering Analysis.* Prentice-Hall, Inc., Englewood Cliffs, NJ.

Bland, D. R. (1956). "The Two Measures of Work-Hardening." *Proc. 9th int. Cong. Appl. Mech.*, Brussels.

Bouwkamp, J. G. and Stephen, R. M. (1974). "Full-Scale Studies on the Structural Behavior of Large Diameter Pipes under Combined Loading." *Report No. UC-SESM 74-1*, Dept. of Civil Engineering, University of California, Berkeley.

Bouwkamp, J. G. and Stephen, R. M. (1973). "Large Diameter Pipe under Combined Loading." *Transportation Journal of the ASCE*, Vol. 99, No. TE3, pp. 521-536.

Calladine, C. R. (1983). "Plastic Buckling of Tubes in Pure Bending." *Collapse – The Buckling of Structures in Theory and Practice*, J. M. T. Thompson and G. W. Hunt, eds., Cambridge University Press, New York, NY, pp. 111-124.

CAN/CS-Z662-94, Oil and Gas Pipeline Systems. (1994). Canadian Standard Association, Toronto, Ontario M9W 1R3.

Chen, W. F. and Han, D. J. (1988). *Plasticity for Structural Engineers.* Springer-Verlag New York Inc.

Crandall, S. H. and Dahl, N. C. (1959). *An Introduction to the Mechanics of Solids.* McGraw-Hill, New York, NY.

Fung, Y. C. (1965). *Foundations of Solid Mechanics.* Prentice-Hall, Inc., Englewood Cliffs, NJ.

Gresnigt, A. M. (1986). "Plastic Design of Buried Steel Pipelines in Settlement Areas." *Heron*, Vol. 31, No. 4.

Hibbit, H. D., Karlson, B. I., and Sorensen, P. (1993a). *ABAQUS Theory Manual version 5.3.* Hibbit, Karlson, and Sorensen Inc., Pawtucket, RI 02860-4847.

Hibbit, H. D., Karlson, B. I., and Sorensen, P. (1993b). *ABAQUS User's Manual I version 5.3.* Hibbit, Karlson, and Sorensen Inc., Pawtucket, RI 02860-4847.

Hill, R. (1950). *The Mathematical Theory of Plasticity.* Oxford University Press, London.

Hu, S. Z., Prion, H. G. L., and Birkmoe, P. C. (1993). "Influence of Imperfections on the Strength of Unstiffened, Fabricated, Tubular Beam-Columns." *J. Construct. Steel Research*, Vol. 25, pp. 43–61.

Jirsa, J. O., Lee, F. H., Wilhoit, J. C., and Merwin, J. E. (1972). "Ovaling of Pipelines under Pure Bending." *Offshore Technology Conference*, Paper No. OTC 1569.

Ju, G. T. and Kyriakides, S. (1992). "Bifurcation and Localization Instabilities in Cylindrical Shells under Bending – II. Predictions." *Int. J. Solids Structures*, Vol. 29, No. 9, pp. 1143–1171.

Kim, H. O. (1992). "Plastic Buckling of Pipes under Bending and Internal Pressure." *Proceedings of the Second International Offshore and Polar Engineering Conference*, San Francisco, Vol. 2, pp. 46–51.

Korol, R. M. (1979). "Critical Buckling Strains of Round Tubes in Flexure." *Int. J. Mech. Sci.*, Vol. 21, pp. 719-730.

Kyriakides, S. and Ju, G. T. (1992). "Bifurcation and Localization Instabilities in Cylindrical Shells under Bending – I. Experiments." *Int. J. Solids Structures*, Vol. 29, No. 9, pp. 1117–1142.

LabVIEW 2 User Manual version 4.2. (1990). National Instrument Corporation, Austin, TX 78730-5039.

Lara, P. F. (1987). "Revisiting the Failure Criteria of Buried Pipelines." *ASME, Petroleum Division (Publication)*, PD. Vol. 6, pp. 143–154.

Mohareb, M., Elwi, A. E., Kulak, G. L., and Murray, D. W. (1994). *Deformational Behavior of Line Pipe*. Structural Engineering Report 202, Dept. of Civil Engineering, University of Alberta, Edmonton, Alberta.

Mroz, Z. (1969). "An Attempt to Describe the Behavior of Metals under Cycling Loads Using a More General Work-Hardening Model." *Acta Mechanica*, Vol. 7, pp. 199–212.

Price, P. St. J. and Anderson, H. A. (1991). "Integrity Monitoring and Maintenance Criteria for New and Existing on Land and Marine Pipelines." *Proceedings of the First International Offshore and Polar Engineering Conference*, Edinburgh, pp. 386–393.

Price, P. St. J. and Barnette, J. A. (1987). "Pipeline Codes and Structural Criteria for Pipelines in Arctic and Earthquake Regions." *Offshore and Arctic Pipelines*, J. S. Chung and K. Karal, eds., ASME, New York, NY, pp. 89–97.

Price, P. St. J. (1978). "Basis of Structural Design Criteria for Buried Gas Transmission Pipelines." *ASME, 78-PET-73.*

Reddy, B. D. (1979). "An Experimental Study of the Plastic Buckling of Circular Cylinders in Pure Bending." *Int. J. Solids Structures,* Vol. 15, pp. 669–683.

Rice, J. R. (1975). "Continuum Mechanics and Thermodynamics of Plasticity in Relation to Microscale Deformation Mechanics." *Constitutive Equations in Plasticity,* A. S. Argon, editor, MIT Press, Cambridge, Massachusetts.

Row, D. G., Hollings, J. P., Sause, R., and Der Kiureghian, A. (1987). "Limit State Probabilistic Design of Offshore Arctic Pipelines." *Offshore and Arctic Pipelines,* J. S. Chung and K. Karal, eds., ASME, New York, NY, pp. 115–123.

Sanders, J. L. (1963). "Nonlinear Theories of Thin Shells." *Quart. Appl. Math.,* Vol. 21, pp. 21–36.

Sherman, D. R. (1986). "Inelastic Flexural Buckling of Cylinders," in *Steel Structures – Recent Advances and Their Applications to Design,* M. N. Povlovic, editor, Elsevier Applied Science Publishers, New York, NY.

Souza, L. T. and Murray, D. W. (1994). *Prediction of Wrinkling Behavior of Girth-welded Line Pipe.* Structural Engineering Report 197, Dept. of Civil Engineering, University of Alberta, Edmonton, Alberta.

Souza, L. T. (1991). *FORTRAN Subroutine for Cubic Spline Method.* Dept. of Civil Engineering, University of Alberta, Edmonton, Alberta.

Tvergaard, V. and Needleman, A. (1983). "On the Development of Localized Buckling Patterns." *Collapse – The Buckling of Structures in Theory and Practice,* J. M. T. Thompson and G. W. Hunt, eds., Cambridge University Press, New York, NY, pp. 1–17.

Zhou, Z. and Murray, D. W. (1993). *Numerical Structural Analysis of Buried Pipelines.* Structural Engineering Report 181, Dept. of Civil Engineering, University of Alberta, Edmonton, Alberta.

Ziegler, H. (1959). "A Modification of Prager's Hardening Rule." *Quart. Appl. Math.,* Vol. 17, pp. 55–65.

APPENDIX A

User's Manual for Program PAPS

A.1 General

Program PAPS computes the moment vs. curvature response for the cross-section of a closed-ended pipe subjected to internal pressure and external axial load. The program employs a variety of incremental theories of plasticity considering no change in the cross-section configuration. Thus, ovalization and local buckling are not taken into account.

The loading sequence is similar to that for eccentric column types of test specimens: pressure is applied first, axial load is applied next, and finally the bending moment is applied. In the first and second stages of loading, the entire cross-section has uniform states of stress and strain. Upon bending, however, the cross-section is discretized into a number of discrete elements in order to represent the variation in the stress and strain values around the cross-section (see Fig. 5.4). Only one-half of the cross-section needs to be considered because of the symmetry about the plane of bending.

The program is equipped with different choices of stress and strain measures, namely, engineering stress and strain, 2nd Piola-Kirchhoff stress and Green-Lagrange strain, and true stress and logarithmic strain. In addition, the program contains a mixed hardening model using the Prager and Ziegler kinematic hardening rules as alternatives. The calculations can be carried out in two or three dimensions.

Program PAPS is written in FORTRAN 77 language. The program is unit independent. That is, any consistent set of units can be used. The input and output files for program PAPS are described in the following sections.

A.2 Input

The input file for program PAPS consists of the geometric measures of the pipe cross-section, the magnitudes of the loads, the indices prescribing desired options for the solution procedure, and the material stress vs. strain response. The input file must be under the name IN and located in the same directory as that of the program. The input file structure is described in the following subsections.

A.2.1 Line 1

TITLE   Format (A80)

This line allows for inputting a title. The title will appear on the top of the output file.

A.2.2 Line 2

ID, ISS, HM, NP, LOP   Format (*)

ID: Index for the dimension of the stress and strain space in the solution

EQ. 0; calculations in two-dimensional space

EQ. 1; calculations in three-dimensional space

ISS: Index for the type of the stress and strain measures used in the analysis

EQ. -1; 2nd Piola-Kirchhoff stress and Green-Lagrange strain

EQ. 0; engineering stress and strain

EQ. 1; true (Cauchy) stress and logarithmic strain

HM: Mixed hardening parameter (a real value)

$-1 \leq HM \leq 0$; mixed hardening using the Prager kinematic hardening rule

$0 \leq HM \leq 1$; mixed hardening using the Ziegler kinematic hardening rule

Note: the actual hardening parameter (denoted by M in Chapter 5) is always equal to the absolute value of HM. Therefore, for HM equal to zero, the mixed hardening model reduces to the isotropic hardening model. Also, for $HM = \pm 1$, the mixed hardening model becomes an entirely kinematic hardening model.

NP: Number of the data points defining the material stress vs. strain curve

Note: the first data point is taken as zero stress and zero strain by default. Therefore, this point should not be included in the data points input herein.

LOP: Index for saving the values of stress and strain around the cross-section at each curvature step

EQ. 0; no stress and strain data saved

EQ. 1; stress and strain data saved

A.2.3 Line 3

R, T, PR, P, X0   Format (*)

R: Inside radius of the pipe

T: Thickness of the pipe wall

PR: Poisson's ratio of the pipe material

P: Internal pressure

X0:   External axial load

A.2.4 Line 4

NE, NPR, NAX, CM, NC   Format (*)

NE: Number of divisions (elements) around one-half of the cross-section (see Fig. 5.4)

   Note: It is recommended that NE be in the range of 40 to 60. Values too small for NE decrease the accuracy of the results, and values too large for NE increase the cost of the computation unnecessarily.

NPR: Number of the pressure increments subsequent to the initiation of yielding

   Note: The NPR value is used only if plastification starts during the pressurization before the application of other loads. Since the elastic–plastic loading at this stage is done for the entire cross-section and without any iteration, using large values for NPR will not be costly. Therefore, to increase the accuracy of the results, values in the range of 1000 to 2000 are recommended for NPR.

NAX: Number of the axial force increments subsequent to the initiation of yielding

   Note: The NAX value is used only if plastification starts during the application of axial load before the imposition of curvature. Since the elastic–plastic loading at this stage is done for the entire cross-section and with no iteration, using large values for NAX will not be costly. Therefore, to increase the accuracy of the results, values in the range of 500 to 2000 are recommended for NAX.

CM: Final value of curvature

NC: Number of the curvature increments subsequent to the initiation of yielding

   Note: The choice of the value for NC depends on the distance between the yielding curvature (or zero when plastification has already started at the beginning of bending) and the final value of curvature, CM. However, the following range can be used as a tentative guide.

$$0.25 \times 10^7 \, CM \le NC \le 10^7 \, CM$$

where CM is in terms of (1/mm). Moreover, by choosing an appropriate value for the tolerance B0 (described in the following), a lower value for NC can be used.

A.2.5 Line 5

DEL, C0, TOL, B0   Format (*)

DEL: Angular increment for the position of the assumed bending neutral axis (corresponding to $\delta\psi$ in Section 5.4.1, Step 4e.2); values in the order of 10^{-3} radians are recommended.

C0: Modifying value for the initial curvature increment.

Note: When the curvature increments are very small, the bending neutral axis sometimes tends to be very close to the edge of the cross-section for the first curvature increment. This leads to the failure of the program to determine the position of the bending neutral axis. In such a case, the first curvature increment is increased by successive values of C0 until the bending neutral axis can be located. Values of the order of 10^{-7} (1/mm) are recommended for C0.

TOL: Tolerance for the axial force of the cross-section (corresponding to β in Section 5.4.1, Step 4e); values of the order of 10^{-6} are recommended.

B0: Step tolerance for effective stress in elastic–plastic increments (dimensionless)

Note: The formulation implemented in the program is based on small stress and strain increments. To make sure that the increments taken are small, the relative increase in the value of σ_e due to the increment is compared with B0. If the relative increase in σ_e exceeds B0, the increment will be broken into sub-increments that satisfy the requirement. A value of 0.01 for B0 is recommended herein.

A.2.6 Pipe Material Property

The data points for the stress vs. strain response of the pipe material are given in NP lines (see Section A.2.2) as follows.

STRAIN, STRESS   Format (*)   repeat for all data points

A.3 Output

Program PAPS generates two output files. These are

(a) file OU, containing the moment vs. curvature response for the cross-section, and

(b) file OS, containing stress and strain values around the cross-section of the pipe for each curvature increment.

Since the latter output file (OS) can be very large, the generation of the file is optional. (It is controlled by the parameter LOP described in Section A2.2.)

In the output file OU, the curvature values are scaled by a factor of 10^4, and the moment values are scaled by a factor of 10^{-6}. In addition, FO is the position angle (radians) for the bending neutral axis (corresponding to ψ_0 in Fig. 5.4) and EYave is the average hoop strain around the cross-section in percent.

In the output file OS, SX is the longitudinal stress; EX, EY, and EZ are total strain values in longitudinal, hoop, and through-thickness directions; and PEX, PEY, and PEZ are the corresponding plastic strains. For each curvature step, there is a block of data containing rows of above-mentioned values for elements around one-half of the cross-section (see Fig. 5.4). These rows from top to bottom correspond to the element number one to the element number NE, sequentially.

A.4 Example

As examples of input and output files, those used to model specimen DGA12W (see Table 2.1) are presented in the following. These results form the basis for the plots designated by PAPS-UL (Iso.) in Figs. 5.11 and 5.16.

A.4.1 Input File

DGA12W/3-D analysis/true stress vs. log. strain/isotropic hardening

1, 1, 0, 11, 1

155.7365, 6.477. 0.3, 10.45, 964E3

40, 2000, 2000, 2E-4, 50

1E-3, 1E-7, 1E-5, 0.01

0.001	199.6
0.002	314.1
0.003	356.3
0.005	378.0
0.01	384.1
0.02	397.3
0.04	419.5
0.06	433.6
0.08	442.1

0.14   454.3
0.2   455.5

A.4.2 Output File

A.4.2.1 File OU

DGA12W/3-D analysis/true stress vs. log. strain/isotropic hardening

ISOTROPIC HARDENING, HM = 0.0

3-DIMENSION STI. :SS

TRUE STRESS & STRAIN

STEP TOLERANCE B0 = 0.100E-01

No. OF ELEMENTS = 40

INTERNAL RADIUS = 155.7365

THICKNESS   = 6.4770

POISSON RATIO = 0.3000

AXIAL LOAD   = 0.96400E+06

INTERNAL PRESSURE= 10.450

INITIAL CURVATURE INCREMENT= 0.100E-06

FINAL CURVATURE = 0.200E-03

TOLERANCE FOR AXIAL LOAD = 0.100E-04

ANGULAR INCREMENT FOR N.A.= 0.100E-02 rad.

No. OF DIVISIONS FOR PLAS. COMP.= 2000

No. OF DIVISIONS FOR PLAS. PRES.= 2000

No. OF CURVATURE INCREMENTS =   50

THE GIVEN STRESS-STRAIN CURVE:

STRAIN	STRESS
0.000000	0.000000
0.001000	199.600000
0.002000	314.100000
0.003000	356.300000

```
0.005000  378.000000
0.010000  384.100000
0.020000  397.300000
0.040000  419.500000
0.060000  433.600000
0.080000  442.100000
0.140000  454.300000
0.200000  455.500000
```

****

NON-LINEARITY STARTS DURING PRESSURIZING THE PIPE

PRESSURE AT FIRST YIELD = 0.959439E+01

CURV. x 1E-4	MOMENT x 1E6	F0(rad)	EYave(%)
0.00000	0.00000	0.000000	0.00
0.04000	53.6942	0.225137	0.16
0.08000	88.6580	0.263??4	0.19
0.12000	108.8171	0.??????	?.2?
0.16000	123.0783	?.??????	?.??
0.20000	131.2061	?.?????	?.?1
0.24000	136.9002	?.??·??	0.35
0.28000	141.1112	0.508097	0.40
0.32000	144.6289	0.530327	0.45
0.36000	147.8192	0.548147	0.50
0.40000	150.6206	0.563001	0.55
0.44000	153.0986	0.572974	0.59
0.48000	155.3909	0.580489	0.64
0.52000	157.5699	0.586440	0.69
0.56000	159.6541	0.590890	0.73
0.60000	161.6472	0.594253	0.78
0.64000	163.6130	0.597147	0.83
0.68000	165.4374	0.599575	0.87
0.72000	167.1408	0.600935	0.92

0.76000 , 168.7764 , 0.601179 , 0.96

0.80000 , 170.3681 , 0.600948 , 1.01

0.84000 , 171.8991 , 0.599759 , 1.05

0.88000 , 173.3979 , 0.598306 , 1.09

0.92000 , 174.8816 , 0.596948 , 1.14

0.96000 , 176.3352 , 0.595542 , 1.18

1.00000 , 177.7856 , 0.594214 , 1.22

1.04000 , 179.1971 , 0.592274 , 1.26

1.08000 , 180.5528 , 0.589513 , 1.31

1.12000 , 181.9053 , 0.586942 , 1.35

1.16000 , 183.2569 , 0.584532 , 1.39

1.20000 , 184.6058 , 0.582274 , 1.43

1.24000 , 185.9349 , 0.579921 , 1.47

1.28000 , 187.2591 , 0.577588 , 1.51

1.32000 , 188.5418 , 0.575310 , 1.55

1.36000 , 189.7483 , 0.572815 , 1.59

1.40000 , 190.9323 , 0.570491 , 1.63

1.44000 , 192.0980 , 0.568313 , 1.67

1.48000 , 193.2346 , 0.566091 , 1.71

1.52000 , 194.3295 , 0.563394 , 1.74

1.56000 , 195.4147 , 0.560847 , 1.78

1.60000 , 196.4928 , 0.558437 , 1.82

1.64000 , 197.5662 , 0.556149 , 1.86

1.68000 , 198.6317 , 0.553982 , 1.90

1.72000 , 199.6939 , 0.551917 , 1.94

1.76000 , 200.7512 , 0.549953 , 1.97

1.80000 , 201.8014 , 0.548061 , 2.01

1.84000 , 202.8229 , 0.545824 , 2.05

1.88000 , 203.8355 , 0.543631 , 2.09

1.92000 , 204.8457 , 0.541536 , 2.12

1.96000 , 205.8564 , 0.539525 , 2.16

2.00000 , 206.8578 , 0.537616 , 2.20

END OF THE PROGRAM

A.4.2.2 File OS

The first block of data in the output file OS is presented below as a typical block. It contains the values of longitudinal stress and strains for the first curvature increment for all the elements around the cross-section.

CURV.=0.04000   MOMENT= 53.6942

SX	EX	EY	EZ	PEX	PEY	PEZ
-116.045	-0.128E-02	0.202E-02	-0.463E-03	-0.327E-03	0.587E-03	-0.260E-03
-115.784	-0.128E-02	0.201E-02	-0.463E-03	-0.324E-03	0.584E-03	-0.260E-03
-115.264	-0.127E-02	0.201E-02	-0.462E-03	-0.319E-03	0.577E-03	-0.258E-03
-114.504	-0.126E-02	0.200E-02	-0.461E-03	-0.311E-03	0.567E-03	-0.256E-03
-113.471	-0.125E-02	0.198E-02	-0.460E-03	-0.301E-03	0.554E-03	-0.253E-03
-112.189	-0.123E-02	0.196E-02	-0.458E-03	-0.288E-03	0.537E-03	-0.249E-03
-110.681	-0.120E-02	0.194E-02	-0.456E-03	-0.273E-03	0.518E-03	-0.245E-03
-108.916	-0.118E-02	0.192E-02	-0.453E-03	-0.256E-03	0.495E-03	-0.239E-03
-106.926	-0.115E-02	0.189E-02	-0.450E-03	-0.236E-03	0.470E-03	-0.233E-03
-105.372	-0.112E-02	0.185E-02	-0.444E-03	-0.212E-03	0.437E-03	-0.225E-03
-102.434	-0.108E-02	0.182E-02	-0.442E-03	-0.191E-03	0.410E-03	-0.219E-03
-96.922	-0.104E-02	0.180E-02	-0.447E-03	-0.181E-03	0.396E-03	-0.215E-03
-91.027	-0.100E-02	0.177E-02	-0.451E-03	-0.170E-03	0.381E-03	-0.211E-03
-84.752	-0.960E-03	0.175E-02	-0.456E-03	-0.159E-03	0.365E-03	-0.207E-03
-78.153	-0.915E-03	0.172E-02	-0.462E-03	-0.147E-03	0.349E-03	-0.202E-03
-71.232	-0.869E-03	0.170E-02	-0.467E-03	-0.136E-03	0.332E-03	-0.196E-03
-64.049	-0.822E-03	0.167E-02	-0.472E-03	-0.124E-03	0.315E-03	-0.191E-03
-56.626	-0.773E-03	0.164E-02	-0.477E-03	-0.113E-03	0.298E-03	-0.185E-03
-48.985	-0.724E-03	0.161E-02	-0.482E-03	-0.102E-03	0.280E-03	-0.179E-03
-41.191	-0.674E-03	0.158E-02	-0.487E-03	-0.907E-04	0.263E-03	-0.172E-03
-33.272	-0.624E-03	0.155E-02	-0.492E-03	-0.804E-04	0.245E-03	-0.165E-03
-25.116	-0.574E-03	0.152E-02	-0.498E-03	-0.714E-04	0.230E-03	-0.158E-03
-15.258	-0.525E-03	0.151E-02	-0.513E-03	-0.714E-04	0.230E-03	-0.158E-03
-5.552	-0.476E-03	0.150E-02	-0.527E-03	-0.714E-04	0.230E-03	-0.158E-03
3.940	-0.429E-03	0.148E-02	-0.541E-03	-0.714E-04	0.230E-03	-0.158E-03
13.160	-0.383E-03	0.147E-02	-0.555E-03	-0.714E-04	0.230E-03	-0.158E-03
22.052	-0.338E-03	0.145E-02	-0.569E-03	-0.714E-04	0.230E-03	-0.158E-03
30.561	-0.296E-03	0.144E-02	-0.581E-03	-0.714E-04	0.230E-03	-0.158E-03

38.634 -0.255E-03 0.143E-02 -0.593E-03 -0.714E-04 0.230E-03 -0.158E-03

46.221 -0.217E-03 0.142E-02 -0.605E-03 -0.714E-04 0.230E-03 -0.158E-03

53.277 -0.182E-03 0.141E-02 -0.615E-03 -0.714E-04 0.230E-03 -0.158E-03

59.757 -0.150E-03 0.140E-02 -0.625E-03 -0.714E-04 0.230E-03 -0.158E-03

65.621 -0.120E-03 0.139E-02 -0.634E-03 -0.714E-04 0.230E-03 -0.158E-03

70.834 -0.942E-04 0.138E-02 -0.642E-03 -0.714E-04 0.230E-03 -0.158E-03

75.364 -0.715E-04 0.137E-02 -0.649E-03 -0.714E-04 0.230E-03 -0.158E-03

79.182 -0.524E-04 0.137E-02 -0.654E-03 -0.714E-04 0.230E-03 -0.158E-03

82.265 -0.370E-04 0.136E-02 -0.659E-03 -0.714E-04 0.230E-03 -0.158E-03

84.594 -0.253E-04 0.136E-02 -0.662E-03 -0.714E-04 0.230E-03 -0.158E-03

86.154 -0.175E-04 0.136E-02 -0.665E-03 -0.714E-04 0.230E-03 -0.158E-03

86.937 -0.136E-04 0.136E-02 -0.666E-03 -0.714E-04 0.230E-03 -0.158E-03

APPENDIX B

Program Listing for

PLASTIC ANALYSIS OF PIPE SECTIONS (PAPS)

```
C     PLASTIC ANALYSIS OF PIPE SECTIONS
C
C     NADER YOOSEF-GHODSI & D.W. MURRAY
C
C     MARCH 1995
C
C     THIS PROGRAM IS CAPABLE OF MODELING THE CROSS-SECTION OF A
C     CLOSED-ENDED PIPE THAT UNDERGOES FIRST PRESSURE THEN AXIAL LOAD
C     AND FINALLY BENDING MOMENT. IN THE FIRST OUTPUT FILE (OU) THE
C     MOMENT VS CURVATURE IS TABULATED. IN THE SECOND OUTPUT FILE
C     (OPTIONAL) AT EACH CURVATURE, THE VALUES OF STRESSES, STRAINS,
C     AND PLASTIC STRAINS FOR ALL THE ELEMENTS OF THE CROSS-SECTION
C     ARE GIVEN.
C     IN THIS PROGRAM YIELD STRESS IS A FUNCTION OF EFFECTIVE PLASTIC
C     STRAIN.
C     THE PRAGER'S MIXED HARDENING IS INHERENTLY THREE DIMENSIONAL.
C     THUS, IT SHOULD ALWAYS BE WITH THE CHOICE OF THREE DIMENSIONAL
C     ANALYSIS.

      IMPLICIT REAL*8 (A-H,O-Z)
      CHARACTER*80 TITLE
      COMMON E0,F0,C,A,NE,EM,PI,RM,AE,SY,SS(30),SP(30),DSX,DS1(3),
     + EEP2,SA(3),SM,AZ(3),DE(3),DP(3),B0,ST(300),S(300),E(3,300),
     + ET(3,300),PE(3,300),PET(3,300),EE(3,3),EEP(300),LL(300),
     + AL(3,300),NP,PR,N,LAST,EEP1,DS(3),SX,A1L(3),EPR(3),EPP(3),
     + IND,EE2(2,2),EEPT(300),ALT(3,300),HM,ID,ISS,EFAC
      COMMON /L1/ DEL,CS,NC,X,TOL,CM,LOP,C0,CCC
      DIMENSION SN(30)
      OPEN(1,FILE='IN')
      OPEN(2,FILE='OU')
      PI=4*DATAN(1.D+0)
      READ(1,'(A)')TITLE
      READ(1,*)ID,ISS,HM,NP,LOP
      READ(1,*)R,T,PR,P,X0
      READ(1,*)NE,NPR,NAX,CM,NC
      READ(1,*)DEL,C0,TOL,B0
      IF (HM.LT.0.0D+0.AND.ID.EQ.0) THEN
      WRITE(*,'(/'' CANNOT USE PRAGER IN TWO DIMENSIONS'')')
      STOP
      ENDIF
      READ(1,*)(SN(I),SS(I),I=1,NP)
      IF (LOP.NE.0) OPEN(3,FILE='OS')
      WRITE(2,'(1X,A)') TITLE
      IF(HM.EQ.0)WRITE(2,'('' ISOTROPIC HARDENING, HM ='',F4.1)') HM
      IF(HM.GT.0)WRITE(2,'('' MIXED HARDENING - ZIEGLER, HM ='',F7.3)
     +') HM
      IF(HM.LT.0)WRITE(2,'('' MIXED HARDENING - PRAGER, HM ='',F7.3)'
     +) HM
      IF(ID.EQ.0)WRITE(2,'('' 2-DIMENSION STRESS (1 AND 2)'')')
      IF(ID.EQ.1)WRITE(2,'('' 3-DIMENSION STRESS'')')
      IF(ISS.EQ.0)WRITE(2,'('' ENGINEERING STRESS & STRAIN'')')
      IF(ISS.GT.0)WRITE(2,'('' TRUE STRESS & STRAIN'')')
      IF(ISS.LT.0)WRITE(2,'('' PIOLA-KIRCHHOFF STRESS AND LAGRANGE ST
     +RAIN'')')
      WRITE(2,'('' STEP TOLERANCE B0 ='',E10.3)') B0
      WRITE(2,'('' No. OF ELEMENTS ='',I4)') NE
      WRITE(2,'('' INTERNAL RADIUS ='',F10.4)') R
      WRITE(2,'('' THICKNESS      ='',F10.4)') T
      WRITE(2,'('' POISSON RATIO   ='',F10.4)') PR
      WRITE(2,'('' AXIAL LOAD    ='',E12.5)') X0
      WRITE(2,'('' INTERNAL PRESSURE='',F10.3)') P
      WRITE(2,'('' INITIAL CURVATURE INCREMENT='',E10.3)') C0
      WRITE(2,'('' FINAL CURVATURE  ='',E10.3)') CM
      WRITE(2,'('' TOLERANCE FOR AXIAL LOAD ='',E10.3)') TOL
      WRITE(2,'('' ANGULAR INCREMENT FOR N.A='',E10.3,'' rad'')')DEL
      WRITE(2,'('' No. OF DIVISIONS FOR PLAS. COMP='',I7)')NAX
      WRITE(2,'('' No. OF DIVISIONS FOR PLAS. PRES.='',I7)')NPR
      WRITE(2,'('' No. OF CURVATURE INCREMENTS  ='',I7))NC
      WRITE(2,'('' THE GIVEN STRESS-STRAIN CURVE:'')')
      WRITE(2,'(2F11.6)') 0D+0,0D+0
      WRITE(2,'(2F11.6)')(SN(I),SS(I),I=1,NP)
      WRITE(2,'(''*********************'')')
      DO 555 K=1,NE
      LL(K)=0
      EEP(K)=0
      EEPT(K)=0
      DO 555 I=1,3
      A1L(I)=0
      EPP(I)=0
      EPR(I)=0
      ALT(I,K)=0
  555 AL(I,K)=0
      EEP1=0
      F0=0
      RO=R+T
      DO=2*R+2*T
      DI=2*R
      A=(DO**2-DI**2)*PI/4
      AE=A/NE
      RM=R+T/2
      S0=(DO**4-DI**4)*PI/32/DO
```

```
C CONVERT THE INPUT ENGINEERING STRESS-STRAIN CURVE TO THAT
C FOR THE PROCEDURE
C ISS=0 ENGINEERING STRESS-STRAIN
C ISS>0 TRUE STRESS-STRAIN
C ISS<0 2nd PIOLA-KIRCHHOFF STRESS AND LAGRANGIAN STRAIN

      IF (ISS.GT.0) THEN
      DO 8 I=1,NP
      SS(I)=SS(I)*(1.+SN(I))
      SN(I)=DLOG(1.+SN(I))
      ELSEIF (ISS.LT.0) THEN
      DO 9 I=1,NP
      SS(I)=SS(I)*(1.+SN(I))
    9 SN(I)=SN(I)*(1.+SN(I)/2.)
      ENDIF

      EM=SS(1)/SN(1)
      DO 10 I=1,NP
   10 SP(I)=SN(I)-SS(I)/EM

C ELASTIC STIFFNESS MATRIX
      EL=PR*EM/(1+PR)/(1-2*PR)
      G=EM/2/(1+PR)
      DO 55 I=1,3
      DO 55 J=1,3
   55 EE(I,J)=EL
      DO 60 I=1,3
   60 EE(I,I)=2*G+EL
      IF(ID.EQ.0) THEN
      ADD=EL*EL/(2*G+EL)
      EFAC=4*G*(G+EL-ADD)/(2*G+EL-ADD)
      DO 65 I=1,2
      DO 65 J=1,2
   65 EE2(I,J)=EE(I,J)-ADD
      ENDIF

C SOME PRELIMINARY VALUES OF STRAIN AND STRESS
      X=X0-PI*PI*R**2
      VAL=SS(1)**2-.75*(P*R/T)**2
      IF(VAL.GE.0) RN=DSQRT(VAL)-X/A-P*R/2/T
      IF(VAL.LT.0) THEN

C NONLINEARITY STARTS DURING PRESSURIZING THE PIPE
      WRITE(2,(" NON-LINEARITY STARTS DURING PRESSURIZING THE PIPE"
     + /))


C

C FIND THE YIELD PRESSURE
      IND=0
      ALFA=PI/A*R**2
      BETA=R/T
      PY=SS(1)/DSQRT(ALFA**2+BETA**2-ALFA*BETA) PY
      WRITE(2,(" PRESSURE AT FIRST YIELD = ",E13.6/)) PY
      WRITE(2,("  CURV.     MOMENT    F0(rad)  EYave(%)"))
      WRITE(2,("   x 1E-4     x 1E-4"))
      WRITE(2,(1X,4("..."))
      WRITE(2,("   0.00000    0.0000 , 0.000000 ,   0.00"))
      SX=ALFA*PY
      SY=BETA*PY
      EPR(1)=(SX-PR*SY)/EM
      EPR(2)=(SY-PR*SX)/EM
      EPR(3)=-PR*(SX+SY)/EM*ID
      DPR=(P-PY)/NPR

C PRESSURIZE FROM YIELD PRESSURE TO FINAL PRESSURE
      DS(3)=0
      DS(2)=DPR*BETA
      DS(1)=DPR*ALFA
      CALL APS(NPR)

      IF (LOP.NE.0) THEN
      SA1=SX-AIL(1)
      SA2=SY-AIL(2)
      SI=DSQRT(SA1*(SA1+AIL(3)-SA2)+SA2*(S. 2+AIL(3))-AIL(3)*AIL(3))
      WRITE(3,(" THE EFFECTIVE STRESS AFTER PRESS. = ",F10.4/))SI
      ENDIF

C COMPRESS THE SECTION
      SXA=SX-AIL(1)
      SYA=SY-AIL(2)
      SM=(SXA+SYA-ID*AIL(3))/3
      SA(1)=SXA-SM
      IF ((SA(1)*X0).GT.0.0D+0) THEN

C MOVE INSIDE THE YIELD SURFACE.  FIRST, ELASTIC LOAD
      CALL HS(EEP1,H,SI,SIV,IH)
      C1=AIL(1)+(SY-AIL(2)-AIL(3)*ID)/2.
      ROO=DSQRT(4*SI*SI-3*(SY-AIL(2)+AIL(3)*ID)**2)/2
      IF (SA(1).GT.0) THEN

C INITIALLY TENSILE
      SX1=C1-ROO
      ELSE
```

```fortran
C INITIALLY COMPRESSIVE
      SX1=C1+ROO
      ENDIF
      D1=SX1-SX
      D2=-X0/A
      IF (ABS(D2).GT.ABS(D1)) THEN

C FINALLY PLASTIC WITH FIRST AN ELASTIC THEN A PLASTIC LOADING
      EPR(1)=EPR(1)+D1/EM
      EPR(2)=EPR(2)-D1/EM*PR
      EPR(3)=EPR(3)-D1/EM*PR
      SX=SX1
      DS(1)=(D2-D1)/NAX
      DS(2)=0
      CALL APS(NAX)

      IF (LOP.NE.0) THEN
      SA1=SX-AIL(1)
      SA2=SY-AIL(2)
      SI=DSQRT(SA1*(SA1+AIL(3)-SA2)+SA2*(SA2+AIL(3))-AIL(3)*AIL(3))
      WRITE(3,("THE EFFECTIVE STRESS AFTER COMPR. =",F10.4//)SI
      ENDIF

C LL(I)=1: THE Ith ELEMENT IS PLASTIC (ON THE YIELD SURFACE)
      DO 41 I=1,NE
41    LL(I)=1
      ELSE

C FINALLY ELASTIC
      EPR(1)=EPR(1)+D2/EM
      EPR(2)=EPR(2)-D2/EM*PR
      EPR(3)=EPR(3)-D2/EM*PR
      SX=SX+D2
      ENDIF

      ELSE

C MOVE OUTSIDE THE YIELD SURFACE; ONLY PLASTIC LOADING
      DS(1)=-X0/A/NAX
      DS(2)=0
      CALL APS(NAX)

      IF (LOP.NE.0) THEN
      SA1=SX-AIL(1)
      SA2=SY-AIL(2)
      SI=DSQRT(SA1*(SA1+AIL(3)-SA2)+SA2*(SA2+AIL(3))-AIL(3)*AIL(3))


      WRITE(3,("THE EFFECTIVE STRESS AFTER COMPR. =",F10.4//)SI
      ENDIF

      DO 42 I=1,NE
42    LL(I)=1
      ENDIF

C SUBSTITUTING FOR THE VARIABLE USED IN BENDING
      DO 104 K=1,NE
      DO 106 I=1,2,+ID
      E(1,K)=EPR(I)
      PE(1,K)=EPP(I)
106   AL(1,K)=AIL(I)
      EEP(K)=EEP1
104   S(K)=SX
      E0=(SX-PR*SY)/EM

C ROTATE THE SECTION
      CALL MO
      ELSEIF(RN.LT.0) THEN

C NONLINEARITY STARTS DURING APPLICATION OF AXIAL LOAD
      WRITE(2,("NON-LINEARITY STARTS DURING APPLICATION OF AXIAL LO
     +AD"//))
      IND=1

C FIND THE YIELD COMPRESSION
      SY=P*R/T
      SX=(SY-DSQRT(4*SS(1)**2-3*SY**2))/2
      XY=A*SX
      XYT=XY+PI*P*R**2
      WRITE(2,("AXIAL LOAD AT FIRST YIELD =",E13.6/)) XYT
      WRITE(2,(" CURVATURE  MOMENT   F0(rad)  %(EYave)"))
      WRITE(2,(1X,47("-")))
      WRITE(2,("  0.00000,  0.000000 ,0.000000 ,  0.00"))
      EPR(1)=(SX-PR*SY)/EM
      EPR(2)=(SY-PR*SX)/EM
      EPR(3)=-PR*(SX+SY)*ID

C COMPRESS FROM ...      ...T TO FINAL COMP.
      DS(1)=(-X-XY)/A/N..
      DS(2)=0
      DS(3)=0
      CALL APS(NAX)
```

```fortran
      IF (LOP.NE.0) THEN
      SA1=SX-AIL(1)
      SA2=SY-AIL(2)
      SI=DSQRT(SA1*(SA1+AIL(3)-SA2)+SA2*(SA2+AIL(3))-AIL(3)*AIL(3))
      WRITE(3,'(" THE EFFECTIVE STRESS AFTER COMPR. = ",F10.4)')SI
      ENDIF

      DO 114 K=1,NE
      DO 116 I=1,3
      E(I,K)=EPR(I)
      PE(I,K)=EPP(I)
116   AIL(I,K)=AIL(I)
      LL(K)=I
      EEP(K)=EEP1
114   S(K)=SX
      E0=(SX-PR*SY)/EM

C ROTATE THE CROSS-SECTION
      CALL MO
      STOP
      ELSE

C NONLINEARITY STARTS DURING APPLICATION OF MOMENT

      WRITE(2,'(" NON-LINEARITY STARTS DURING APPLICATION OF MOMENT'
     + /)')
      IND=2

C FIND THE YIELD MOMENT
      XM=S0*RN
      C=RN/EM/(DO/2)
      CCC=C
      WRITE(2,'(" CURVATURE AT FIRST YIELD = ",E13.6)')C
      WRITE(2,'(" MOMENT AT FIRST YIELD    = ",E13.6)')XM
      WRITE(2,'(" CURVATURE  MOMENT      F0(rad)  %(EYave)')')
      WRITE(2,'(1X,47("-"))')
      WRITE(2,'("   0.000000 ,    0.0000, 0.000000 ,   0.00")')
      SY=PR/T
      SX=-X/A
      ROOT=DSQRT(VAL)
      SXC=SY/2-ROOT
      SXT=SY/2+ROOT

C INITIAL VALUES OF STRAINS AND LONG. STRESS
      E0=(SX-PR*SY)/EM
      DO 5 K=1,NE
      TE=PI/2*((2.*K-1.)/NE-1)
```

```fortran
      Y=RM*DSIN(TE)
      S(K)=(SX-SXC)/RO*(RO+Y)+SXC
      E(1,K)=E0+C*Y
      E(2,K)=(SY-PR*S(K))/EM
5     E(3,K)=PR/EM*(S(K)+SY)*ID
      SUM=0
      DO 767 K2=1,NE
767   SUM=SUM+E(2,K2)
      SUM=SUM*100/NE
      WRITE(2,'(3X,F9.5," ,",F9.4," ,",F9.6," ,",F6.2)')
     + C*1e4,XM/1e6,F0,SUM
      DO 323 J3=1,NE
323   LL(J3)=0

C ROTATE THE SECTION FROM YIELD MOMENT T? FINAL CURVATURE
      CALL MO
      STOP
      ENDIF
      END

      SUBROUTINE MO

C ROTATES THE CROSS-SECTION BY IMPOSING CURVATURE. EMPLOYS AN
C ITERATIVE PROCEDURE TO FIND THE LOCATION OF BENDING NEUTRAL
C AXIS. CALCULATES THE MOMENT FOR EACH CURVATURE INCREMENT.

      IMPLICIT REAL*8 (A-H,O-Z)
      COMMON E0,F0,C,A,NE,EM,PI,RM,AE,SY,SS(30),SP(30),DSX,DSI(3),
     + EEP2,SA(3),SM,A21(3),DE(3),DP(3),B0,ST(300),S(300),E(3,300),
     + ET(3,300),PE(3,300),PET(3,300),EE(3,3),EEP(300),LL(300),
     + AL(3,300),NP,PR,N,LAST,EEP1,DS(3),SX,AIL(3),EPR(3),EPP(3),
     + IND,EE2(2,2),EEPT(300),ALT(3,300),HM,ID,ISS,EFAC
      COMMON /L1/ DEL,CS,NC,X,TOL,CM,LOP,C0,CCC
      LUCK=1
6     IF (IND.NE.2) THEN
      C=0.0D+0
      ELSE
      C=CCC
      ENDIF

C STEP BY STEP INCREASE OF THE INITIAL CURVATURE UNTIL B.N.A. COULD BE
C LOCATED

      LUCK=LUCK+1
      C=C+LUCK*C0
```

```
        CS=(CM-C)/NC
        DO 1 N=1,NC
        NN=N

C START WITH A NEW CURVATURE (INCREASED)
        C=C+CS

C START OFF WITH SETTING THE B.N.A. AT THE LATEST POSITION
        CALL BAS(0.0D+0,X1,0)

C START MOVING THE B.N.A. (F0) FORWARD OR BACKWARD, DEPENDING ON
C WHETHER THE AXIAL FORCE USING THE LAST POSITION IS LOWER OR HIGHER
C THAN THE ASSIGNED VALUE. ONCE THE B.N.A. IS WITHIN THE INCREMENT
C (DEL), WE START BISECTING THE INTERVAL (BISECTION METHOD) UNTIL THE
C REQUIRED ACCURACY (INTRODUCED BY TOL) IS OBTAINED.

        IF (X1.GT.X) THEN

C MOVE FORWARD
        J=0
35      J=J+1
        D=J*DEL
        CALL BAS(D,X1,0)
        IF (LAST.EQ.1) GOTO 6
        IF (X1.GT.X) GO TO 35
        M=1
        D=D+DEL/2
37      CALL BAS(D,X1,0)
        ERR=ABS((X-X1)/X)
        IF (ERR.LT.TOL) GO TO 26
        M=M+1
        DAS=DEL/2**M
        IF (X1.LT.X) THEN
        D=D+DAS
        ELSF
        D=D-DAS
        ENDIF
        GO TO 37
        ELSE

C MOVE BACKWARD
        J=0
25      J=J+1
        D=J*DEL
        CALL BAS(D,X1,0)
        IF (LAST.EQ.1) GOTO 6
        IF (X1.LT.X) GO TO 25

        M=1
        D=D-DEL/2
27      CALL BAS(D,X1,0)
        ERR=ABS((X-X1)/X)
        IF (ERR.LT.TOL) GO TO 26
        M=M+1
        DAS=DEL/2**M
        IF (X1.LT.X) THEN
        D=D+DAS
        ELSE
        D=D-DAS
        ENDIF
        GO TO 27
        ENDIF
26      CALL BAS(D,X1,1)
        F0=F0+D

C UPDATE STRAINS AND STRESSES
        DO 100 K=1,NE
        S(K)=ST(K)
        DO 105 I=1,2+iD
        E(I,K)=ET(I,K)
105     PE(I,K)=PET(I,K)
        EEP(K)=EEPT(K)
        DO 110 I=1,2+iD
110     AL(I,K)=ALT(I,K)
100     CONTINUE

C CALCULATE THE MOMENT
        XM=0
        DO 2 K=1,NE
        TE=PI/2*((2.*K-1.)/NE-1)

        IF (ISS.LT.0) THEN

C 2nd PIOLA-KIRCHHOFF STRESS & LAGRANGIAN STRAIN
        CC=DSQRT(1+2*E(1,K))
        ELSEIF (ISS.GT.0) THEN

C TRUE STRESS & STRAIN
        CC=1./DEXP(E(1,K))
        ELSE

C ENGINEERING STRESS & STRAIN
        CC=1.D+0
        ENDIF
```

```
2    XM=XM+AE*S(K)*RM*DSIN(TE)*CC
     WRITE(*,'(" N =",I4,5X,"C =",F7.5,5X,"M =",F9.4)')
    + N,C*1e4,XM/1e6
     IF (LOP.NE.0) THEN
     WRITE(3,'(1X,"CURV.=",F7.5,5X,"MOMENT=",F9.4)')C*1e4,XM/1e6
     WRITE(3,'("  SX     EX     EY     EZ     PEX
    +     PEY    PEZ")')
     DO 207 L4=1,NE

     SA1=S(L4)-AL(1,L4)
     SA2=SY-AL(2,L4)
     SI=DSQRT(SA1*(SAI+AL(3,L4)-SA2)+SA2*(SA2+AL(3,L4))-AL(3,L4)*
    1 AL(3,L4))

207  WRITE(3,'(1X,F8.3,2X,E10.3,2(1X,E10.3),1X,3(1X,E10.3),F10.4)')
    + S(L4),E(1,L4),E(2,L4),E(3,L4),PE(1,L4),PE(2,L4),PE(3,L4),SI
     WRITE(3,'(1X,89("-")')
     ENDIF
     SUM=0
     DO 747 K2=1,NE
747  SUM=SUM+E(2,K2)
     SUM=SUM*100.D+0/NE
1    WRITE(2,'(3X,F9.5,",",F9.4,",",F9.6,",",F6.2)')
    + C*1e4,XM/1e6,F0,SUM
     WRITE(2,'(" END OF THE PROGRAM")')
     END


     SUBROUTINE MUL(A,B,C,M,L,N)

C MULTIPLIES TWO MATRICES

     IMPLICIT REAL*8 (A-H,O-Z)
     DIMENSION A(M,L),B(L,N),C(M,N)
     DO 3 I=1,M
     DO 3 J=1,N
     C(I,J)=0
     DO 3 K=1,L
3    C(I,J)=C(I,J)+A(I,K)*B(K,J)
     END


     SUBROUTINE HS(Q,H,SI,SIV,IH)

C CALCULATES THE YIELD STRESS & PLASTIC MODULUS.

C Q: EFFECTIVE PLASTIC STRAIN
C H: PLASTIC MODULUS
C SI: REDUCED YIELD STRESS
C SIV: YIELD STRESS
C IH: INDEX TO INDICATE THE INTERVAL WHERE Q IS LOCATED

     IMPLICIT REAL*8 (A-H,O-Z)
     COMMON E0,F0,C,A,NE,EM,PI,RM,AE,SY,SS(30),SP(30),DSX,DS1(3).
    + EEP2,SA(3),SM,A2L(3),DE(3),DP(3),B0,ST(300),S(300),E(3,300),
    + ET(3,300),PE(3,300),PET(3,300),EE(3,3),EEP(300),LL(300),
    + AL(3,300),NP,PR,N,LAST,EEP1,DS(3),SX,A1L(3),EPR(3),EPP(3),
    + IND,EE2(2,2),EEPT(300),ALT(3,300),HM,ID,ISS,EFAC
     DO 20 I=1,NP-1
     IF (Q.GE.SP(I).AND.Q.LT.SP(I+1)) THEN
     H=(SS(I+1)-SS(I))/(SP(I+1)-SP(I))
     SIV=H*(Q-SP(I))+SS(I)
     SI=SS(1)+(1.D+0-ABS(HM))*(SIV-SS(1))
     IH=I
     RETURN
     ENDIF
20    CONTINUE
     IF (Q.GE.SP(NP)) THEN
     IH=NP
     H=(SS(NP)-SS(NP-1))/(SP(NP)-SP(NP-1))
     SIV=H*(Q-SP(NP))+SS(NP)
     SI=SS(1)+(1.D+0-ABS(HM))*(SIV-SS(1))
     RETURN
     ENDIF
     WRITE(2,'(" EEP=",F10.6," OUT OF RANGE")')Q
     STOP
     END


     SUBROUTINE APS(N1)

C CARRIES OUT A PLASTIC LOADING OF PRESSURIZATION OR AXIAL
C COMPRESSION IN N1 INCREMENTS TO ATTAIN THE PRESCRIBED VALUE OF
C THE LOAD (PRESSURE OR AXIAL LOAD).
C IF AN INCREMENT STRADDLES AT LEAST ONE DATA POINT (KINK) ON THE
C STRESS-STRAIN CURVE INPUT, THE INCREMENT IS BROKEN INTO
C SUB INCREMENTS AT THESE POINTS (USING INDEX IH).  NOW IF A
C SUB INCREMENT (OR AN INCREMENT WITH NO KINK) IS TOO LARGE
C (COMPARED WITH B0), IT IS DIVIDED INTO SMALLER EQUAL PORTIONS.
```

```fortran
C SXA, SYA: LONG. & HOOP REDUCED STRESSES
C SM: MEAN REDUCED STRESS
C SA(I): REDUCED DEVIATORIC STRESS
C EPR(I): STRAIN IN Ith DIRECTION
C EPP(I): PLASTIC STRAIN IN Ith DIRECTION
C AIL(I): COORDINATES OF YIELD SURFACE CENTER
C A2L(I): TRIAL VALUE FOR AIL(I)

      IMPLICIT REAL*8 (A-H,O-Z)
      COMMON E0,F0,C,A,NE,EM,PI,RM,AE,SY,SS(30),SP(30),DSX,DSI(3),
     + EEP2,SA(3),SM,A2L(3),DE(3),DP(3),B0,ST(300),S(300),E(3,300),
     + ET(3,300),PE(3,300),PET(3,300),EE(3,3),EEP(300),LL(300),
     + AL(3,300),NP,PR,N,  'T,EEP1,DS(3),SX,AIL(3),EPR(3),EPP(3),
     + IND,EE2(2,2),EEPT(300),ALT(3,300),HM,ID,ISS,EFAC
      DO 11 MI=1,N1
      DO 12 I=1,3
12    DSI(I)=DS(I)

99    SXA=SX-AIL(1)
      SYA=SY-AIL(2)
      SM=(SXA+SYA-ID*AIL(3))/3
      SA(1)=SXA-SM
      SA(2)=SYA-SM
      SA(3)=(-AIL(3)-SM)*ID

      CALL HS(EEP1,H1,SI1,SIV1,IH1)
      CALL PL1
      CALL HS(EEP2,H2,SI2,SIV2,IH2)
      IF (IH2.EQ.IH1) THEN

C NO KINK
      B1=(SIV2-SIV1)/SIV1
      NRT=INT(B1/B0)+1
      DO 5 I=1,2+ID
      DSI(I)=DSI(I)/NRT
      AIL(I)=AIL(I)+(A2L(I)-AIL(I))/NRT
      EPR(I)=EPR(I)+DE(I)/NRT
5     EPP(I)=EPP(I)+DP(I)/NRT
      SX=SX+DSI(1)
      SY=SY+DSI(2)
      EEP1=EEP1+(EEP2-EEP1)/NRT
      DO 10 I=1,NRT-1
      SXA=SX-AIL(1)
      SYA=SY-AIL(2)
      SM=(SXA-SYA-ID*AIL(3))/3
      SA(1)=SXA-SM
      SA(2)=SYA-SM
      SA(3)=(-AIL(3)-SM)*ID
      CALL PL1
      EEP1=EEP2
      DO 15 I=1,2+ID
      AIL(I)=A2L(I)
      EPR(I)=EPR(I)+DE(I)
15    EPP(I)=EPP(I)+DP(I)
      SX=SX+DSI(1)
      SY=SY+DSI(2)
10    CONTINUE

      ELSE

C WITH KINK
      B=(SP(IH1+1)-EEP1)/(EEP2-EEP1)
      B1=(SS(IH1+1)-SIV1)/SIV1
      IF (B1.GT.B0) THEN
      B=B*B0/B1
      EEP1=EEP1+B*(EEP2-EEP1)
      ELSE
      EEP1=SP(IH1+1)
      ENDIF
      DO 20 I=1,2+ID
      AIL(I)=AIL(I)+(A2L(I)-AIL(I))*B
      EPR(I)=EPR(I)+DE(I)*B
20    EPP(I)=EPP(I)+DP(I)*B
      SX=SX+DSI(1)*B
      SY=SY+DSI(2)*B
      DSI(1)=DSI(1)*(1.-B)
      DSI(2)=DSI(2)*(1.-B)
      GO TO 99
      ENDIF

11    CONTINUE
      END


      SUBROUTINE PL1

C UTILIZES THE PLASTIC CONSTITUTIVE MATRIX FOR A GIVEN DISPLACEMENT
C INCREMENT TO CALCULATE THE VARIATION IN STRAINS & STRESSES.

      IMPLICIT REAL*8 (A-H,O-Z)
      COMMON E0,F0,C,A,NE,EM,PI,RM,AE,SY,SS(30),SP(30),DSX,DSI(3),
     + EEP2,SA(3),SM,A2L(3),DE(3),DP(3),B0,ST(300),S(300),E(3,300),
     + ET(3,300),PE(3,300),PET(3,300),EE(3,3),EEP(300),LL(300),
```

```
        DLA=DLA*3./BOT

C CALCULATE PLASTIC STRAIN INCREMENTS
        DO 80 I=1,2+ID
80      DP(I)=3.*SA(I)*DLA

C CALCULATE THE NEW EFFECTIVE PLASTIC STRAIN (EEP2)
        DEEP=2*SI*DLA
        EEP2=EEP1+DEEP
        IF (HM.GE.0) THEN

C CALCULATE THE COORDINATES OF NEW YIELD SURFACE CENTER
        DO 15 I=1,2+ID
15      A2L(I)=A1L(I)+2*HM*H*DLA*(SA(I)+SM)
        ELSE
        DO 16 I=1,2+ID
16      A2L(I)=A1L(I)+2*HM*H*DLA*SA(I)
        ENDIF
        END


        SUBROUTINE BAS(D,XN,L)

C CALCULATES THE AXIAL FORCE CORRESPONDING TO A GIVEN POSITION OF
C BENDING NEUTRAL AXIS.

        IMPLICIT REAL*8 (A-H,O-Z)
        COMMON E0,F0,C,A,NE,EM,P1,RM,AE,SY,SS(30),SP(30),DSX,DS1(3),
     +  EEP2,SA(3),SM,A2L(3),DE(3),DP(3),B0,ST(300),S(300),E(3,300),
     ,  ET(3,300),PE(3,300),PET(3,300),EE(3,3),EEP(300),LL(300),
     +  AL(3,300),NP,PR,N,LAST,EEP1,DS(3),SX,A1L(3),EPR(3),
     +  IND,F2(2,2),EEPT(300),ALT(3,300),HM,ID,ISS,EFAC
        XN=0
        F1=F0+D
        ZZZ=PI/2*(1.-1./NE)
        IF(F1.GT.ZZZ.OR.F1.LT.-ZZZ)THEN
        IF (N.GT.1) THEN
        WRITE(*,*(' N.A. HAS GONE OFF'))
        STOP
        ELSE
        LAST=1
        RETURN
        ENDIF
        ELSE
        LAST=0
        ENDIF
```

```
     +  AL(3,300),NP,PR,N,LAST,EEP1,DS(3),SX,A1L(3),EPR(3),EPP(3),
     +  IND,EE2(2,2),EEPT(300),ALT(3,300),HM,ID,ISS,EFAC
        DIMENSION PR2(3),SPR2(3,3),S2R2(2,2),EP2(2,2),EP(3,3)

        IF (ID.EQ.0) THEN
        CALL MUL(SA,EE2,PR2,1,2,2)
        CALL MUL(PR2,PR2,S2R2,2,1,2)
        ELSEIF (ID.EQ.1) THEN
        CALL MUL(SA,EE,PR2,1,3,3)
        CALL MUL(PR2,PR2,SPR2,3,1,3)
        ELSE
        WRITE(*,*)(5X,'ERROR: ID MUST BE EITHER 0 OR 1')
        STOP
        ENDIF
        CALL MUL(PR2,SA,PR3,1,2+ID,1)
        CALL HS(EEP1,H,SI,SIV,IH)
        BOT=9*PR3+4*H*SI*SI
        IF (ID.EQ.0) THEN

C 2-D ANALYSIS
        DO 70 I=1,2
        DO 70 J=1,2
70      EP2(I,J)=EE2(I,J)-S2R2(I,J)*9/BOT

C CALCULATE STRAIN INCREMENTS
        DEN=EP2(1,1)*EP2(2,2)-EP2(1,2)*EP2(2,1)
        DE(1)=(DS1(1)*EP2(2,2)-DS1(2)*EP2(1,2))/DEN
        DE(2)=(DS1(2)*EP2(1,1)-DS1(1)*EP2(2,1))/DEN

        ELSE

C 3-D ANALYSIS
        DO 71 I=1,3
        DO 71 J=1,3
71      EP(I,J)=EE(I,J)-SPR2(I,J)*9/BOT

        DEN=EP(1,1)*(EP(2,2)*EP(3,3)-EP(2,3)*EP(3,2))-EP(1,2)*(EP(2,1)*
     1  EP(3,3)-EP(2,3)*EP(3,1))+EP(1,3)*(EP(2,1)*EP(3,2)-EP(2,2)*EP(3,1))
        DE(1)=(DS1(1)*(EP(2,2)*EP(3,3)-EP(2,3)*EP(3,2))-DS1(2)*
     1  (EP(1,2)*EP(3,3)-EP(3,3)-EP(1,3)*EP(3,2)))/DEN
        DE(2)=(-DS1(1)*(EP(2,1)*EP(3,3)-EP(2,3)*EP(3,1))+EP(3,1))+DS1(2)*
     1  (EP(1,1)*EP(3,3)-EP(1,3)*EP(3,1)))/DEN
        DE(3)=(DS1(1)*(EP(3,2)-EP(3,2)-EP(2,2)*EP(3,1))-DS1(2)*
     1  (EP(1,1)*EP(3,2)-EP(1,2)*EP(3,1)))/DEN

        ENDIF
        CALL MUL(PR2,DE,DLA,1,2+ID,1)
```

185

```fortran
      DO 5 K=1,NE
      TE=PI/2*((2.*K-1.)/NE-1)
C FIND THE INCREASED ENGINEERING STRAIN
      EXN=E0+C*RM*(DSIN(TE)-DSIN(F1))*(1.+E0)
      IF (ISS.GT.0) THEN
C CONVERT TO TRUE STRAIN
      EXN=DLOG(1.+EXN)
      ELSEIF (ISS.LT.0) THEN
C CONVERT TO LAGRANGIAN STRAIN
      EXN=EXN*(1.+EXN/2.)
      ENDIF
C CALCULATE THE STRAIN INCREMENT (DEX)
      DEX=EXN-E(1,K)
      CALL HS(EEP(K),H,SI,SIV,IH)
      C1=AL(1,K)+(SY-AL(2,K)-AL(3,K)*ID)/2.
      ROO=DSQRT(4*SI*SI-3*(SY-AL(2,K)+AL(3,K)*ID)**2)/2
      SXC=C1-ROO
      SXT=C1+ROO
C LL(K)=0: INITIALLY ELASTIC; LL(K)=1: INITIALLY PLASTIC
      IF (LL(K).EQ.0) THEN
C INITIALLY ELASTIC
      IF (DEX.GT.0) THEN
      DSXY=SXT-S(K)
      ELSE
      DSXY=SXC-S(K)
      ENDIF
      DEXY=DSXY/EM
      IF (ABS(DEX).LE.ABS(DEXY)) THEN
C FINALLY ELASTIC
      CALL EL(K,DEX)
      ELSE
C FINALLY PLASTIC
      CALL EL(K,DEXY)
      DPD=DEX-DEXY
      CALL PL(K,DPD,1)
      IF (LEQ.1) LL(K)=1
      ENDIF
C
      ELSE
C INITIALLY PLASTIC
      SXA=S(K)-AL(1,K)
      SYA=SY-AL(2,K)
      SM=(SXA+SYA-ID*AL(3,K))/3
      SA(1)=SXA-SM

      TES=EFAC*DEX
      TES=TES*(TES+2*S(K)-SY-2*AL(1,K)+AL(2,K)+AL(3,K))
      IF (TES.GT.0.0D+0) THEN
C REMAINS PLASTIC (ONLY PLASTIC LOADING)
      CALL PL(K,DEX,0)
      ELSE
C UNLOAD FROM YIELD (FIRST AN ELASTIC LOADING)
      IF (SA(1).LE.0) THEN
C INITIALLY IN COMP. YIELD
      DSXY=SXT-S(K)
      ELSE
C INITIALLY IN TENSION YIELD
      DSXY=SXC-S(K)
      ENDIF
      DEXY=DSXY/EM
      IF (ABS(DEX).LE.ABS(DEXY)) THEN
C FINALLY ELASTIC
      CALL EL(K,DEX)
      IF (LEQ.1) LL(K)=0
      ELSE
C FINALLY PLASTIC
      CALL EL(K,DEXY)
      DPD=DEX-DEXY
      CALL PL(K,DPD,1)
      IF (LEQ.1) LL(K)=1
      ENDIF
      ENDIF

      ENDIF

      IF (ISS.LT.0) THEN
C 2nd PIOLA-KIRCHHOFF STRESS & LAGRANGIAN STRAIN
      CC=DSQRT(1+2*ET(1,K))
      ELSEIF (ISS.GT.0) THEN
```

```
C TRUE STRESS & STRAIN
      CC=1./DEXP(ET(1,K))
      ELSE
C ENGINEERING STRESS & STRAIN
      CC=1.D-0
      ENDIF
5     XN=XN-AE*ST(K)*CC
      END


      SUBROUTINE EL(K,EX)

C CALCULATES THE ELASTIC LONG. STRESS AND STRAIN INCREMENTS
C FOR A GIVEN LONG. STRAIN INCREMENT

      IMPLICIT REAL*8 (A-H,O-Z)
      COMMON E0,F0,C,A,NE,EM,PI,RM,AE,SY,SS(30),SP(30),DSX,DS1(3),
     + EEP2,SA(3),SM,A2L(3),DE(3),DP(3),B0,ST(300),S(300),E(3,300),
     + ET(3,300),PE(3,300),PET(3,300),EE(3,3),EEP(300),LL(300),
     + AL(3,300),NP,PR,N,LAST,EEP1,DS(3),SX,A1L(3),EPR(3),EPP(3),
     + IND,EE2(2,2),EEPT(300),ALT(3,300),HM,ID,ISS,EFAC
      ST(K)=S(K)+EM*EX
      ET(1,K)=E(1,K)+EX
      ET(2,K)=E(2,K)-EX*PR
      ET(3,K)=E(3,K)-EX*PR
      EEP(K)=EEP(K)
      DO 5 I=1,3
      ALT(1,K)=AL(1,K)
5     PET(1,K)=PE(1,K)
      END


      SUBROUTINE PL(K,EX,ICODE)

C BREAKS A PLASTIC LOADING INCREMENT TO SUB INCREMENTS (IF
C NECESSARY) AS DESCRIBED UNDER SUBROUTINE APS.  THEN THROUGH
C SUBROUTINE PL2, CALCULATES THE NEW VALUES OF STRAIN, STRESS, ETC.
C ICODE=0 MEANS THAT THIS EXECUTION IS A TRIAL AND THE POSITION OF
C THE BENDING NEUTRAL AXIS IS NOT FINALIZED YET.
C ICODE=1 MEANS THAT THE POSITION OF THE BENDING NEUTRAL AXIS IS
C FINAL FOR THE CURVATURE INCREMENT AND THE RESULTS WILL BE USED IN
C THE OUTPUT.

C E(I,K): STRAIN OF Kth ELEMENT IN Ith DIRECTION


C ET(I,K): TRIAL VALUE FOR E(I,K)
C PE(I,K): PLASTIC STRAIN OF ELEMENT Kth ELEMENT IN Ith DIRECTION
C PET(I,K): TRIAL VALUE FOR PE(I,K)
C AL(I,K): Ith COORDINATE OF THE YIELD SURFACE CENTER FOR Kth ELEMENT
C ALT(I,K): TRIAL VALUE FOR AL(I,K)
C S(K): LONGITUDINAL STRESS FOR Kth ELEMENT
C ST(K): TRIAL VALUE FOR S(K)
C EEP(K): EFFECTIVE PLASTIC STRAIN FOR Kth ELEMENT
C EEPT(K): TRIAL VALUE FOR EEP(K)

      IMPLICIT REAL*8 (A-H,O-Z)
      COMMON E0,F0,C,A,NE,EM,PI,RM,AE,SY,SS(30),SP(30),DSX,DS1(3),
     + EEP2,SA(3),SM,A2L(3),DE(3),DP(3),B0,ST(300),S(300),E(3,300),
     + ET(3,300),PE(3,300),PET(3,300),EE(3,3),EEP(300),LL(300),
     + AL(3,300),NP,PR,N,LAST,EEP1,DS(3),SX,A1L(3),EPR(3),EPP(3),
     + IND,EE2(2,2),EEPT(300),ALT(3,300),HM,ID,ISS,EFAC
      IF (ICODE.EQ.0) THEN
      DO 2 I=1,2+ID
      ET(I,K)=E(I,K)
      PET(I,K)=PE(I,K)
2     ALT(I,K)=AL(I,K)
      ST(K)=S(K)
      EEPT(K)=EEP(K)
      ENDIF

      DE(1)=EX

99    SXA=ST(K)-ALT(1,K)
      SYA=SY-ALT(2,K)
      SM=(SXA+SYA-ID*ALT(3,K))/3
      SA(1)=SXA-SM
      SA(2)=SYA-SM
      SA(3)=(-ALT(3,K)-SM)*ID

      CALL HS(EEPT(K),H1,SI1,SIV1,IH1)
      CALL PL2(K)
      CALL HS(EEP2,H2,SI2,SIV2,IH2)
      IF (IH2.EQ.IH1) THEN

C NO KINK
      B1=(SIV2-SIV1)/SIV1
      NRT=INT(B1/B0)+1
      DO 5 I=1,2+ID
      ALT(I,K)=ALT(I,K)+(A2L(I)-ALT(I,K))/NRT
      PET(I,K)=PET(I,K)+DP(I)/NR (
      ET(I,K)=ET(I,K)+DE(I)/NRT
5     ST(K)=ST(K)+DSX/NRT
```

187

```
EEPT(K)=EEPT(K)+(EEP2-EEPT(K))/NRT
DE(I)=DE(I)/NRT
DO 10 J=1,NRT-1
SXA=ST(K)-ALT(1,K)
SYA=SY-ALT(2,K)
SM=(SXA+SYA-ID*ALT(3,K))/3
SA(1)=SXA-SM
SA(2)=SYA-SM
SA(3)=(-ALT(3,K)-SM)*ID
CALL PL2(K)
DO 15 I=1,2+ID
ALT(1,K)=A2L(I)
PET(1,K)=PET(1,K)+DP(I)
15   ET(1,K)=ET(1,K)+DE(I)
ST(K)=ST(K)+DSX
EEPT(K)=EEP2
10   CONTINUE

     ELSE

C    WITH KINK
     B=(SP(IH1+1)-EEPT(K))/(EEP2-EEPT(K))
     B1=(SS(IH1+1)-SIV1)/SIV1
     IF (B1.GT.B0) THEN
     B=B*B0/B1
     EEPT(K)=EEPT(K)+B*(EEP2-EEPT(K))
     ELSE
     EEPT(K)=SP(IH1+1)
     ENDIF
     DO 20 I=1,2+ID
     ALT(1,K)=ALT(1,K)+(A2L(I)-ALT(1,K))*B
     PET(1,K)=PET(1,K)+DP(I)*B
20   ET(1,K)=ET(1,K)+DE(I)*B
     ST(K)=ST(K)+DSX*B
     DE(I)=DE(I)*(1.-B)
     GO TO 99
     ENDIF

     END


     SUBROUTINE PL2(K)

C    CALCULATES THE PLASTIC LONG. STRESS INCREMENT AND STRAIN
C    INCREMENTS FOR A GIVEN LONG. STRAIN INCREMENT.

C    [EP]: PLASTIC MATERIAL STIFFNESS MATRIX

     IMPLICIT REAL*8 (A-H,O-Z)
     DIMENSION PR2(3),SPR2(3,3),S2R2(2,2,
    + EP(3,3)
     COMMON E0,F0,C,A,NE,EM,PI,RM,AE,SY,SS(30),SP(30),DSX,DSI(3),
    + EEP2,SA(3),SM,A2L(3),DE(3),DP(3),B0,ST(300),S(300),E(3,300),
    + ET(3,300),PE(3,300),PET(3,300),EE(3,3),EEP(300),LL(300),
    + AL(3,300),NP,PR,N,LAST,EEP1,DS(3),SX,A1L(3),EPR(3),EPR(3),
    + IND,EE2(2,2),EEPT(300),ALT(3,300),HM,ID,ISS,EFAC

     IF (ID.EQ.0) THEN
     CALL MUL(SA,EE2,PR2,1,2,2)
     CALL MUL(PR2,PR2,S2R2,2,1,2)
     ELSEIF (ID.EQ.1) THEN
     CALL MUL(SA,EE,PR2,1,3,3)
     CALL MUL(PR2,PR2,SPR2,3,1,3)
     ELSE
     WRITE(*,'(5X,"ERROR: ID MUST BE EITHER 0 OR 1")')
     STOP
     ENDIF
     CALL MUL(PR2,SA,PR3,1,2+ID,1)
     CALL HS(EEPT(K),H,SI,SIV,IH)
     BOT=9*PR3+4*H*SI*SI
     IF (ID.EQ.0) THEN

C    2-D ANALYSIS
     DO 70 I=1,2
     DO 70 J=1,2
70   EP(I,J)=EE2(I,J)-S2R2(I,J)*9/BOT

C    CALCULATE HOOP STRAIN INCREMENT
     DE(2)=-EP(2,1)*DE(1)/EP(2,2)

C    CALCULATE LONG. STRESS INCREMENT
     DSX=EP(1,1)*DE(1)+EP(1,2)*DE(2)
     ELSE

C    3-D ANALYSIS
     DO 71 I=1,3
     DO 71 J=1,3
71   EP(I,J)=EE(I,J)-SPR2(I,J)*9/BOT
     DETT=EP(2,2)*EP(3,3)-EP(2,3)*EP(3,2)

C    CALCULATE HOOP AND THROUGH-THICKNESS STRAIN INCREMENTS
     DE(2)=-DE(1)*(EP(2,1)*EP(3,3)-EP(2,3)*EP(3,1))/DETT
     DE(3)=-DE(1)*(EP(2,1)*EP(3,2)-EP(2,2)*EP(3,1))/DETT
```

```
C CALCULATE LONG. STRESS INCREMENT
      DSX=EP(1,1)*DE(1)+EP(1,2)*DE(2)+EP(1,3)*DE(3)
      ENDIF

      CALL MUL(PR2,DE,DLA,1,2+ID,1)
      DLA=DLA*3./BOT
      DO 80 I=1,2+ID

C CALCULATE PLASTIC STRAIN INCREMENTS
80    DP(I)=3.*SA(I)*DLA

C CALCULATE THE NEW EFFECTIVE PLASTIC STRAIN (EEP2)
      DEEP=2*SI*DLA
      EEP2=EEPT(K)+DEEP
      IF (HM.GE.0) THEN

C CALCULATE THE COORDINATES OF NEW YIELD SURFACE CENTER
      DO 15 I=1,2+ID
15    A2L(I)=ALT(I,K)+2*HM*H*DLA*(SA(I)+SM)
      ELSE
      DO 16 I=1,2+ID
16    A2L(I)=ALT(I,K)-2*HM*H*DLA*SA(I)
      ENDIF

      END
```

APPENDIX C

User's Manual for Program PDA

C.1 General

Program PDA computes the global moment vs. curvature response of a closed-ended pipe using the local moment vs. curvature curve output from PAPS. The program uses an iterative procedure to incorporate secondary moments. These moments must be added to the end moments in order to obtain the moment value at any section along the length of the pipe. The secondary moments consist of axial force correction and the pressure force correction as described in Section 3.2.5.2.

The program is capable of tracking the global response of the pipe only up to the limit point (peak) of the response. In other words, it can follow the response as long as it is ascending. It is possible to draw closer to the limit point by executing the program several times. In each of these executions, some input parameters must be updated based on the previous results.

Program PDA is written in FORTRAN 77 language. The moment and curvature values input to the program must be consistent with the PAPS output. It means that the curvature values must be scaled by a factor of 10^4, and the moment values are scaled by a factor of 10^{-6}. The output values are also scaled by the same factors (i.e., consistent with the PAPS output). The input and output files for program PDA are described in the following sections.

C.2 Input

The input file for program PDA consists of the geometric measures of the pipe, the magnitudes of the loads, the values prescribing the refinement of the increments and tolerances, and the local moment vs. curvature response. The input file must be under the name INX and located in the same directory as that of the program. The structure of input file is described in the following subsections.

C.2.1 Line 1

TITLE   Format (A80)

This line allows for inputting a title to be printed at the top of the output file.

C.2.2 Line 2

LR   Format (A80)

LR: Name of the file containing the local moment vs. curvature of the pipe

Note: The values of curvature and moment must comprise the first two columns of a block of data in the input file LR, respectively. The file OU presented in Section A.4.2.1 of Appendix A is an example for the input file containing the local moment vs. curvature of the pipe. The values of moment and curvature in the file OU are in the block of data below the dashed line

C.2.3 Line 3

N1, NP   Format (*)

N1:   Number of rows of data in the LR file preceding the block of the local moment vs. curvature data (for the file OU in Section A.4.2.1, N1 is the number of rows from the beginning to the dashed line.)

NP: Number of rows of data in the block containing the local moment vs. curvature data

C.2.4 Line 4

RI, XL, PR, P   Format (*)

RI: Inside radius of the pipe

XL: Length of the pipe

PR: Internal pressure

P: External axial load

C.2.5 Line 5

NE, CM, NC, TOL   Format (*)

NE: Number of longitudinal divisions (elements) of the half-pipe (see Fig. 5.5)

CM: Final value of curvature at the end of the pipe

Note: It is possible that the peak point of the global response occurs prior to the attainment of CM. In this case the program fails to continue beyond the peak point.

NC: Number of the end curvature increments

Note: The initial end curvature increment is equal to CM/NC. The number of the curvature increments equals NC if the peak point of the response occurs after the attainment of CM. Otherwise, the number of output points will be less than NC. However, there is an option of refining the magnitude of the increments so as to approach th ͟ ͟ ͟ ͟ point more closely. The following range is recommended for NC.

$$10^2 \, CM \le NC \le 4 \times 10^2 \, CM$$

TOL: Tolerance for the relative change of the end curvature (dimensionless) used to check the convergence of the iterative procedure; a value of 10^{-5} is recommended for TOL.

C.2.6 Line 6

N, CL1, CL2, CL3, CL4, FAC   Format (*)

N: Positive integer used to refine the end curvature increment once the overall curvature exceeds CL1 (described below); a value of 2 is recommended for N.

Note: The parameters CL1, CL2, CL3, and CL4 are limits of curvature for a sequence of solutions. The values of CL1, CL2, CL3, and CL4 are improved with successive runs of the program.

CL1:   Limit for the overall curvature increment after which the first refinement in the size of the increments is made

Note: The program carries out a refinement internally as follows.

$$DC1 = \frac{DC}{10^N}$$ (C.1)

where DC is the initial value of the end curvature increment (= CM/NC) and DC1 is the new, refined value of the end curvature increment.

For the first execution of the program, CL1, CL2, CL3, and CL4 must be given values greater than or equal CM to make sure they do not interfere with the procedure. If the first execution of the program stops before attaining CM, the value of CL1 is recommended to be set equal to the last overall curvature in the output for the second execution (CL1 should not exceed that value). Meanwhile, CL2, CL3, and CL4 must not be changed.

CL2:   Second overall curvature limit ($\ge$ CL1) after which the current size of the end curvature increment (DC1) is divided by 10

Note: The program carries out a refinement internally as follows.

$$DC2 = \frac{DC1}{10} \qquad\qquad (C.2)$$

where DC2 is the new, refined value of the end curvature increment.

For the third execution of the program, the value of CL2 is recommended to be set equal to the last overall curvature in the output for the second execution (CL2 should not exceed that value). Meanwhile, CL1, CL3, and CL4 must not be changed.

CL3: Third overall curvature limit ($\geq$ CL2) after which the current size of the end curvature increment (DC2) is divided by 10

Note: The program carries out a refinement internally as follows.

$$DC3 = \frac{DC2}{10} \qquad\qquad (C.3)$$

where DC3 is the new, refined value of the end curvature increment.

For the fourth execution of the program, the value of CL3 is recommended to be set equal to the last overall curvature in the output for the third execution (CL3 should rot exceed that value). Meanwhile, CL1, CL2, and CL4 must not be changed.

CL4: Fourth overall curvature limit ($\geq$ CL3) after which the current size of the end curvature increment (DC3) is divided by FAC (the next item described below)

Note: The refinement is carried out as follows.

$$DC4 = \frac{DC3}{FAC} \qquad\qquad (C.4)$$

where DC4 is the new, refined value of the end curvature increment.

For the fifth execution of the program, the value of CL4 is recommended to be set equal to the last overall curvature in the output for the fourth execution (CL4 should not exceed that value). Meanwhile, CL1, CL2, and CL3 must not be changed.

FAC: Positive integer used to refine the end curvature increment once the overall curvature exceeds CL4 (as described above); a value of 100 can be recommended for FAC.

C.2.7 Line 7

CLT, FT   Format (*)

CLT: Overall curvature limit after which the tolerance (TOL) is divided by FT (the next item described below)

Note: The refinement is carried out as follows.

$$(TOL)_{new} = \frac{TOL}{FT} \qquad\qquad (C.5)$$

·   where $(TOL)_{new}$ is the new value of the tolerance.

The current tolerance may be too large for the refined values of the end curvature increment. This results in the divergence of the solution. Upon obtaining a diverging solution, the value of CLT should be set at a value slightly less than the last value of overall curvature in the output file. However, to prevent divergence, it is recommended that the value of CLT be always set equal to CL2.

FT: Positive integer used to refine the tolerance (TOL) once the overall curvature exceeds CLT (as described above); a value in the range of 5 to 10 is recommended for FT.

C.3 Output

Program PDA generates an output file by the name of OUT. The first two columns of the output file contain the overall curvature and end moment values. The rest of the columns give the values of the secondary moment at the mid-length of the original pipe (i.e., at the support of the half-pipe model shown in Fig. 5.5). The third column, under the SM1 heading, contains the values of the secondary moment due to the axial force in the pipe and the deflection of the pipe centerline. The fourth and fifth columns of data under the SM2 and SM3 headings contain the values of two components of the secondary moment due to internal pressure (i.e., pressure force correction, as described in Section 3.2.5.2). The fourth column gives the values of the secondary moment resulting from the component of the pressure force acting at the end of the pipe (i.e., P_i in Fig. 5.5) perpendicular to the original centerline of the pipe. The fifth column gives the values of the secondary moment due to the pressure force acting on the body of the pipe in a deformed configuration (see Section 3.2.5.2).

C.4 Example

As examples of input and output files, those used to model specimen DGA12W are presented herein. The PAPS output file OU, presented in Section A.4.2.1, is used as the input file for the local moment vs. curvature response. In the following, the input and output files for only the first execution of the PDA program are presented. These results form the basis for the curve designated by PAPS-UL-Iso. in Fig. 5.22.

C.4.1 Input File

DGA12W Global Response

OU

46,51

155.7365,1687,10.45,964E3

100,2.000,200,1E-5

2,2.000,2.000,2.0000,2.0000,100

2.0000,5

C.4.2 Output File

DGA12W Global Response

OVERALL CURV. x 1E-4	END MOMENT x 1E6	SM1	SM2	SM3
0.00000,	0.00000	0.00000	0.00000	0.00000
0.01017,	13.42355	0.06157	0.57349	-0.28407
0.02035,	26.84710	0.12314	1.14698	-0.56813
0.03052,	40.27065	0.18471	1.72047	-0.85220
0.04108,	53.69420	0.24918	2.31565	-1.14431
0.05135,	62.43515	0.31147	2.89454	-1.43038
0.06162,	71.17610	0.37377	3.47346	-1.71646
0.07189,	79.91705	0.43607	4.05237	-2.00254
0.08384,	88.65800	0.51100	4.72588	-2.32367
0.09432,	93.69778	0.57488	5.31661	-2.61413
0.10480,	98.73755	0.63875	5.90735	-2.90459
0.11528,	103.77733	0.70263	6.49808	-3.19504
0.12834,	108.81710	0.78595	7.23423	-3.53932

0.13903,	112.38240	0.85145	7.83708	-3.83426
0.14973,	115.94770	0.91694	8.43994	-4.12920
0.16242,	119.51300	1.00076	9.15564	-4.45056
0.18082,	123.07830	1.12117	10.19251	-4.92103
0.19250,	125.11025	1.19511	10.85108	-5.23186
0.20702,	127.14220	1.29319	11.66967	-5.58892
0.22310,	129.17415	1.39948	12.57576	-5.99495
0.24358,	131.20610	1.53986	13.73059	-6.48914
0.26006,	132.62963	1.65219	14.65951	-6.88942
0.27912,	134.05315	1.78388	15.73344	-7.34354
0.30043,	135.47668	1.93095	16.93474	-7.85264
0.32425,	136.90020	2.09508	18.27759	-8.42301
0.34407,	137.95295	2.23291	19.39499	-8.89171
0.36653,	139.00570	2.39186	20.66097	-9.40941
0.39177,	140.05845	2.57194	22.08374	-9.98436
0.42004,	141.11120	2.77458	23.67738	-10.62395
0.44603,	141.99063	2.96137	25.14243	-11.20958
0.47436,	142.87005	3.16563	26.73933	-11.84473
0.50504,	143.74947	3.38705	28.46868	-12.53156
0.53865,	144.62890	3.63080	30.36298	-13.27816
0.57376,	145.42648	3.88949	32.34211	-14.03906
0.61433,	146.22405	4.19188	34.62937	-14.90214
0.66166,	147.02163	4.54786	37.29712	-15.89322
0.71664,	147.81920	4.96354	40.39649	-17.03468
0.77168,	148.51955	5.38053	43.49879	-18.17281
0.83752,	149.21990	5.88365	47.21001	-19.51404
0.91339,	149.92025	6.46379	51.48692	-21.05815
1.01458,	150.62060	7.24815	57.19073	-23.06671

APPENDIX D

Program Listing for

P – DELTA ANALYSIS (PDA)

```
C     P-DELTA ANALYSIS
C
C     NADER YOOSEF-GHODSI  &  D. W. MURRAY
C
C     MARCH 1995
C
C A P-DELTA ANALYSIS OF A CLOSED-ENDED PIPE UNDER INTERNAL PRESSURE,
C AXIAL LOAD AND EQUAL END MOMENTS (SINGLE CURVATURE) UP TO THE
C LIMIT POINT.

      IMPLICIT REAL*8 (A-H,O-Z)
      DIMENSION C(4000),X(4000),KI(1000),XX(1000),CC(1000),
     + Y(1000),S(1000),SS(1000),G1(1000),G2(1000),UU(1000)
      CHARACTER*80 LR,ZZ,TITLE
      OPEN(1,FILE='INX')
      OPEN(3,FILE='OUT')
      READ(1,'(A)')TITLE
      WRITE(3,'(1X,A)') TITLE
      WRITE(3,'('  OVERALL CURV.  END MOMENT   SM1      SM2
     +    SM3')')
      WRITE(3,'(4x,66('-'))')
      WRITE(3,'(1x,F13.5,'' '',4F13.5)')0D0,0D0,0D0,0D0,0D0
      READ(1,'(A)')LR
      OPEN(2,FILE=LR)
      READ(1,*)N1,NP
      READ(1,*)RL,XL,PR,P
      READ(1,*)NE,CM,NC,TOL
      READ(1,*)N,CL1,CL2,CL3,CL4,FAC
      READ(1,*)CL,T,FT
      PP=DATAN(1.D+0)*4*RI*RI*PR

C READ THE MOMENT CURVATURE DIAGRAM (FOR CROSS-SECTION)
      DO 1 I=1,N1
1     READ(2,'(A)').ZZ

      DO 5 I=1,NP
5     READ(2,*)C(I),X(I)

C SCALE THE MOMENT AND CURVATURES BACK TO THE REAL ONE
      DO 6 I=1,NP
      C(I)=C(I)/1E4
      X(I)=X(I)*1E6
6     CM=CM/1E4

C DEFINE THE END CURVATURE INCREMENTS (USE FINER ONES LATER ON)
      DC=CM/NC
      DC1=DC/10.**N

      DC2=DC1/10
      DC3=DC2/10
      DC4=DC3/FAC

C DEFINE THE LENGTH OF ELEMENTS
      DL=.5*XL/NE

C DEFINE A CODE INDICATING THE POSITION OF EACH ELEMENT ON THE
C CROSS-SECTION MOMENT-CURVATURE DIAGRAM (K(I))
      DO 7 I=1,NE
7     KI(I)=1
      KE=1
      XE=0
      CE=0
10    IF(CO*1E4.GE.CL1)DC=DC1
      IF(CO*1E4.GE.CL2)DC=DC2
      IF(CO*1E4.GE.CL3)DC=DC3
      IF(CO*1E4.GE.CL4)DC=DC4
      IF(CO*1E4.GE.CL1)TOL=TOL/FT
      CE=CE+DC
      TEMP=XE

C FIND THE MOMENT FOR THE NEW END CURVATURE
12    IF(CE.GE.C(KE).AND.CE.LE.C(KE+1)) THEN
      XE=X(KE)+(X(KE+1)-X(KE))/(C(KE+1)-C(KE))*(CE-C(KE))
      ELSE
      KE=KE+1
      GO TO 12
      ENDIF
      DME=XE-TEMP

C ADD THE INCREASE IN END MOMENT TO ALL ELEMENT MOMENTS
      DO 20 K=1,NE
20    XX(K)=XX(K)+DME
      IF(XX(1).GT.X(NP))THEN
      WRITE(3,'('' REACHED THE END OF THE GIVEN CURVE'')')
      STOP
      ENDIF
32    TT=CC(1)
      SUM=0
      DO 25 K=1,NE
22    IF(XX(K).GE.X(KI(K)).AND.XX(K).LE.X(KI(K)+1)) THEN
      CC(K)=C(KI(K))+(C(KI(K)+1)-C(KI(K)))/(X(KI(K)+1)-X(KI(K)))*
     + (XX(K)-X(KI(K)))
      ELSE
      IF(KI(K).EQ.NP) THEN
      WRITE(*,'('' REACHED THE MAX. MOMENT'')')
```

```fortran
        STOP
        ENDIF
        KI(K)=KI(K)+1
        GO TO 22
        ENDIF
C CHECK IF THE CONVERGENCE IS ENOUGH
        IF (K.EQ.1) THEN
        ERR=ABS((CC(1)-IT)/CC(1))
        IF (ERR.LT.TOL)GO TO 42
        ENDIF
C INTEGRATE THE ELEMENT CURVATURES TO GET SLOPE
        SUM=SUM+DL*CC(K)
        S(K)=SUM
C INTEGRATE THE ELEMENT SLOPES TO GET DEFLECTION
        SS(K)=0
        DO 30 J=1,K
30      SS(K)=SS(K)+S(J)*DL
25      CONTINUE
        DO 40 K=1,NE
40      Y(K)=SS(NE)-SS(K)
        DO 35 K=1,NE
C UU: MOMENT OF PRESSURE FORCES ACTING ON ELEMENTS FROM PIPE END
C TO CURRENT ELEMENT
        UU(K)=0
        DO 60 I=K+1,NE
60      UU(K)=UU(K)+CC(I)*(I-K)
        UU(K)=UU(K)*PP*DL*DL
C S(NE): END SLOPE
C PI: INSIDE AREA OF PIPE TIMES PRESSURE
        G1(K)=(P-PP)*Y(K)
        G2(K)=PP*S(NE)*.5*(XL-(2*K-1)*DL)
35      XX(K)=XE-UU(K)+G1(K)+G2(K)
        GO TO 32
C CO: THE OVERALL CURVATURE
42      CO=S(NE)*2/XL
        WRITE(3,(1x,F13.5,' ',4F13.5))CO*1E4,XE/1E6,G1(1)/1E6
     +  ,G2(1)/1E6,-UU(1)/1E6
        WRITE(*,(5F13.5))CE*1e4,CO*1E4,XE/1E6,CC(1)*1E4,XX(1)/1E6
        GO TO 10
        END
```

APPENDIX E

STRAIN, STRESS AND CURVATURE FORMULATION

E.1 Strain Measures

In the program PAPS, at each curvature increment, the longitudinal strains for the elements around the cross-section are calculated in engineering strain measure. If any formulation other than ESS is chosen (i.e., UL or TL), the engineering strains need to be converted into a different type of strain (see Sect. 5.2.2.1). The definition and conversion formulas for different strain measures are descussed in the following.

a. Lagrangian Strain

Figure E.1 shows the original and deformed configurations of an infinitesimal element of the pipe. The directions in the figure are as defined in Sect. 5.2.2.3.3 (i.e., subscripts 1, 2, and 3 correspond to the longitudinal, circumferential, and through-thickness directions, respectively. In the program PAPS, an infinitesimally short pipe is considered to undergo symmetric bending. Therefore, the deformation of each element of the pipe is only straining with no rigid body motion. As a result, the three principal directions remain fixed throughout the deformation.

As Fig. E.1 shows, a_i and x_i are the ith coordinates of a body point in the original and deformed configurations, respectively. The Lagrangian strain (or Green's strain in the longitudinal direction, E_x is expressed as (Fung, 1965)

$$E_x = E_1 = \frac{\partial u_1}{\partial a_1} + \frac{1}{2}\left[\left(\frac{\partial u_1}{\partial a_1}\right)^2 + \left(\frac{\partial u_2}{\partial a_1}\right)^2 + \left(\frac{\partial u_3}{\partial a_1}\right)^2\right] \tag{E.1}$$

Where u_i is the displacement in the ith direction defined by

$$u_i = x_i - a_i \tag{E.2}$$

Hence in differential form,

$$du_i = dx_i - da_i \tag{E.3}$$

Since the directions 1, 2, and 3 are the principal axes and always remain fixed,

$$\frac{\partial u_2}{\partial a_1} = \frac{\partial u_3}{\partial a_1} = 0 \tag{E.4}$$

Thus, Eq. (E.1) becomes

$$E_x = E_1 = \frac{\partial u_1}{\partial a_1} + \frac{1}{2}\left(\frac{\partial u_1}{\partial a_1}\right)^2 \tag{E.5}$$

where $\dfrac{\partial u_1}{\partial a_1}$ is, by definition, the engineering strain, e_1.

$$e_x = e_1 = \frac{\partial u_1}{\partial a_1} \tag{E.6}$$

Hence,

$$E_x = e_x + \frac{e_x^2}{2} \tag{E.7}$$

Similarly, for the ith direction,

$$E_i = e_i + \frac{e_i^2}{2} \tag{E.8}$$

b. Logarithmic (true) strain

The updated Lagrangian strains can be reduced to the logarithmic strains when the principal axes remain fixed during deformation. The logarithmic strain in the ith direction, ε_i, can be expressed in terms of the engineering strain, e_i, as (Hill, 1950)

$$\varepsilon_i = \ln(1 + e_i) \qquad \text{(no sum)} \tag{E.9}$$

E.2 Area

Two measures of area are used in the formulations herein. They are the original and deformed areas, shown by dA_0 and dA in Fig. E.1, respectively. Assuming the volume of the element in Fig. E.1 remains constant during the deformation (this is a direct result of the flow rule for a plastic deformation, and is approximately valid for an elastic deformation),

$$dA\ dx_1 = dA_0\ da_1 \tag{E.10}$$

By substituting dx_1 from Eq. (E.3),

$$dA\left(1 + \frac{du_1}{da_1}\right) = dA_0 \tag{E.11}$$

where $\dfrac{du_1}{da_1}$ is the engineering longitudinal strain, e_1. Hence,

$$dA = \frac{dA_0}{1 + e_1} \tag{E.12}$$

E.3 Stress Measures

a. Engineering stress

Engineering stress is defined by the force per unit of the original area. Thus, the engineering longitudinal stress in Fig. E.1b can be expressed as

$$\sigma_1 = \frac{dT_1}{dA_0} \tag{E.13}$$

where dT_1 is the longitudinal component of the infinitesimal force vector acting on the area perpendicular to the longitudinal direction (part of the cross-section area). Here the longitudinal direction is a principal direction, therefore, dT_1 is the total force acting on the element surface.

b. True (Cauchy) stress

True stress is defined by the force per unit of the current area. Thus, the true longitudinal stress in Fig. E.1b can be written as

$$\tau_1 = \frac{dT_1}{dA} \tag{E.14}$$

From Eqs. (E.12), (E.13), and (E.14), the true stress is expressed in terms of the engineering stress as

$$\tau_1 = \sigma_1 (1 + e_1) \tag{E.15}$$

similarly, in general,

$$\tau_i = \sigma_i (1 + e_i) \qquad \text{(no sum)} \qquad \text{(E.16)}$$

c. 2nd Piola-Kirchhoff stress

Virtual forces $dT_i^{(k)}$, used to define 2nd Piola-Kirchhoff stress, are defined by (Fung, 1965)

$$dT_i^{(k)} = \frac{\partial a_i}{\partial x_j} dT_j \qquad \text{(E.17)}$$

Substituting for x_j from Eq. (E.2) and summing on j in Eq. (E.17) gives

$$dT_i^{(k)} = \frac{da_i}{da_i + du_i} dT_i = \frac{dT_i}{1 + e_i} \qquad \text{(no sum)} \qquad \text{(E.18)}$$

The 2nd Piola-Kirchhoff stress in the ith direction, s_i, (for the element shown in Fig. E.1) is defined by

$$s_i = \frac{dT_i^{(k)}}{(dA_0)_i} \qquad \text{(no sum)} \qquad \text{(E.19)}$$

where $(dA_0)_i$ is the original area perpendicular to the ith direction. Thus, for the longitudinal direction (note that $(dA_0)_1 = dA_0$)

$$s_1 = \frac{dT_1^{(k)}}{dA_0} \qquad \text{(E.20)}$$

Substituting $dT_1^{(k)}$ from Eq. (E.18) yields

$$s_1 = \frac{1}{1 + e_1} \frac{dT_1}{dA_0} = \frac{\sigma_1}{1 + e_1} \qquad \text{(E.21)}$$

Similarly, in the ith direction,

$$s_i = \frac{\sigma_i}{1 + e_i} \qquad \text{(no sum)} \qquad \text{(E.22)}$$

E.4 Calculation of Force in Different Formulations

The longitudinal force for each element, dT_1, is used to calculate the axial force and bending moment of the cross-section. The longitudinal force, dT_1, is obtained for different formulations as follows.

a. Engineering stress and strain (ESS)

From Eq. (E.13),

$$dT_1 = \sigma_1 \, dA_0 \qquad\qquad (E.23)$$

b. Updated Lagrangian formulation (UL)

From Eqs. (E.12) and (E.14),

$$dT_1 = \tau_1 \frac{dA_0}{1 + e_1} \qquad\qquad (E.24)$$

c. Total Lagrangian formulation (TL)

Equations (E.18), (E.20), and (E.21) yield

$$dT_1 = s_1 (1 + e_1) \, dA_0 \qquad\qquad (E.25)$$

E.5 Curvature Formulation

For the infinitesimally short slice of the pipe shown in Fig. E.2,

$$d\bar{a} = R \, d\alpha \qquad\qquad (E.26)$$

where $d\bar{a}$ is the length of the slice after the application of internal pressure and axial load, R is the radius of the bending neutral axis, and $d\alpha$ is the angle made by the end surfaces of the slice due to bending. By assuming that e_0 is the engineering strain of the cross-section at the start of bending, $d\bar{a}$ can be expressed as

$$d\bar{a} = da (1 + e_0) \qquad\qquad (E.27)$$

where da is the original length of the slice prior to any loading (see Fig. E.2).

Curvature in this study is defined as the inverse of the radius of the bending neutral axis. Thus, from Eqs. (E.26) and (E.27), the curvature, ϕ, can be written as

$$\phi = \frac{1}{R} = \frac{d\alpha}{da\,(1+e_0)} \qquad\qquad (E.28)$$

Hence,

$$d\alpha = \phi\,da\,(1+e_0) \qquad\qquad (E.29)$$

From the geometry of the deformed configuration in Fig. E.2,

$$d\alpha = \frac{dx - da\,(1+e_0)}{y} \qquad\qquad (E.30)$$

where dx is the length of the slice at the ordinate y, measured from the bending neutral axis (Fig. E.2). Eliminating $d\alpha$ from Eqs. (E.29) and (E.30) gives

$$\frac{dx - da}{da} - e_0 = \phi\,y\,(1+e_0) \qquad\qquad (E.31)$$

Here, $\dfrac{dx - da}{da}$ is, by definition, the engineering strain (e) at the ordinate y. Hence,

$$e = e_0 + \phi\,y\,(1+e_0) \qquad\qquad (E.32)$$

or

$$\phi = \frac{e - e_0}{y\,(1+e_0)} \qquad\qquad (E.33)$$

If $(1+e_0)$ in Eq. (E.33) is replaced by 1, Eq. (E.33) is consistent with the expressions used in Chapter 3 (e.g., Eq. (3.2)) for the experimental curvatures, . In fact, for the test specimens, the value of e_0 is negligible compared to 1. Therefore, the curvature formulas in Chapter 3 are in accord with the definition of curvature herein.
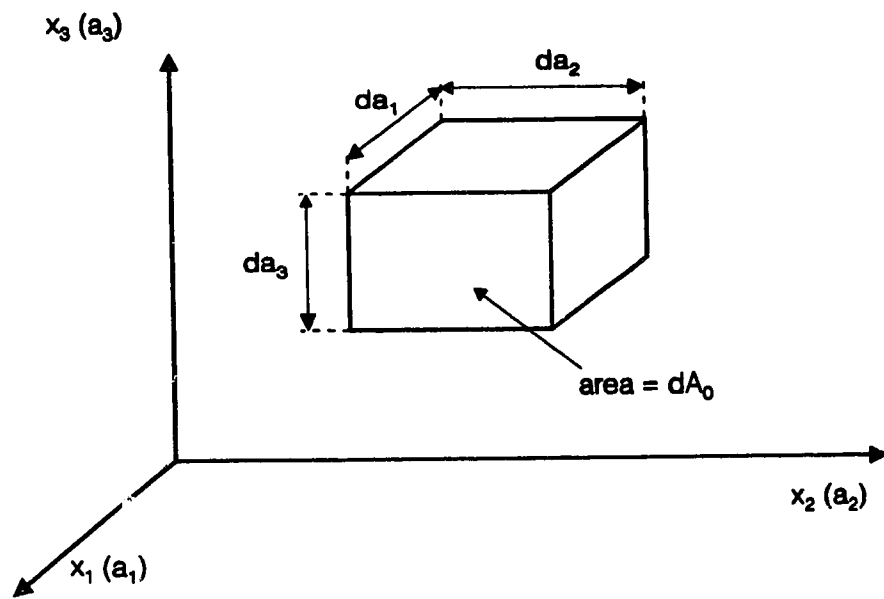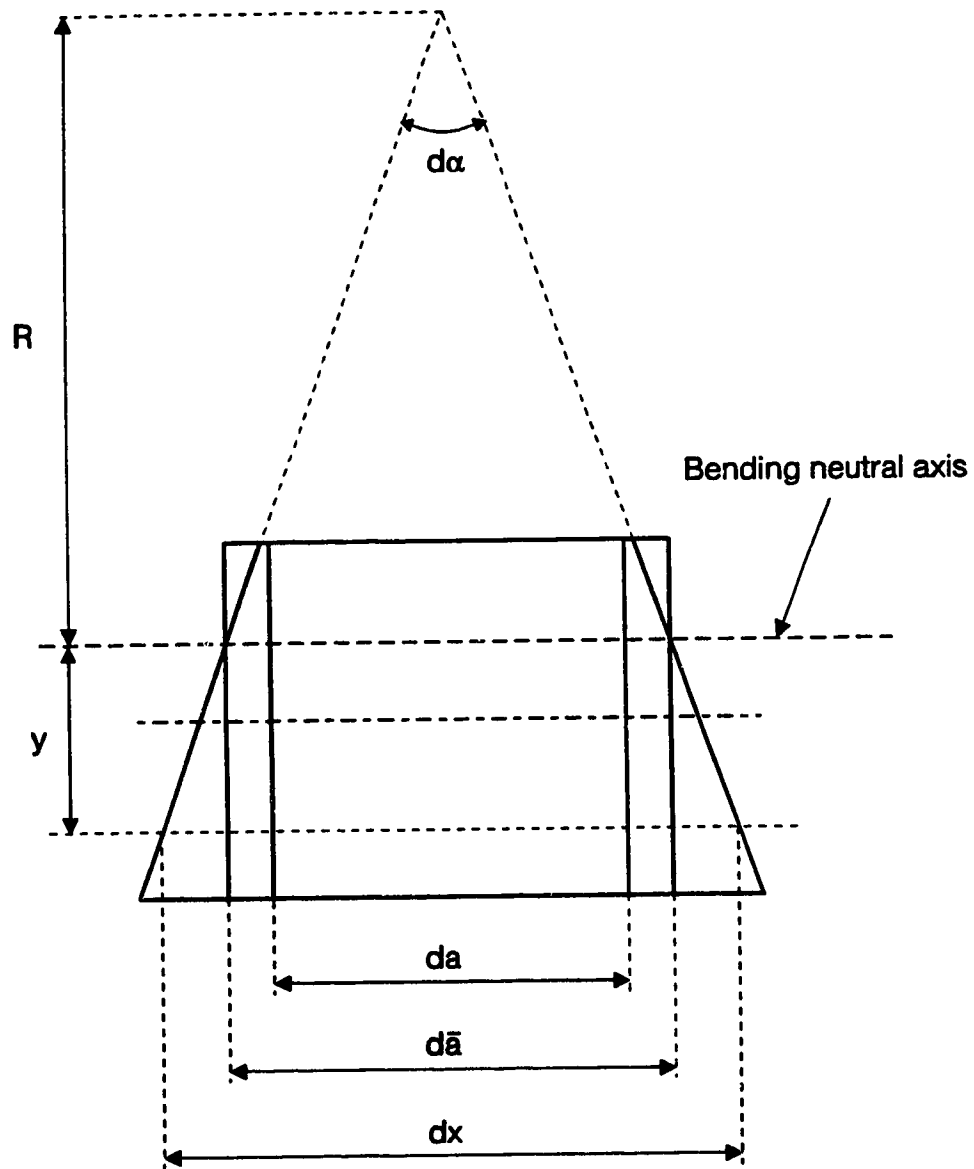
(a) Original element configuration
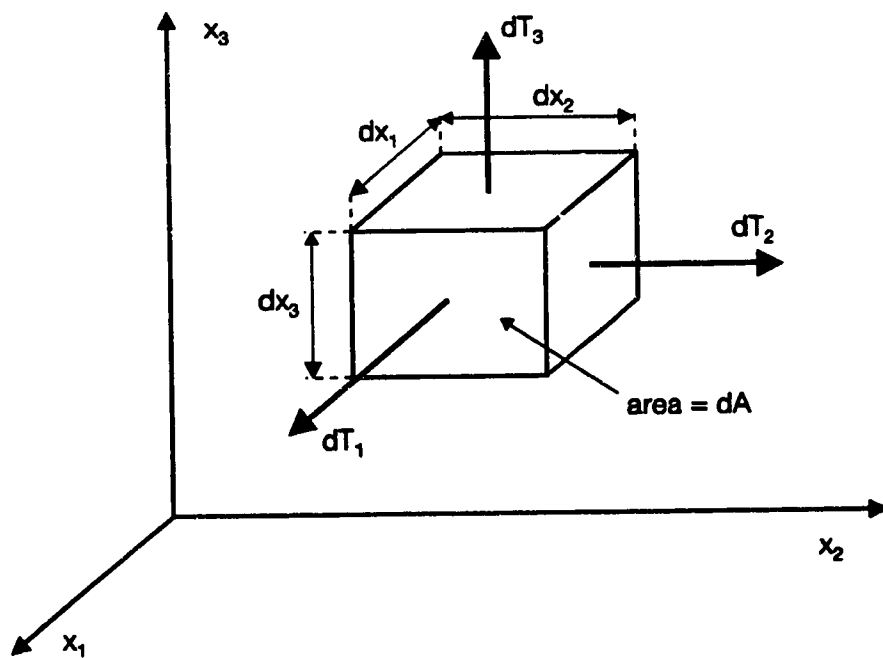
(b) Deformed element configuration

Fig. E.1 Original and deformed configurations of an element of pipe slice

Fig. E.2 Original and deformed configurations of pipe slice